
Bolted Connections for Rectangular Hollow Sections under Tensile Loading

Zur Erlangung des akademischen Grades eines

DOKTOR-INGENIEURS

von der Fakultät für
Bauingenieur-, Geo- und Umweltwissenschaften
der Universität Fridericiana zu Karlsruhe (TH)

genehmigte

DISSERTATION

von

Dipl. Ing. Silke Willibald
aus Karlsruhe

Tag der mündlichen Prüfung: 23. Mai 2003

Hauptreferent: Prof. Dr. Eur.-Ing. R. Puthli

Korreferenten: Prof. Dr. J. A. Packer

Prof. Dr.-Ing. F. Mang

Karlsruhe 2003

VORWORT

Hiermit möchte ich mich ganz herzlich bei allen bedanken, die diese Arbeit ermöglicht haben. Auf fachlicher Seite gilt meine Dankbarkeit insbesondere Professor Puthli und Professor Packer, die mir diesseits und jenseits des Atlantiks immer mit Rat und Tat zur Seite standen. Weiterhin gilt mein Dank auch Professor Mang, der sich durch seine jahrelange Erfahrung im Bereich der Hohlprofile auszeichnet.

Die beiden erstgenannten Professoren eröffneten mir die Möglichkeit zur Arbeit an der University of Toronto in Kanada, durch die ich fachlich und menschlich unbeschreiblich viel gewonnen habe. Viele Mitarbeiter, die mittlerweile sehr enge Freunde geworden sind, haben mir geholfen mich leicht in Kanada einzuleben. Spezieller Dank gilt hierbei den direkten Mitarbeitern von Professor Packer und dem Laborpersonal ("Thank you guys").

Der gleiche Dank für tolle Kollegialität und interessante Gespräche gilt den wissenschaftlichen Mitarbeitern an der Versuchsanstalt für Stahl, Holz und Steine, die mir teilweise bereits seit der Vertieferarbeit mit Rat und Tat zur Seite gestanden haben.

Zuletzt und am meisten möchte ich meinen Eltern danken. Sie haben mich von Anfang an sowohl in meinem Studium als auch bei meiner Doktorarbeit durch Zuspruch wie auch finanzielle Hilfe unterstützt. Der gleiche Dank gilt auch für meinen lieben Mann Nick, der mir mit moralischer und fachlicher Unterstützung sowie extremer Geduld beigestanden hat.

Karlsruhe, im Mai 2003

Silke Willibald

SUMMARY

The static strength of bolted, spliced connections for rectangular hollow sections under tensile loading is the topic of the presented study. A very common spliced connection type, the bolted flange-plate connection as well as a more recent connection type, the hidden joint connection have been studied. For clarity of presentation, the presented thesis has therefore been divided into two parts:

- Part I: Bolted flange-plate connections;
- Part II: Hidden joint connections.

Prying forces are the main concern with bolted flange-plate connections. Prying forces occur if the flange-plates lever against each other due to deformations of the plates under tensile loading. Depending on the bolt layout and flange-plate thickness, these prying forces can differ very significantly. Additionally, the formation of a complete yield line mechanism can also result in the collapse of connections with flexible flange-plates and strong bolts. Within the framework of the presented work, an experimental investigation with square and rectangular hollow sections has been carried out. State-of-the-art equipment has been used to record the load in the bolts. The subsequent non-linear Finite Element analyses (using 3D solids as well as contact elements), verified by the results of the experimental investigations, extended the database. A parallel analytical study, inter alia using yield line analysis, served as the basis for the derivation of specific design rules.

Part II of the presented thesis deals with so-called hidden joint connections, which are a modification of the more typical gusset plate connection with slotted hollow sections. In contrast to the more common gusset plate connections where the gusset plate protrudes beyond the width of the slotted member, the gusset plate of the hidden joint connection is fitted into the inside width of the unslotted hollow section. The aim of this research has been the derivation of a design model for shear lag failure, in particular the rupture of the hollow section due to shear lag. A limited number of tensile tests on hidden joint connections for square hollow sections has been carried out. Technical feasibility of welding inside the hollow section has been of special interest. The tests have been used to verify the numerical investigation, which again has been used as a basis for a new calculation method for shear lag failure of the hollow section.

KURZFASSUNG

Die vorliegende Arbeit beschäftigt sich mit der statischen Tragfähigkeit von geschraubten Stoßverbindungen für rechteckige Hohlprofile unter Zugbelastung. Eine weit verbreitete Stoßverbindung, die geschraubte Kopfplattenverbindung, sowie auch eine eher neuere Verbindung, der verdeckte Knoten, sind untersucht worden. Die vorliegende Arbeit wurde zur besseren Übersicht deshalb in zwei Abschnitte geteilt:

- Teil I: Geschraubte Kopfplattenverbindungen;
- Teil II: Verdeckte Knotenverbindungen.

Das Hauptproblem bei der Verwendung von Kopfplattenverbindungen besteht in den Abstützkräften. Diese Zusatzkräfte entstehen, wenn sich die Kopfplatten aufgrund der Verformungen unter Zugbelastung gegenseitig abstützen. Die Abstützkräfte können in Abhängigkeit von der Schraubenverteilung und Kopfplattendicke stark variieren. Andererseits kann die Bildung eines kompletten Fließlinienmechanismus für Verbindungen mit flexiblen Kopfplatten und sehr festen Schrauben auch zu einem Versagen führen. Im Rahmen der vorliegenden Arbeit ist eine experimentelle Untersuchung mit quadratischen und rechteckigen Hohlprofilen durchgeführt worden. Modernste Ausrüstung wurde zur Messung der Kräfte in den Schrauben verwendet. Die nachfolgenden nichtlinearen finiten Elementuntersuchungen (mit 3D Volumen- sowie Kontaktelementen) wurden mit den Ergebnissen der experimentellen Studie verifiziert und dienen der Erweiterung der Datenmenge. Eine parallel durchgeführte analytische Studie, die unter anderem Fließlinientheorie verwendet, diente als Basis zur Herleitung spezieller Bemessungsregeln.

Teil II der vorliegenden Arbeit behandelt sogenannte verdeckte Knoten, welche eine Abwandlung der gängigeren Knotenblechverbindungen mit geschlitzten Hohlprofilen darstellen. Im Gegensatz zu der verbreiteteren Knotenblechverbindung, bei der das Knotenblech über die Breite des Hohlprofils hinausragt, wird das Knotenblech bei verdeckten Knoten in die Innenseite des ungeschlitzten Hohlprofils eingepaßt. Ziel der Forschung war die Herleitung eines Bemessungsmodells gegen ein Versagen durch die örtlich begrenzte Lasteinleitung, insbesondere eines plötzlichen Risses des Hohlprofils durch die lokalen Spannungsspitzen. Eine begrenzte Anzahl von Zugversuchen an verdeckten Knoten für Quadrathohlprofile ist durchgeführt worden. Die technische Umsetzung der Schweißarbeiten im Innern des Hohlprofils war von speziellem Interesse. Die Versuche wurden zur Verifizierung einer numerischen Untersuchung verwendet, welche wiederum als Basis für neue Bemessungsformeln gegen ein Versagen des Hohlprofils durch örtlich begrenzte Lasteinleitung diente.

TABLE OF CONTENTS

INTRODUCTION	1
General Introduction	1
Scope of Work	3
PART I BOLTED FLANGE-PLATE CONNECTIONS	
1 <i>LITERATURE REVIEW</i>	4
1.1 Experimental Research on Bolted Flange-Plate Connections	5
1.2 Numerical Research on Bolted Flange-Plate Connections	6
1.3 Analytical Research and Design Models for Bolted Flange-Plate Connections	7
1.3.1 General Model (Timoshenko and Woinowsky- Krieger [1959])	7
1.3.2 Two-Dimensional Yield Line Model (Kato and Mukai [1982])	8
1.3.3 One-Dimensional Yield Line Models	9
1.3.3.1 General T-Stub Model (Struik and de Back [1969])	9
1.3.3.2 One-Dimensional Yield Line Model for Rectangular Flange-Plate Connections with Bolts on Two Sides of the Hollow Section (Packer et al. [1989])	11
1.3.3.3 Current Design Models (Packer et al. [1992] and AISC [1997])	14
2 <i>EXPERIMENTAL INVESTIGATION</i>	16
2.1 Introduction	16
2.2 Scope of Experimental Program	16
2.2.1 Geometrical Properties	17
2.2.2 Material Properties	19
2.3 Testing and Measuring Equipment	20
2.3.1 Bolt Measuring Equipment	21
2.3.2 Bolt Calibration	26

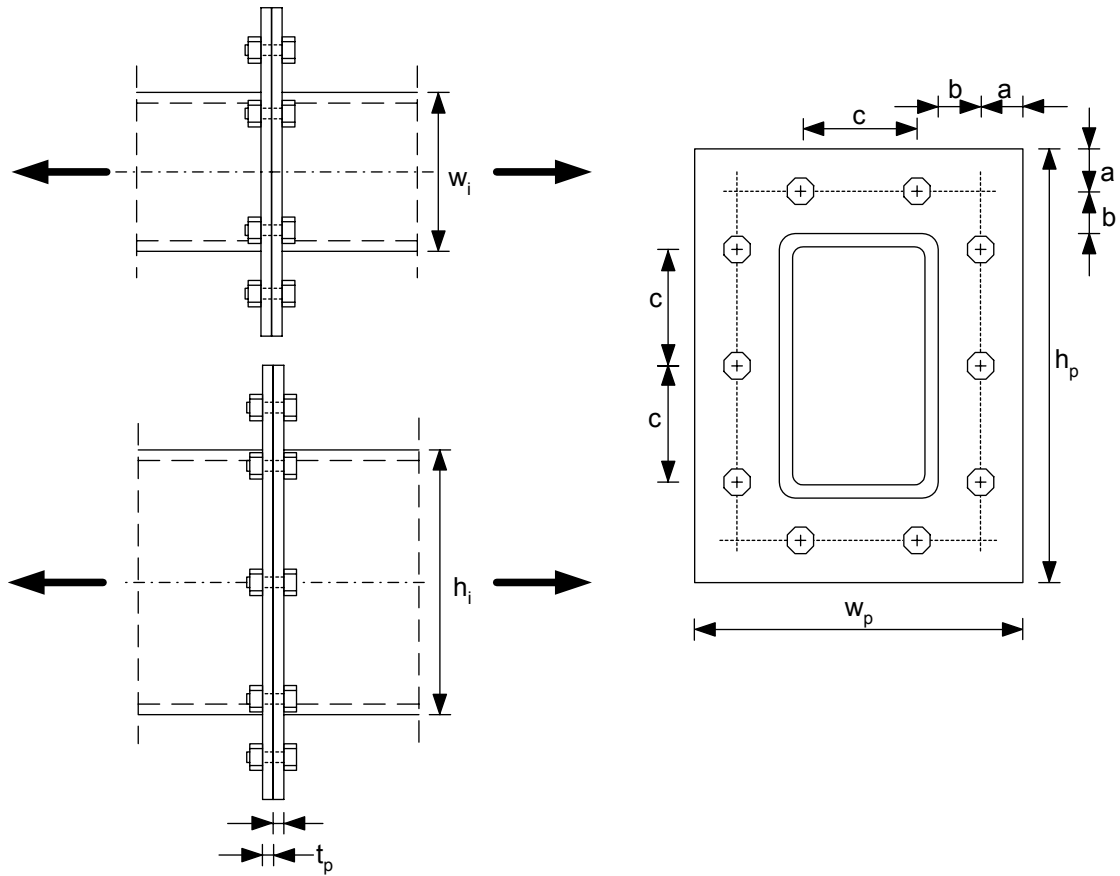
2.4	Specimen Fabrication and Testing	27
2.5	Test Results	31
2.5.1	Square Flange-Plate Connections	32
2.5.1.1	Specimens with Four Bolts	32
2.5.1.2	Specimens with Eight Bolts	34
2.5.2	Rectangular Flange-Plate Connections	39
2.6	General Observations from the Testing Program	42
3	<i>VALIDATION OF NUMERICAL MODELS</i>	45
3.1	General Introduction	45
3.2	Software and Hardware	45
3.3	General Considerations	45
3.3.1	Element Types used in the Study	46
3.3.2	Geometrical and Material Non-Linearities	49
3.3.3	Solution Techniques used in the Study	51
3.3.4	Boundary Conditions	51
3.3.5	Discretisation	55
3.3.5.1	Bolt Discretisation	55
3.3.5.2	Flange-Plate Discretisation	56
3.3.5.3	Hollow Section Discretisation	61
3.3.5.4	Weld Discretisation	62
3.4	Validation of the Numerical Models with the Experimental Results	62
3.4.1	Square Flange-Plate Connections	63
3.4.2	Rectangular Flange-Plate Connections	68
4	<i>NUMERICAL STUDY</i>	70
4.1	Numerical Model	70
4.2	Scope of Numerical Study	71
4.3	General Aspects	74
4.3.1	Deformation Limits	74
4.3.2	Fabrication Tolerances	75
4.4	Ultimate Load Capacity	78

4.4.1	Square Flange-Plate Connections	78
4.4.1.1	Specimens with Four Bolts	78
4.4.1.2	Specimens with Eight Bolts	80
4.4.2	Rectangular Flange-Plate Connections	82
5	<i>ANALYTICAL STUDY AND SOLUTIONS</i>	85
5.1	Introduction	85
5.2	Yield Line Models	85
5.2.1	One-Dimensional Yield Line Model	85
5.2.2	Two-Dimensional Yield Line Model	92
5.3	Summary	96
 PART II HIDDEN JOINT CONNECTIONS		
6	<i>LITERATURE REVIEW</i>	98
6.1	Shear Lag Failure of the Hollow Section	100
6.1.1	International Specifications	100
6.1.2	Recent Research on Shear Lag	103
7	<i>EXPERIMENTAL INVESTIGATION</i>	106
7.1	Introduction	106
7.2	Scope of Experimental Programme	106
7.3	Testing and Measuring Equipment	107
7.4	Specimen Fabrication and Testing	107
7.5	Test Results	110
7.5.1	Results of Strain Gauge Measurements	112
7.6	General Observations from the Testing Program	115
8	<i>VALIDATION OF NUMERICAL MODELS</i>	116
8.1	General Considerations	116
8.1.1	Element Type used in the Study	116
8.1.2	Geometrical and Material Non-Linearities	117
8.1.3	Solution Techniques used in the Study	119

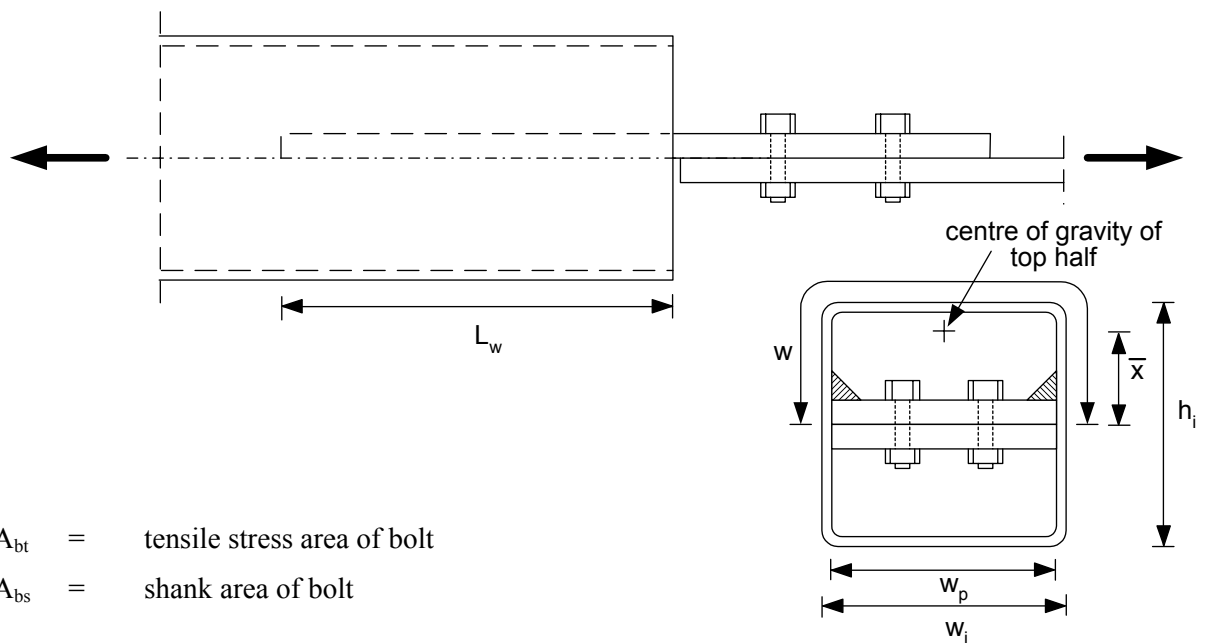
8.1.4	Discretisation and Boundary Conditions	119
8.2	Validation of the Numerical Models with the Experimental Results	121
9	<i>NUMERICAL STUDY</i>	124
9.1	Numerical Model	124
9.2	Scope of Numerical Study	125
9.3	Numerical Results and Observations	126
9.3.1	Square Hidden Joint Connections	126
9.3.2	Rectangular Hidden Joint Connections	131
10	<i>ANALYTICAL STUDY AND SOLUTIONS</i>	134
10.1	Introduction	134
10.2	Determination of $\sigma_{ }$, σ_{\perp} and τ	135
10.3	Summary	138
	CONCLUSIONS AND RECOMMENDATIONS	140
	Bolted Flange-Plate Connections	140
	Hidden Joint Connections	141
	REFERENCES	143
	APPENDIX PART I	
	APPENDIX PART II	

SYMBOLS

FLANGE-PLATE CONNECTION



GUSSET-PLATE CONNECTION



A_{bt} = tensile stress area of bolt

A_{bs} = shank area of bolt

A_g	=	gross section area
A_i	=	cross sectional area of hollow section
A_{ne}	=	net section area
A'_{ne}	=	net section area for shear lag failure calculation
A_w	=	cross sectional area of weld
CHS	=	circular hollow section
E	=	Young's modulus
F_{b0}	=	bolt force after pretensioning
F_{br}	=	factored bolt tensile resistance
F_{bs}	=	bolt force at separation load of the flange-plates
F_{bu}	=	measured bolt tensile strength in bolt tension test
F_{by}	=	measured bolt yield strength in bolt tension test
L	=	connection length
L_w	=	weld length
N	=	connection load
N_b	=	connection load for each bolt (= N/n)
N_{flange}	=	load transferred in hollow section flange
N_i	=	axial tension force under factored loads applied to member i
N_s	=	separation load of flange-plates
N_u	=	theoretical connection strength
N_{uFE}	=	connection strength as predicted by numerical model
N_{ui}	=	ultimate tensile strength of hollow section (calculated)
N_{up}	=	ultimate tensile strength of the gusset plate (calculated or predicted)
N_{ux}	=	measured connection strength
$N_u(i)$	=	connection strength prediction of mechanism i
N_{web}	=	load transferred in hollow section web
N_{yp}	=	yield strength of the flange-plate (applying two-dimensional yield line model)
N_{yi}	=	yield strength of hollow section
Q	=	prying force
Q_b	=	prying force resisted by a single bolt
Q_u	=	predicted total prying force at ultimate load
Q_{ux}	=	measured total prying force at ultimate load
R^2	=	correlation coefficient in regression analysis
RHS	=	Rectangular Hollow Section
U	=	coefficient for shear lag net section failure calculation
a	=	throat thickness of fillet weld

a	=	half the height of the web of the hollow section $(= \frac{h_i}{2} - r_{out})$
a	=	edge distance
a'	=	effective value of a $(= a + d/2)$
b	=	distance from bolt line to hollow section face
b*	=	distance from bolt line to inner yield line along hollow section (see Figure 4.10)
b'	=	effective value of b $(= b - d/2)$
b''	=	effective value of b including the fillet weld reduction $(= b - d/2 - w/2 + (1 - \chi) t_i)$
c	=	distance between bolts parallel to hollow section face
d	=	nominal bolt diameter
d'	=	bolt hole diameter
d _i	=	external diameter of circular hollow section
f _u	=	ultimate tensile stress
f _{ub}	=	ultimate tensile stress of bolt material
f _{ui}	=	ultimate tensile stress of hollow section material
f _{up}	=	ultimate tensile stress of flange-plate material
f _y	=	yield tensile stress
f _{yi}	=	yield tensile stress of hollow section material
f _{yp}	=	yield tensile stress of flange-plate material
f _{ySt}	=	static yield tensile stress
h _i	=	external height of rectangular hollow section
h _p	=	flange-plate height
k	=	coefficient for determining t _{req} (see Figure 1.2)
l _{we}	=	“length” of weld shell elements
m _u	=	ultimate moment of flange-plate per unit length $(= \frac{1}{4} t_p^2 F_{up})$
m _{up}	=	maximum usable bending moment capacity of flange-plate $(= \frac{1}{4} t_p^2 \frac{F_{yp} + 2F_{up}}{3})$
m _y	=	plastic moment of flange-plate per unit length $(= \frac{1}{4} t_p^2 F_{yp})$
n	=	number of bolts in a connection
n _s	=	number of bolts on one side parallel to flange-plate height or width
p	=	tributary flange-plate width, per bolt $(= \frac{h_p}{n_s} \text{ or } = \frac{w_p}{n_s})$

p'	=	tributary hollow section width, per bolt ($= \frac{h_i}{n_s}$ or $\frac{w_i}{n_s}$)
p_1	=	tributary flange-plate width along bolt line, per bolt ($= p_2 - d'$)
p'_1	=	modified tributary flange-plate width along bolt line, per bolt ($= p'_2 - d'$)
p_2	=	tributary flange-plate width along outer hollow section wall, per bolt
p'_2	=	modified tributary flange-plate width along outer hollow section wall, per bolt
r_s	=	radius of bolt shank
r_t	=	effective radius of bolt threaded portion
r_{out}	=	outside corner radius of hollow section
s	=	effective bolt line length on one side of the connection ($= c (n_s - 1) + 2d'$)
s_{1h}	=	auxiliary length along the height of the connection for the calculation of the yield strength of the flange-plate ($= h_i - s_{2h}$)
s_{1w}	=	auxiliary length along the width of the connection for the calculation of the yield strength of the flange-plate ($= w_i - s_{2w}$)
s_{2h}	=	auxiliary length along the height of the connection for the calculation of the yield strength of the flange-plate ($= n_s c$)
s_{2w}	=	auxiliary length along the width of the connection for the calculation of the yield strength of the flange-plate ($= n_s c$)
t_c	=	required flange-plate thickness for which no prying action occurs
t_e	=	effective wall thickness of hollow section
t_i	=	actual wall thickness of hollow section
t_{req}	=	required flange-plate thickness
t_p	=	flange-plate thickness
t_p	=	gusset plate thickness
t_{q1}	=	minimum flange-plate thickness for which no prying action occurs
t_{q2}	=	minimum flange-plate thickness for which bolt failure will govern
t_{we}	=	assumed thickness of weld shell elements
w	=	distance between the welds, measured around the tube perimeter
w	=	weld (leg) size connecting the tube and the flange-plate
w_i	=	external width of rectangular hollow section
w_p	=	flange-plate width
w_p	=	gusset-plate width
x	=	distance from hollow section face towards hollow section centre line representing plasticized zone in hollow section and locating negative moment plastic hinge
\bar{x}	=	eccentricity for shear lag, distance between welds and centre of gravity of connected part
x_{minh}	=	x_h (height) corresponding to the minimum collapse load (see Figure 5.6)
x_{minw}	=	x_w (width) corresponding to the minimum collapse load (see Figure 5.6)

Δx	=	distance from gusset plate centre line
Δy	=	distance from hollow section centre line
α	=	angle between deformed flange-plate and plane of symmetry (see Figure 3.12)
α	=	coefficient for shear lag net section failure calculation
α	=	coefficient for prying action
β_u	=	predicted prying ratio at ultimate load $(= \frac{\sum F_{bu} - N_u}{N_u} = \frac{Q_u}{N_u})$
β_{ux}	=	measured prying ratio at ultimate load $(= \frac{\sum F_{bu} - N_{ux}}{N_{ux}} = \frac{Q_{ux}}{N_{ux}})$
β_{uFE}	=	prying ratio at ultimate load as predicted by numerical model
χ	=	reduction factor for plastic moment of flange-plate $(= \frac{t_i^2 F_{yi}}{t_p^2 F_{yp}} \leq 1)$
δ	=	coefficient $(= 1 - \frac{d'}{p})$
δ	=	deformation of the connection in direction of loading (see Figure 4.4)
δ_p	=	gap between the flange-plates due to out of straightness of the plates
ϵ_{ul}	=	ultimate strain at rupture
ϕ_p	=	flange-plate resistance factor $(= 0.9)$
γ	=	half width to thickness ratio $(= \frac{w_i}{2t_i})$
λ	=	factor for length over which stress normal to hollow section acts
ρ	=	coefficient $(= \frac{b'}{a'})$
$\sigma_{ }$	=	stress parallel to hollow section axis
σ_{\perp}	=	stress normal to hollow section axis
τ	=	shear stress
ω	=	coefficient $(= \frac{w - 2a}{L_w})$
ψ	=	correction factor for tributary flange-plate width

INTRODUCTION

General Introduction

As Louis Henry Sullivan stated, “Form ever follows function”. Yet sometimes form and function can be combined. In addition to offering outstanding properties for resisting compression, tension, bending and torsional forces, hollow structural sections provide architects with attractive design options (see Figure 1).



Figure 1 **The London Eye**

In the past, the use of hollow sections was restricted to the transportation of fluids (e.g. lead and clay pipes in ancient Rome). The use of hollow sections as structural members is a more recent development in civil engineering. In many aspects, structures using structural

hollow sections can be superior to those designed with open sections. The higher strength to weight ratio of hollow sections compared to open sections such as I-beams allows lighter structures, thus saving steel and simplifying erection. The small surface area of hollow sections lowers the costs for protection against corrosion and general maintenance of the structure. Within the hollow section family, the rectangular sections in general are particularly easy for site handling. Straight cuts and straight welds make connection fabrication easy and less expensive.



Figure 2 Toronto SkyDome roof structure and the Baregg bridge in Switzerland

Structural hollow sections are often found in truss girders of roof or bridge structures (see Figure 2) because of their inherent qualities. Since hollow sections are particularly used for long girder spans, it is often necessary to splice the top and bottom chords (see Figure 3) because of the limited stock lengths or transportation problems. Two, very typical designs for splicing members are:

- Bolted flange-plate connections.
- Hidden joint connections - connecting plate welded inside the RHS.

For both connection types the welding can be done in the shop ensuring high quality. The on site handling is limited to bolting operations only.

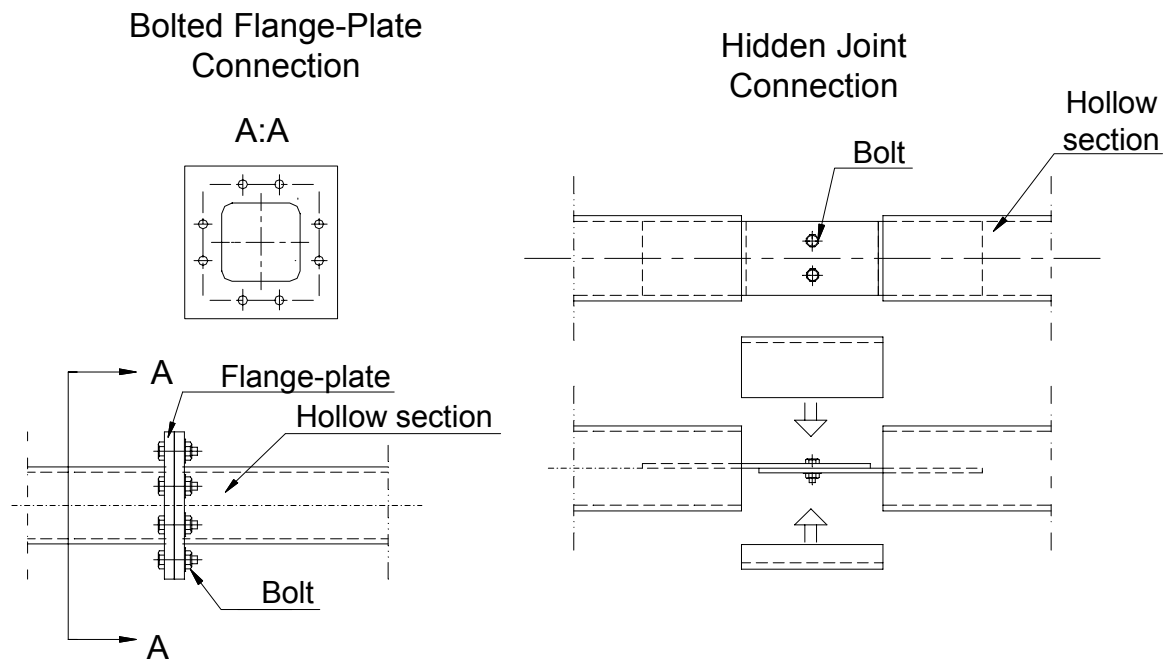


Figure 3 Bolted flange-plate and hidden joint connections

Scope of Work

The final aim of this research work is to provide readily applicable, efficient and safe design methods for typical splice connections for rectangular hollow sections. The study concentrates on tensile loading as most applications of hollow section splice connections are found in truss structures and tension loading is the governing design condition for such splice connections. Bending moment loading, or combined bending plus axial load, as required for frame structures, has not been studied. The spliced connections were bolted flange-plate connections of square and rectangular hollow sections with bolts on all four sides as well as hidden joint connections. The following steps were taken for each connection type:

- Literature study to review existing design rules.
- Experimental investigation.
- Parametric (FE) study.
- Derivation of analytical models and strength formulae using the results of the finite element parametric study.

PART I BOLTED FLANGE-PLATE CONNECTIONS

1 LITERATURE REVIEW

While bolted flange-plate connections for hollow sections represent a more recent connection type, end-plate connections for open sections have been introduced for a long time. Beginning with the early analytical T-Stub models by Struik and de Back [1969], extensive studies on the subject of prying action have been carried out. The results of these studies are reflected in all current design guides and Codes [e.g. Kulak et al. 1987, Eurocode 3 1992, AISC 2001, CISC 2000].

The subject of prying action in connection with hollow structural sections has mainly focused on connections for circular hollow sections. Bolted flange-plate connections for square or rectangular hollow sections (RHS) with bolts on all four sides have not yet been studied enough to allow the derivation of specific design methods. Table 1.1 gives an overview of existing pertinent codes and design recommendations. Figure 1.1 shows the typical dimensions of a bolted flange-plate connection which are required for the understanding of the design methods in the following chapters.

Table 1.1 Overview of existing codes and design guides for bolted flange-plate connections

Code or design guide	Flange-plates for circular hollow sections	Flange-plates for rectangular hollow sections with bolts on all four sides
Wardenier et al. [CIDECT 1991]	Yes	No
Packer et al. [CIDECT 1992]	No	No
Eurocode 3 [1992]	Yes	No
DIN 18808 [1984] and Anpassungsrichtlinie [1994]	Yes	No
Syam and Chapman [AISC 1996]	No	No
American Institute of Steel Construction [1997]	Yes	Yes ¹⁾
Packer and Henderson [CISC 1997]	Yes	No

¹⁾ Derived from model for rectangular RHS with bolts on two sides of the hollow section

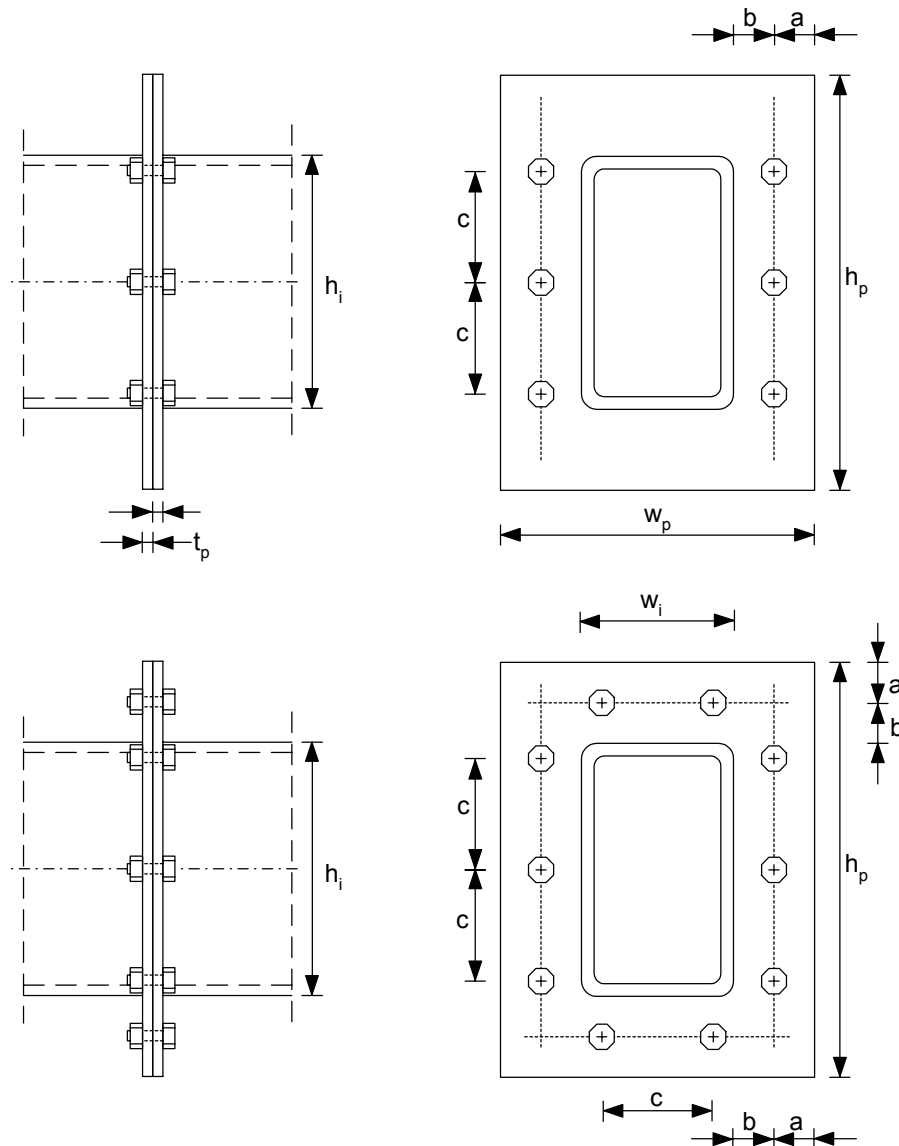


Figure 1.1 Dimensions of bolted flange-plate connections

1.1 Experimental Research on Bolted Flange-Plate Connections

Based on the test results for a large number of tests on circular flange-plate connections empirical rules were proposed by Rockey and Griffiths [1970]. Mang [1980] and Igarashi et al. [1985] continued the experimental study on bolted flange-plate connections for circular hollow sections. Experimental research on flange-plate connections for rectangular hollow sections with bolts along two opposite sides of the hollow section only was initially done by Kato and Mukai [1985], but followed by an extensive study by Packer et al. [1989].

Research on connections bolted on four sides started with Mang [1980] summing up practical testing and giving qualitative recommendations for the bolt positioning. It was

observed that bolt placements beyond the hollow section height or width (at the corners of the flange-plates) are less favourable as these bolts tend to get loaded far less relative to the bolts placed within the hollow section height or width. The experimental research was continued by Kato and Mukai [1982] with a large test series consisting of 36 specimens under tension loading. The study comprised of square hollow section connections using four or eight bolts, different hollow section sizes and different flange-plate thicknesses. Bolt failure governed for most connections. A failure of the flange-plates could only be reported for extremely thin plates and this was accompanied by failure of the bolts. The prying ratios (ratio of prying forces to connection capacity) varied between 0% and 233%. The prying forces equal the sum of the ultimate tensile strength of the bolts minus the connection capacity. Based on the results of the experimental investigation, a complicated design model derived from a two-dimensional yield line model was proposed.

In conjunction with the erection of the Toronto SkyDome, numerous tests on the steel roof connections were carried out, including three tension tests on bolted flange-plate connections [Caravaggio 1988]. These tests showed that the earlier model by Kato and Mukai [1982] overestimated the actual connection strength.

1.2 Numerical Research on Bolted Flange-Plate Connections

Cao and Bell [1994] carried out finite element analyses for circular hollow sections with bolted flange-plate connections. Using the FE package ABAQUS, the study comprised of axisymmetric and 3-D models. For the application with circular flange-plate connections it was found that the equally spaced discrete bolt arrangement can be represented by a uniformly distributed annular arrangement without significant error. In a more recent study by Schaumann and Kleineidam [2002] using ANSYS as the FE solver, the influence of the modelling of the bolts on the structural behaviour of ring connections was shown. An extremely fine bolt mesh including a full representation of the thread was found to give only marginally different results to a simpler 3-D bolt model assembled from cylindrical sections without a specific thread discretisation. The representation of the bolts by simple spring elements was not recommended in this study. Also recently, Cao et al. [2000] provided a general overview on finite element modelling of bolted flange connections.

Bolted moment end-plate connections for rectangular hollow sections which are subjected to pure bending were investigated by Wheeler et al. [2000]. The bolting pattern in this study consisted of four bolts, each placed in a corner of the flange-plate. The model included the individual modelling of the bolts, modelling of the welds and contact surfaces as

well as the introduction of initial deformations to model the heat distortions due to the welding process.

1.3 Analytical Research and Design Models for Bolted Flange-Plate Connections

1.3.1 General Model (Timoshenko and Woinowsky-Krieger [1959])

A very early empirical model derived from experiments with circular hollow structures in which the flange-plate was intended to remain elastic was given by Timoshenko and Woinowsky-Krieger [1959]. It is supposed to be applicable for any type of flange-plate connection; circular as well as rectangular. Prying action does not take place and the flange-plate thickness must be kept large enough to serve this premise. The connection capacity is calculated by two independent formulae which can be found in the Stelco Manual [1981]:

$$t_{\text{req}} = \sqrt{\frac{N_i k}{f_{\text{yp}}}} \quad \text{with } k \text{ given in Figure 1.2} \quad (\text{Equation 1.1})$$

$$F_{\text{br}} \geq \frac{N_i}{n} \quad (\text{Equation 1.2})$$

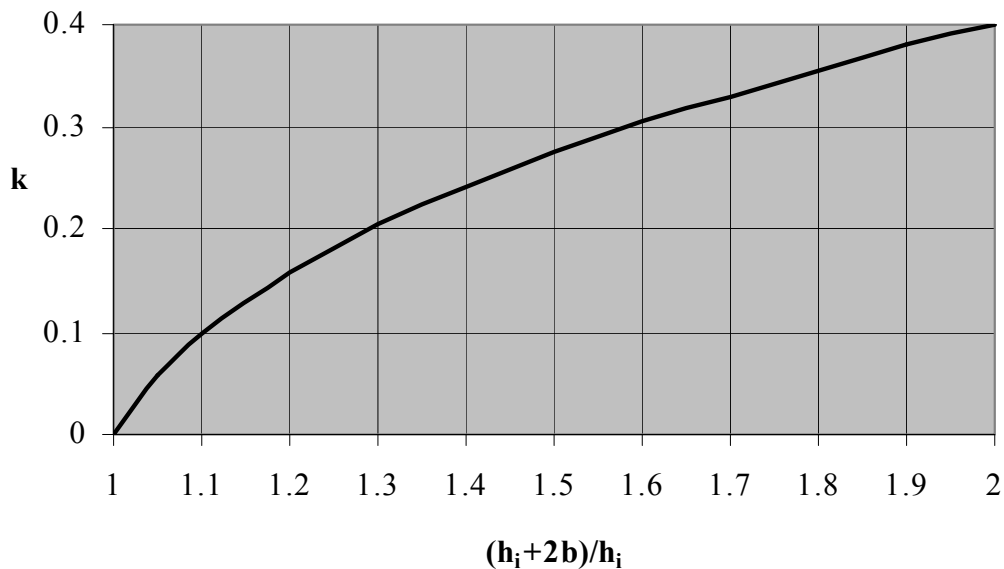


Figure 1.2 Eccentricity ratio factor k

The first formula calculates the flange-plate thickness, ensuring that no prying action takes place. The second equation checks the bolt strength against the applied tensile loading per bolt (without any additional prying forces). The equations represent a very conservative

approach to the ultimate load capacity of bolted flange-plate connections, resulting in very large flange-plate thicknesses if used for routine structural design. If any prying action has to be excluded, for example to avoid fluid losses in pipes, this design approach can be very quick and safe.

1.3.2 Two-Dimensional Yield Line Model (Kato and Mukai [1982])

Based on an extensive experimental study on square flange-plate connections with four and eight bolts, Kato and Mukai [1982] developed new models with two-dimensional yield line patterns (see Figure 1.3). In these models six failure modes covering flange-plate and bolt failure were established (see Table 1.2). The models assume the full development of the ultimate bending moment in the flange-plates:

$$m_u = \frac{1}{4} t_p^2 f_{up} \quad (\text{Equation 1.3})$$

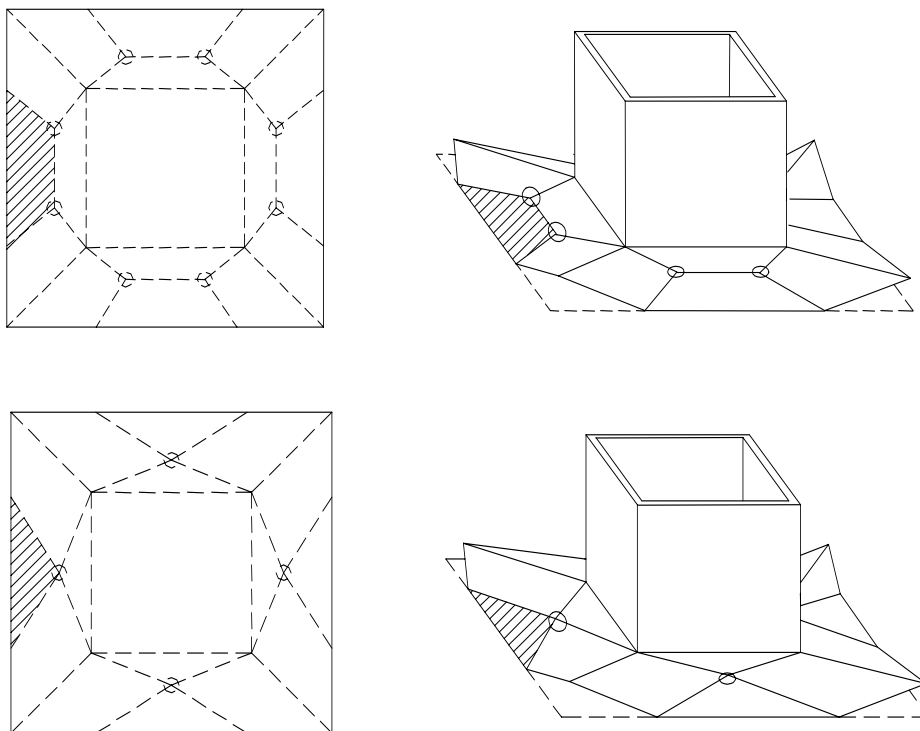


Figure 1.3 Assumed yield line patterns of Kato and Mukai [1982]

The equations of Kato and Mukai [1982] are restricted to use in square connections having bolt layouts that are covered by the yield line patterns provided (see Figure 1.3). Rectangular flange-plate connections cannot be designed with this method. The exact formulae for the

calculation of the flange-plate capacity are numerous and unwieldy and therefore less appropriate for general use. It was found, in comparisons with experimental data derived from later studies, that the predictions of this model tend to overestimate the connection capacities [Willibald et al. 2001, Willibald et al. 2002]. This overestimation is attributed to the assumption that the flange-plate material can form an ultimate stress state throughout the plate material thickness.

Table 1.2 Proposed failure modes of the flange plates and the bolts

	Flange-plate failure	Bolt failure
Before separation of the flange-plates	(Failure mode 1) Flange-plates reach ultimate strength	
At separation of the flange-plates	(Failure mode 2) Due to the separation, the rigid zones around the bolts suddenly disappear, changing the ultimate flange-plate strength	
After separation of the flange-plates		(Failure mode 4) Rupture of the bolts before the flange-plates reach yield level (no prying)
		(Failure mode 5) Rupture of the bolts being suddenly subjected to prying forces as the flange-plates reach yield load
	(Failure mode 3) Flange-plates reach ultimate strength before the rupture of the bolts	(Failure mode 6) Rupture of the bolts between the yield load and the ultimate strength of the flange-plates

1.3.3 One-Dimensional Yield Line Models

1.3.3.1 General T-Stub Model (Struik and de Back [1969])

One of the first theoretical models dealing with the analysis of prying forces was established by Struik and de Back [1969]. It uses yield line theory for a T-stub connection (see Figure 1.4).

The yield lines in this model always form parallel to the T-stub web resulting in a one-dimensional prying model. In the first version of their model the outer yield line follows the bolt line. According to this assumption a term " α " has been introduced representing the ratio of bending moment per unit plate width at the bolt line to the bending moment per unit plate width at the inner (hogging) plastic hinge. Due to test results it was later on inferred that the flexural deformations of the flange cause the resultant bolt force to act somewhere between the bolt axis and the edge of the bolt head. Thus, a modified version was introduced in which the outer

plastic hinge was shifted half of the bolt diameter towards the inner yield line. Therefore, "a" and "b" are replaced by "a'" and "b'", with "a'" and "b'" given by:

$$a' = a + d/2, \text{ with } a \leq 1.25 b \text{ in calculation but not necessarily in practise} \quad (\text{Equation 1.4})$$

$$b' = b - d/2 \quad (\text{Equation 1.5})$$

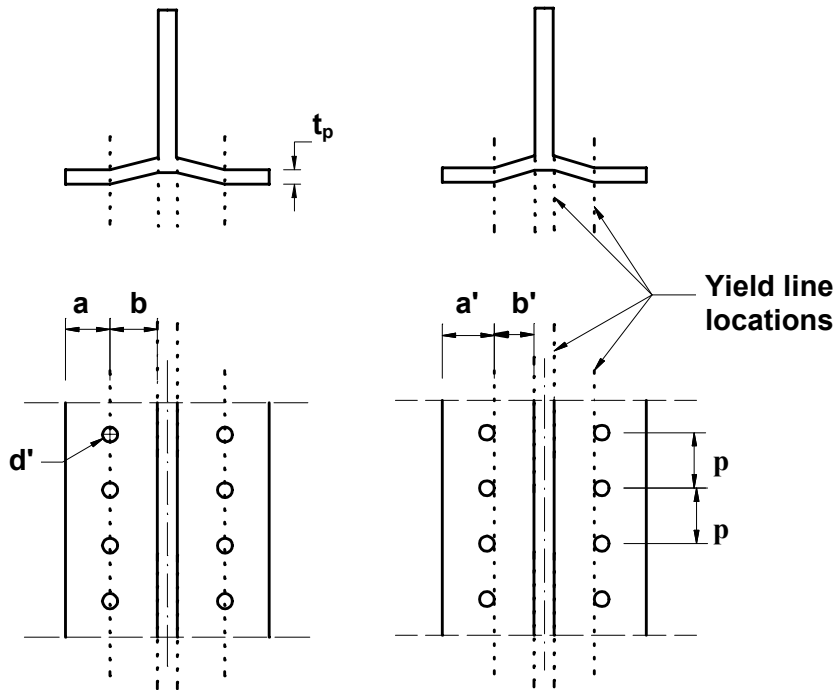


Figure 1.4 Example of a T-stub with a flexible flange-plate

In both models, the plate strength is restricted to the yield strength, and strain hardening is not taken into account. The plastic moment of the flange-plate per unit length is:

$$m_y = \frac{1}{4} t_p^2 f_{yp} \quad (\text{Equation 1.6})$$

Two limit states are established, $\alpha = 0$ and $\alpha = 1$ representing a rigid plate and a flexible plate in double curvature respectively. For $\alpha = 0$ (no prying action), with the bolts loaded to their tensile strength, the required flange-plate thickness is:

$$t_c = \sqrt{\frac{4F_{bu} b'}{p f_{yp}}} \quad (\text{Equation 1.7})$$

The appropriate value of " α " for a connection can be calculated by comparing the flange-plate thickness " t_p " of a connection with " t_c ":

$$\alpha = \frac{1}{\delta(1+\rho)} \left[\left(\frac{t_c}{t_p} \right)^2 - 1 \right] \quad (\text{Equation 1.8})$$

$$\text{where } \delta = 1 - \frac{d'}{p} \quad (\text{Equation 1.9})$$

$$\text{and } \rho = \frac{b'}{a'} \quad (\text{Equation 1.10})$$

The theoretical connection strength is then:

If $\alpha \leq 0$ (no prying action):

$$N_u = n F_{bu} \quad (\text{Equation 1.11})$$

Or if $0 < \alpha \leq 1$ (prying action):

$$N_u = n F_{bu} \left(\frac{t_p}{t_c} \right)^2 \cdot (1 + \delta \alpha) \quad (\text{Equation 1.12})$$

Later research, done on flange-plate connections bolted along two sides of a hollow section, performed by Birkemoe and Packer [1986] and Packer et al. [1989] is based on this traditional model. The location of the inner plastic hinge and the maximum bending moment per unit plate width are varied. Due to the location change of the inner yield line, values of α greater than one are now possible. For $\alpha > 1$ Equation (1.13) is added:

$$N_u = n F_{bu} \left(\frac{t_p}{t_c} \right)^2 \cdot (1 + \delta) \quad (\text{Equation 1.13})$$

1.3.3.2 One-Dimensional Yield Line Model for Rectangular Flange-Plate Connections with Bolts on Two Sides of the RHS (Packer et al. [1989])

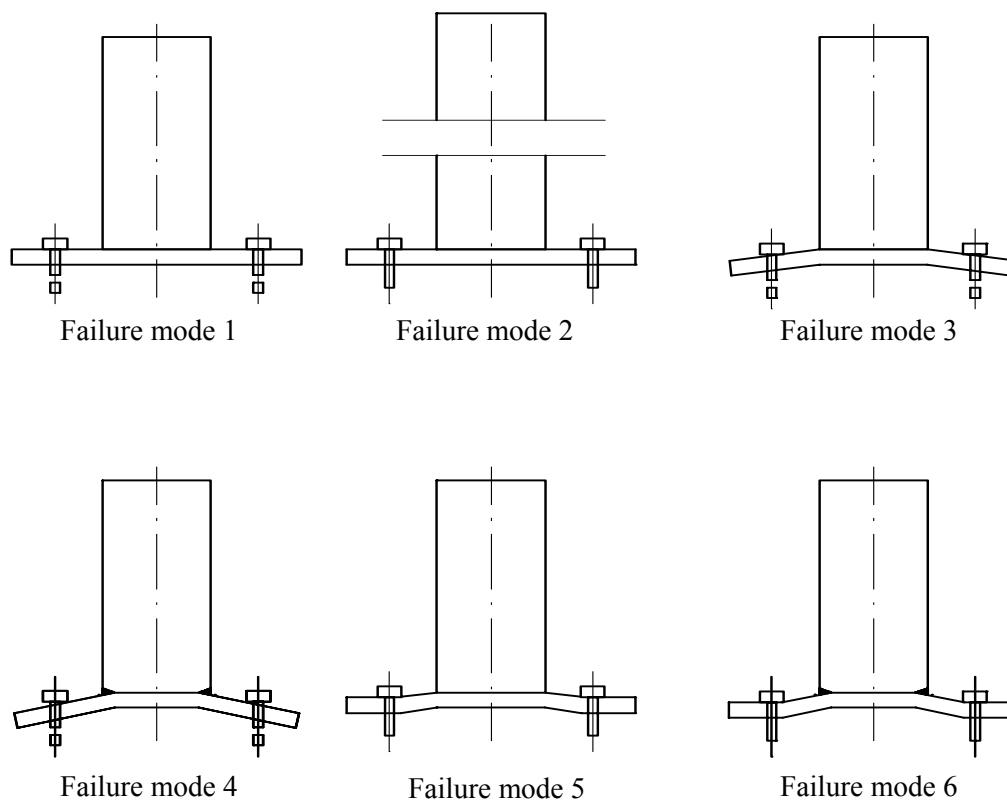
Based on the results of an experimental study, Packer et al. [1989] developed a design model for rectangular flange-plate connections bolted on two sides of the connection. Packer et al. [1989] postulated six failure modes (see Figure 1.5 and Table 1.3).

As a further development of the earlier models of Struik and de Back [1969], formulae are given to calculate the exact location of the inner plastic hinge depending on the relation between flange-plate and hollow section rigidity. A stress distribution in the flange-plate is assumed, whereby the stress at the neutral axis is at yield level and then increases linearly to the ultimate stress (strain hardening) at the extreme fibres. This stress distribution results in a maximum usable bending moment capacity per unit plate width of

$$m_{up} = \frac{1}{4} t_p^2 \frac{f_{yp} + 2f_{up}}{3} \quad (\text{Equation 1.14})$$

Table 1.3 Postulated failure modes

Failure Mode	Prying Parameter α	Bolts	Flange-Plate	RHS
1	$\alpha = 0$	failure	no yielding	no yielding
2	--	no failure	no yielding	failure
3	$0 < \alpha < 1$	failure	yield line forming along weld line	no yielding
4	$0 < \alpha < 1$	failure	yield line forming within hollow section dimension	yielding
5	$\alpha = 1$	no failure	yield lines forming along weld line and bolt line	no yielding
6	$\alpha = 1$	no failure	yield lines forming within hollow section dimension and bolt line	yielding

**Figure 1.5** Limit states postulated by Packer et al. [1989]

To consider the rounded corners of the RHS with respect to the thickness of the RHS an effective thickness of the RHS " t_e " was introduced:

$$t_e = \frac{1}{4} \left[2h_i - \sqrt{4h_i^2 - 4A_i} \right] \quad (\text{Equation 1.15})$$

Thus the ultimate connection strengths for the six Mechanisms are:

Failure mode 1 (rupture of the bolts, no prying):

$$N_u(1) = n F_{bu} \quad (\text{Equation 1.16})$$

Failure mode 2 (yielding of the hollow section):

$$N_u(2) = f_{yi} A_i \quad (\text{Equation 1.17})$$

Failure mode 3 (bolt failure, plastic hinge in the flange-plates at the weld line):

$$N_u(3) = \frac{2m_{up} h_p + nF_{bu} a}{a + b} \quad (\text{Equation 1.18})$$

Failure mode 4 (bolt failure and plastic hinge in the flange-plates within the hollow section dimension, with x designating the location of the plastic hinge):

$$\text{If } x \leq t_e \text{ with } x = \sqrt{(a + b)^2 + \frac{nF_{bu} a + 2m_{up} h_p}{h_i f_{yi}}} - (a + b) \quad (\text{Equation 1.19})$$

$$\text{Then } N_u(4) = (2 m_{up} h_p + n F_{bu} a) \frac{1}{a + b + x} + h_i f_{yi} \frac{x^2}{a + b + x} \quad (\text{Equation 1.20})$$

Or, if $t_e < x \leq \frac{h_i}{2}$, with

$$x = \sqrt{(a + b)^2 - (h_i - 2t_e) \left(a + b + \frac{t_e}{2} \right) + \frac{m_{up} h_p + \frac{nF_{bu} a}{2}}{f_{yi} t_e}} - (a + b) \quad (\text{Equation 1.21})$$

$$N_u(4) = 2 \left[m_{up} h_p + \frac{nF_{bu} a}{2} + f_{yi} t_e^2 \left(t_e - \frac{h_i}{2} \right) \right] \frac{1}{a + b + x} + 2f_{yi} t_e (h_i - 2t_e) \frac{x}{a + b + x} + 2f_{yi} t_e \frac{x^2}{a + b + x} \quad (\text{Equation 1.22})$$

Failure mode 5 (flange-plate failure, flange-plate bent in double curvature, no bolt failure):

$$N_u(5) = 2 m_{up} h_p \frac{1 + \delta}{b} \quad (\text{Equation 1.23})$$

$$\text{with } \delta = 1 - \frac{d'}{p} \quad (\text{Equation 1.24})$$

Failure mode 6 (flange-plate failure, flange-plate bent in double curvature, inner plastic hinge within the hollow section dimension, with x designating the location of the plastic hinge, no bolt failure):

$$\text{If } x \leq t_e \text{ with } x = \sqrt{b^2 + 2m_{up}h_p \frac{1+\delta}{f_{yi}h_i}} - b \quad (\text{Equation 1.25})$$

$$N_u(6) = 2 m_{up}h_p \frac{1+\delta}{b+x} + h_i f_{yi} \frac{x^2}{b+x} \quad (\text{Equation 1.26})$$

Or, if $t_e < x \leq \frac{h_i}{2}$, with

$$x = \sqrt{b^2 + \frac{m_{up}h_p(1+\delta)}{f_{yi}t_e} - (h_i - 2t_e)\left(b + \frac{t_e}{2}\right)} - b \quad (\text{Equation 1.27})$$

$$N_u(6) = 2 m_{up}h_p \frac{1+\delta}{b+x} + 2h_i t_e f_{yi} \frac{x - \frac{t_e}{2}}{b+x} + 2f_{yi} t_e \frac{(x - t_e)^2}{b+x} \quad (\text{Equation 1.28})$$

During experimental testing to verify this theoretical model, only failure modes 1, 2 and 4 could be reported. Thus, Packer et al. [1989] recommended using only the equations established for these failure modes for future design methods.

1.3.3.3 Current Design Models (Packer et al. [1992] and AISC [1997])

The latest design guides of CIDECT [Packer et al. 1992] and the Canadian Institute of Steel Construction [Packer and Henderson 1997] only considers formulae for connections having bolts along two sides of the hollow section. The equations are based on the model of Struik and de Back [1969]. Modifications were made concerning the location of the inner plastic hinge, replacing equation (1.5) with:

$$b' = b - \frac{d}{2} + t_i \quad (\text{Equation 1.29})$$

A resistance factor " ϕ_p " was also introduced ($\phi_p = 0.9$ for limit states design). Thus, equation (1.7) was changed to:

$$t_e = \sqrt{\frac{4F_{bu} b'}{\phi_p p f_{yp}}} \quad (\text{Equation 1.30})$$

The AISC HSS Connections Manual [1997] provides design procedures for RHS connections bolted along all four sides. The formulae also revert back to the models based on one dimensional prying [Struik and de Back 1969]. It appears that the design method is not based upon established research results but on intuitive extrapolation of existing data. As in this early model, the inner yield line is positioned along the outside of the hollow section. Equation (1.5) is also used. The resistance factor " ϕ_p " (with $\phi_p = 0.9$) is not stated explicitly but is merged into equation (1.7) to give:

$$t_c = \sqrt{\frac{4.44F_{bu} b'}{pf_{yp}}} = \sqrt{\frac{4F_{bu} b'}{0.9pf_{yp}}} \quad (\text{Equation 1.31})$$

Differences exist in the interpretation of the value for the bolt pitch " p " (see Equations 1.7, 1.30, 1.31). The calculation method provided by CIDECT [Packer et al. 1992] regards " p " as the related flange-plate width of each bolt, hence:

$$p = \frac{h_p}{n_s} \quad (\text{Equation 1.32})$$

In the AISC HSS Connections Manual [1997] the length " p " is specified as the "length of end-plate, parallel to the RHS wall, tributary to each bolt". The example given in the Manual, however, interprets " p " as the length of the RHS wall divided by the number of bolts on this side; i.e.,

$$p' = \frac{h_i}{n_s} \quad (\text{Equation 1.33})$$

The comparisons with experimental data of square and rectangular flange-plate connections with bolts on all four sides [Willibald et al. 2001, Willibald et al. 2002, Willibald et al. 2003] currently support the use of the design procedure that can be found in the AISC HSS Connections Manual [1997]. This is provided that the flange-plate width/height is used to calculate the bolt pitch. Unfortunately, the AISC HSS Connections Manual illustrates the (more conservative) use of the RHS width/height instead of the flange-plate width/height for determining the bolt pitch. For rectangular hollow section connections the connection strength should be calculated for both the short and long side individually, using the minimum of both values as the actual connection resistance. Provided that the edge distance, " a ", and the distance from bolt line to hollow section face, " b ", are the same for the short and long side of the connection the side having the smaller bolt pitch " p " will govern.

2 EXPERIMENTAL INVESTIGATION

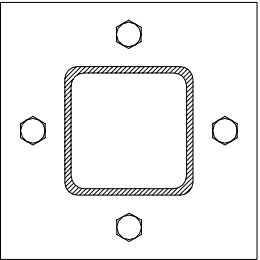
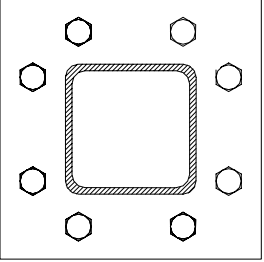
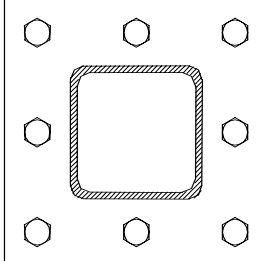
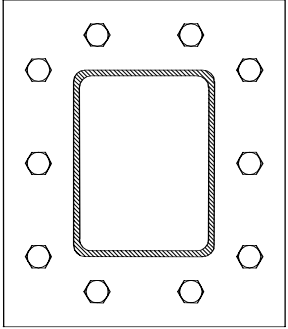
2.1 Introduction

The experimental study has been carried out with the financial support of CIDECT (Programme 8D "Bolted Flange-Plate Connections for RHS Tension Members"). The experimental work studies the interaction between hollow section, flange-plates, connecting welds and bolts. In addition, the results of the experimental work have been used to develop and validate numerical models for a parameter study, so that costly additional tests could be avoided.

2.2 Scope of Experimental Program

The scope of the experimental work comprises of flange-plate connections for square as well as rectangular hollow sections. The flange-plate connections for square hollow sections had either four or eight bolts, while the rectangular specimens had ten bolts throughout. The bolt layout as well as the flange-plate thickness have been varied for each connection type. Table 2.1 gives an overview of the different bolt layouts that are covered in the research program. A total of 16 square flange-plate connections and four rectangular flange-plate connections has been tested.

Table 2.1 Bolt layout of tested specimens

Square Flange-Plate Connections		Rectangular Flange-Plate Connections with 10 Bolts
4-Bolt Specimens	8-Bolt Specimens	
 <p>Bolt layout S4</p>	 <p>Bolt layout S8</p>  <p>Bolt layout S'8</p>	 <p>Bolt layout R10</p>

2.2.1 Geometrical Properties

The hollow sections for the square flange-plate connection tests are cold-formed square structural hollow sections 152 x 152 x 9.5. For the rectangular flange-plate connections cold-formed rectangular hollow sections 254 x 152 x 7.4 were used. At the ends of the hollow sections, away from the flange-plate connection, very strong plates (tongues) have been slotted into the hollow sections which were later gripped by the testing machine. The length of the hollow section between the end of the tongue and the flange-plate is about four times its height, ensuring an even stress distribution around the hollow section during the tests, before the flange-plate area was reached. The even stress distribution has been checked by additional strain gauges on the hollow section.

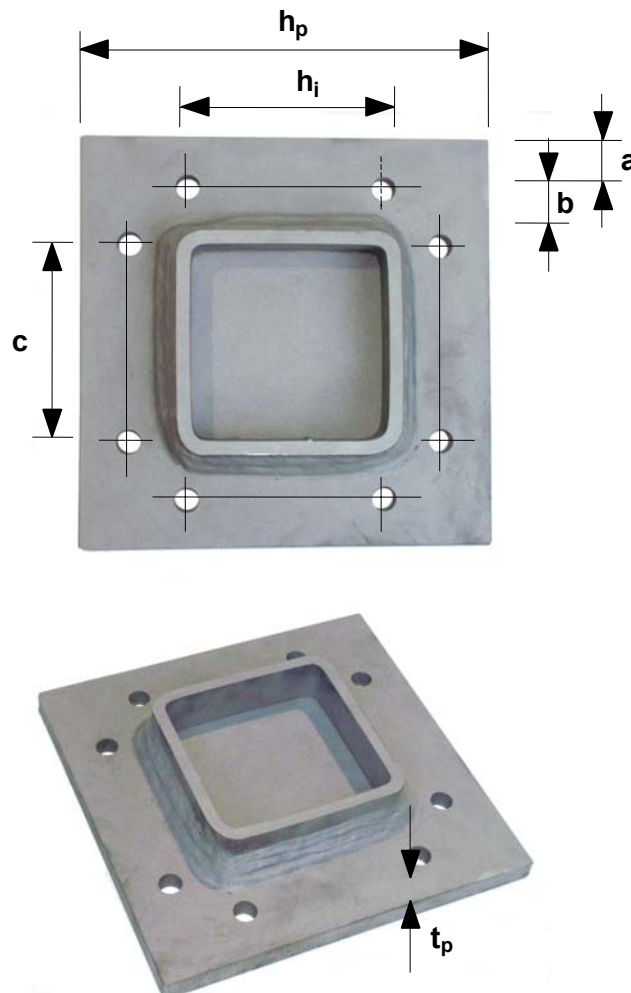


Figure 2.1 Bolt layout definitions

The flange-plate thickness varied between 12 and 20 mm for the square and 12 and 16 mm for the rectangular flange-plate connections. The relevant bolt layout parameters are

shown in Figure 2.1. Table 2.2 and Table 2.3 present the geometric properties of the tested square and rectangular flange-plate connections respectively.

Table 2.2 Measured dimensions of square test specimens

Specimen	Hollow section	Flange-plate		Bolts	Weld	Bolt layout				
		t_p (mm)	h_p (mm)	d (mm)	$w^{1)}$ (mm)	n	a (mm)	b (mm)	c (mm)	
S4-1	152.8 x 152.8 x 9.4 mm $A_i^{2)} = 5187 \text{ mm}^2$	12.6	311.7	18.9	15.3	4	40.3	38.7	--	
S4-2		15.8	312.1		14.8		39.9	38.9		
S4-3		12.6	312.5		15.6		35.1	43.8		
S4-4		15.8	312.4		15.6		35.0	43.9		
S8-1		152.8 x 152.8 x 9.4 mm $A_i^{2)} = 5187 \text{ mm}^2$	16.2	293.2	15.7	16.6	8	35.7	34.6	139.6
S8-2			20.1	293.4		17.0		35.8	34.4	139.7
S8-3			16.3	292.8		16.1		35.6	34.5	69.7
S8-4			20.1	294.5		17.1		36.4	34.5	69.6
S8-5			12.6	311.8		15.4		39.9	39.8	139.8
S8-6			12.6	311.0		12.8		40.1	39.6	69.7
S8-7	12.8		310.8	14.0		34.6		44.5	139.9	
S8-8	15.9		311.4	14.8		34.9		44.6	139.9	
S8-8	12.5		311.0	13.5		33.6		44.7	69.7	
S8-10	15.9		311.2	15.7		34.4		44.7	69.9	
S'8-1		16.3	293.3		16.3		35.9	34.5	--	
S'8-2		20.0	293.4		16.8		35.9	34.5	--	

¹⁾ Throat thickness = $w / \sqrt{2}$

²⁾ Measured area obtained by weighing a specific length of hollow section and using a density of 7850 kg/m³ [Eurocode 3 Part 1-2 1995]

Table 2.3 Measured dimensions of rectangular test specimens

Specimen	Hollow section	Flange-plate			Bolts	Weld	Bolt layout				
		t_p (mm)	h_p (mm)	w_p (mm)	d (mm)	$w^{1)}$ (mm)	n	a (mm)	b (mm)	c (mm)	
R10-1	253.5 x 151.9 x 7.3 mm $A_i^{2)} = 5455 \text{ mm}^2$	12.5	415.5	313.2	15.8	15.5	10	35.8	45.0	109.5	
R10-2		15.9	416.9	312.3				15.3	35.9	45.0	109.6
R10-3		12.5	417.4	312.1				17.3	40.9	39.7	109.5
R10-4		15.8	414.8	313.9				15.4	40.6	39.9	109.7

¹⁾ Throat thickness = $w / \sqrt{2}$

²⁾ Measured area obtained by weighing a specific length of hollow section and using a density of 7850 kg/m³ [Eurocode 3 Part 1-2 1995]

All welds between flange-plates and hollow sections were fillet welds with the leg length varying between 12.8 and 17.3 mm. The documented weld leg lengths (Table 2.2 and Table 2.3) are the average values for each specimen. For the square flange-plate connections

with eight bolts as well as the rectangular flange-plate connections, 16 mm ($\frac{5}{8}$ " diameter (M16) bolts were used. The bolt diameter for the square flange-plate connections with four bolts was 20 mm ($\frac{3}{4}$ " (M20). The bolt hole diameter was either 17.5 mm ($\frac{11}{16}$ " for the M16 bolts or 21.5 mm ($\frac{13}{16}$ " for the M20 bolts.

2.2.2 Material Properties

Standard cold-formed Class C hollow sections with a minimum specified yield stress of 350 MPa, Grade 350W CSA [1992], comparable with S355 JOH [EN 10219-1 1997], were used throughout. The flange-plate material was Grade 300W steel (roughly comparable to S355 JO [EN 10027-1 1992]) with a minimum specified yield stress of 300 MPa. Some of the flange-plate material was cold-rolled thus explaining the missing yield plateau in the stress strain diagram in Appendix I.

Table 2.4 shows the material properties, as measured from the average of at least two tensile coupon tests of each material. The stress-strain curves of the tensile coupon tests can be found in Appendix Part I.

Table 2.4 Measured material properties of the hollow section and flange-plate material

	f_y (MPa)	f_{ySt} (MPa)	f_u (MPa)	ϵ_{u1} (%) ³⁾	E (MPa)
Square hollow sections	479.2 ¹⁾	465.05	564.7	26.6	207500
Rectangular hollow sections	385.9 ¹⁾	369.1	486.8	33.6	199400
Flange-plate 12 mm	394.8 ²⁾	379.1	515.6	35.7	201800
Flange-plate 16 mm (S8-1 to S8-6 and S'8-1, S'8-2)	324.1	304.9	498.9	40.1	260500
Flange-plate 16 mm (S4-1 to S4-4, S8-5 to S8-10 and R10-1 to R10-4)	410.7 ²⁾	397.2	512.7	35.5	198600
Flange-plate 20 mm	355.9	337.1	521.3	40.5	205000

¹⁾ Using the 0.2% offset method, with tensile coupons taken from the flats of the hollow section

²⁾ Using the 0.2% offset method, as the plates were cold-formed

³⁾ Measured over a gauge length of 2" or 50 mm

Table 2.5 Measured material properties of the bolts

Grade	d (mm)	Specimens	t_p (mm)	Yield load F_{by} (kN)	Ultimate load F_{bu} (kN)
ASTM A325 (comparable to Grade 8.8)	15.7	S8-1, S8-3, S'8-1	16	130.8	160.2
		S8-2, S8-4, S'8-2	20	129.3	151.8
	15.7	S8-5 to S8-7, S8-9	12	115.0	137.9
		S8-8, S8-10	16	112.5	134.2
	15.8	R10-1, R10-3	12	124.0	145.9
		R10-2, R10-4	16	117.7	140.9
ASTM A490 (comparable to Grade 10.9)	18.9	S4-1, S4-3	12	193.0	256.0
		S4-2, S4-4	16	192.0	247.5

American Standard high strength steel bolts were used throughout. For the square flange-plate connections with eight-bolts (Specimens S8-1 to S8-10 and S'8-1, S'8-2) as well as the rectangular flange-plate connections, bolts of Grade ASTM A325 [ASTM 1997a], roughly comparable to Grade 8.8 [ISO 898-1 1999], were used. The M20 ($3/4$ ") bolts for the square flange-plate connections with four bolts were of Grade ASTM A490 [ASTM 1997b] which roughly compares to Grade 10.9 [ISO 898-1 1999]. Bolts of different batches were used as the tests were carried out in separate test series. Therefore, independent measurements of the dimensional and material properties for each batch of bolts were carried out. Table 2.5 presents the measured material properties of the bolts.

2.3 Testing and Measuring Equipment

All the flange-plate connections were tested by quasi-static tensile loading under displacement control in a 2750 kN capacity MTS Universal testing machine. Figure 2.2 shows a typical specimen in the testing machine. The tensile load was applied to the hollow sections through tongue plates. The coupon tests of the flange-plate and hollow section material, as well as the bolt tests and the calibration of the bolt gauge, were carried out with a smaller 1000 kN testing machine. Whereas the coupon tests were done under displacement control, the bolt tests were done with the testing machine being driven under load control until yield load, after which displacement control was introduced.



Figure 2.2 Typical specimen in testing machine (R10-3)

2.3.1 Bolt Measuring Equipment

Two independent measuring methods have been used to study the variation of forces in the bolts during tests on the connections. An ultrasonic bolt gauge (Bolt Gage 3, Power-Dyne, Bidwell Industrial Group, Inc.) monitored the bolt loads during all tests. In the connection tests of specimens S4-1 to S4-4 and S8-5 to S8-10, special strain gauges (TML, Tokyo Sokki Kenkyujo Co., Ltd., Japan, BTM-Series) were used. The strain gauges were inserted into a hole drilled along the bolt axis (see Figure 2.3). The fabrication of the strain gauged bolts requires considerable effort. The insertion hole for the strain gauge has to be cleaned with acetone before filling it with the adhesive (epoxy A-2). A syringe guarantees the exclusion of air bubbles. After insertion of the strain gauge, the adhesive has to cure at room temperature for 12 hours before finalising the curing in an oven at 140°C for another three hours. As the strain gauges could not record the strains accurately for the last load stages of the tests, further use was not considered in the remaining tests. It is assumed that the bending flange-plates caused shear forces in the bolts, causing pressure normal to the wire gauge, thereby causing incorrect output.

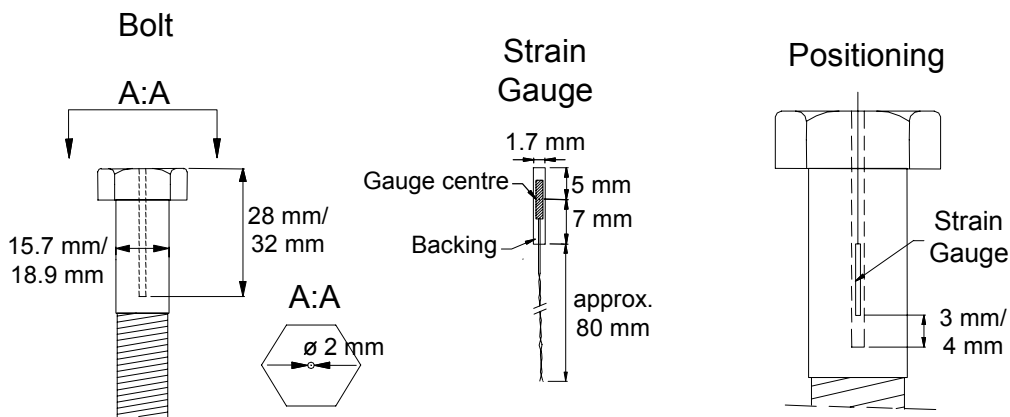


Figure 2.3 Strain gauge placement in the bolts

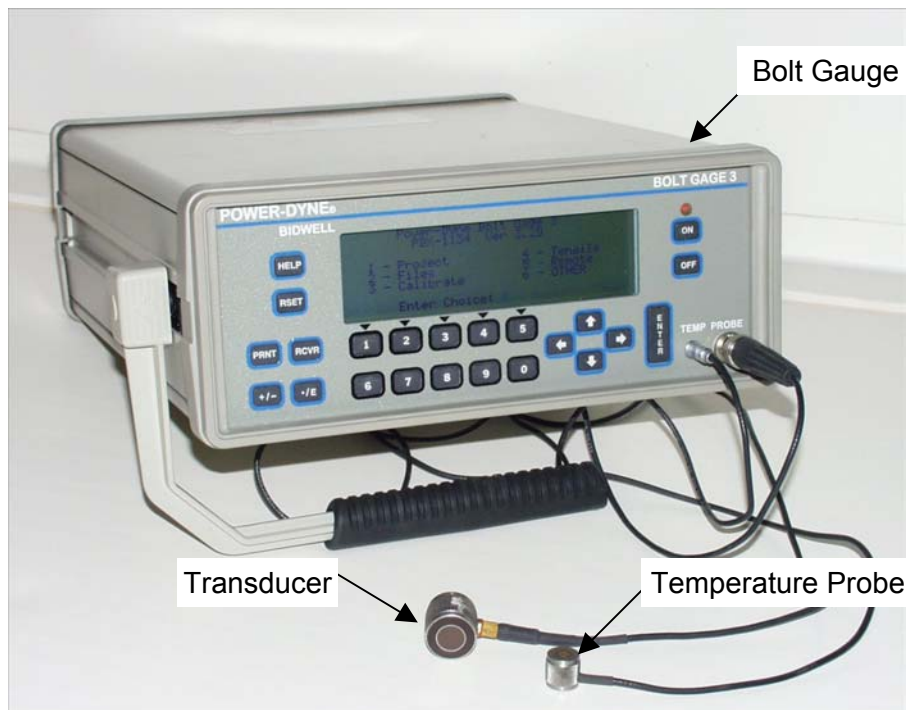


Figure 2.4 Ultrasonic bolt gauge

A very reliable bolt force measuring method was found in the ultrasonic bolt-measuring device (or "bolt gauge"). This instrument (see Figure 2.4) has proven to be very exact in many tests which were carried out for earlier bolt pretension studies [Kulak and Birkemoe 1993]. Other modern methods, such as measuring calipers used by the Institut für Baustatik und Konstruktion Zürich [IBK 1996], have not reported comparable precision.

The ultrasound method measures the bolt length using a shock wave that travels along the length of the bolt. At the end of the bolt most of the wave is reflected back due to the change of density. The reflected wave travels back until it reaches a transducer. At this point, a

small signal is produced by a piezoelectric element to stop a timing counter that had been started with the sending of the shockwave.

As the bolt is stressed in tension, the amount of time required for the ultrasonic wave to make its round trip increases for two reasons:

1. The bolt elongates with axial tension, so the path length increases.
2. The density of the bolt material decreases due to the growing volume. This causes a decreasing velocity of sound within the bolt.

The changes mentioned are linear functions (up to yield stress) of the load in the bolt, so that the total change in transit time is also a linear function of the load. To compensate for the velocity change of the ultrasonic wave due to the change in stress, a stress factor was introduced [Bickford 1995]. Additionally, for correct length measurements a temperature factor to even out the influence of temperature changes on the wave velocity has to be applied. The stress and temperature factors vary with the bolt material.

Tests on the bolts were carried out to find the correlation between the applied load and the elongation. Since the grip length affects the elongation, separate grip length (stressed length) calibrations were made. Figures 2.5 and 2.6 show the load-elongation curves for the different bolts and grip lengths. As not all ASTM A325 M16 ($\frac{5}{8}$ ") bolts came from a single batch, separate calibrations were necessary.

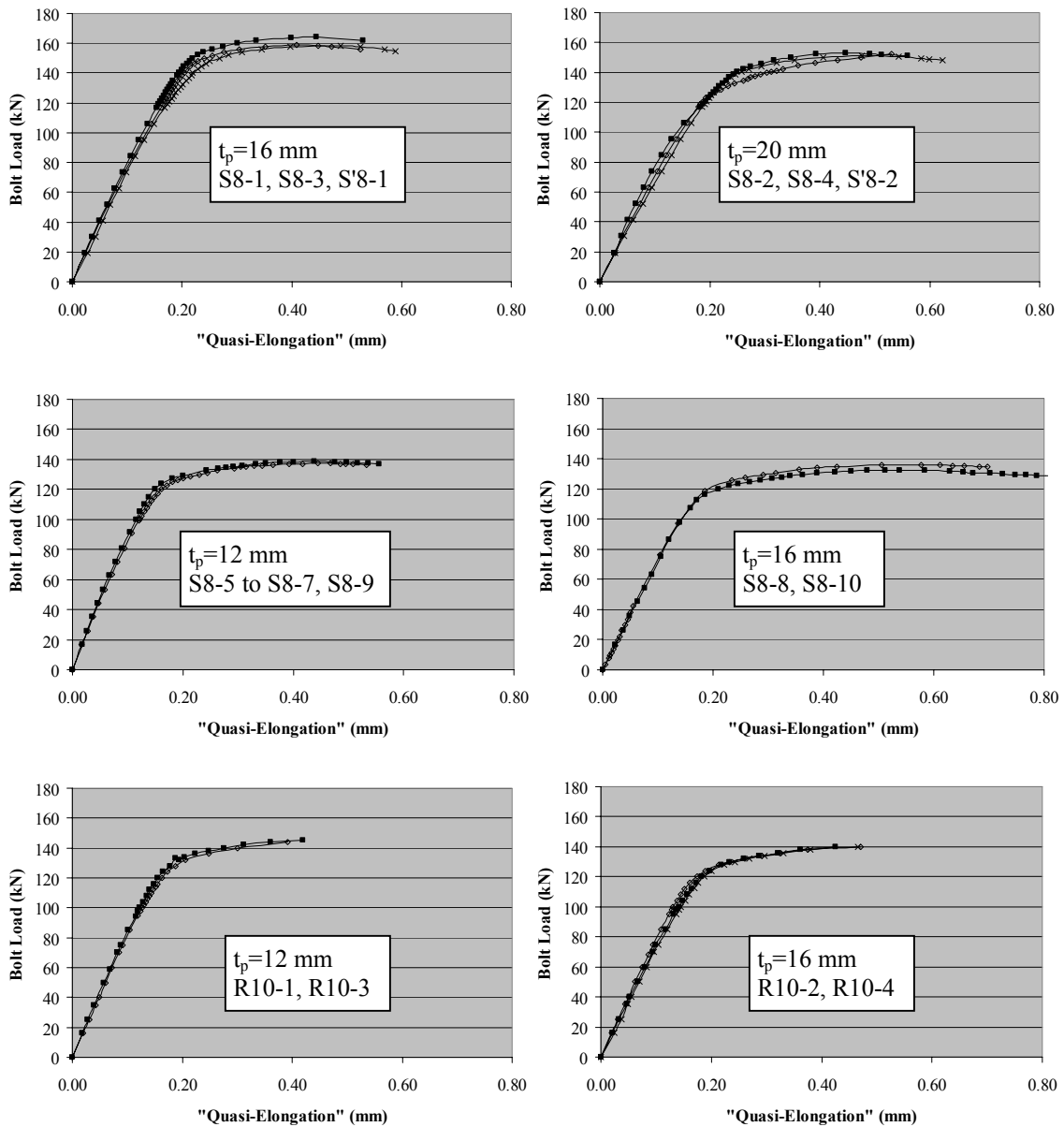


Figure 2.5 Bolt load versus "quasi-elongation" curves for ASTM A325 M16 ($\frac{5}{8}$ ") bolts

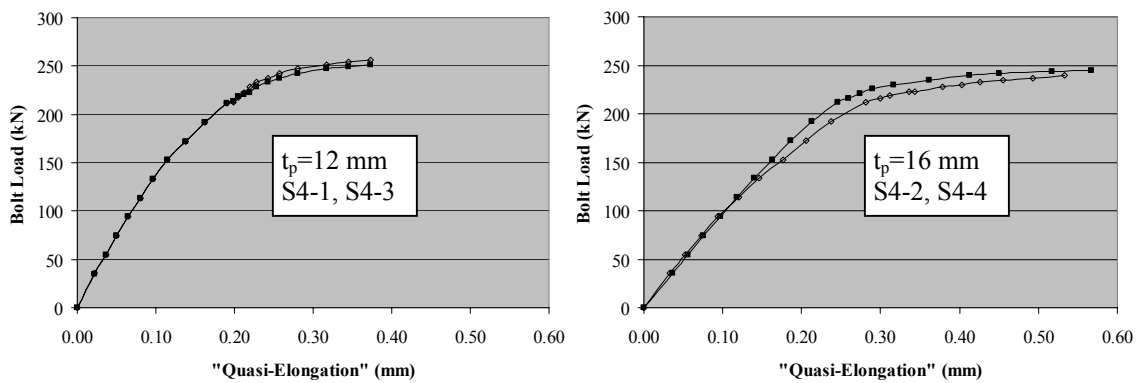


Figure 2.6 Bolt load versus "quasi-elongation" curves for ASTM A490 M20 ($\frac{3}{4}$ ") bolts

The elongation reported by the bolt gauge depends on the stress factor used. The values of the stress and temperature factors as provided by the bolt gauge manual [POWER-DYNE 1997] and Bickford [1995] are 0.281 and 103 (°C) for the ASTM A325 bolts and 0.285 and 101 (°C) for the ASTM A490 bolts respectively. As these stress factors are taken from literature they can only represent an average value for the particular bolt material. Thus, the elongation values can be slightly imprecise. The load vs. bolt-elongation curves should therefore not be used to calculate an Elastic modulus of the bolt material. To differentiate between the actual elongation of the bolt and the elongation as reported by the bolt gauge the term "quasi-elongation" is introduced. Still, the reported displacement values in the load-elongation curves can be used to calibrate a load to "quasi-elongation" curve of the tested bolts. Provided the bolt gauge has the information about the load to "quasi-elongation" behaviour of a specific bolt, the instrument is capable of reporting the applied load of the bolt at any time during testing.

The internal software of the bolt gauge processes the bolt information by creating a "bolt type". The diameter, the pitch, the stress and temperature factor, the load factors and the Y-intercept of the bolt define a bolt type. The load factors and the Y-intercept depend on the load vs. "quasi-elongation" behaviour of the bolt. They can be calculated by doing a regression analysis of the bolt vs. "quasi-elongation" curves obtained in calibration tests. The load factors are represented by the letters A to E and the Y-intercept by the letter Y in a fifth order polynomial function describing the bolt vs. "quasi-elongation" curve as follows:

$$f(x) = Ax + Bx^2 + Cx^3 + Dx^4 + Ex^5 + Y \quad (\text{Equation 2.1})$$

For a more detailed description of the operation mode and the theoretical background of ultrasonic measurement methods, the publications of Bickford [1995] and Krautkrämer and Krautkrämer [1990] can be consulted.

To ensure that the ultrasonic wave travels along the axis of the bolt, from the bolt head to the end of the bolt and back, the head and end of the bolt must be flat and perpendicular to the bolt axis. Instead of flattening (machining) the complete bolt head, as usually recommended, a hole, roughly the size of the transducer was machined into the bolt head. Additionally, the other end of the bolt was machined flat. The hole diameter has to be made slightly bigger than the transducer diameter to allow for possible deformations of the bolt head when the bolt is loaded. Figure 2.7 shows a fully machined bolt.

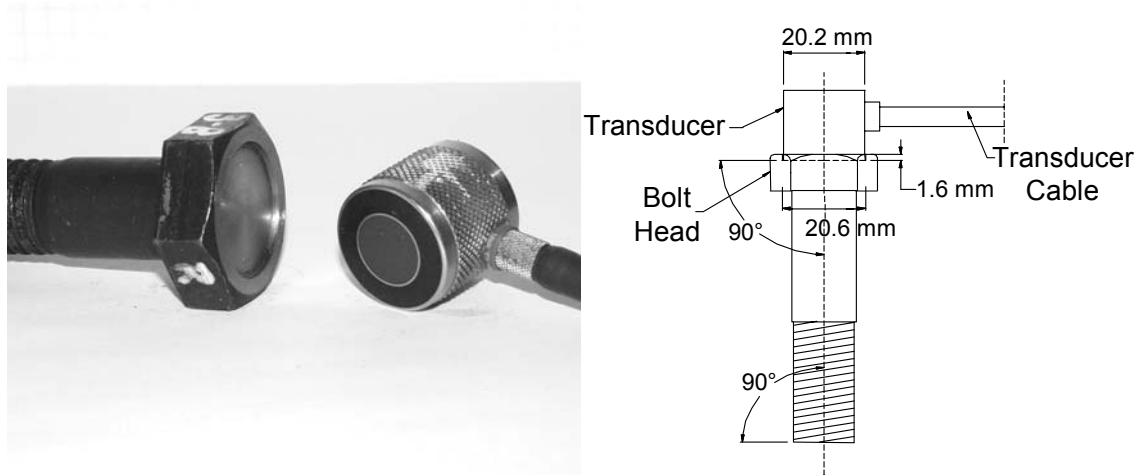


Figure 2.7 Fully machined bolt

2.3.2 Bolt Calibration

The bolts were tested using a special assembly as can be seen in Figure 2.8. This assembly, with fingers protruding from one part of the assembly into the other part of the assembly, converted the compression force applied by the MTS machine into a tensile loading of the bolt. Two very rigid and thick circular plates were used, each having six holes equally spread radially over an outer diameter and one hole in the centre of the plate. The hole in the centre of the plate bore the tested bolt, while the six outer holes were pierced by six fingers. To ensure a good load transfer from the MTS machine into the fingers, a thick plate was attached to the fingers. The location of the outer holes in each bearing plate in relation to the location of the holes in the other bearing plate was such that the fingers would only protrude through one plate while impinging on the other.

The test procedure required the transducer and the temperature probe to be placed on the bolt before any load was applied to the bolt. A measurement of the initial bolt length was taken with the bolt gauge. Then, the MTS machine slowly, applied an increasing load on the bolt. As the transducer could stay in place during the whole test the stroke of the machine did not have to be stopped at any time.

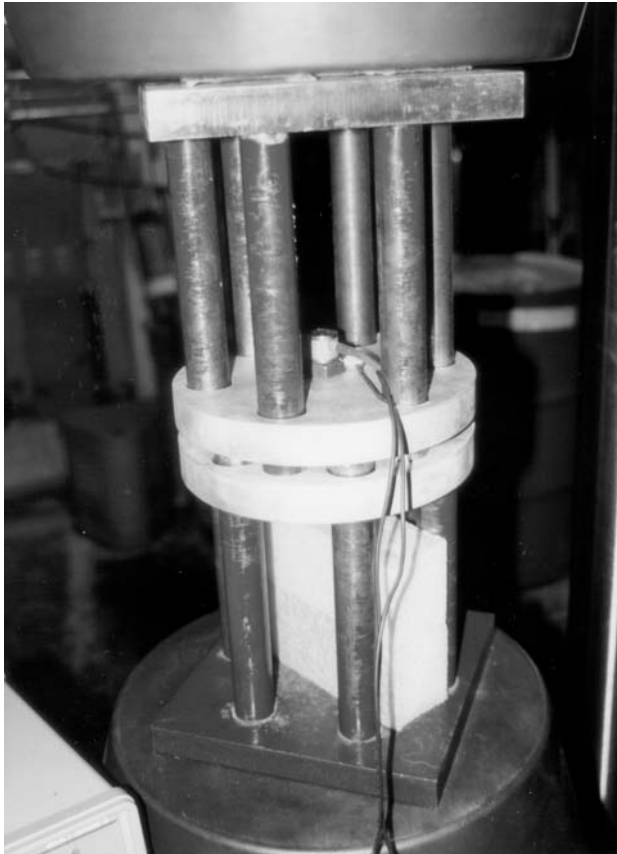


Figure 2.8 Bolt test setup

To gather information about the load-elongation behaviour of the bolt (see preceding section 2.3.1), 10 measurements before the yield load of the bolt and another roughly 20 measurements beyond yield load were taken. The bolt gauge stored the information on a built-in hard drive. After the test, the information was downloaded onto a PC using a data transfer cable. A regression analysis program then calculated a best fit curve for the load vs. "quasi-elongation" behaviour of the tested bolts. Additionally, the yield and ultimate load of each bolt were recorded during the tests. It was assumed that the results for bolts from a single batch are constant.

2.4 Specimen Fabrication and Testing

Figure 2.9 shows a typical fabrication drawing of a square flange-plate connection. All specimens were fabricated with fillet welds (MIG welding) joining the flange-plate and the hollow section. The welding process caused warping of the flange-plates. To guarantee the alignment of the connection the critical flange-plates were heat treated until reasonably flat.

Subsequent specimens were welded with the flange-plates clamped to the welding table to avoid excessive distortions of the flange-plates.

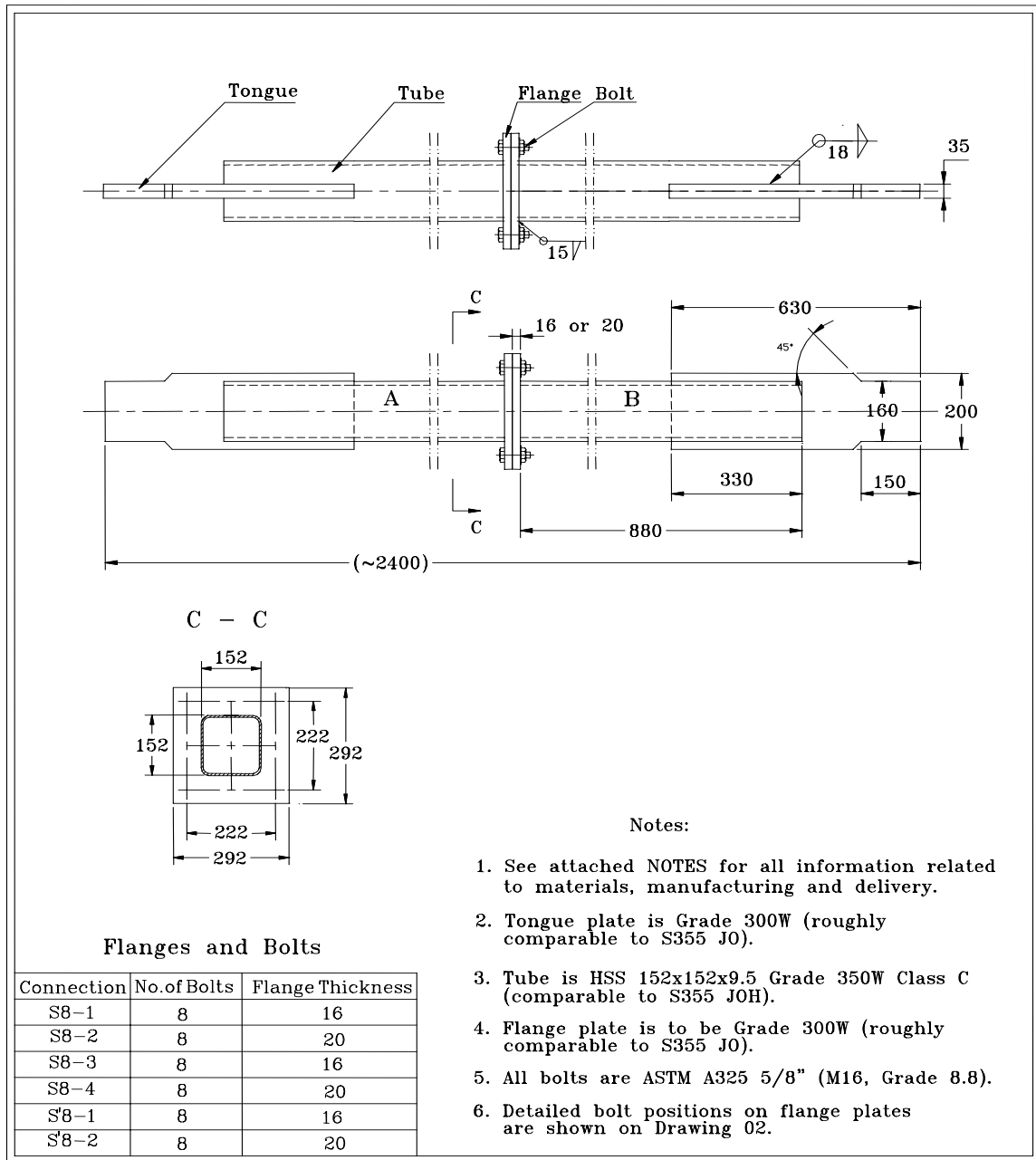


Figure 2.9 Fabrication drawing of square flange-plate connection

One of the first test specimens (specimen S8-4) was equipped with eight strain gauges which were placed in the middle of each side. Figure 2.10 shows the locations of the strain gauges. The data of the strain gauges confirmed a uniform stress distribution along all four sides of the hollow section in the vicinity of the bolted connection. As the length of the

specimens was not varied between the test series, it can be assumed that the influence of the gripping tongues is negligible for all connections.

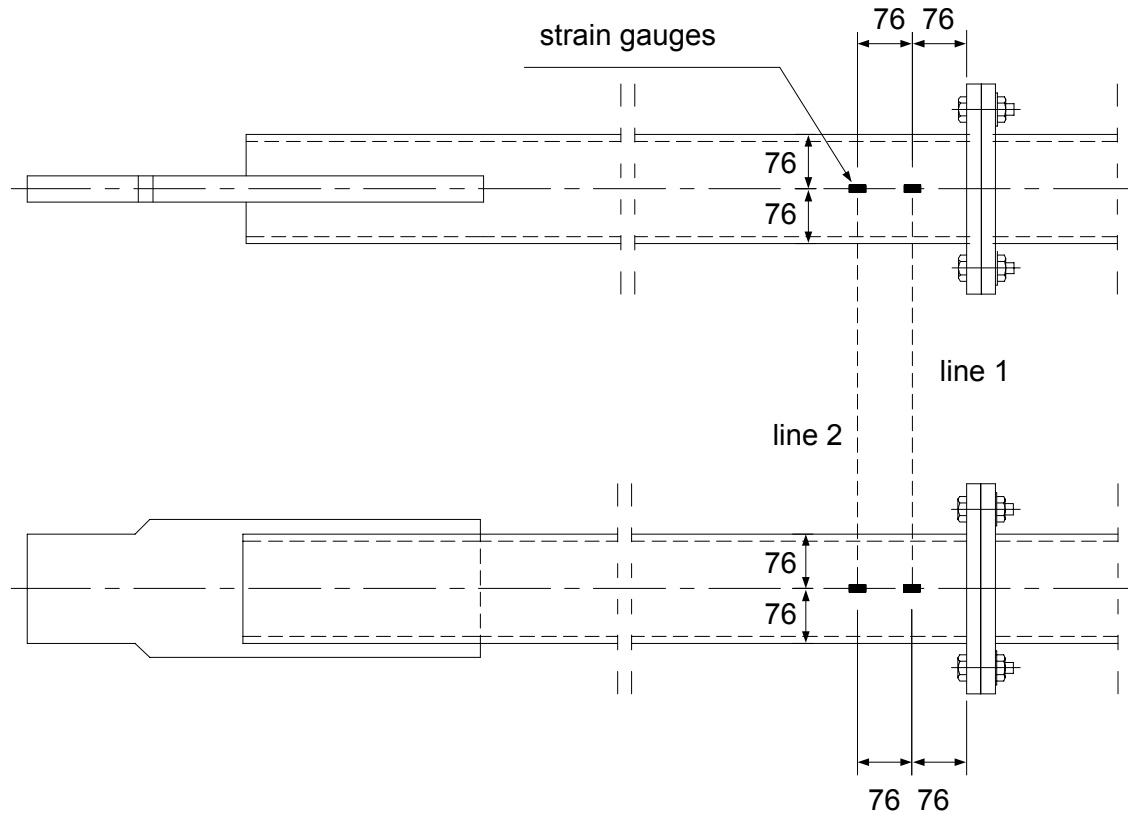


Figure 2.10 Strain gauge locations

An air wrench was used to pretension the bolts. Figure 2.11 shows the typical bolting pattern. To control the pre-tensioning, the bolt forces were measured throughout the tensioning using the ultrasonic bolt gauge.

An unloading of some bolts occurred during the pretension process caused by deformations in the flange-plates. The deformations in the flange-plates were generally rather uniform on all four sides so that, despite the unloading of the bolts during torquing, any single bolt was not expected to be overly stressed. The unloading of bolts due to warped plates was also examined in an earlier study on bolt installation in connections with out-of-flat plates carried out by Birkemoe [1989]. Therefore, a second or third torquing process was carried out until an equal load distribution (± 5 - 10 kN) for all bolts was reached. Visible dirt on the surfaces of the flange-plates had been removed before assembly to minimise the inhomogeneity of the bolt forces.

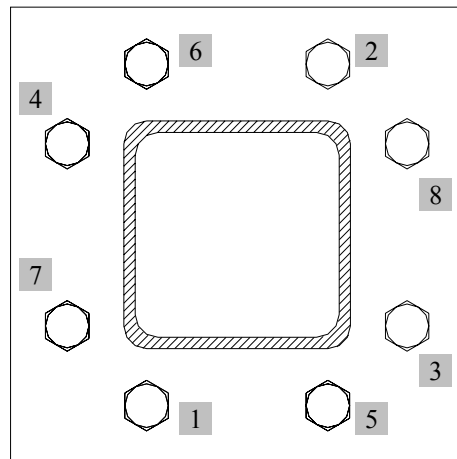


Figure 2.11 Bolt tensioning sequence

To measure the connection elongation, four Linear Variable Differential Transformers (LVDTs) were mounted on each connection (see Figure 2.12). The final stage was to grip the specimens and to begin the loading of the connection.

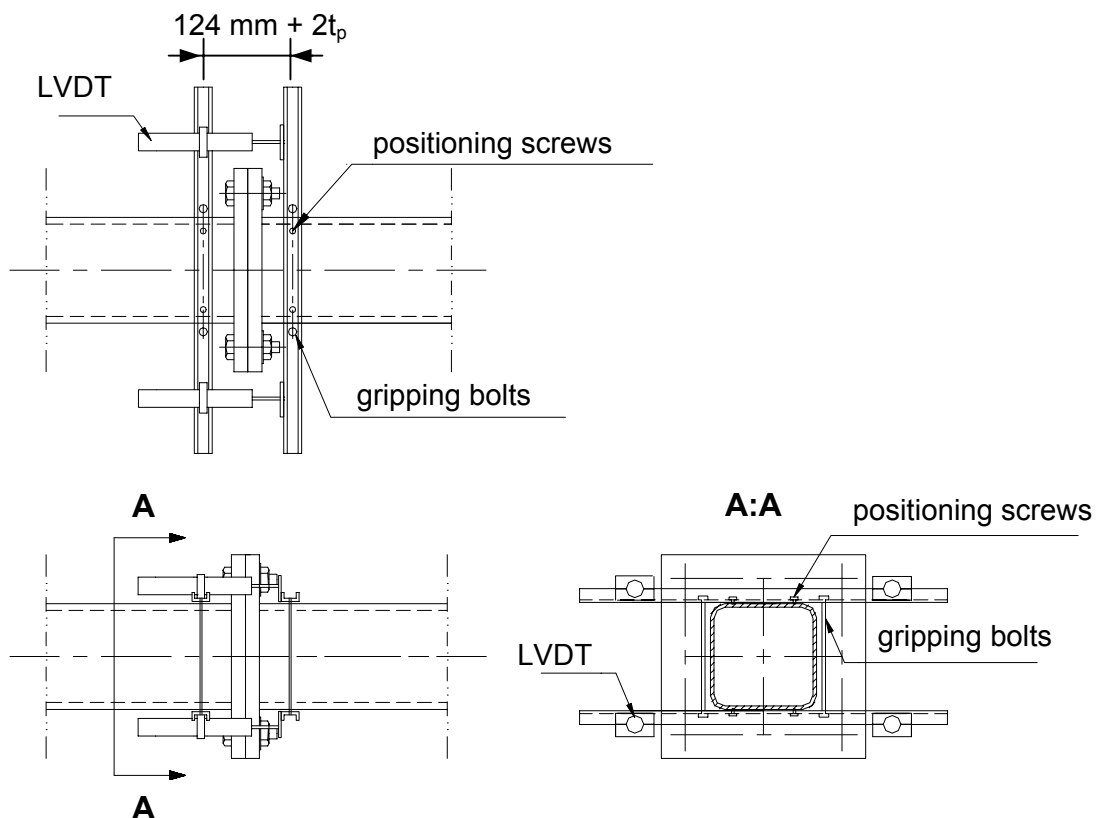


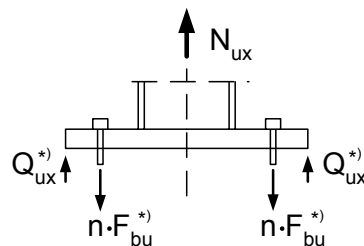
Figure 2.12 LVDT locations

For all specimens, a quasi-static test under tensile loading was carried out. To ensure quasi-static loading conditions the tensile load was applied very slowly (about 50 kN per minute in the elastic range of the test or a stroke of 0.125 mm per minute). During each test, all measurements from the MTS machine, the strain gauges and the LVDTs were read and recorded by a data acquisition system. The testing procedure contained up to 15 load stages during which the forces in the bolts were measured with the bolt gauge. As only a single transducer existed to measure up to ten individual bolts, it was necessary to take the transducer off the bolt head and measure one bolt after the other while keeping the machine stroke constant. After the last load stage, indicated by bolt forces close to rupture load, the bolt gauge as well as all LVDTs were removed from the specimen to avoid any damage. The connections were then wrapped with thick plastic foil to prevent the bolts from becoming projectiles upon rupture.

2.5 Test Results

A total of 20 bolted flange-plate connections has been tested. All specimens failed due to rupture of at least one bolt. The measured prying ratios in the following tables are calculated as follows:

$$\beta_{ux} = \frac{Q_{ux}}{N_{ux}} = \frac{n \cdot F_{bu} - N_{ux}}{N_{ux}}$$



(Equation 2.2),

*) proportion of load on the corresponding side

with Q_{ux} being the total prying force and n the number of bolts in the connection.

The next sections of this chapter will provide the following for each connection type:

- a table with failure loads and corresponding prying ratios,
- a typical picture of the flange-plates after failure,
- a typical connection load versus displacement graph,
- a typical bolt load versus connection load graph.

Full documentation of the connection load versus displacement graphs as well as the bolt load versus connection load graphs can be found in Appendix Part I.

2.5.1 Square Flange-Plate Connections

2.5.1.1 Specimens with Four Bolts

Table 2.6 shows the test results for all tested specimens having four bolts. For the specimens with the thin flange-plates ($t_p = 12$ mm, S4-1 and S4-3), the prying ratios have significant values. The prying action for the specimens with thicker flange-plates ($t_p = 16$ mm, S4-2 and S4-4) is negligible. The ratio of edge distance "a" to distance from bolt line to hollow section face "b", also influences the amount of prying action. A smaller distance between bolts and hollow section, increasing ratio of "a" to "b", results in less prying action.

Plastic deformation in the flange-plates can be reported for all four specimens (see Figure 2.13). For the flange-plate connections with the thin plates the deformations were more pronounced.

Table 2.6 Test results for square flange-plate connections with four bolts

Specimen	t_p (mm)	a/b	Failure load N_{ux} (kN)	Bolt strength F_{bu} (kN)	Prying ratio β_{ux} (%)
S4-1	12	1.00	847	256	20.9
S4-2	16	1.00	955	247	3.7
S4-3	12	0.78	792	256	29.3
S4-4	16	0.78	910	247	8.8



Figure 2.13 Square flange-plate connection (S4-1) with four bolts after failure

Figure 2.14 shows a typical load versus displacement graph as recorded by the four LVDTs. The displacement was measured over a distance of 65 mm (distance between the positioning screws of the top and bottom LVDT mounts, see Figure 2.12). Due to the very high wall thickness of the hollow section, in comparison to the thickness of the flange-plate, the hollow section remained elastic during the whole test, thereby contributing only negligibly to the measured displacement of the LVDT. The bold line in the graph represents the average displacement of all four LVDTs. An initial stiff behaviour of the connection is followed by significant displacement in the later load stages. The transition between stiff and flexible behaviour of the connection coincides with the separation load of the bolts (see Figure 2.15).

A typical bolt load versus connection load graph is given in Figure 2.16. The straight line in the graph represents the bolt load caused by the connection load (without prying forces or pretensioning loads), thus being the connection load divided by the number of bolts. After the separation load, the distance between the measured bolt loads and this line indicates the amount of prying action.

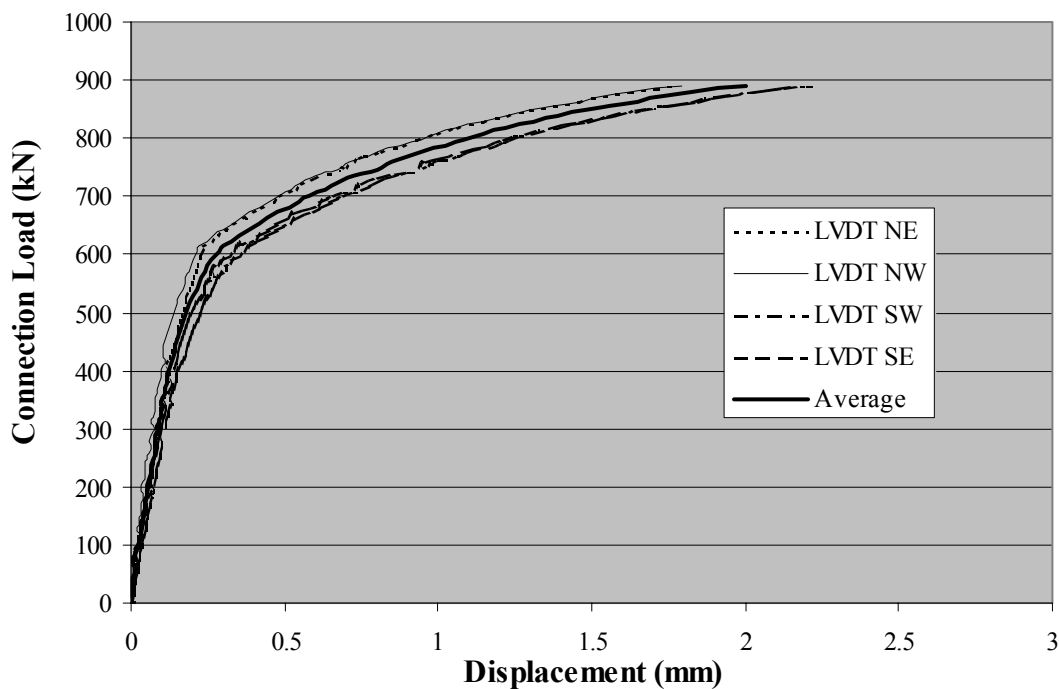


Figure 2.14 Connection load versus displacement graph for specimen S4-2

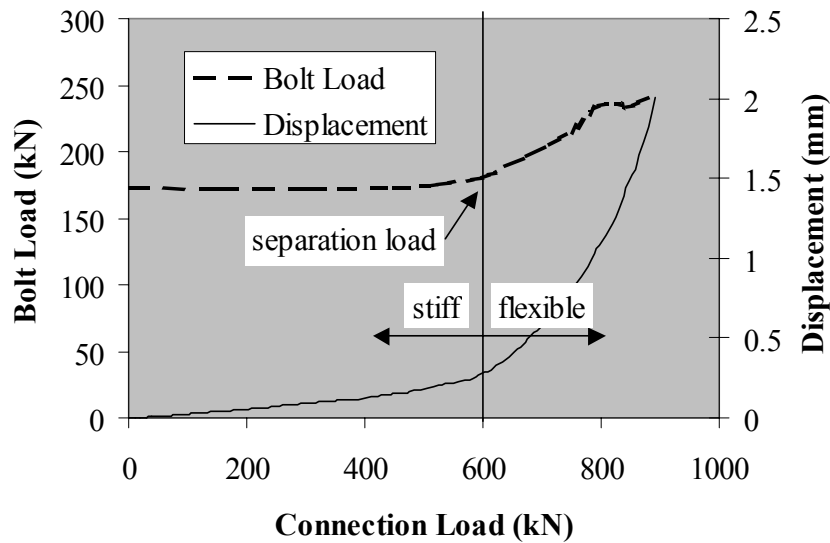


Figure 2.15 Connection load versus average bolt load and average displacement

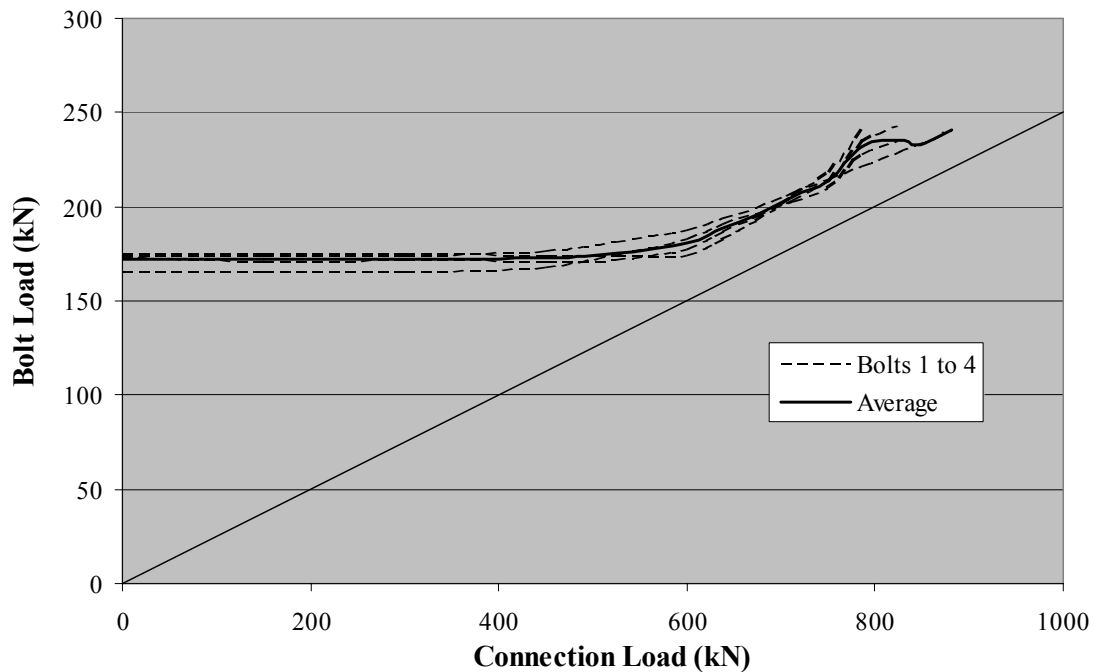


Figure 2.16 Bolt load versus connection load graph for specimen S4-2 (prying ratio of 3.7%)

2.5.1.2 Specimens with Eight Bolts

The test results for the square flange-plate connections with eight bolts can be found in Table 2.7. The prying ratios vary between 2.1% for specimen S8-4 and 30.9% for specimen S8-7. As with the 4-bolt specimens the flange-plate thickness exhibited the biggest influence on the connection strength. A decrease in flange-plate thickness results in an increase in prying action. Comparing the results of specimens S8-5 and S8-6 with the results of specimens S8-7 and S8-9

(each having the same flange-plate thickness and distance between the bolts, "c") the influence of the ratio of edge distance "a" to distance from bolt line to hollow section face "b", can be observed. A decrease in this ratio (increasing the distance between bolts and the hollow section) results in an increase in prying action. The prying ratio was also shown to be influenced by the distance between the bolts on one side, distance "c". The comparison between, e.g., specimens S8-1 and S8-3, or between S8-5 and S8-6, show that an increase in bolt spacing "c" results in an increase in prying action.

Table 2.7 Test results for square flange-plate connections with eight bolts

Specimen	t_p (mm)	a/b	c (mm)	Failure load N_{ux} (kN)	Bolt strength F_{bu} (kN)	Prying ratio β_{ux} (%)
S8-1	16	1.00	140	1108	160	15.7
S8-2	20	1.00	140	1162	152	4.5
S8-3	16	1.00	70	1240	160	3.4
S8-4	20	1.00	70	1190	152	2.1
S8-5	12	1.00	140	903	138	22.2
S8-6	12	1.00	70	946	138	16.6
S8-7	12	0.78	140	843	138	30.9
S8-8	16	0.78	140	946	134	13.5
S8-9	12	0.78	70	881	138	25.2
S8-10	16	0.78	70	1019	134	5.4
S'8-1	16	1.00	--	1049	160	22.2
S'8-2	20	1.00	--	1141	152	6.4

As expected, the deformations in the flange-plates (see Figure 2.17) of the specimens with eight bolts were generally less pronounced than the deformations of the flange-plates in the 4-bolt specimens. The thinner the flange-plates (higher prying ratio) the larger were the observed deformations for all tested specimens.

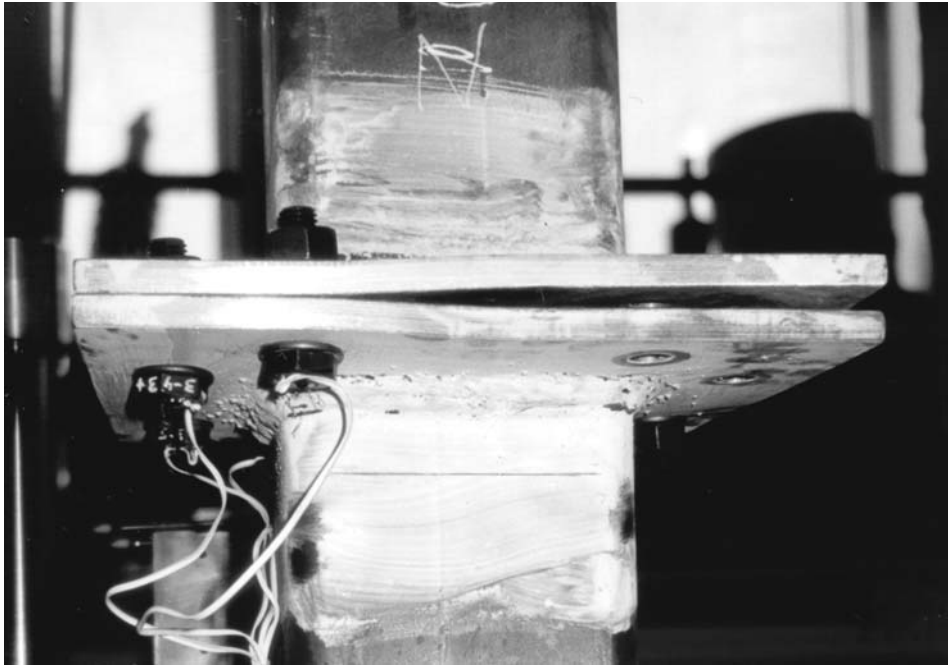


Figure 2.17 Square flange-plate connection (S8-3) with eight bolts after failure

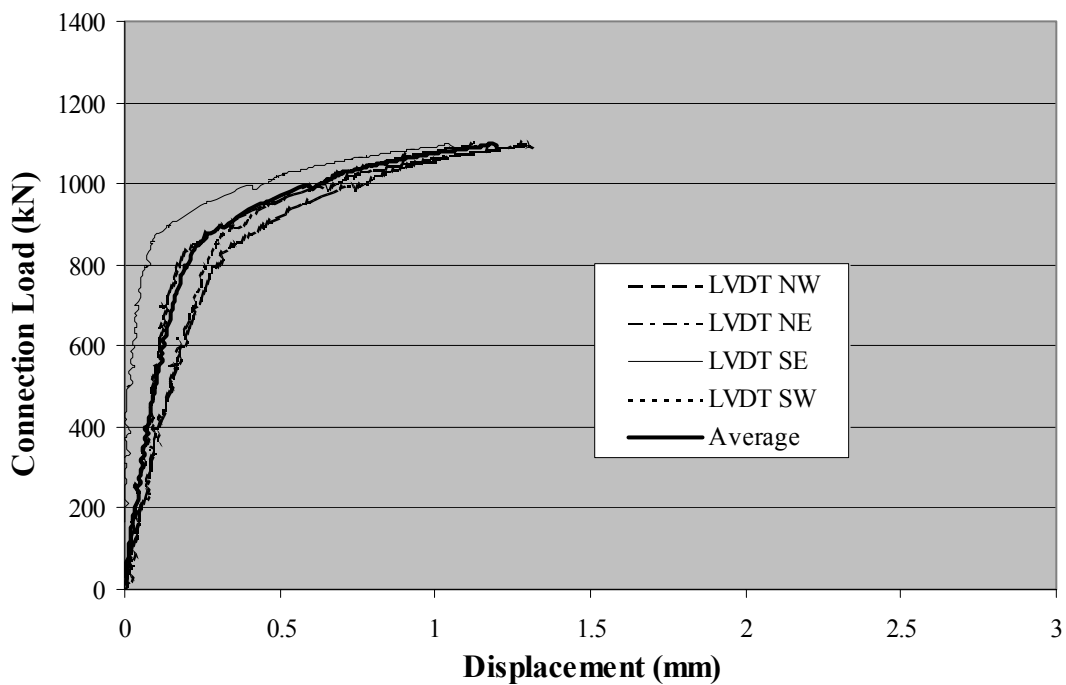


Figure 2.18a Connection load versus displacement graph for specimen S'8-2

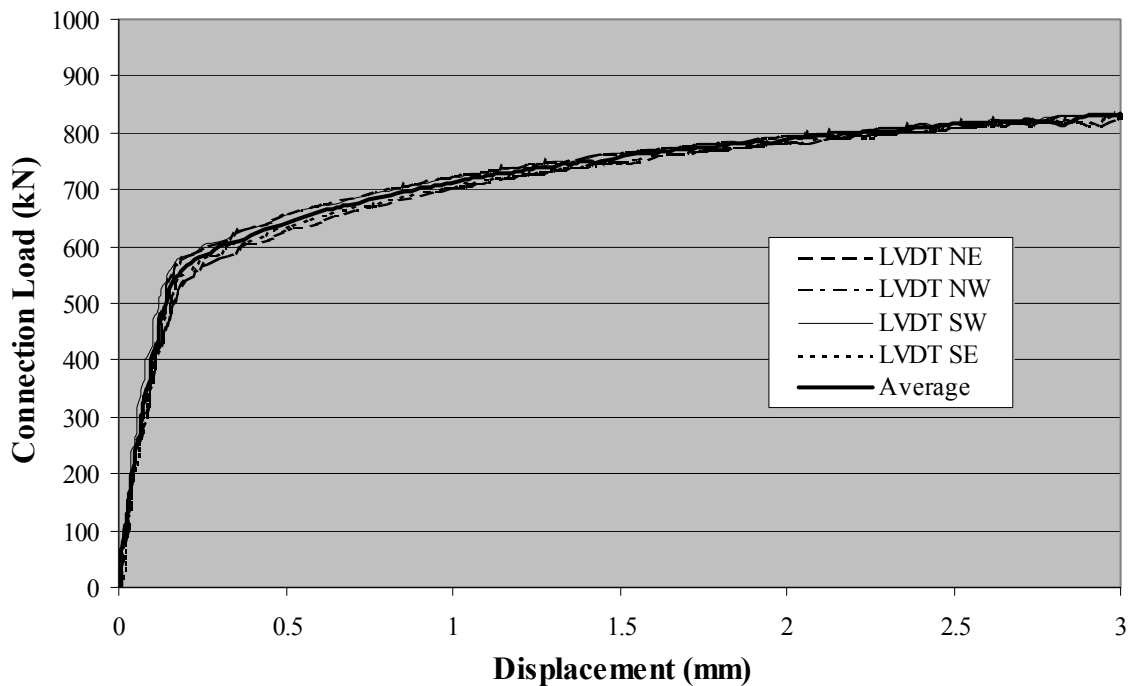


Figure 2.18b Connection load versus displacement graph for specimen S8-5

The results of the LVDTs indicate overall bending in some specimens (see Figures 2.18a and 2.18b). Specimens S8-1 to S8-4, and S'8-1 and S'8-2, generally showed more bending compared to the specimens of the second set of tests (S8-5 to S8-10). The bending of the specimens of the earlier test series was probably caused by deformations in the flange-plates and general misalignment of the connections. For the specimens of the second test series special consideration was taken to achieve perfect alignment of the two connection halves. Due to the warped flange-plates in the first set of tests, it was also more difficult to achieve an equal load distribution between all bolts, as can be seen in Figures 2.19a and 2.19b.

The bolt layout of specimens S'8-1 and S'8-2 (see Table 2.1) inherently caused an uneven load distribution in the bolts (see Figure 2.20). This uneven load distribution caused an early failure of these connections. The prying ratio is calculated based on the assumption that all eight bolts are stressed to their ultimate load at failure of the connection. As some bolts of specimen S'8-2 were not stressed to their ultimate load at failure of the connection the reported prying ratio of 6.4% does not correspond with the average prying ratio shown in Figure 2.19a. Unfortunately, the measurement of the bolt loads cannot be done right up to failure of the connection as the transducer of the bolt gauge would be severely damaged when placed on a breaking bolt. Also, it would be dangerous for the operator.

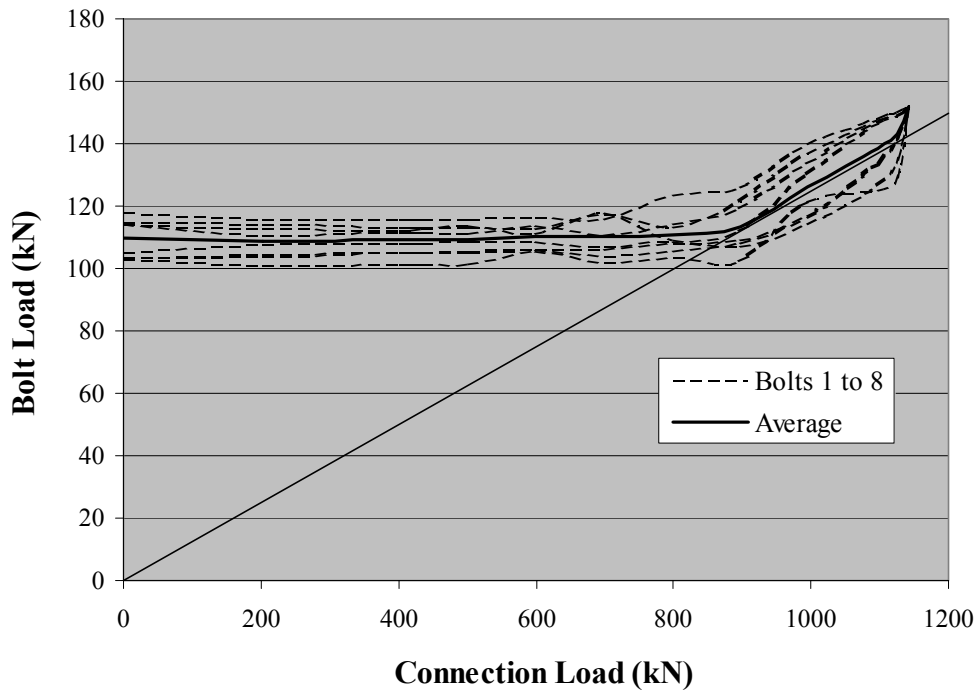


Figure 2.19a Bolt load versus connection load graph for specimen S'8-2 (prying ratio of 6.4%)

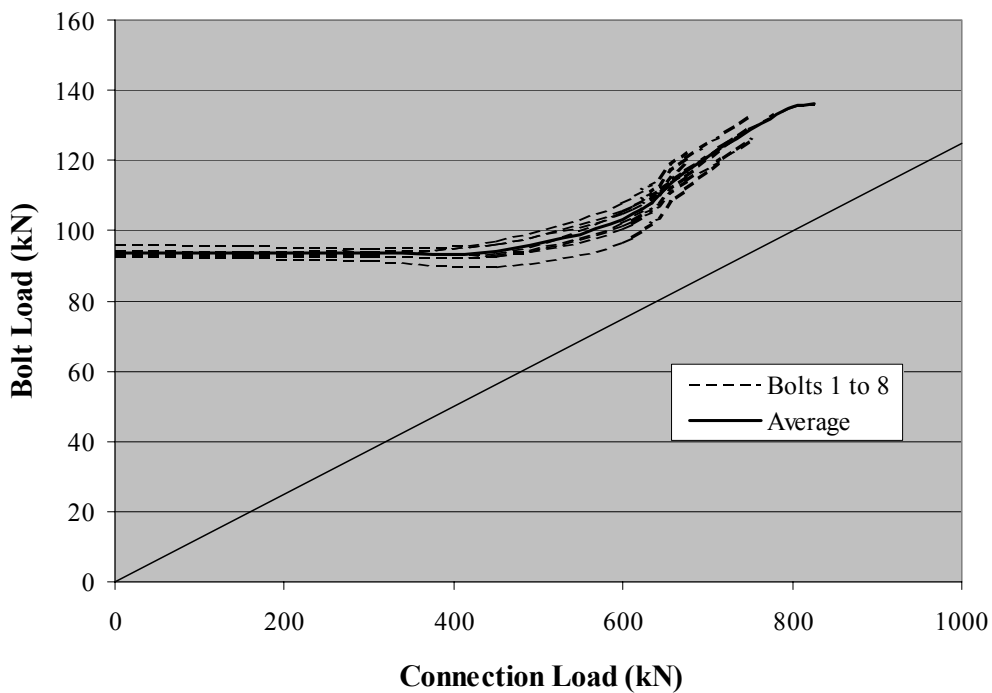


Figure 2.19b Bolt load versus connection load graph for specimen S8-5 (prying ratio of 22.2%)

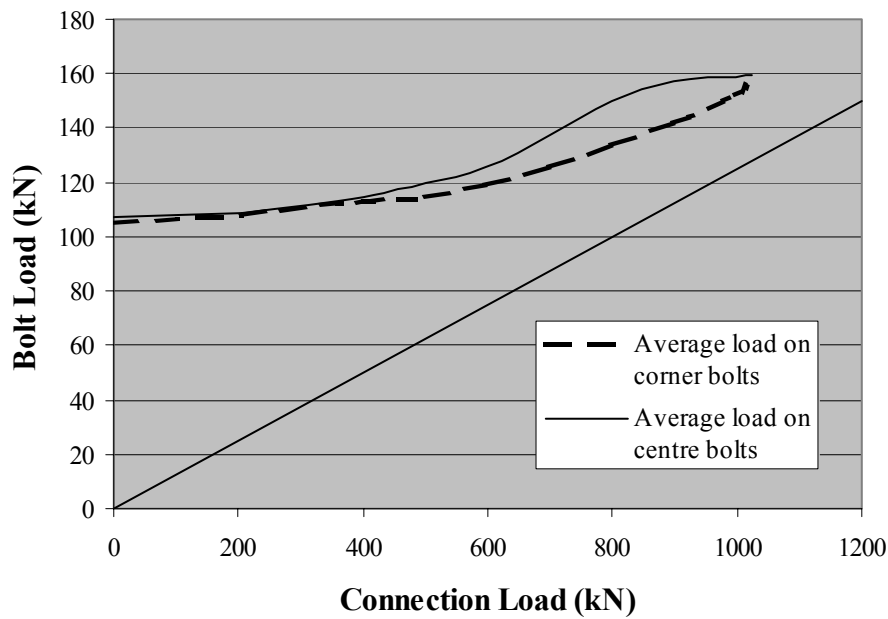


Figure 2.20 Bolt load versus connection load graph for specimen S'8-1 (prying ratio of 22.2%)

2.5.2 Rectangular Flange-Plate Connections

Table 2.8 shows the test results for the rectangular flange-plate connections. As with the earlier connections, the flange-plate thickness had the biggest influence on the connection strength. The influence of the ratio of edge distance "a" to distance from bolt line to hollow section face "b", could also be observed. A decrease in the a/b-ratio caused an increase in prying action. As the distance between the bolts on one side, distance "c", was constant for all four specimens the influence of this dimension could not be studied in the experimental program.

Table 2.8 Test results for rectangular flange-plate connections with ten bolts

Specimen	t_p (mm)	a/b	c (mm)	Failure load N_{ux} (kN)	Bolt strength F_{bu} (kN)	Prying ratio β_{ux} (%)
R10-1	12	0.78	110	1030	146	41.7
R10-2	16	0.78	110	1153	141	22.2
R10-3	12	1.00	110	1105	146	32.1
R10-4	16	1.00	110	1240	141	13.6

Despite high prying ratios, only negligible plastic deformations were found in the flange-plates after the test (see Figure 2.21).



Figure 2.21 Rectangular flange-plate connection (R10-1) with ten bolts after failure

Figure 2.22 shows a typical connection load versus displacement graph for a rectangular specimen. The displacement is measured over a distance of 65 mm. An initial stiff connection behaviour is followed by flexible behaviour after the bolt separation load.

The bolt load versus connection load graphs are given for specimen R10-1 in Figure 2.23. Due to the bolt layout of the rectangular specimens, an uneven load distribution of the bolts was observed (see Figures 2.23 and 2.24). As also demonstrated for the square flange-plate connections with bolt layout type S'8 the inside bolts (bolts 2 and 7 in Figure 2.24) were more stressed compared to the remaining bolts. The uneven load distribution was more pronounced in the connections with thinner flange-plates.

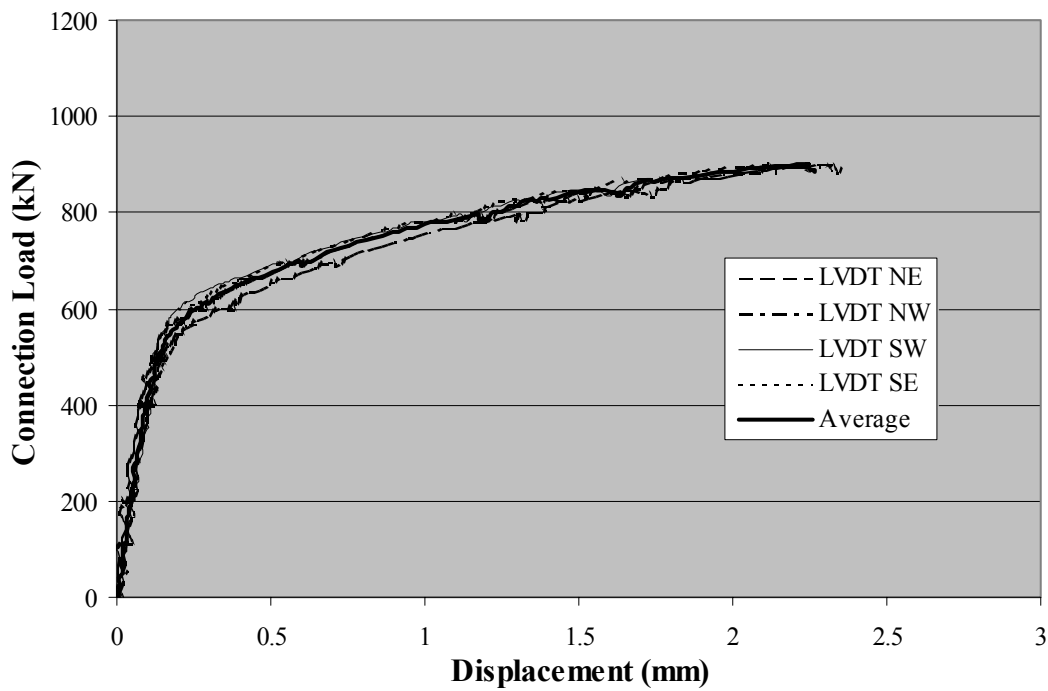


Figure 2.22 Connection load versus displacement graph for specimen R10-1

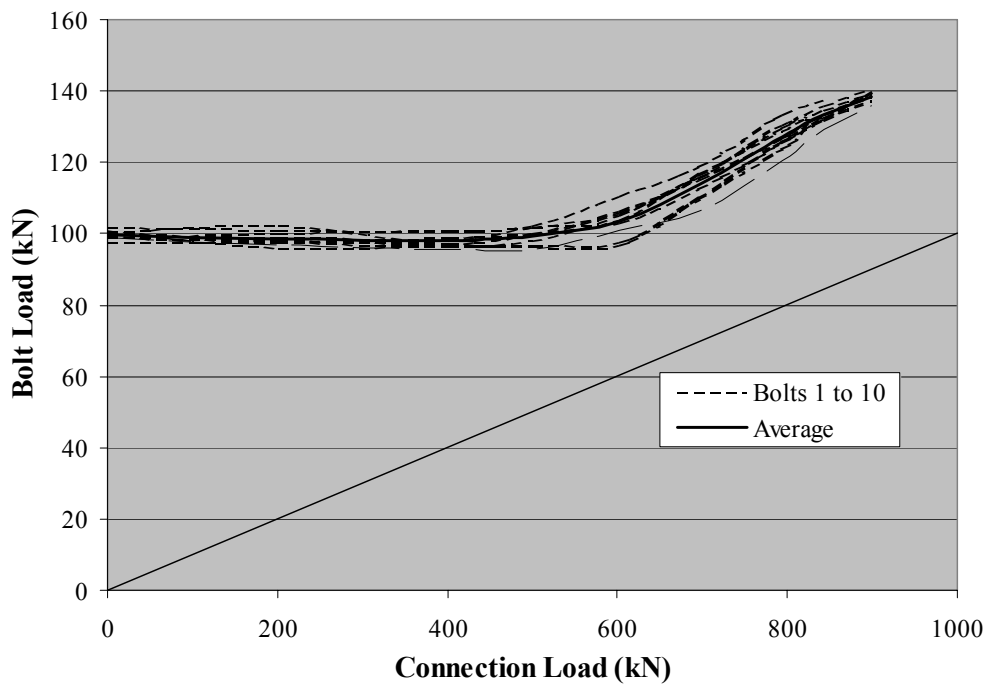


Figure 2.23 Bolt load versus connection load graph for specimen R10-1 (prying ratio of 41.7%)

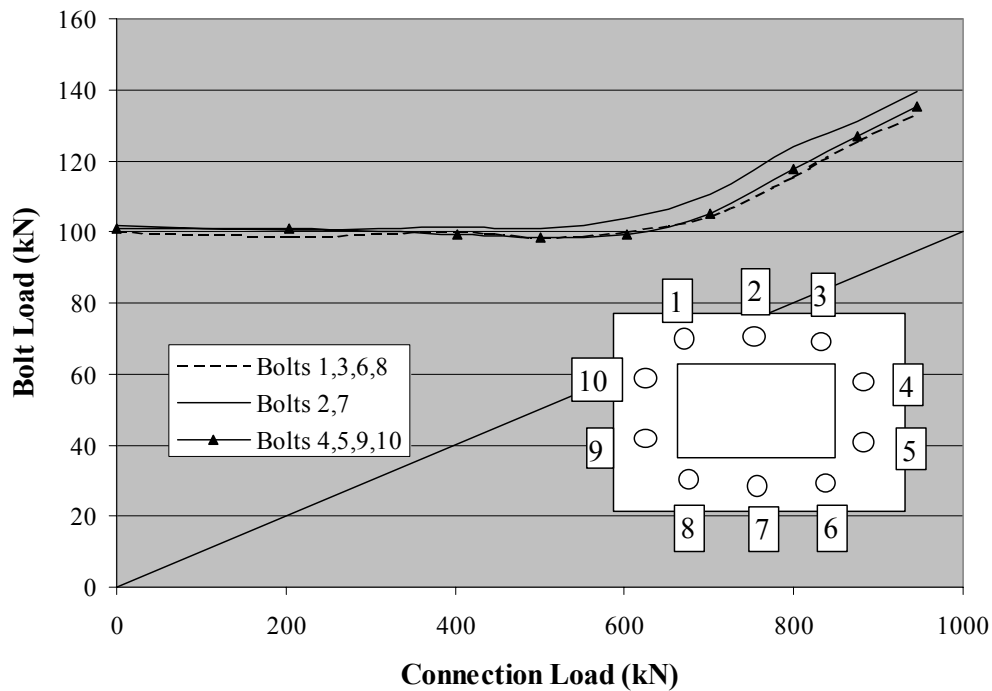


Figure 2.24 Bolt load versus connection load graph for specimen R10-3 (prying ratio of 32.1%)

2.6 General Observations from the Testing Program

The main focus of this investigation was to study the influence of the flange-plate thickness as well as the bolt layout on the connection capacity. Table 2.9 gives an overview of the main parameters and their respective influence on the connection capacity. Tables 2.10a to 2.10c compare the prying ratios of specimen pairs where all but one parameter is constant. Thereby, the influence of the differing parameter becomes apparent.

Table 2.9 Influence of each parameter on the prying action and the connection capacity

Parameter	Prying action	Connection capacity
$t_p \uparrow$	↓	↑
$a/b \uparrow$	↓	↑
$c \uparrow$	↑	↓

Table 2.10a Comparison of prying ratios for specimens with differing parameters (t_p varies)

Specimens	Prying ratio β_{ux} (%) for $t_p =$		
	12mm	16mm	20mm
S8-5, S8-1, S8-2	22.2	15.7	4.5
S8-6, S8-3, S8-4	16.6	3.4	2.1
S'8-1, S'8-2	--	22.2	6.4
S8-7, S8-8	30.9	13.5	--
S8-9, S8-10	25.2	5.4	--
S4-1, S4-2	20.9	3.7	--
S4-3, S4-4	29.3	8.8	--
R10-1, R10-2	41.7	22.2	--
R10-3, R10-4	32.1	13.6	--

Table 2.10b Comparison of prying ratios for specimens with differing parameters (a/b-ratio varies)

Specimens	Prying ratio β_{ux} (%) for a/b =	
	0.78	1.00
S8-7, S8-5	30.9	22.2
S8-9, S8-6	25.2	16.9
S4-3, S4-1	29.3	20.9
S4-4, S4-2	8.8	3.7
R10-1, R10-3	41.7	32.1
R10-2, R10-4	22.2	13.6

Table 2.10c Comparison of prying ratios for specimens with differing parameters (c varies)

Specimens	Prying ratio β_{ux} (%) for c =	
	70mm	140mm
S8-3, S8-1	3.4	15.7
S8-4, S8-2	2.1	4.5
S8-6, S8-5	16.6	22.2
S8-9, S8-7	25.2	30.9
S8-10, S8-8	5.4	13.5

The flange-plate thickness has the biggest influence on the prying action. The plastic bending capacity of the flange-plate is proportional to the square of the thickness, given by $m_y = \frac{1}{4} t_p^2 f_{yp}$. With an increase in flexural strength the prying effect decreases, therefore increasing the connection capacity. The bolt layout dimensions (see Figure 2.1), namely the ratio of edge distance "a" to distance from bolt line to hollow section face "b", as well as the

distance between the bolts on one side, distance "c", also have a significant influence on the prying forces. The lower the "a" to "b" ratio, the further away is the bolt line from the hollow section, thus increasing the lever arm and causing the prying forces, which in turn decreases the connection capacity. The test results show that an increase in bolt spacing "c" increases the prying ratio. This behaviour contradicts the yield line model of Kato and Mukai [1982]. Figure 2.25 shows the predicted prying ratios using the Kato and Mukai model for the tested flange-plate connections with increasing bolt pitches.

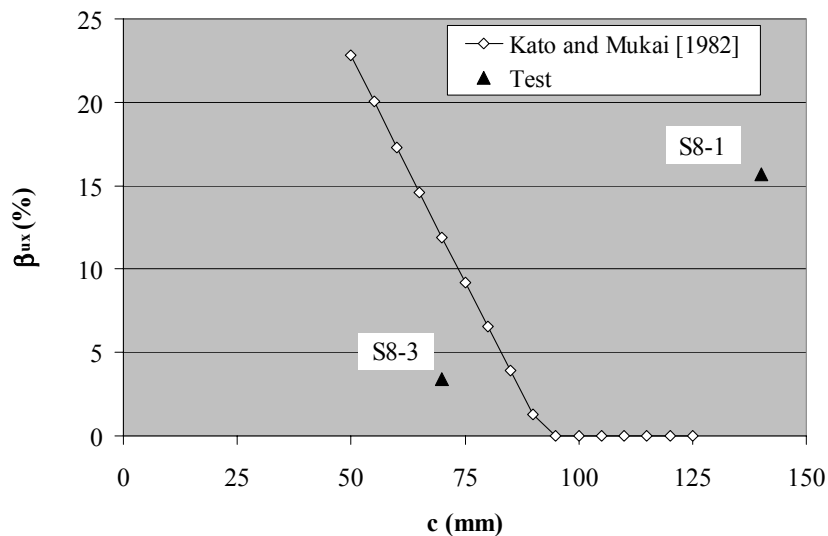


Figure 2.25 Prying ratios as predicted by Kato and Mukai [1982]

With bolt layout S'8 for the square flange-plate connections and with the bolt layout of the rectangular connections (see Figure 2.1), some bolts were stressed more than the remaining bolts. As the uneven load distribution caused early failure, these bolt layouts should be avoided. For square flange-plate connections bolt layout S8 (see Figure 2.1) should be used. For rectangular connections with a high height to width ratio ($h_t/b_t > 2$), bolt layouts with bolts along the two long sides of the connections only seem more suitable. As hollow sections with a height to width ratio of over two are not common, this will hardly ever become critical.

3 *VALIDATION OF NUMERICAL MODELS*

3.1 *General Introduction*

Due to ever-increasing costs as well as the high time factor involved in experimental testing, numerical analyses have become a popular tool for simulations of structural behaviour. The development of suitable finite element programs (element libraries, solvers, material and geometric non-linearity) on the one hand and the knowledge of their use (discretisation, element choice, analysis technique) on the other hand have allowed finite element analysis to become an essential tool in design and research. A lot of knowledge about stress and strain concentration factors for fatigue design of welded tubular connections [van Wingerde 1992, Herion 1994, Romeijn 1994] has been based on the results of numerical analyses. The suitability of FE-analysis for static strength predictions of hollow section connections has been demonstrated, e.g. in the publications of van der Vegte [1995], Lu [1997], Yu [1997] and de Winkel [1998]. Based on a well-calibrated finite element model (verified by experiments within the range of parameters), it is possible to carry out a large number of parametric studies which are cheaper and faster than experimental investigations.

3.2 *Software and Hardware*

The software package ANSYS 5.6 [Swanson Analysis System Inc. 1999] has been used for pre- and post-processing as well as analyses of the FE-models. The hardware used consisted of standard PCs (Intel Pentium 500MHz, 512 MB Ram) and a remotely accessible server SGI Origin 3200, with eight processors and two Gigabytes of memory. The operating systems were Windows NT or Windows 2000 for the PCs and IRIX 6.5 for the workstations.

3.3 *General Considerations*

The accuracy of the numerical results is greatly affected by the following aspects:

1. Element types;
2. Geometrical and material non-linearities;
3. Solution techniques used for the numerical analysis;
4. Boundary conditions;
5. Element discretisation.

3.3.1 Element Types used in the Study

The finite element package ANSYS 5.6 [Swanson Analysis System Inc. 1999] offers a variety of shell and volume elements. For the static analysis of the bolted flange-plate connections the following element types have been tested:

- Solid45: 8-noded (linear) 3D structural solid element with 3 degrees of freedom per node, plasticity, large stress and strain capabilities, stress stiffening and optional reduced integration with hourglass control.
- Solid95: 20-noded (quadratic) 3D structural solid element with 3 degrees of freedom per node, plasticity, large stress and strain capabilities, stress stiffening and optional reduced integration with hourglass control.
- Shell43: 4-noded plastic large strain shell with 6 degrees of freedom per node, plasticity, large stress and strain capabilities and stress stiffening. It has 2x2 in-plane integration and 5 integration points over its thickness.
- Contac52: 2-noded 3D point to point contact element representing two surfaces. Compression in the normal direction and shear (Coulomb friction) in tangential direction is supported.

With regard to the importance of the bolts for the failure of the connection, an independent study on the discretisation and choice of element types for the bolts has been carried out. Shell elements were not considered for the modeling of the bolts as the 3-dimensional mode of action of the bolts does not agree with the planar dimensionality of shell elements. Figure 3.1 shows the force-displacement curves for the bolts used for specimens S8-8 and S8-10 (see Tables 2.1 and 2.2) and their respective FE-models using different element types and discretisations. For the coarse models, the 20-noded models generally gave better results than the 8-noded models. The coarsely meshed 20-noded models perform marginally better than the 8-noded finely meshed models. The difference between the results of the fine and coarsely meshed 20-noded models is negligible. With regard to the CPU time and number of nodes and elements (see Table 3.1) the FE-model with a coarse mesh using 20-noded elements was preferred to the finer meshed model for further use.

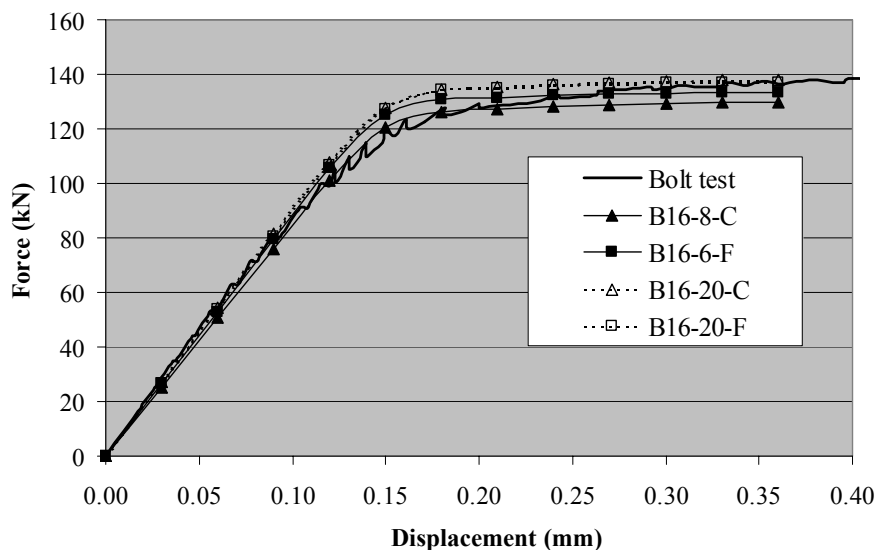


Figure 3.1 Force-Displacement curve of bolts for specimens S8-8 and S8-10

Table 3.1 CPU Time for the different bolt models

Bolt model	d (mm)	Element type	Mesh	CPU-time (min.)	# of nodes	# of elements
B16-8-C	16 mm	8-noded solids	coarse	0.9	256	172
B16-8-F	16 mm		fine	3.7	1212	960
B16-20-C	16 mm	20-noded solids	coarse	3.0	927	172
B16-20-F	16 mm		fine	29.4	4575	960

As with the bolts, different element types were considered for the remaining components of the specimens. Within this study, 4-noded plastic large strain shell elements with 6 degrees of freedom per node (shell43) have been used in an initial FE-model for flange-plate connections. The results of the shell element model showed less agreement with the test results than the FE-models using solid elements. The shell element model required a higher CPU time and the contact between the undersides of the flange-plates as well as the bolts and the flange-plates could only be modelled satisfactorily with extreme difficulties. As for another successful numerical study on bolted flange-plate connections, but under moment loading [Wheeler et al. 2000], only volume elements were considered for the further numerical study.

The comparison between FE-models of Specimen R10-1 using a coarse and a fine mesh, both using 8-noded solids (solid45) and an FE-model with a coarse mesh using 20-noded solid elements (solid95) showed little differences in the results (see Figure 3.2) yet large differences in CPU time (see Table 3.2) caused by the increased number of nodes and elements in the models with the fine mesh and the 20-noded elements. It was not possible to model the

specimen with 20-noded elements using a finer mesh as the maximum number of nodes for the ANSYS version used was exhausted.

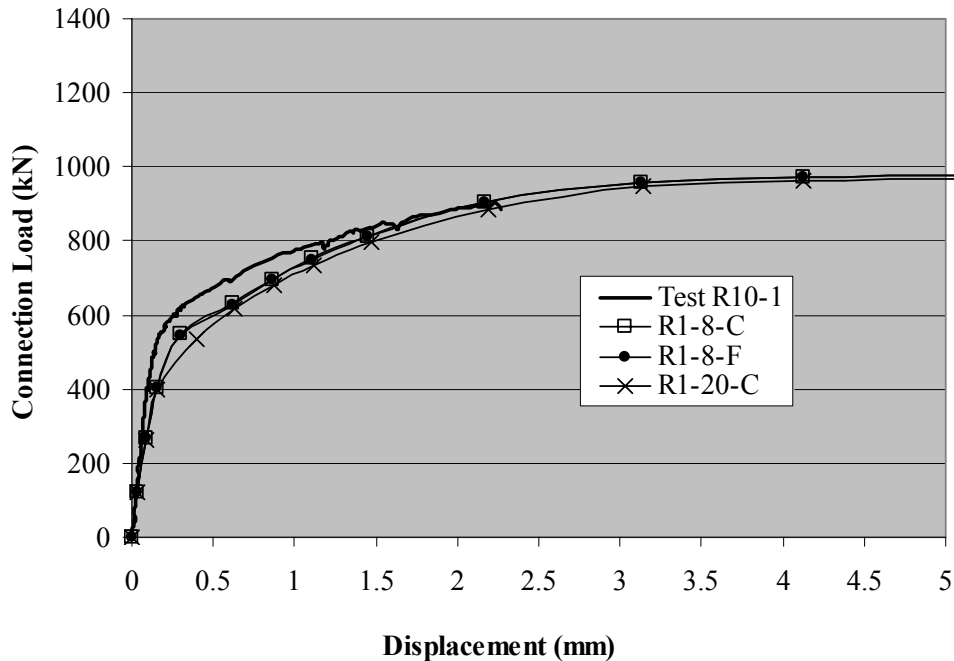


Figure 3.2 Load-Displacement curve of specimen R10-1

Table 3.2 CPU Time for the different models of specimen R10-1

FE-Model	Element type	Mesh	CPU-time (min.)	# of nodes	# of elements
R1-8 C	8-noded solids	coarse	47.4	8304	4581
R1-8-F		fine	82.6	11752	7368
R1-20-C	20-noded solids	coarse	340.8	19329	5394

The contact between the flange-plates as well as the flange-plates and the bolts was modelled using node-to-node contact elements (contac52). Friction was not included in the FE-models. ANSYS supports three contact element types: node-to-node, node-to-surface, and surface-to-surface. Node to node contact elements are the most simple contact elements, thus being more stable (divergence) and minimizing CPU time. Node-to-node contact elements can be used if the nodes of the two surfaces line up, the relative sliding deformation is negligible, and deflections (rotations) of the two surfaces remain small. The contact stiffness of the contact elements was calculated according to the formula provided by the ANSYS 5.6 [Swanson Analysis System Inc. 1999] manual:

$$K \approx f \cdot E \cdot l \quad \text{in } \frac{\text{N}}{\text{mm}}$$

with: K = contact stiffness in normal direction to contacting surface,
 f = contact compatibility factor between 0.01 and 100,
 E = Young's Modulus of contacting area,
 l = element length of elements on contacting surface.

Unfortunately, the ANSYS 5.6 [Swanson Analysis System Inc. 1999] manual does not give any guidelines on the choice for the factor "f". A factor of 1.0 resulted in good contact compatibility and was used for all FE-models.

3.3.2 Geometrical and Material Non-Linearities

Geometrical non-linearities have been accounted for by using the NLGEOM option within ANSYS. For solid elements, "large strains" are allowed. Large strain assumes that the strains are no longer infinitesimal (they are finite). Shape changes (e.g., area, thickness, etc.) are taken into account. Deflections and rotations may be arbitrarily large.

For finite strain problems the true-stress-strain curves of the material should be used. For an uniaxial tensile specimen, the true stress and strain can be calculated as follows:

$$\epsilon_T = \int_1^{1+\Delta l} \frac{dx}{x} = \ln \frac{1+\Delta l}{1} = \ln(1 + \epsilon_E)$$

$$\sigma_T = \frac{A}{A_U} \sigma_E = \frac{A}{\frac{A}{1 + \epsilon_E}} \sigma_E = (1 + \epsilon_E) \cdot \sigma_E$$

with: l : member length,
 A : initial section area,
 A_U : updated section area,
 ϵ_E : engineering strain,
 ϵ_T : true strain,
 σ_E : engineering stress,
 σ_T : true stress.

When necking occurs, the engineering stress-strain curve reaches its maximum. The true stress, however, will still increase after the maximum of the engineering stress due to the decreasing section area. Thus, after the maximum is reached the true stress-strain curve has to be determined by the Ramberg-Osgood power law [van der Vegte 1995]:

$$\frac{\varepsilon_T}{\varepsilon_0} = a \cdot \left(\frac{\sigma_T}{\sigma_0} \right)^b$$

" ε_0 " and " σ_0 " are the reference strain and stress. The constants "a" and "b" have to be determined from the engineering stress-strain curve. Figure 3.3 shows typical stress-strain curves for the flange-plate material.

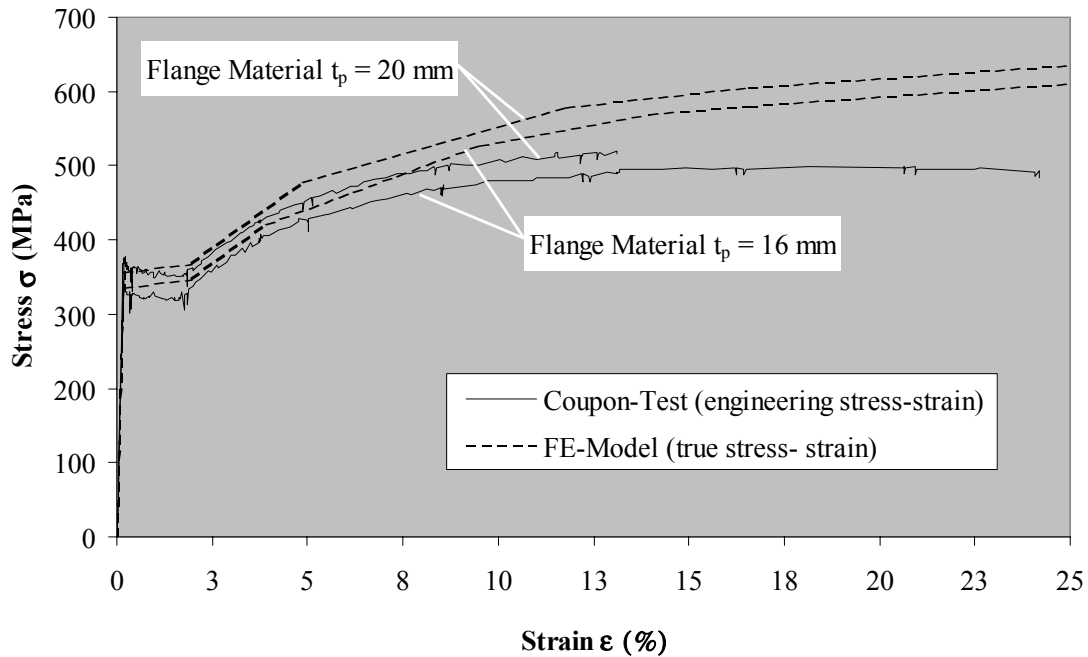


Figure 3.3 Stress-strain curves

The bolt material in the FE-model was chosen so as to give the best results when comparing a tension test of a complete bolt with its corresponding FE-model. The resulting yield and ultimate strengths of the bolt material as used in the FE-model are shown in Table 3.3.

Table 3.3 Bolt material as used in the FE-model

Bolt Material	Specimens	$f_y^{1)}$ (MPa)	f_u (MPa)
ASTM A325 (comparable to Grade 8.8)	S8-1 to S8-4 and S'8-1, S'8-2	1000	1050
	S8-5 to S8-10	750	875
	R10-1 to R10-4	730	905
ASTM A490 (comparable to Grade 10.9)	S4-1 to S4-4	990	1085

¹⁾ Using the 0.2% strain offset method

3.3.3 Solution Techniques used in the Study

Frontal direct equation solver (in-memory only) has been used throughout. The solution was performed in multiple load steps. After each load step, the solver was exited and specific results (displacement, connection load, bolt load) written to a list file. The analysis was then restarted using the restart option which employs the deformed model for the subsequent analyses. This procedure allowed the analysis of the flange-plate connections to be divided into three stages (see Figure 3.4). In the first stage, the gap between bolts and flange is closed to avoid a sudden change from non-contact to large stresses between the contact nodes. In the second load stage, pretension is applied to the bolts. The final load stage applies the tension load to the hollow section member by continuously increasing the displacement of the nodes at the hollow section end.

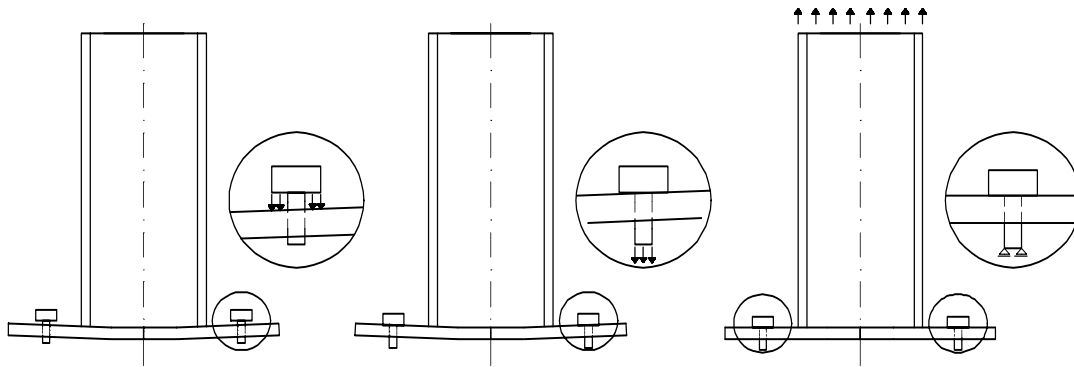


Figure 3.4 The three stages during each analysis

The full Newton-Raphson procedure, in which the stiffness matrix is updated at every equilibrium iteration, has been used for the non-linear analysis of each FE-model. ANSYS uses the tangent stiffness matrix only as long as the iterations remain stable. If divergent trends are detected on an iteration, the program discards the divergent iteration and restarts the solution using a weighted combination of the secant and tangent stiffness matrices. When the iterations return to a convergent pattern, the program will resume using the tangent stiffness matrix.

3.3.4 Boundary Conditions

Due to the geometry and loading symmetry of the specimens, it is sufficient to model only an eighth of the connection, provided symmetrical boundary conditions are applied along the planes of symmetry (see Figure 3.5). The connection loading was applied by displacement of the nodes at the end of the hollow section (see Figure 3.6), thereby simulating the displacement controlled loading of the connection in the tests. Pretension of the bolts was generated by predisplacement of the bolt shank end nodes (see Figure 3.7). The required predisplacement for

the specific pretension of the bolt was found in a separate analysis of the connection. In this analysis, prior to the analysis in which the connection was loaded under tension, the end nodes of the bolts were displaced in small increments until the reaction force in the bolt equalled the pretension from the experiments. The predisplacement found was then used in the second load stage (application of the pretension, see previous section 3.3.3, Figure 3.4) of the analysis of the connection under tensile loading. This procedure matches an earlier study on finite element modelling of bolted flange-plate connections [Cao et al. 2000].

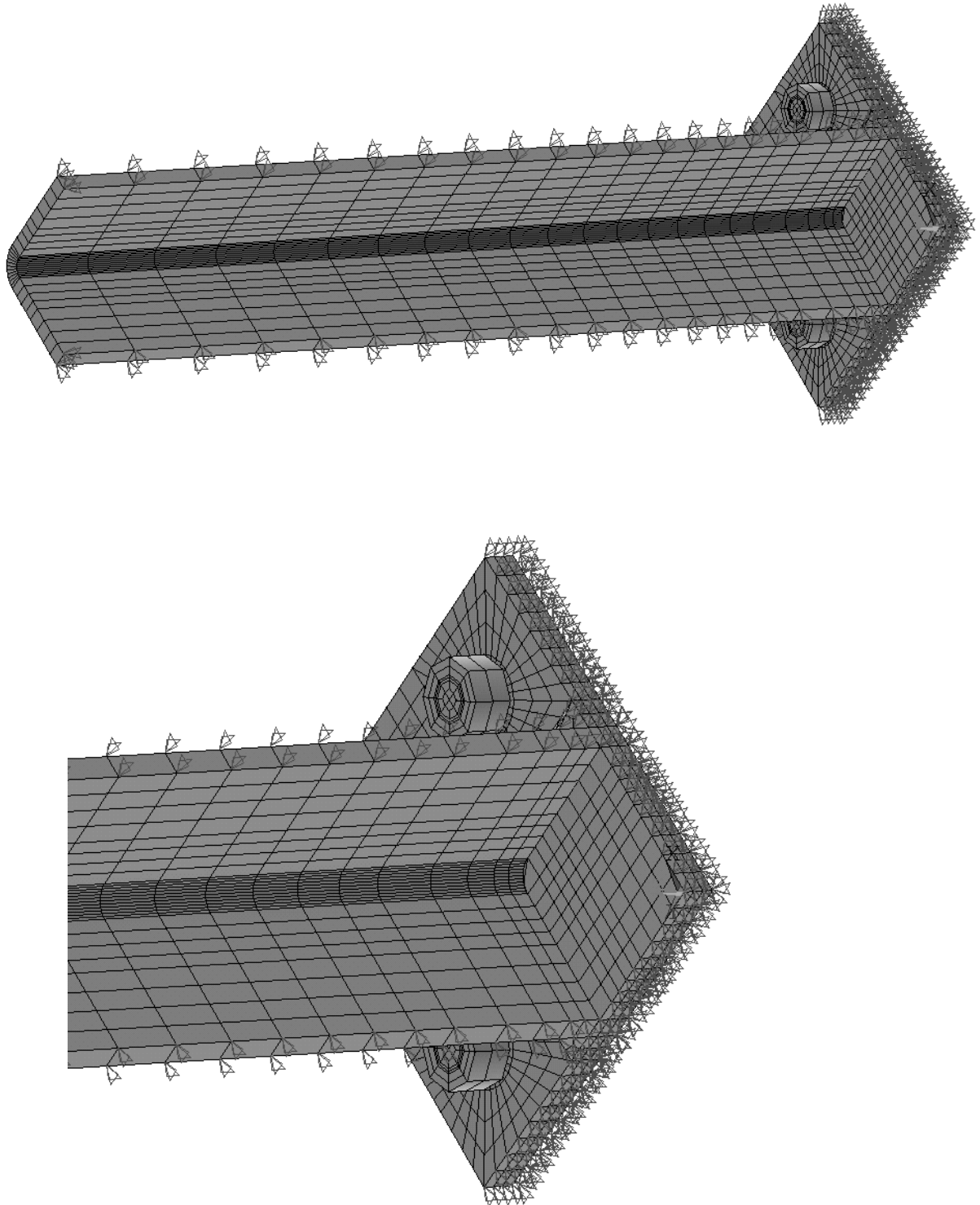


Figure 3.5 Symmetric boundary conditions along the planes of symmetry

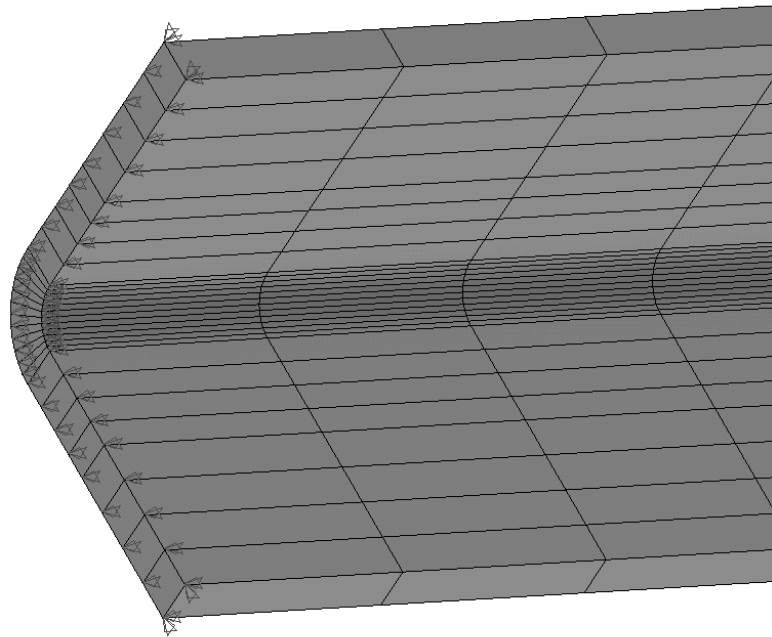


Figure 3.6 Connection loading by displacement of the nodes at the end of the hollow section

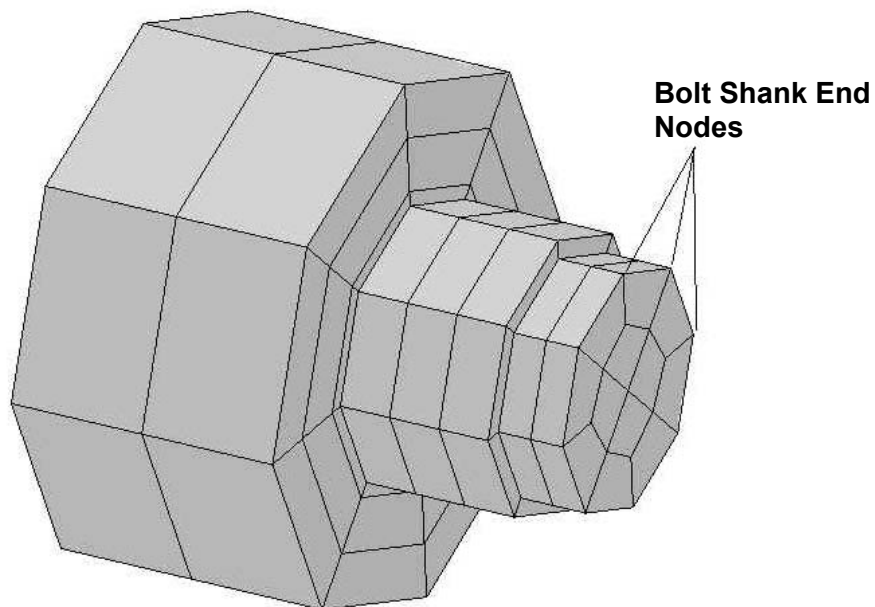


Figure 3.7 Bolt mesh

3.3.5 Discretisation

3.3.5.1 Bolt Discretisation

Due to the central role of the bolts in the flange-plate connection, special consideration was given to the modelling of the bolts. In addition to the earlier mentioned uncertainty concerning the bolt material, assumptions had to be made about the nominal tensile area of the bolts. According to ANSI B18.2.1 [ANSI 1999] and ASME B1.1 [ASME 2001], the ratio between the nominal tensile area to the nominal shank area for $5/8$ " (16 mm) bolts equals:

$$\frac{0.226 \text{in}^2}{\frac{\pi}{4} (5/8 \text{in})^2} = 0.74 = 74\% .$$

Therefore, the radius for the threaded part in the bolt in the tensile area was chosen as follows:

$$\frac{A_{\text{bt}}}{A_{\text{bs}}} = \frac{\frac{\pi}{4} r_t^2}{\frac{\pi}{4} r_s^2} = \frac{r_t^2}{r_s^2} = 0.74$$

$$\Rightarrow r_t = \sqrt{0.74} \cdot r_s = 0.86 \cdot r_s$$

Further assumptions had to be made concerning the grip length of the bolt in the nut. According to Bickford [1995], it takes up to $1/2$ of the nut height until the tensile stress level in the bolt has decreased to zero. To simulate this effect, the grip length of the modelled bolt was increased by $1/3$ of the nut height. The $1/3$ value was obtained as a best fit to modelling results of a separate analysis in which the bolt tests for the calibration of the bolt gauge (see section 2.3.2) have been simulated. As mentioned in the preceding section on element types (section 3.3.1), different models using coarse and a fine meshes were analysed. Figure 3.8 shows the coarse and fine bolt mesh as used for the simulation of the tensile bolt tests. Using the chosen coarse mesh with 20-noded volume elements, very good compliance between FE-models and tensile bolt tests was achieved (see Figure 3.9).

In the FE analysis of the flange-plate connection tests, the grip length of the bolt was halved (see Figure 3.7) as only one side of the connection was modelled because of symmetry. By having the same ratio of unthreaded to threaded length over the grip length in the FE-model as in the test specimen, the bolt response in the FE-model was expected to replicate the behaviour of the real bolt.

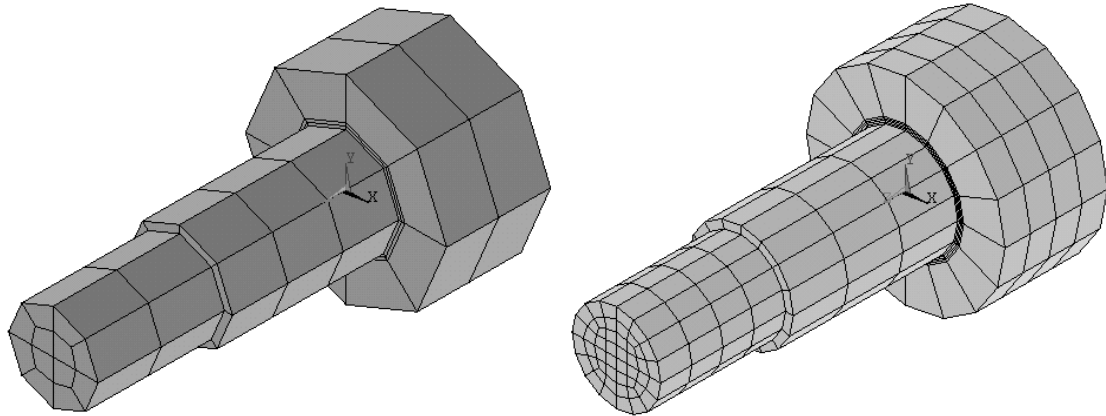


Figure 3.8 Coarse and fine bolt mesh

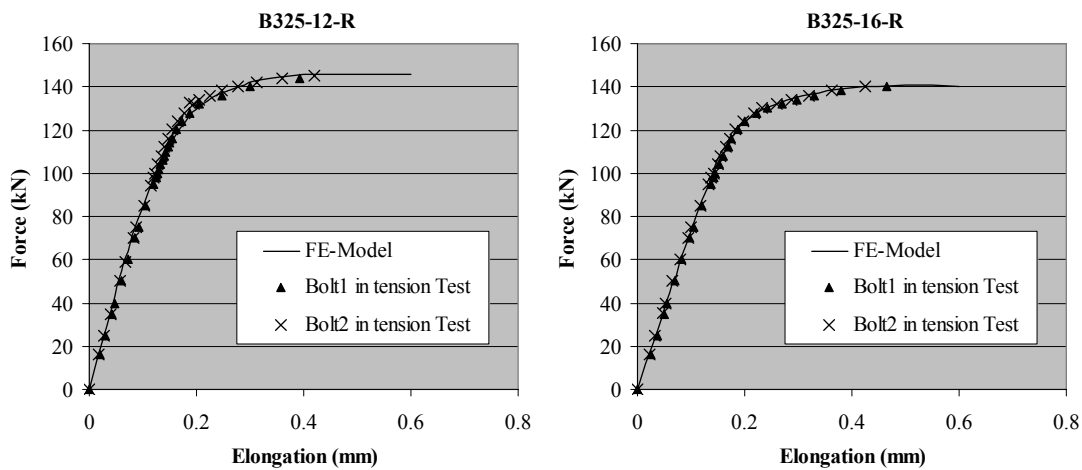


Figure 3.9 Force-displacement curves of the ASTM A325 bolts for rectangular specimens ($t_p=12$ mm and $t_p=16$ mm)

3.3.5.2 Flange-Plate Discretisation

Figures 3.10 and 3.11 show the coarse and fine FE-model of specimen R10-1. The results of the model with a fine discretization varied negligibly to those of the FE-model having a coarse mesh (see Figure 3.2 in section 3.3.1). As mentioned in section 3.3.1, because of CPU time, a coarse mesh was chosen for all models. The coarse mesh uses three elements over the thickness of the flange. For the rectangular connections this results in a total of 2313 elements in the flange-plate. The fine mesh results in 4528 elements in the flange-plate.

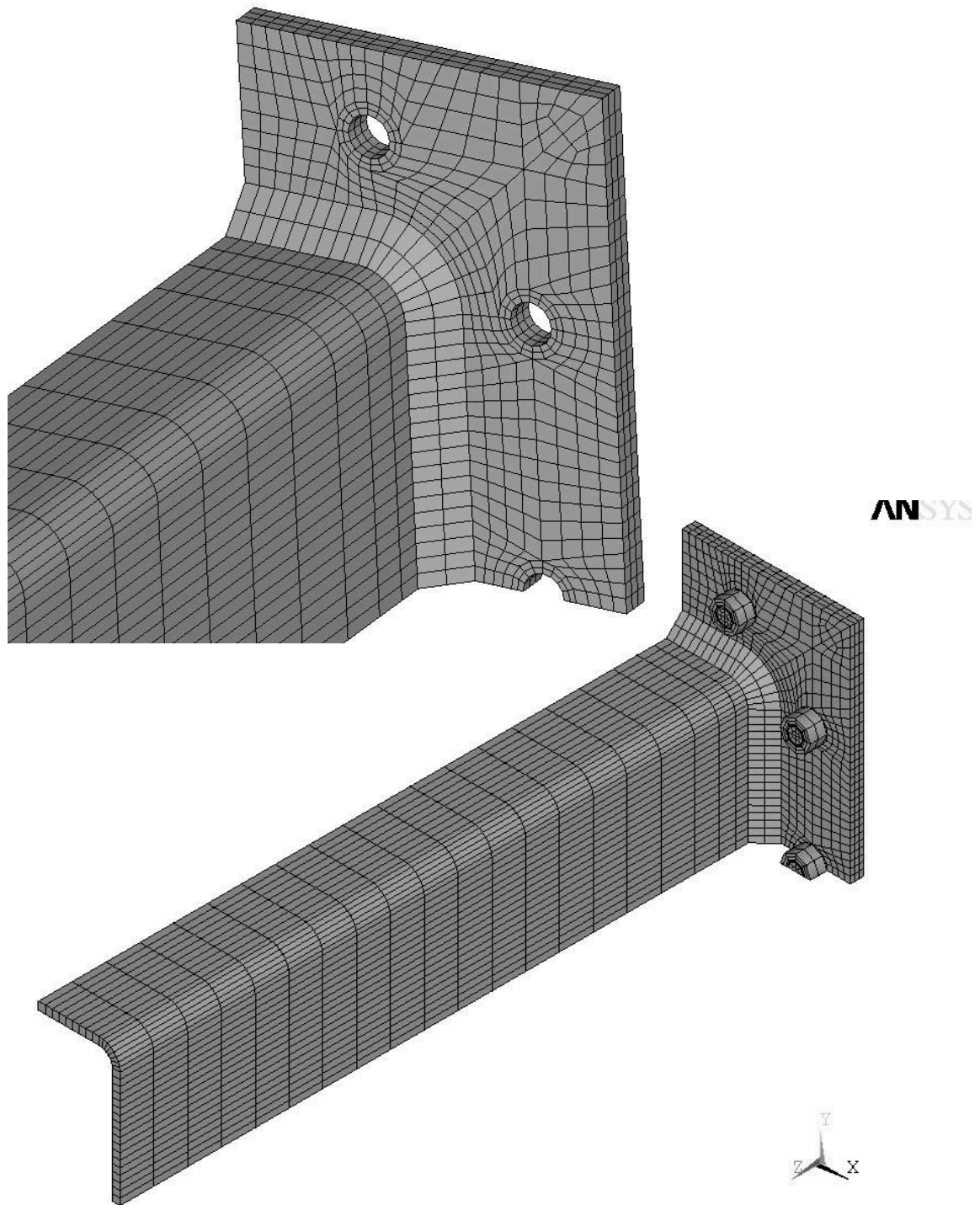


Figure 3.10 FE-Model with coarse discretisation

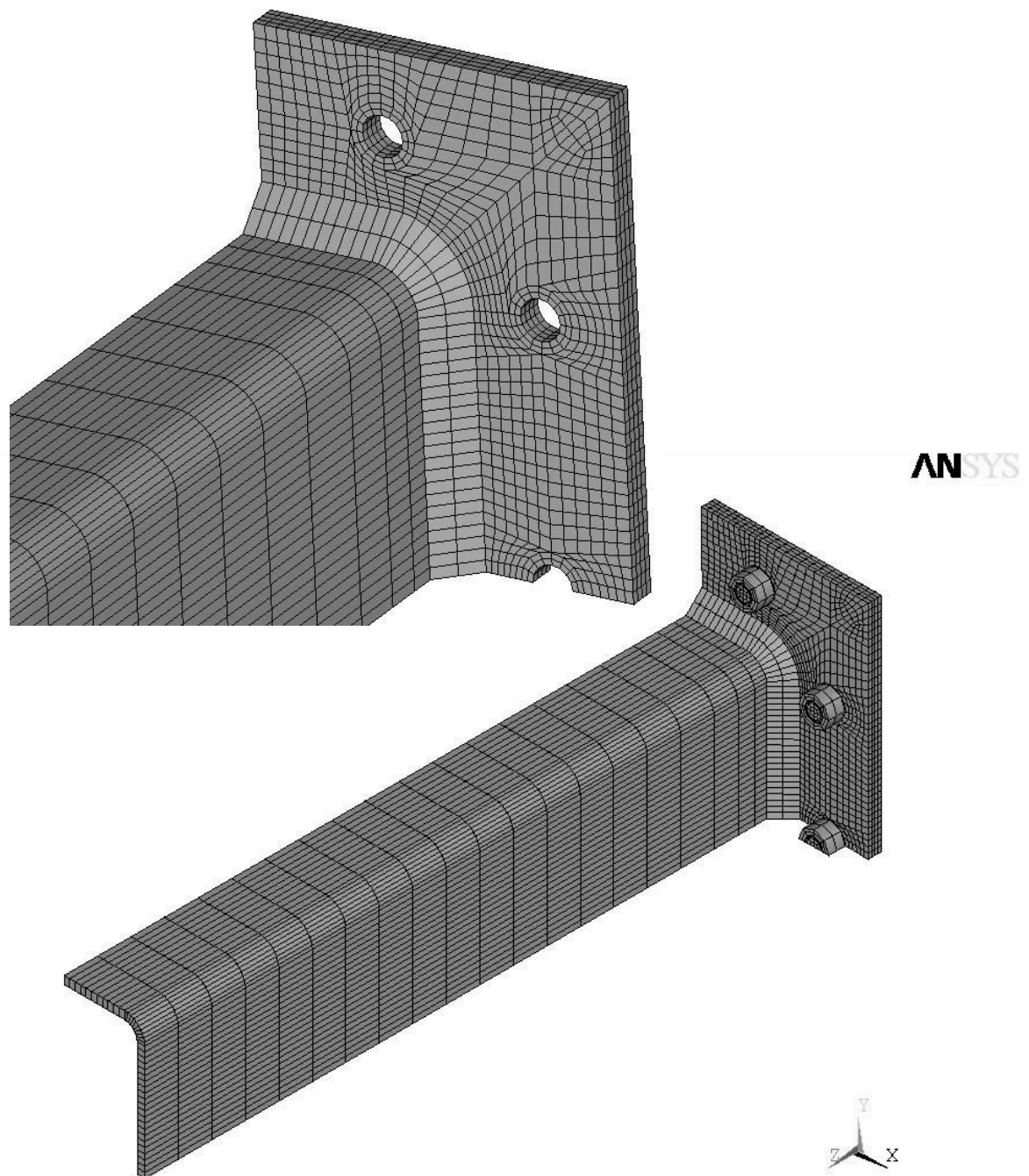


Figure 3.11 FE-Model with fine discretisation

The flange-plate connections in the experimental test program showed large deformations of the end-plates caused by the welding procedure. To achieve a good agreement between FE-models and tests, these deformations of the flange-plates have to be included in the FE-models [Wheeler et al. 2000]. The out-of-straightness of the flange-plates was modelled

three dimensionally by bends in the flange-plate along the outside of the hollow section (see Figure 3.12). The flange-plate inside the hollow section remains flat. The resulting gap at the edge of the flange can be calculated as follows:

$$\delta_p = \tan\alpha \cdot (a+b) \approx \alpha \cdot (a+b). \quad (\text{Equation 3.1})$$

Figures 3.13 and 3.14 compare the Load-Displacement curves and the bolt versus connection load curves of specimen S8-4 with the results of an FE-model including the flange deformation and an FE-model with a straight flange-plate. While the agreement of the model with the deformation is very good, the results of the model without the deformations are rather poor. Unfortunately, the gap between the flange-plates was not measured in the experimental program, so the values for " δ_p " had to be chosen according to an earlier numerical study by Wheeler et al. [2000] in which the deformation depends on the flange-plate thickness (the thinner the flange-plate the higher the deformations).

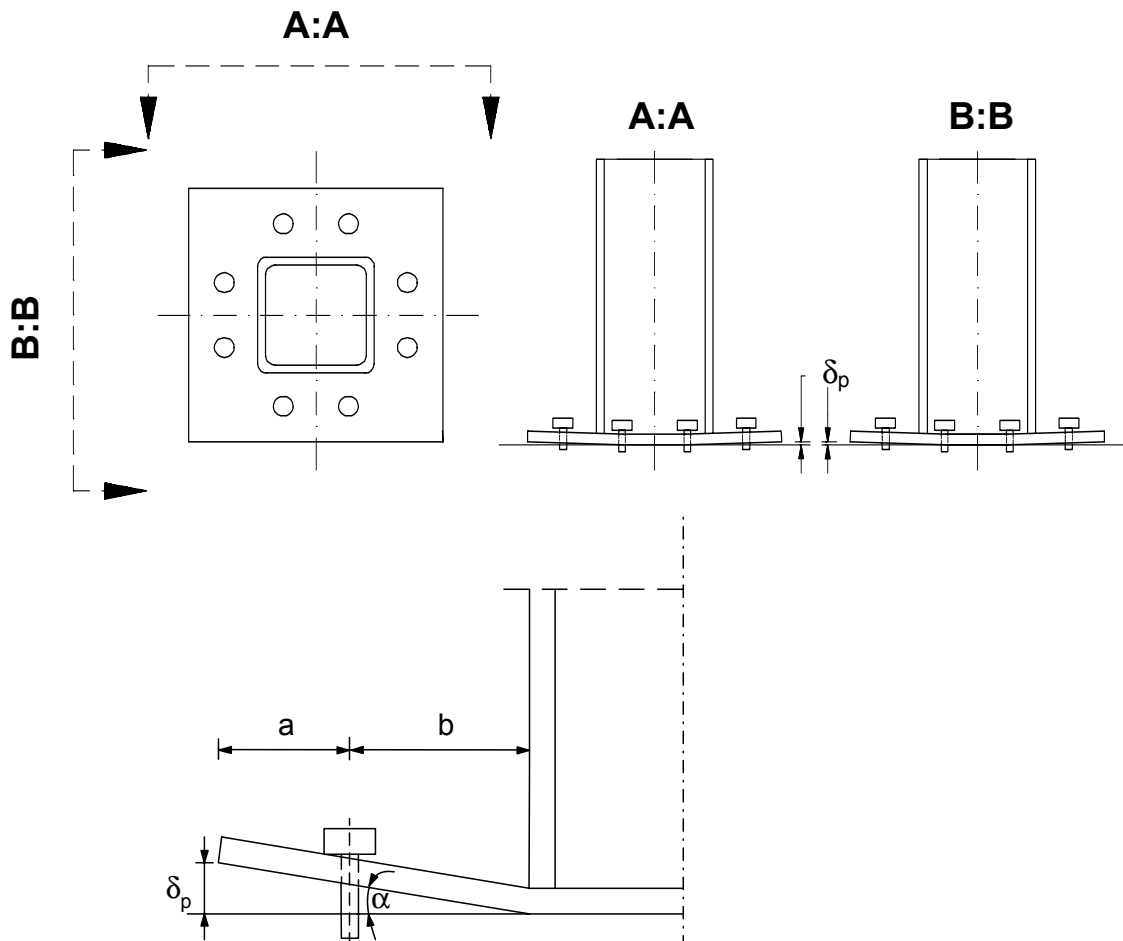


Figure 3.12 Modelled deformation in the flange-plate due to welding

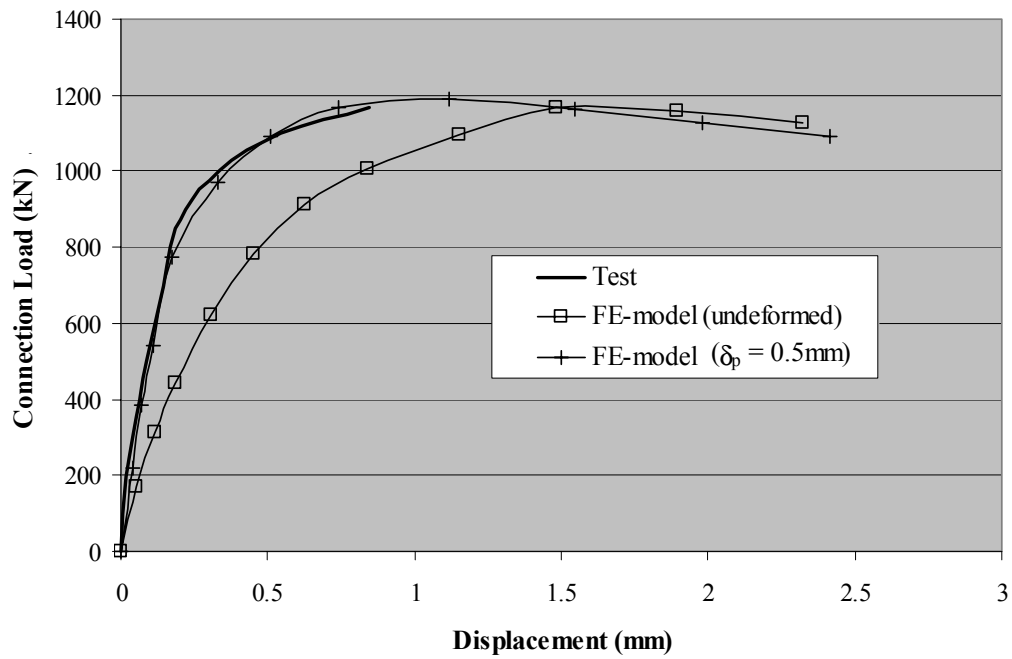


Figure 3.13 Load-Displacement curves of specimen S8-4

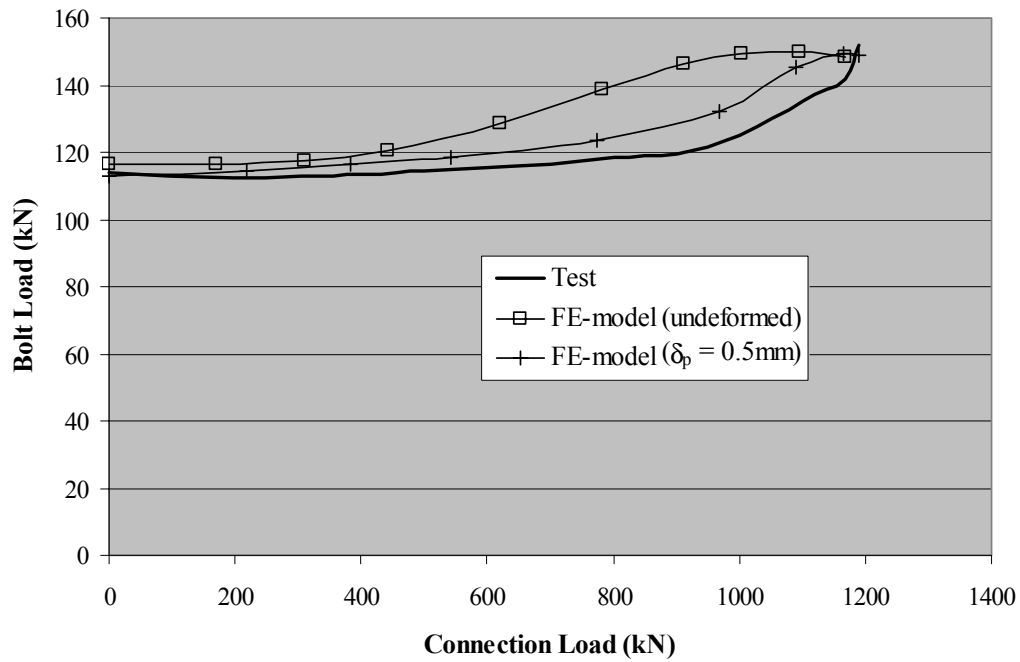


Figure 3.14 Bolt versus connection load curves of specimen S8-4

3.3.5.3 Hollow Section Discretisation

The significance of the hollow section behaviour on the connection behaviour and strength is rather small compared to the behaviour of the bolts and the flange-plates. To save CPU time, only a single element was used over the thickness of the hollow section and the element size was increased towards the hollow section end away from the connection.

The dimensions/shape of the hollow section have to be modelled very precisely as the footprint of the hollow section on the flange-plates influences the lever arm and the yield line location. The shape of the hollow section, including the rounded corners, were therefore exactly copied in the FE-models. A hollow section length four times the width of the hollow section eliminated any effects of the hollow section end on the connection behaviour. A small gap between flange-plate and hollow section was modelled so that load transfer between hollow section and flange was only through the welds (see Figure 3.15).

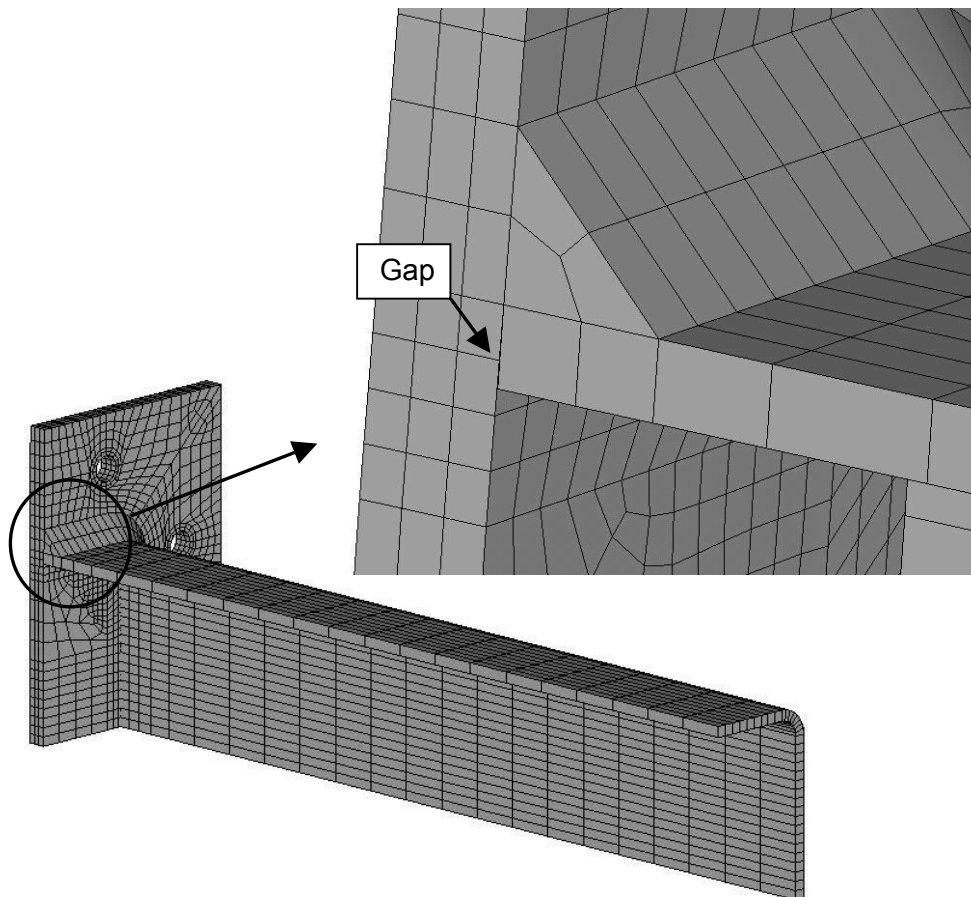


Figure 3.15 Gap between hollow section and flange-plate

3.3.5.4 Weld Discretisation

The fillet weld connecting the hollow section and the flange-plate was modelled assuming a triangular shape (see Figure 3.15). As the material properties of the weld were not known, the material properties of the hollow section were used for the weld.

3.4 Validation of the Numerical Models with the Experimental Results

To validate the numerical modelling all specimens of the experimental programme have been modelled and analysed numerically. The experimental programme had shown obvious shortcomings (see section 2.6) of the bolt layout of specimens S'8-1 and S'8-2. Therefore, specimens S'8-1 and S'8-2 were excluded, since their bolt layout would have required a completely new finite element model. The predicted connection loads of the FE-models have been compared to the test results in Table 3.4. The numerical and experimental connection capacities agree very well, having a mean of test to predicted ratio of 0.99 and coefficient of variation of 2.6%.

Table 3.4 Comparison of the numerical and experimental results

Specimen	t_p (mm)	δ_p (mm)	Test		FE-Model N_{uFE} (kN)	N_{ux}/N_{uFE}
			N_{ux} (kN)	β_{ux} (%)		
S4-1	12	2.0	847	20.9	891	0.95
S4-2	16	1.0	955	3.7	957	1.00
S4-3	12	2.0	792	29.3	834	0.95
S4-4	16	1.0	910	8.8	945	0.96
S8-1	16	1.0	1108	15.7	1149	0.96
S8-2	20	1.0	1162	4.5	1155	1.01
S8-3	16	1.0	1240	3.4	1274	0.97
S8-4	20	1.0	1190	2.1	1202	0.99
S8-5	12	2.0	903	22.2	903	1.00
S8-6	12	2.0	946	16.6	938	1.01
S8-7	12	2.0	843	30.9	846	1.00
S8-8	16	1.0	946	13.5	926	1.02
S8-9	12	2.0	881	25.2	881	1.00
S8-10	16	1.0	1019	5.4	1009	1.01
R10-1	12	2.0	1030	41.7	996	1.03
R10-2	16	1.0	1153	22.2	1146	1.01
R10-3	12	2.0	1105	32.1	1086	1.02
R10-4	16	1.0	1240	13.6	1188	1.04

Mean 0.99

Coefficient of variation (%) 2.64

3.4.1 Square Flange-Plate Connections

Prior to and during the testing of the square connections, the deformation of the flange-plate was not measured. Therefore, assumptions had to be made for the size of the gap between the flanges. Wheeler et al. [2000] recommend for the imposed initial maximum flange-plate deformation " δ_p " (see Figure 3.12) a value ranging from $\delta_p = 1$ mm (for $t_p = 20$ mm) up to $\delta_p = 3$ mm (for $t_p = 12$ mm) depending on the flange-plate thickness t_p . A variety of flange-plate deformations δ_p were studied for the different specimens (see Tables 3.5 and 3.6). For the tests reported in Chapter 2, a value of $\delta_p = 3$ mm appears to be too high, as the flange-plates in the second test series (S8-5 to S8-10 and S4-1 to S4-4) were welded to the hollow section with the flange-plates clamped down to prevent too much bending in these parts. In the first series of tests (specimens S8-1 to S8-4), the distance between the face of the hollow section and edge of the flange-plate of $a+b = 70$ mm was smaller than the corresponding distance of $a+b = 80$ mm for the second test series (specimens S8-5 to S8-10 and S4-1 to S4-4). As the first series of tests was not fabricated with the flange-plates clamped down to the welding table, a bigger angle " α " (see Figure 3.12) between the deformed flange-plate and the plane of symmetry can be expected for the specimens in the first series compared to the second set of tests. In the calculation of the gap " δ_p " (Equation 3.1) the bigger value for " α " is cancelled out by the smaller distance between the face of the hollow section and the edge of the flange-plate. Therefore, the resulting gaps " δ_p " become about the same for the two test series.

The assumed flange-plate deformations " δ_p " depending on the flange-plate thickness for comparison between numerical and experimental results (see Table 3.4) were chosen as:

- $\delta_p = 1$ mm for $t_p = 16$ mm and $t_p = 20$ mm,
- $\delta_p = 2$ mm for $t_p = 12$ mm.

Table 3.5 Comparison of the numerical and experimental results of 4-bolt square specimens for different flange deformations " δ_p "

Specimen	Test N_{ux} (kN)	t_p (mm)	FE-Model			
			$\delta_p = 1.0$ mm		$\delta_p = 2.0$ mm	
			N_{uFE} (kN)	N_{ux}/N_{uFE}	N_{uFE} (kN)	N_{ux}/N_{uFE}
S4-1	847	12.0	883	0.96	891	0.95
S4-2	955	16.0	957	1.00	983	0.97
S4-3	792	12.0	827	0.96	834	0.95
S4-4	910	16.0	945	0.96	977	0.93

Table 3.6 Comparison of the numerical and experimental results of 8-bolt square specimens for different flange deformations " δ_p "

Specimen	Test		FE-Model					
	N_{ux} (kN)	t_p (mm)	$\delta_p = 0.5\text{mm}$		$\delta_p = 1.0\text{mm}$		$\delta_p = 2.0\text{mm}$	
			N_{uFE} (kN)	N_{ux}/N_{uFE}	N_{uFE} (kN)	N_{ux}/N_{uFE}	N_{uFE} (kN)	N_{ux}/N_{uFE}
S8-1	1108	16.0	1140	0.97	1149	0.96	--	--
S8-2	1162	20.0	1130	1.03	1155	1.01	--	--
S8-3	1240	16.0	1251	0.99	1274	0.97	--	--
S8-4	1190	20.0	1191	1.00	1202	0.99	--	--
S8-5	903	12.0	--	--	887	1.02	903	1.00
S8-6	946	12.0	--	--	914	1.03	938	1.01
S8-7	843	12.0	--	--	828	1.02	846	1.00
S8-8	946	16.0	--	--	926	1.02	945	1.00
S8-9	881	12.0	--	--	860	1.02	881	1.00
S8-10	1019	16.0	--	--	1009	1.01	1059	0.96

To show the influence of the initial flange-plate deformation at the sides of the plate on the various connection types, the stress distribution (von Mises stresses) of the flange face after tensioning of the bolts is shown in Figures 3.16a to c. Figures 3.17a to c show the face of the flange at ultimate load. Figures 3.18a to c give an impression of the deformations in the connections at ultimate load (displacement scaling of 5). As expected, the flange-plate deformations at ultimate load for the 4-bolt specimens are far more pronounced than the deformations for the 8-bolt specimens. This agrees with observations from the experimental work.

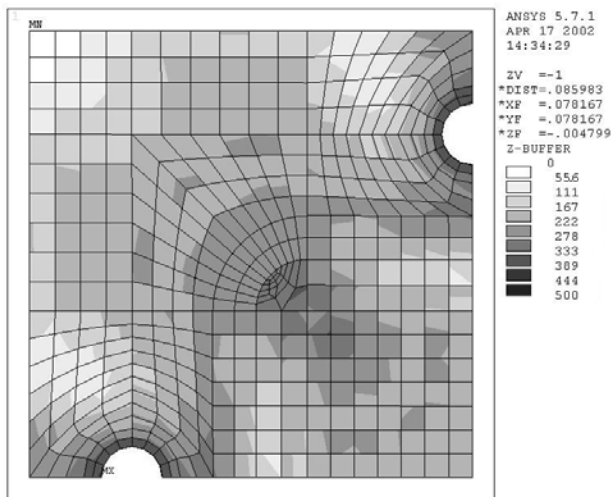


Figure 3.16a Flange-plate face equivalent stresses caused by pretensioning (4-bolt specimen)

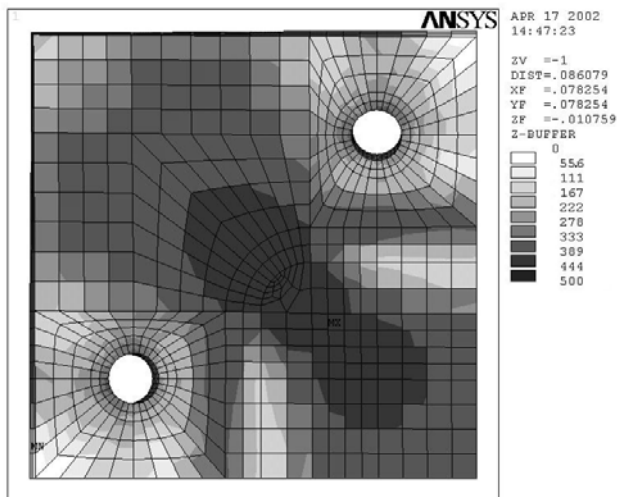


Figure 3.16b Flange-plate face equivalent stresses caused by pretensioning (8-bolt specimen, $c = 70$ mm)

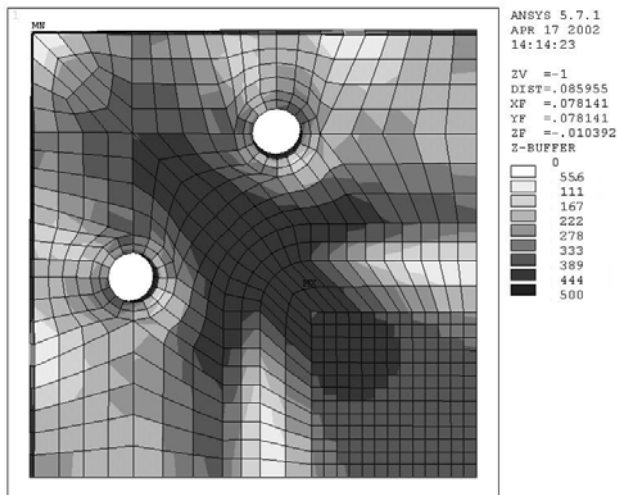


Figure 3.16c Flange-plate face equivalent stresses caused by pretensioning (8-bolt specimen, $c = 140$ mm)

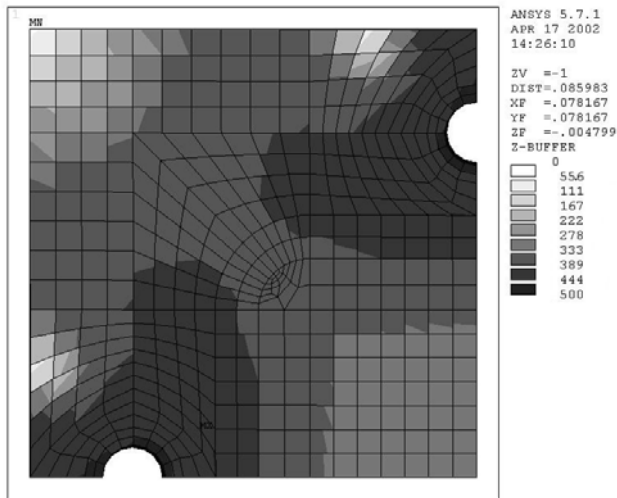


Figure 3.17a Flange-plate face equivalent stresses at ultimate load (4-bolt specimen)

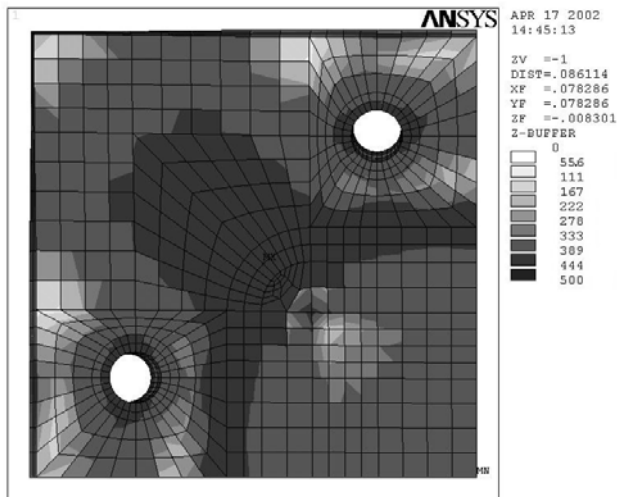


Figure 3.17b Flange-plate face equivalent stresses at ultimate load (8-bolt specimen, c = 70 mm)

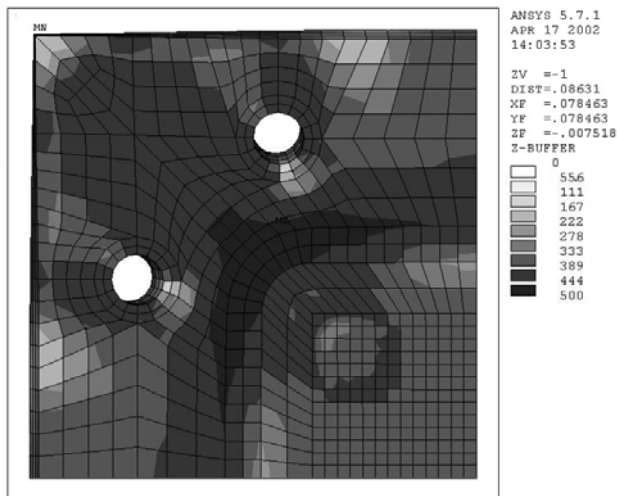


Figure 3.17c Flange-plate face equivalent stresses at ultimate load (8-bolt specimen, c = 140 mm)

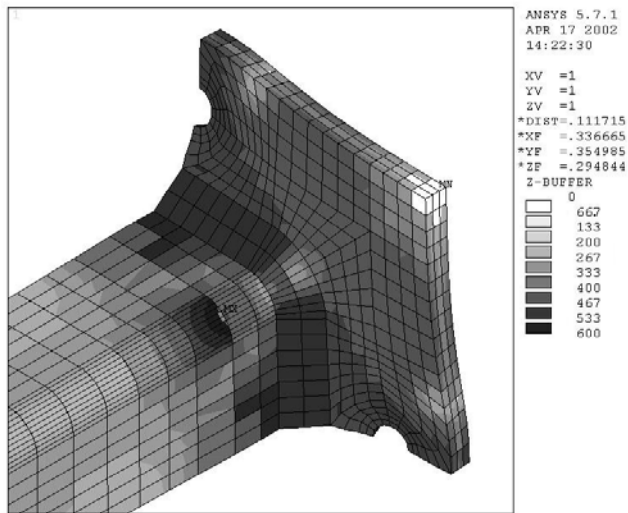


Figure 3.18a Deformation (disp. x 5) at ultimate load (4-bolt specimen)

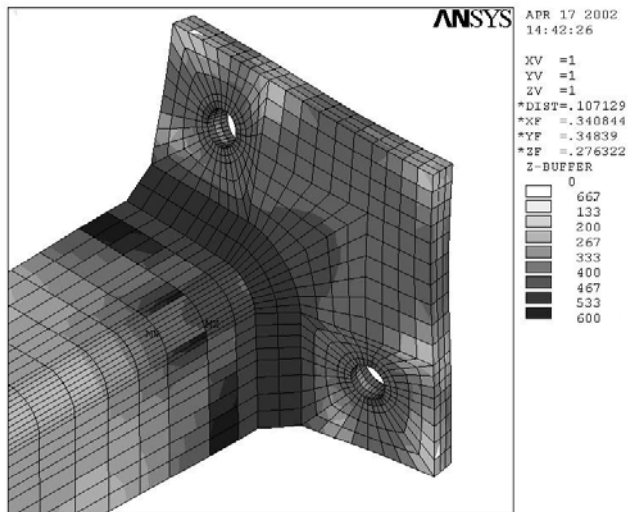


Figure 3.18b Deformation (disp. x 5) at ultimate load (8-bolt specimen, c = 70 mm)

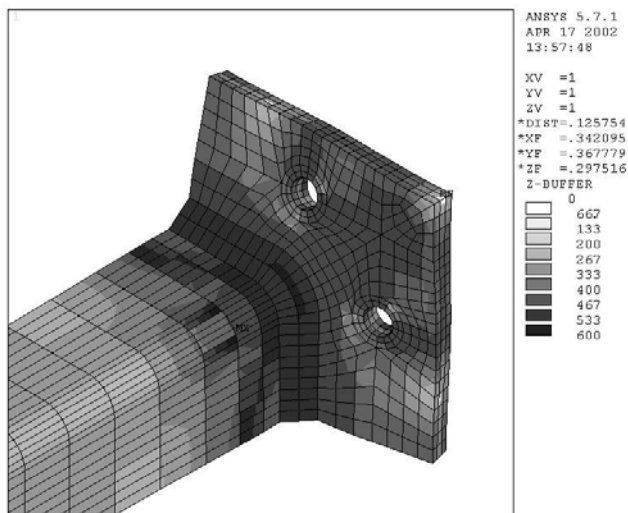


Figure 3.18c Deformation (disp. x 5) at ultimate load (8-bolt specimen, c = 140 mm)

3.4.2 Rectangular Flange-Plate Connections

Table 3.7 shows the numerical results of the rectangular flange-plate connections for different values of flange deformations " δ_p ". The flange-plate deformation was chosen as $\delta_p = 2.0$ mm for $t_p = 12$ mm and $\delta_p = 1.0$ mm for $t_p = 16$ mm, in accordance with the assumptions for the square flange-plate models (see shaded areas in Table 3.7).

Table 3.7 Comparison of the numerical and experimental results of rectangular specimens for different flange deformations " δ_p "

Specimen	Test N_{ux} (kN)	t_p (mm)	FE-Model			
			$\delta_p = 1.0$ mm		$\delta_p = 2.0$ mm	
			N_{uFE} (kN)	N_{ux}/N_{uFE}	N_{uFE} (kN)	N_{ux}/N_{uFE}
R10-1	1030	12.0	979	1.05	996	1.03
R10-2	1153	16.0	1146	1.01	1176	0.98
R10-3	1105	12.0	1064	1.04	1086	1.02
R10-4	1240	16.0	1188	1.04	1219	1.02

Figures 3.19 to 3.21 correspond to the Figures 3.16 to 3.18 showing the stress distribution after pretensioning, at ultimate load as well as the displacement of the connection at ultimate load, for a typical rectangular hollow section connection.

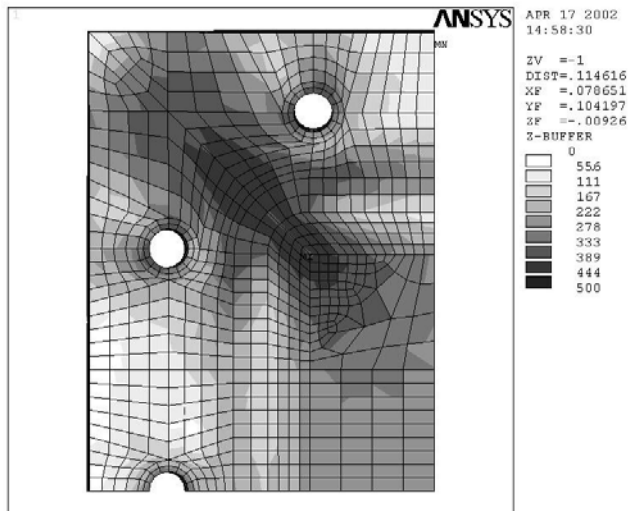


Figure 3.19 Flange-plate face equivalent stresses caused by pretensioning (rectangular specimen)

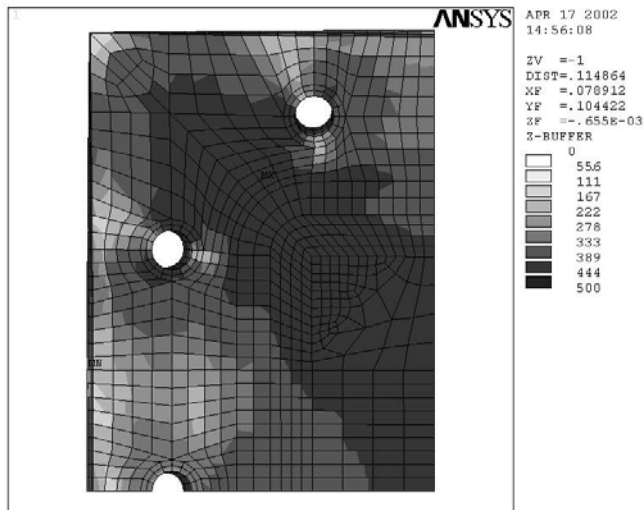


Figure 3.20 Flange-plate face equivalent stresses at ultimate load (rectangular specimen)

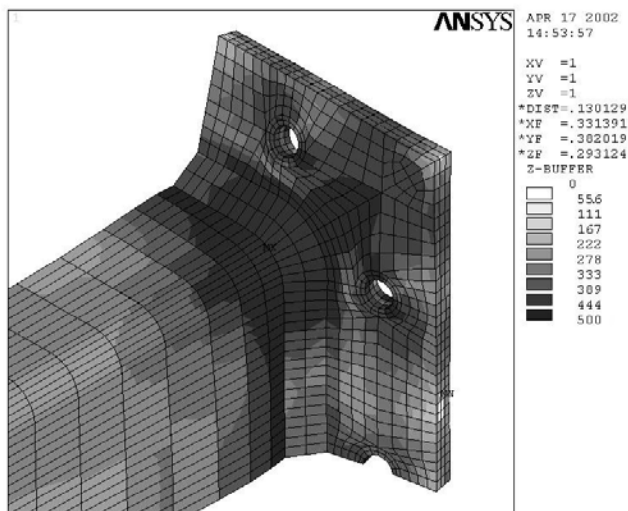


Figure 3.21 Deformation (disp. x 5) at ultimate load (rectangular specimen)

4 *NUMERICAL STUDY*

4.1 Numerical Model

For the finite element models of the subsequent numerical parameter study, the following generalizations were made:

- Solid elements, 8-noded for hollow section, weld and flange and 20-noded for bolts, were used throughout. Node to node contact elements modelled the contact between the flange-plates and the bolts as well as the flange-plates with each other.
- Symmetry of the connection was taken into account by modelling only an eighth of the connection and applying suitable boundary conditions. Displacement controlled loading conditions were simulated by applying axial displacements to the nodes of the hollow section end.
- Nominal dimensions of the members were used for the parameter study. The hollow sections for the square connections are cold-formed 150 x 150 x 10 mm hollow sections. For the rectangular connections, 250 x 150 x 8 mm cold-formed hollow sections have been modelled. The corner radii have been chosen according to European Standards [EN10219-2 1997] as $2.5 \cdot t_i$ (see Table 10.1 in Chapter 10.2). The flange-plate dimensions were 310 x 310 mm and 410 x 310 mm for the square and rectangular connections respectively.
- The hollow section steel grade was S355 with a yield strength of 355 MPa and an ultimate strength of 510 MPa [EN 10219-1 1997]. The flange-plate steel grade assumed was S355 with a yield strength of 355 MPa and an ultimate strength of 490 MPa [EN 10025 1990].
- M16, Grade 8.8 bolts with an ultimate strength of 126 kN were assumed for the 8-bolt square and 10-bolt rectangular flange-plate connections. For the 4-bolt square connection M20, Grade 10.9 bolts with an ultimate strength of 245 kN were assumed. Figure 4.1 shows the force-displacement curves assumed for the modelled bolts. The ultimate tensile strength f_{ub} taken for the bolt material was 800 MPa and 1000 MPa for the Grade 8.8 and Grade 10.9 bolts respectively [Table 3, ISO 898-1 1999]. The ultimate bolt strength was calculated as $F_{bu} = A_{bt} f_{ub}$ with the tensile area A_{bt} according to Tables 6/7 ISO 898-1 [1999] ($A_{bt} = 157 \text{ mm}^2$ for the M16 bolts and $A_{bt} = 245 \text{ mm}^2$ for the M20 bolts).
- The preload in the bolts was chosen according to ENV 1090-1 [1996] as $0.7 F_{bu}$, resulting in a preload of 88 kN and 170 kN for the Grade 8.8 and Grade 10.9 bolts respectively.
- For the deformation of the flange-plates due to welding (see section 3.3.5.2) a value of $\delta_p = 2 \text{ mm}$ was used. The value was chosen according to allowable tolerances in Table 11.2.2, ENV 1090-1 [1996], with $\delta_p = w/150 = 310/150 \approx 2 \text{ mm}$. For the rectangular

connections, this value was also chosen for the longer side of the connection as the long and short side have to be equally deformed at the corner they meet.

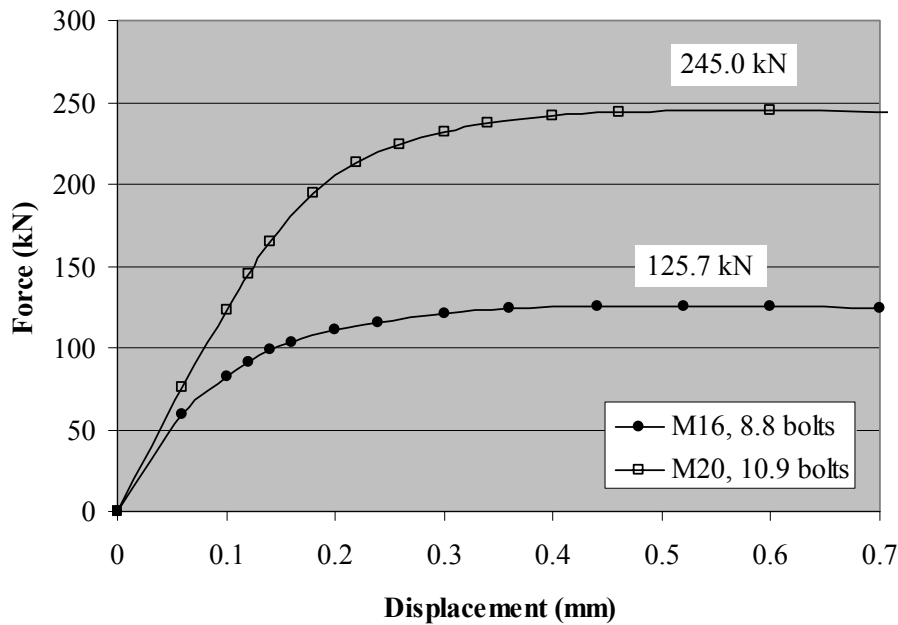


Figure 4.1 Force-displacement curves assumed for the bolts used in the numerical study

A closer description of the discretisation, element choice and boundary conditions of the numerical model can be found in the preceding section.

4.2 Scope of Numerical Study

The influence of the following parameters (see Figure 4.2) on the capacity of bolted flange-plate connections was studied in the numerical analyses:

- Flange-plate thickness " t_p ";
- Ratio of edge distance " a " to distance from bolt line to hollow section face " b ";
- Distance between bolts parallel to hollow section face " c ";
- Shape (aspect ratio) of hollow section and flange-plate;
- Weld type (fillet versus butt).

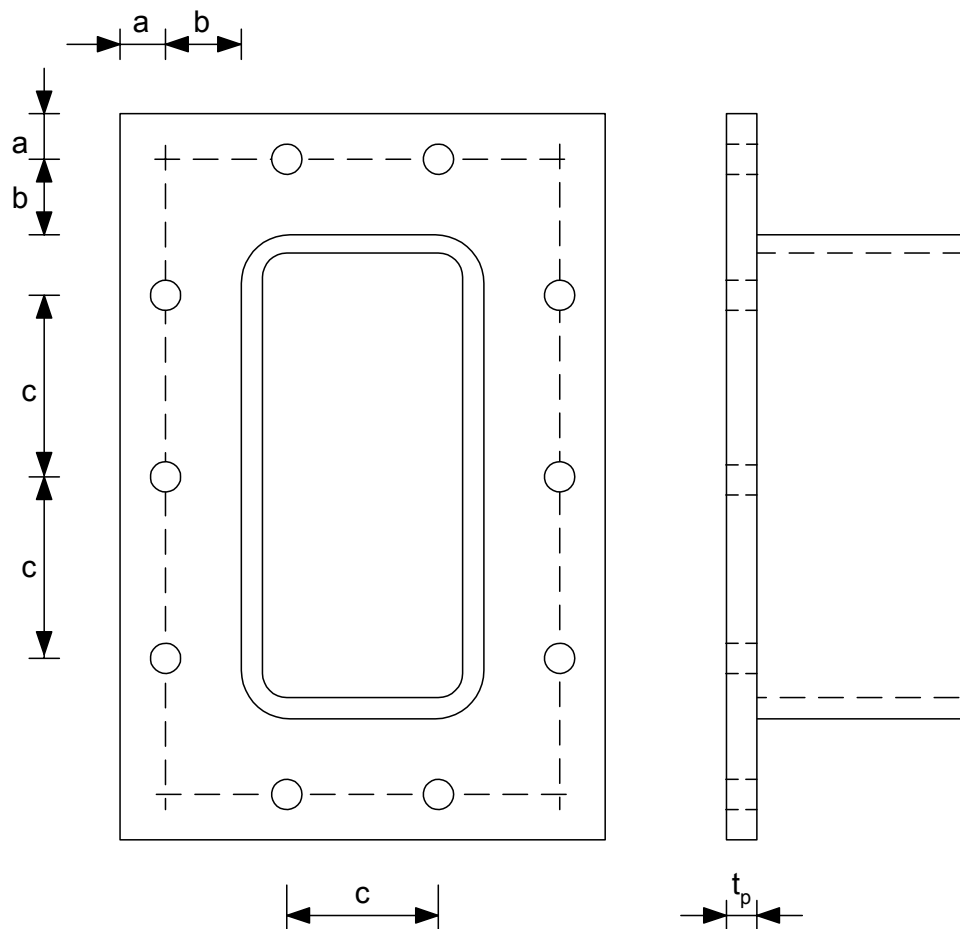


Figure 4.2 Parameters studied in the numerical study

The numerical analyses comprised of square flange-plate connections with four and eight bolts as well as connections for rectangular hollow sections with ten bolts. Each connection has been modelled twice, one with a fillet weld and one with a butt weld connecting the flange-plate and the hollow section. The weld leg size of the fillet weld equalled the hollow section thickness. In agreement with the results of the experimental study, the fillet weld showed to have a significant influence on the connection capacity. To provide the designer with a safe design method for connections employing butt welds for the connection of hollow section and flange-plate, additional models were made in which the hollow section and flange-plates were directly connected (see Figure 4.3). The "butt" weld model simplifies the weld as it disregards the portion of the butt weld that protrudes beyond the hollow section wall ($0.25t_f$) in a real specimen. As this portion of the weld increases the capacity of the connection the chosen simplification is on the safe side. The elements of the hollow section and the flange-plate in the fillet weld models are not connected to exclude any direct load transfer between hollow section and flange-plate.

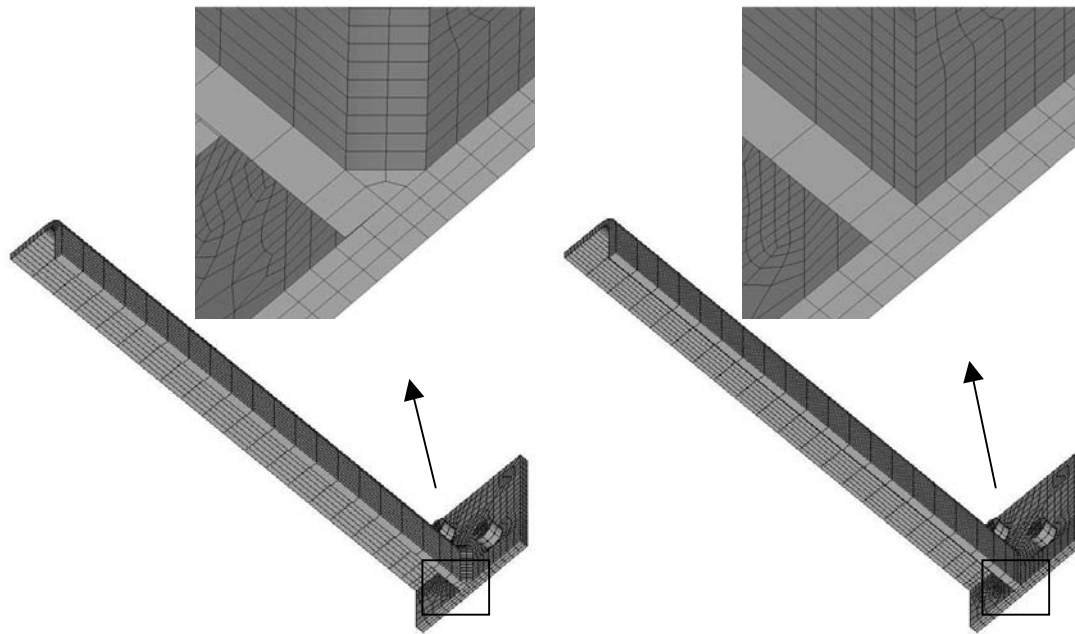


Figure 4.3 Model with fillet weld (gap between hollow section and flange-plate) and "butt" weld (direct connection of hollow section and flange-plate)

Table 4.1 gives an overview of the different parameters as well as their respective scopes. A total of 234 flange-plate connections have been studied with

- 18 connections for square flange-plate connections with four bolts;
- 126 connections for square flange-plate connections with eight bolts;
- 90 connections for rectangular flange-plate connections with ten bolts.

Table 4.1 Scope of numerical study

Models			
Parameters			
t_p	10, 12 and 16 mm		
a/b	0.60, 0.78 and 1.00		
c	--	70 - 140 mm every 10 mm	90 - 140 mm every 10 mm
Weld	Fillet weld and "butt" weld (no weld)		

4.3 General Aspects

4.3.1 Deformation Limits

With very thin flange-plates large deformations in the bolted flange-plate connections can occur without the connection/bolts failing. In recent years a 1% w_i deformation limit for serviceability loads [Wardenier 1982 and IIW 1989], and a 3% w_i deformation limit for ultimate loads [Lu et al. 1994] has become widely accepted for hollow section connections. The deformation limits are necessary to exclude large deformations or large distortions in the hollow section. Membrane effects occur with large deformations, and generally after an inflection point in the load displacement curve. Due to the interaction of bolt failure and membrane action of the flange-plates, it was not possible to detect a clear inflection point of the load displacement curves for the bolted flange-plate connections. Following the earlier research, 1% w_p and 3% w_p deformation limits for " δ " were used for the analyses of the results (see Figure 4.4).

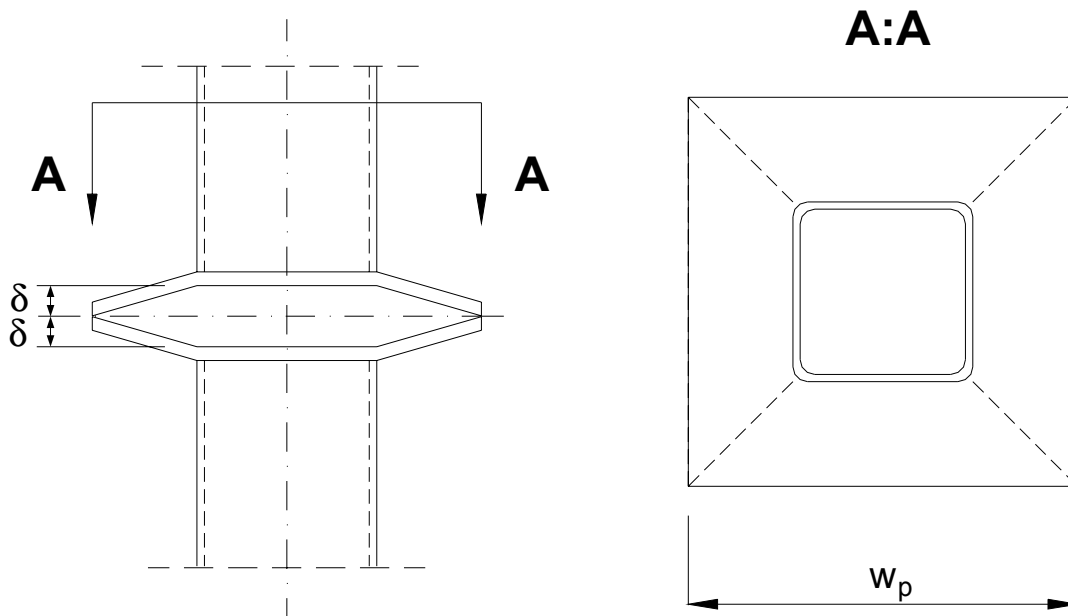


Figure 4.4 Deformation " δ " of the connection

According to Eurocode [EN 1990, 2002] and Eurocode 3 [ENV 1993-1-1, 1992], the partial factors for permanent actions $\gamma_{G,i}$ and the partial factors for transient/live loads, $\gamma_{Q,i}$, are generally 1.0 when checking for serviceability of a structure. For serviceability limit states the partial factors for the material properties, γ_M should also be taken as 1.0 according to Eurocode [2002]. Thus, the design check at serviceability limit state is:

$$N_{Sserv} = \sum G_{k,j} + \sum Q_{k,i} \leq \frac{N_{1\%}}{\gamma_M} = N_{1\%},$$

with: $G_{k,j}$: characteristic value of permanent/dead loads,
 $N_{1\%}$: connection load at 1% w_p deformation ($\delta = 1\% w_p$, see Figure 4.4)
 $Q_{k,i}$: characteristic value of transient/live loads.

For the most common static situations the design check at ultimate limit state is:

$$N_{Sd} = \sum \gamma_{G,i} G_{k,j} + 0.9 \sum \gamma_{Q,i} Q_{k,i} \leq N_{Rd} = \frac{N_{3\%}}{\gamma_M}$$

with $N_{3\%}$: connection load at 3% w_p deformation ($\delta = 3\% w_p$, see Figure 4.4)
 $\gamma_{G,i}$: partial factor for permanent/dead loads (=1.35),
 $\gamma_{Q,i}$: partial factor for transient/live loads (= 1.5),
 γ_M : partial resistance safety factor (= 1.1).

Thus the above equation can be written as:

$$\begin{aligned} \sum 1.35 G_{k,j} + 0.9 \sum 1.5 Q_{k,i} &\leq \frac{N_{3\%}}{1.1} \\ \Leftrightarrow 1.35 \sum G_{k,j} + 0.9 \cdot 1.5 \sum Q_{k,i} &\leq \frac{N_{3\%}}{1.1} \\ \Leftrightarrow 1.35 (\sum G_{k,j} + \sum Q_{k,i}) &\leq \frac{N_{3\%}}{1.1} \end{aligned}$$

Therefore, the resistance value at ultimate limit state $N_{3\%}$ becomes critical if:

$$\frac{N_{3\%}}{1.1 \cdot 1.35} \leq N_{1\%} \Leftrightarrow N_{3\%} \leq 1.5 N_{1\%}$$

If the load deflection curve reaches a peak load N_p before the 3% deflection limit, the connection capacity equals the peak load. The connection capacity is thus:

$$N_u = \begin{cases} N_p & \text{if } \delta_p \leq 3\% w_p, \\ N_{1\%} & \text{if } N_{3\%} \geq 1.5 N_{1\%}, \\ N_{3\%} & \text{if } N_{3\%} \leq 1.5 N_{1\%}. \end{cases}$$

4.3.2 Fabrication Tolerances

According to ENV 1090-1 [1996] the fabrication tolerance for a single bolt hole placement is ± 2 mm. To study the influence of fabrication tolerances on the connection capacity of bolted flange-plate connections, an asymmetric FE-model was made for one complete side of the connection (one RHS member and flange-plate, see Figure 4.5). Figure 4.6 shows the eccentricity applied to the top right bolt. The comparison (Figure 4.7) of the results for specimens with varying eccentricities shows that the influence on the results due to eccentricities of a single bolt is negligible. Due to the very high number of nodes and elements

in this model, the discretisation as well as the computation of this connection is very costly. Despite the negligible differences in the capacity for the chosen connection, a further investigation of the influence on fabrication tolerances for this connection type, as well as other bolted flange-plate connections, is recommended.

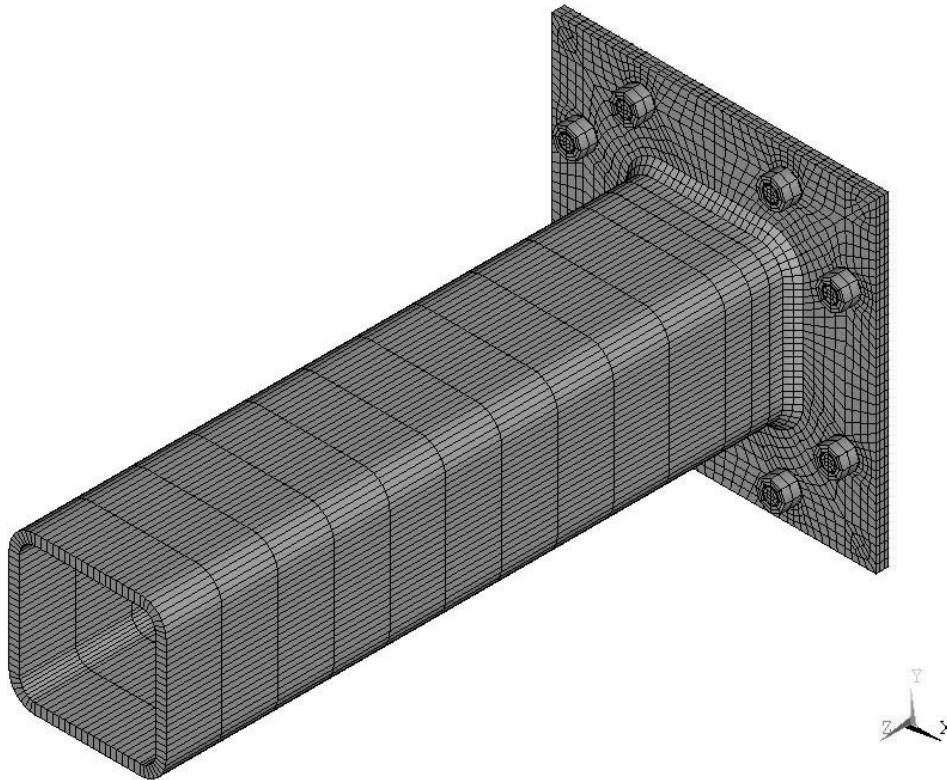


Figure 4.5 Asymmetric FE-model including eccentricity of a single bolt (top right hand side)

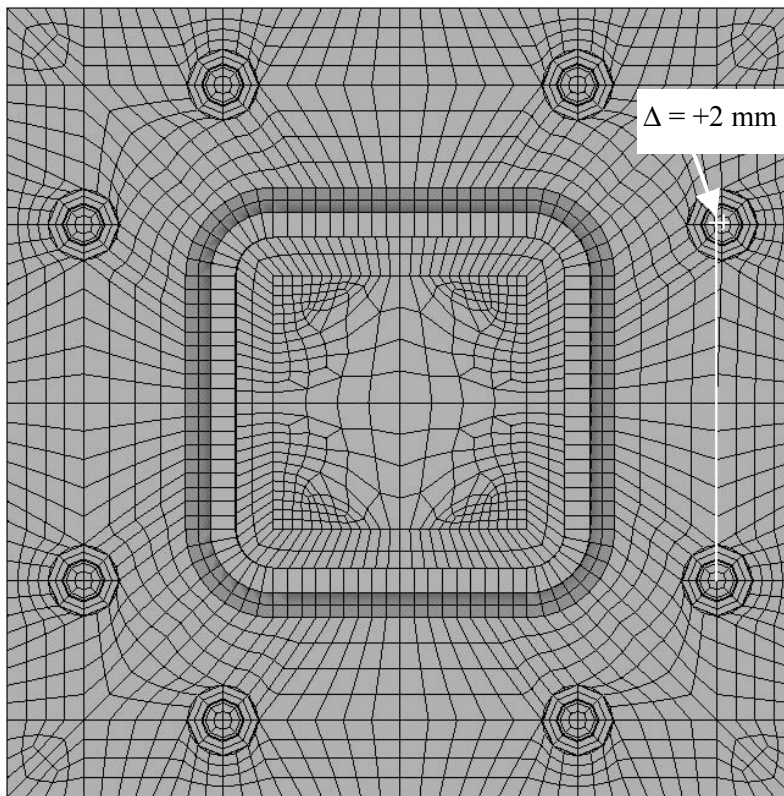


Figure 4.6 Eccentricity of top right hand bolt

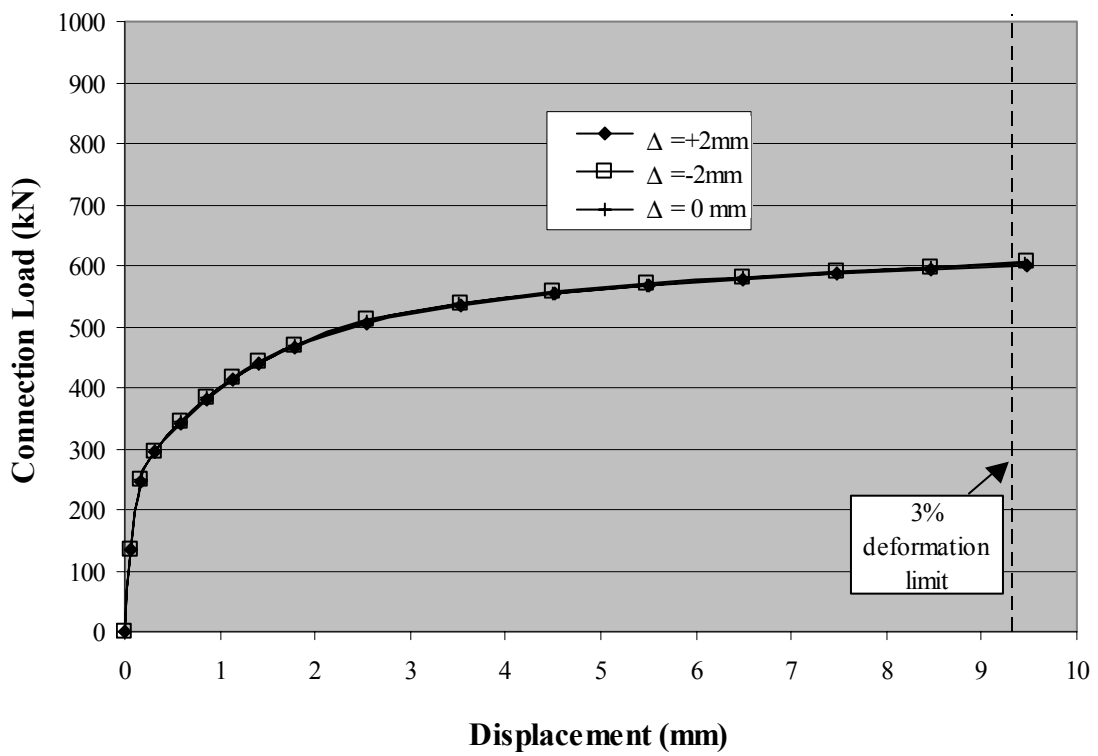


Figure 4.7 Load-Deformation curves of connections with misplaced bolt

4.4 Ultimate Load Capacity

The Load-Displacement curves of all connections investigated in the numerical study can be found in Appendix Part I. The ultimate load of the specimens is restricted to the load at the 3% deformation limit if no peak load has occurred up to that point. As the load at the 3% deformation limit is generally less than 1.5 times the load at the 1% deformation limit (see section 4.3.1), the 1% deformation limit was not further taken into account. The Tables with the results of all models are shown in Appendix Part I.

4.4.1 Square Flange-Plate Connections

4.4.1.1 Specimens with Four Bolts

Deformations increase with a decrease in flange-plate thickness (see Figure 4.8). Also the connection capacity decreases with a decrease in flange-plate thickness as well as a decrease in the a/b ratio (see Figure 4.9). These findings correspond with the experience from the experimental study.

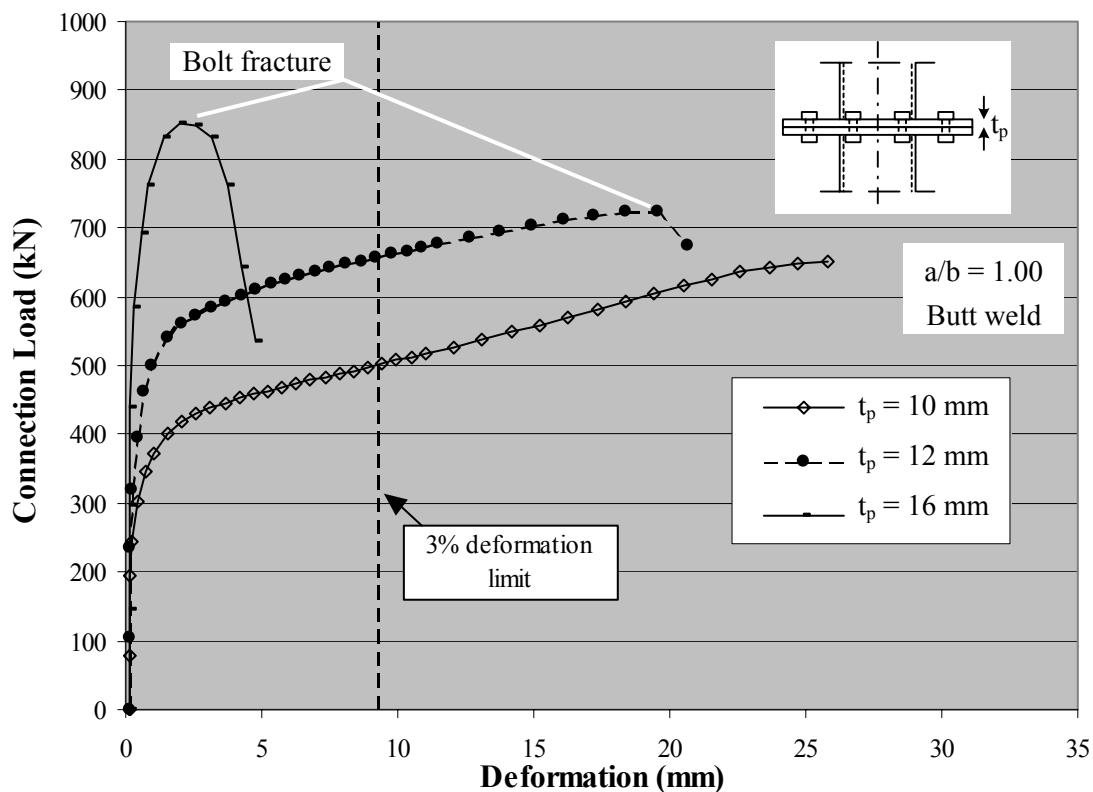


Figure 4.8 Load-Deformation curves of connections with different flange-plate thicknesses (Plate: 310 x 310 mm)

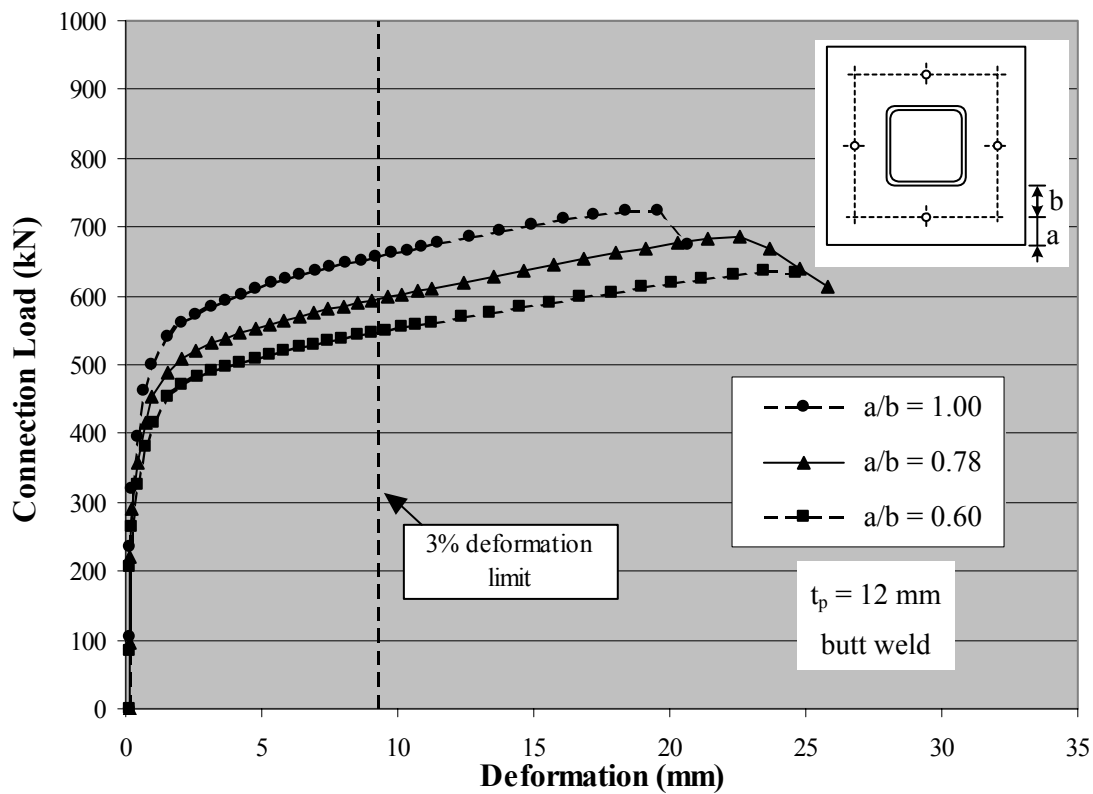


Figure 4.9 Load-Deformation curves of connections with different a/b ratios (Plate: 310 x 310 mm)

The difference in connection capacity between the FE-models with and without fillet weld is apparent. The fillet weld causes the yield line along the hollow section to shift towards the bolt line (see Figure 4.10). By assuming a reduction of the distance between bolt line and hollow section (distance "b") of half the weld leg length of the fillet weld ($w = 10$ mm for the presented FE-models) the results of the corresponding numerical models compare well. Table 4.2 compares the results of the models with corresponding flange-plate thickness and distance between hollow section and bolt line, where:

$$b^* = b \quad \text{for connections with "butt" weld} \quad (\text{Equation 4.1a}),$$

$$b^* = b - w/2 \quad \text{for connections with fillet weld} \quad (\text{Equation 4.1b})$$

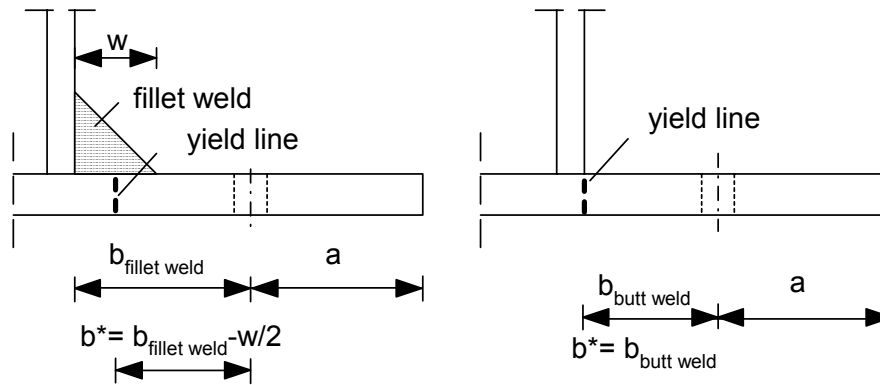


Figure 4.10 Shift of the yield line towards the bolt line due to fillet weld

Table 4.2 Comparison of models with and without fillet weld

		Model with fillet weld N_{uFE} (fillet weld model) (kN)	Corresponding model with butt weld N_{uFE} (butt weld model) (kN)	Ratio of N_{uFE} (fillet weld model) to N_{uFE} (butt weld model)
$t_p = 10$ mm	$b^* = 40$ mm	506	501	1.01
	$b^* = 45$ mm	455	451	1.01
$t_p = 12$ mm	$b^* = 40$ mm	654	658	0.99
	$b^* = 45$ mm	594	596	1.00
$t_p = 16$ mm	$b^* = 40$ mm	860	852	1.01
	$b^* = 45$ mm	812	806	1.01

4.4.1.2 Specimens with Eight Bolts

All FE-models with thin flange-plates ($t_p = 10$ mm) show excessive deformations restricting their ultimate load capacity to the 3% deformation criterion. The models with a medium flange-plate thickness ($t_p = 12$ mm) are hardly affected by the deformation criteria, either reaching peak load before deformations are beyond the 3% limit or having reached a load plateau at 3% deformation. As expected, ultimate load is always reached well before 3% deformations for the models with thick flange-plates ($t_p = 16$ mm). Figure 4.11 shows the load deformation curves for connections with an a/b ratio of 0.78, a distance between two bolts on one side of $c = 130$ mm and varying flange-plate thicknesses (all connections without fillet weld).

Besides the flange-plate thickness, the distance between bolt line and hollow section, distance "b", affects the extent of deformations. A lower a/b -ratio (increase in distance "b") results in a more flexible and less strong connection. The distance "c" between the bolts should be kept low (see Figure 4.12). For low values of "c", e.g. $c = 70$ mm, the length of flange-plate

being clamped down by the bolts, roughly the distance "c" plus 2 times the bolt hole diameter (thus including the size of the bolt head/nut or washer), $c+2d' = 70 \text{ mm} + 2 \cdot (17 \text{ mm}) = 104 \text{ mm}$, equals the hollow section width minus the outside corner radii, $h_i - 2r_{\text{out}} = 150 \text{ mm} - 2 \cdot (25 \text{ mm}) = 100 \text{ mm}$, allowing a direct load transfer. Figure 4.12 shows the connections capacities depending on the distance between the bolts on one side, value "c".

As with the connections with four bolts the difference between the models having a butt weld or fillet weld can be explained with the distance between bolt line and hollow section (distance "b"). By reducing the distance "b" by half the weld leg length of the fillet weld the connection capacities of the specimens become comparable (see Figure 4.12).

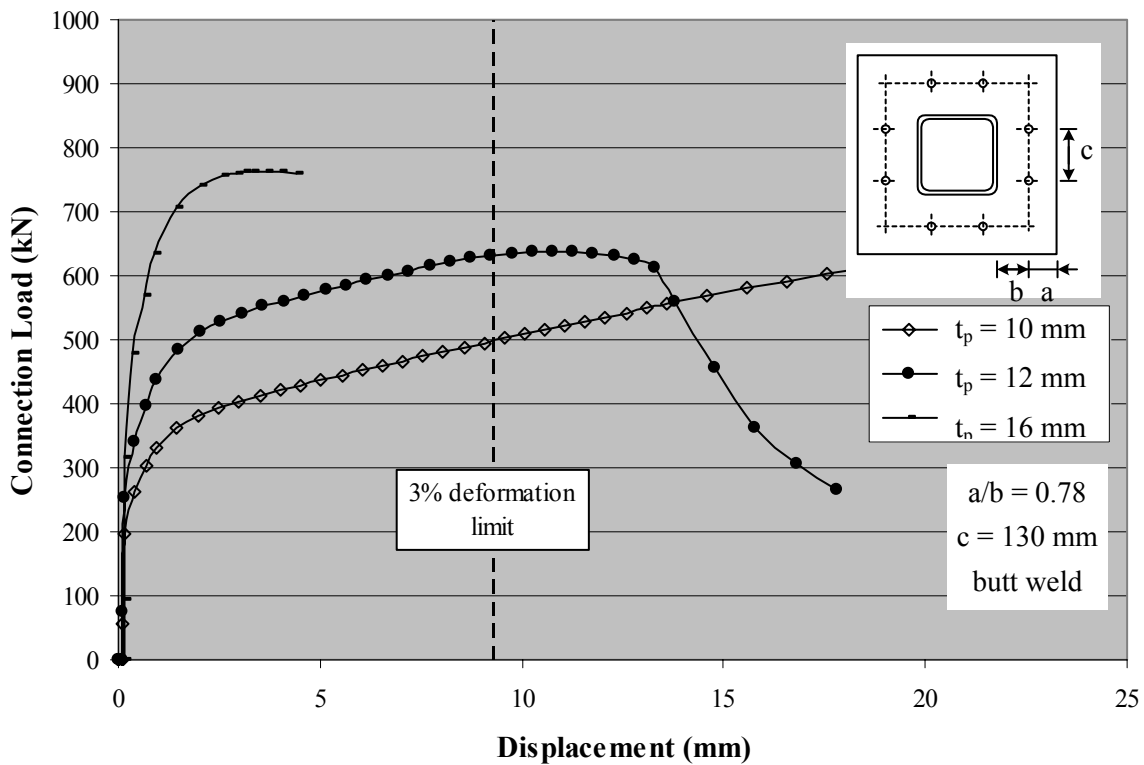


Figure 4.11 Load-Deformation curves of connections with different flange-plate thicknesses

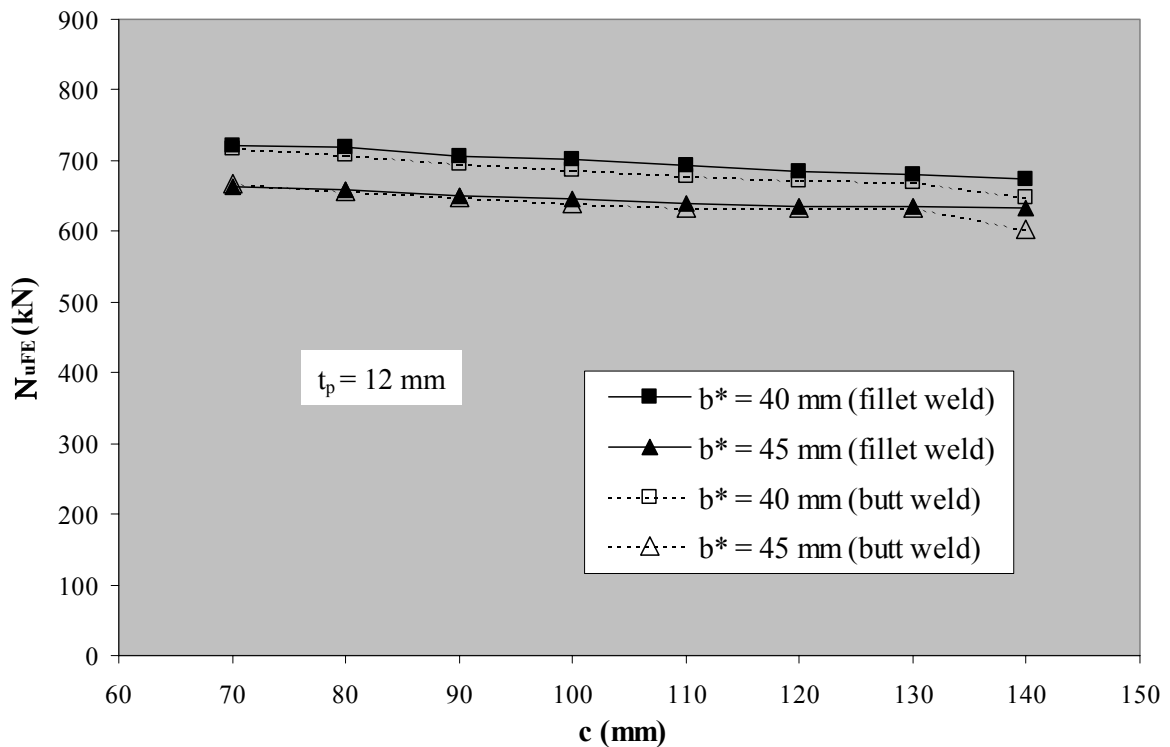


Figure 4.12 Connection capacity for varying values of "c" ($t_p = 12\text{mm}$)

4.4.2 Rectangular Flange-Plate Connections

The findings for the rectangular connections resemble the results of the square flange-plate connections. A decrease in flange-plate thickness results in more deformations and less capacity (see Figure 4.13). An increase in the distance between bolt line and hollow section, distance "b", increases the deformations and decreases the connection capacity. As with the square flange-plate connections with eight bolts, the distance "c" between the bolts on one side has an effect on the ultimate connection strength. If the value of the clamped down flange-plate ($c+2d'$ for the short side and $2c+2d'$ for the long side of the connection) equals the hollow section width/height minus the corner radii ($b_i - 2r_{out}$ for the short side and $h_i - 2r_{out}$ for the long side), the connections have the highest capacities. Figure 4.14 shows the results of the connection capacity for varying values of "c". The models in this numerical study have the same distance between the bolts on the short and long side of the connection.

For comparison of the FE-models with fillet welds and without fillet welds, a reduction of the distance between the bolt line and the hollow section is required. The results of the models without fillet welds agree reasonably well if compared to the respective models with fillet welds but with a reduced distance between bolt line and hollow section. The reduction can again conservatively be chosen as half the weld leg length (see Figure 4.14) assuming the yield

line to form within the height of the weld. Due to the automatic meshing, the FE-models having fillet welds and a distance between the bolts of $c = 70$ mm and $c = 80$ mm showed very distorted elements. The analysis of these models therefore gave implausible or no results (convergence problems). A model with a changed discretisation is very time consuming. As the comparable models with higher values of "c" did not indicate sudden changes in the connection capacity, the author abandoned the numerical results for these connections. The 3% deformation limit for the rectangular connections was conservatively chosen according to the shorter side of the connection ($= 3\%$ of 310 mm).

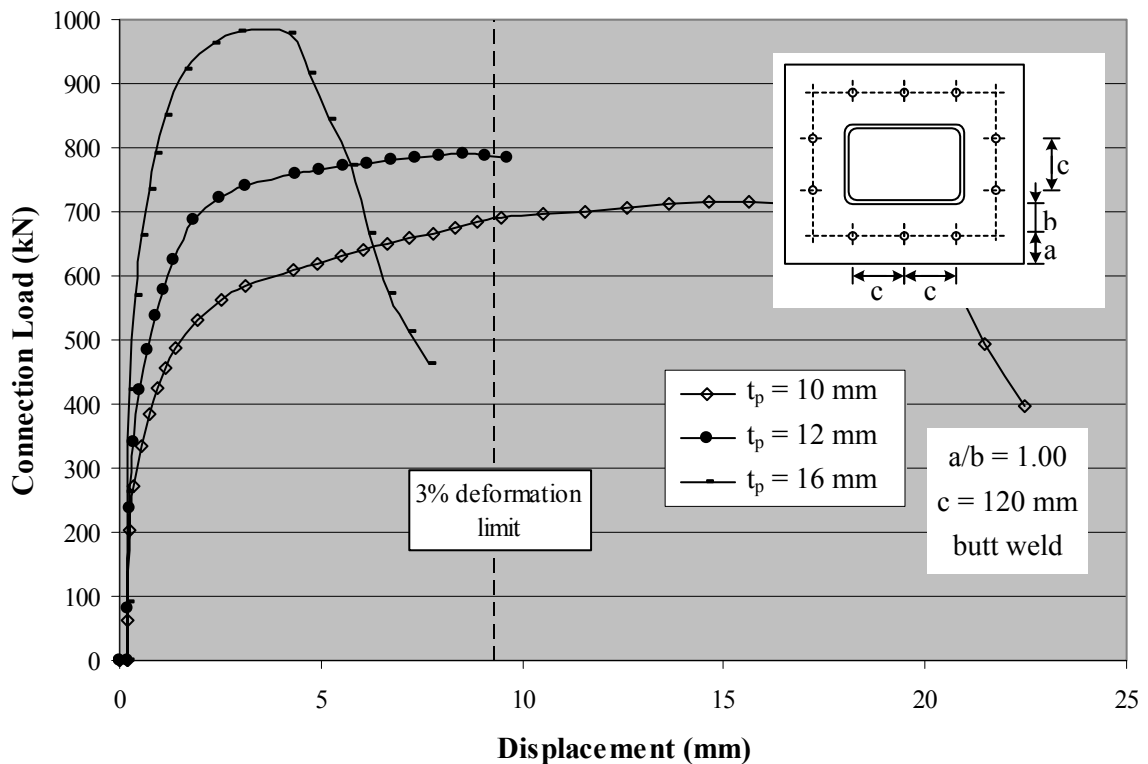


Figure 4.13 Load-Deformation curves of connections with different flange-plate thicknesses (Plate: 410 x 310 mm)

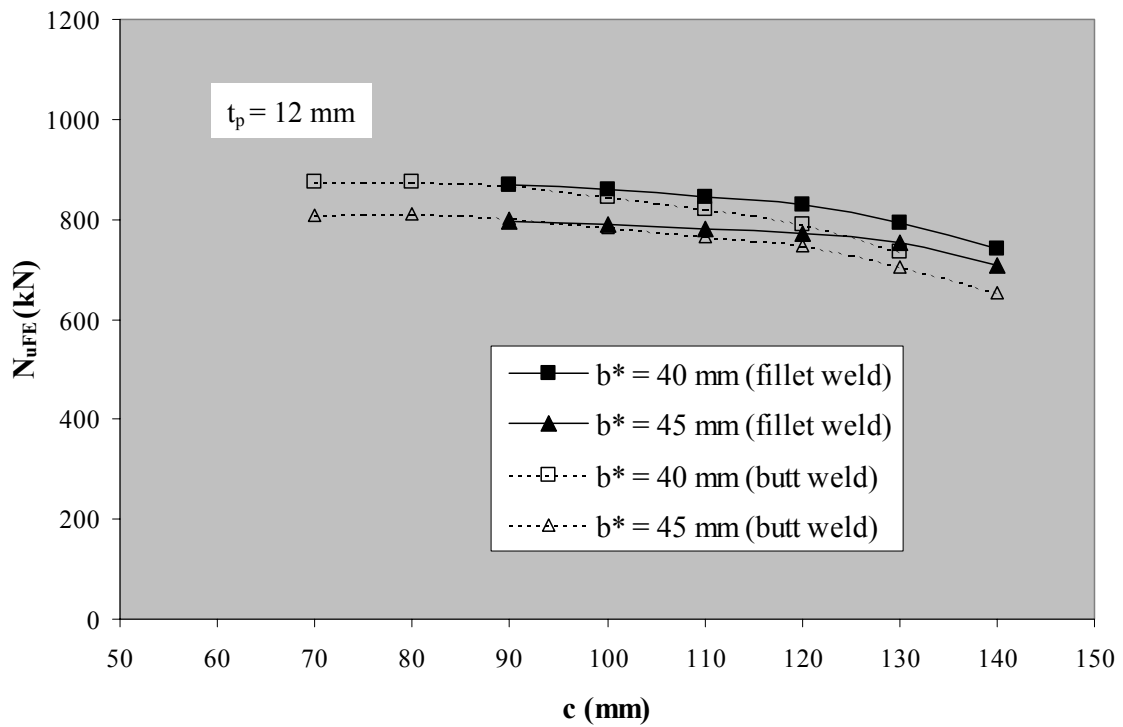


Figure 4.14 Connection capacity for varying values of "c" ($t_p = 12$ mm)

5 ANALYTICAL STUDY AND SOLUTIONS

5.1 Introduction

For the design of bolted flange-plate connections for rectangular hollow section connections under tension, two basic approaches can be found. First, a yield line analysis which uses a two-dimensional yield line pattern and applies the virtual work principle. Secondly, in contrast to this two-dimensional yield line analysis, a model can be assumed which disregards the influence of the bordering sides and analyses each side of the connection individually. The yield lines in this one-dimensional model form parallel to the hollow section.

5.2 Yield Line Models

5.2.1 One-Dimensional Yield Line Model

Depending on the flange-plate and bolt properties three basic failure mechanisms can occur for a flange-plate connection:

1. Bolt failure, no plastic hinge in the flange-plate (see Figure 5.1);
2. Bolt failure, plastic hinge along the hollow section/weld line (see Figure 5.2);
3. No bolt failure, plastic hinge along the hollow section/weld line and at the bolt line (see Figure 5.3).

For all three failure mechanisms, the connection strength is calculated by adding up the proportion of the connection load that is transferred by each bolt:

$$N = \sum_{i=1}^n N_{b,i} \quad (\text{Equation 5.1}).$$

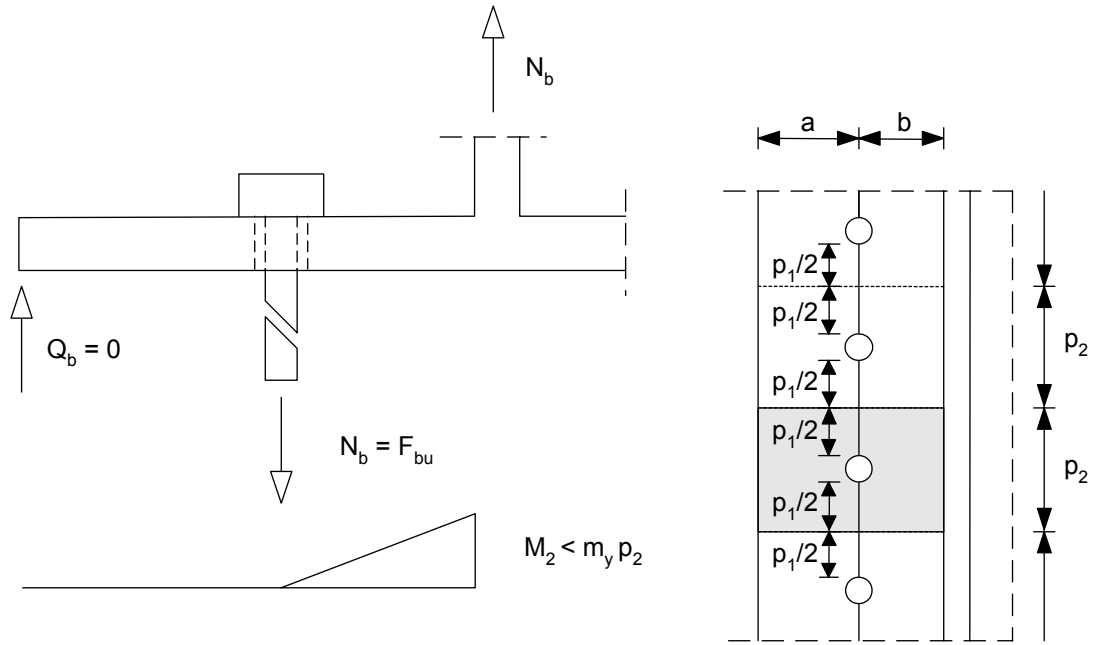


Figure 5.1 Failure mechanism 1

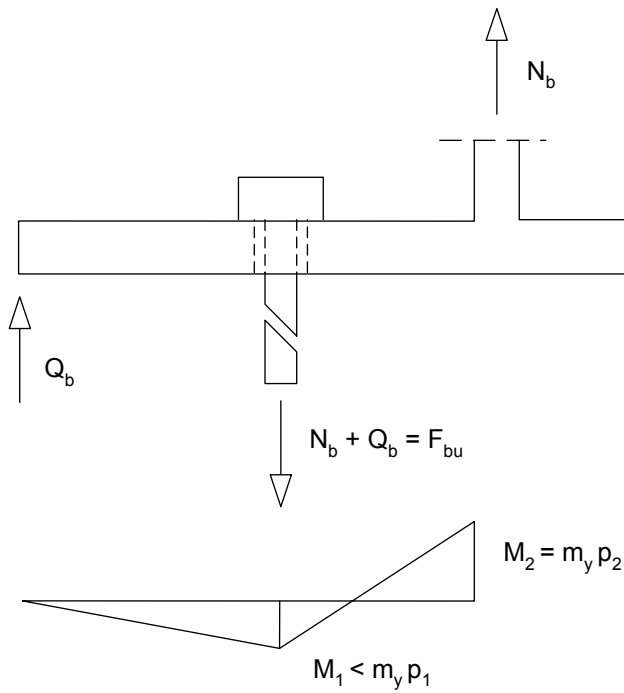


Figure 5.2 Failure mechanism 2

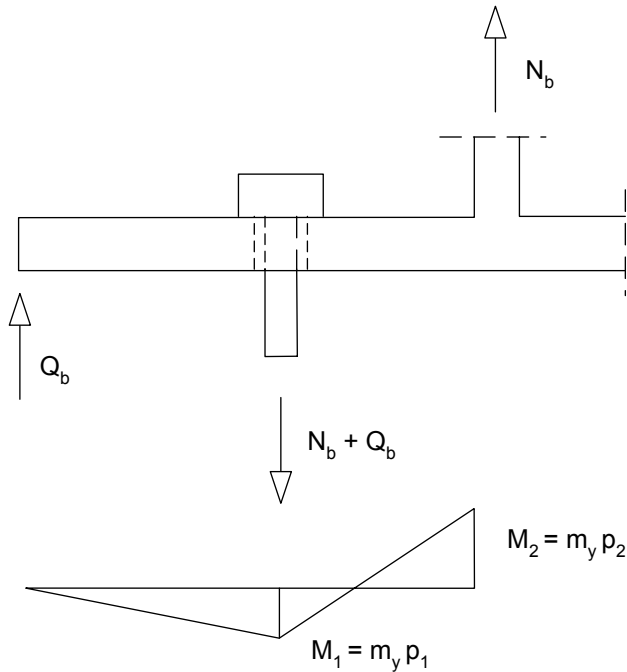


Figure 5.3 Failure mechanism 3

Applying the force and bending moment equilibria (exact derivation of formulae can be found in Appendix Part I) for each failure mechanism the connection load of a single bolt can be calculated as:

Failure mechanism 1:

$$N_{b1} = F_{bu} \quad (\text{Equation 5.2})$$

Failure mechanism 2:

$$N_{b2} = \frac{1}{a+b} (F_{bu} \cdot a + m_y \cdot p_2) \quad (\text{Equation 5.3a})$$

$$\Leftrightarrow N_{b2} = \frac{1}{a+b} (F_{bu} \cdot a + \frac{1}{4} f_{yp} t_p^2 \cdot p_2) \quad (\text{Equation 5.3b})$$

Failure mechanism 3:

$$N_{b3} = \frac{p_1 + p_2}{b} m_y \quad (\text{Equation 5.4a})$$

$$\Leftrightarrow N_{b3} = \frac{p_1 + p_2}{b} \cdot \frac{1}{4} f_{yp} t_p^2 \quad (\text{Equation 5.4b})$$

The corresponding prying force Q_b resisted by a single bolt is then:

Failure mechanism 1:

$$Q_{b1} = 0$$

Failure mechanism 2:

$$Q_{b2} = \frac{1}{a+b} (F_{bu} \cdot b - m_y \cdot p_2) \quad (\text{Equation 5.5a})$$

$$\Leftrightarrow Q_{b2} = \frac{1}{a+b} (F_{bu} \cdot b - \frac{1}{4} f_{yp} t_p^2 \cdot p_2) \quad (\text{Equation 5.5b})$$

Failure mechanism 3:

$$Q_{b3} = \frac{p_1}{a} m_y \quad (\text{Equation 5.6a})$$

$$\Leftrightarrow Q_{b3} = \frac{p_1}{a} \cdot \frac{1}{4} f_{yp} t_p^2 \cdot \quad (\text{Equation 5.6b})$$

Two flange-plate thickness limits determine which failure mechanism will rule for a certain connection:

- Failure mechanism 1 for $t_p > t_{q1}$;
- Failure mechanism 2 for $t_{q1} \geq t_p \geq t_{q2}$;
- Failure mechanism 3 for $t_p < t_{q2}$.

With:

$$t_{q1} = \sqrt{\frac{4F_{bu} b}{p_2 f_{yp}}} \quad (\text{Equation 5.7})$$

and

$$t_{q2} = \sqrt{\frac{4F_{bu}}{(\frac{p_1 + p_2}{b} + \frac{p_1}{a}) f_{yp}}} \quad (\text{Equation 5.8})$$

In accordance with the results of former studies (modified T-Stub model, Struik and de Back [1969]) the resultant bolt force is assumed to act somewhere between the bolt axis and the edge of the bolt head. Therefore, "a" and "b" are replaced by "a'" and "b'", with "a'" and "b'" given by:

$$a' = a + d/2, \text{ with } a \leq 1.25 b \quad \text{in calculation (but not necessarily in practise)} \quad (\text{Equation 5.9})$$

$$b' = b - d/2 \quad (\text{Equation 5.10})$$

In accordance with the results of the numerical study further adjustments of the effective values for the distance between the inside and outside yield line, the distance "b", as

well as the length of the effective bolt pitch "p", are made. The following formulae have been derived based on a best-fit assumption in a regression analyses.

For connections with fillet welds, the results of the parametric study indicate that the plastic hinge along the outer wall of the hollow section is shifted by half the weld leg length ($w/2 \approx 0.7 a$) towards the bolt line. For flange-plate connections with very thin-walled hollow sections, the bending moment of the flange-plate along the outer face of the hollow section does not equal the plastic moment of the flange-plate. The plastic hinge is located within the hollow section. To accommodate this effect, Equation 5.10 becomes:

$$b'' = b' - w/2 + (1 - \chi) t_i = b - d/2 - w/2 + (1 - \chi) t_i \quad (\text{Equation 5.11})$$

$$\text{with: } \chi = \frac{t_i^2 f_{yi}}{t_p^2 f_{yp}} \leq 1 \quad (\text{Equation 5.12})$$

Transferring this design model to flange-plate connections with bolts on all four sides, the tributary flange-plate width of each bolt "p₁" and "p₂" has to be determined. In theoretical models for flange-plate connections with bolts on two sides of the hollow section, the tributary length "p₂" is calculated as the flange-plate width divided by the number of bolts on one side and the length "p₁" as the corresponding length p₂ less the diameter of the bolt hole (see Figure 5.4), therefore

$$p_2 = \begin{cases} \frac{h_p}{n_s} & (\text{connection height}) \\ \frac{w_p}{n_s} & (\text{connection width}) \end{cases} \quad (\text{Equation 5.13})$$

$$p_1 = p_2 - d' \quad (\text{Equation 5.14})$$

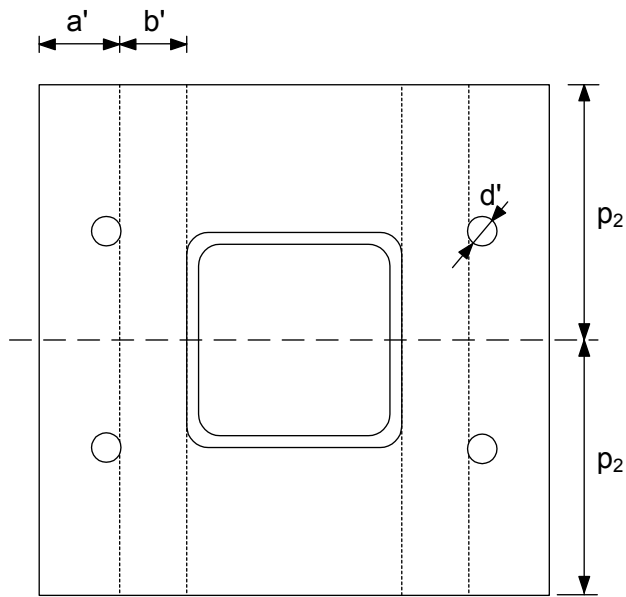


Figure 5.4 Definition of tributary flange-plate width p for flange-plate connections with bolts on two sides of the connection

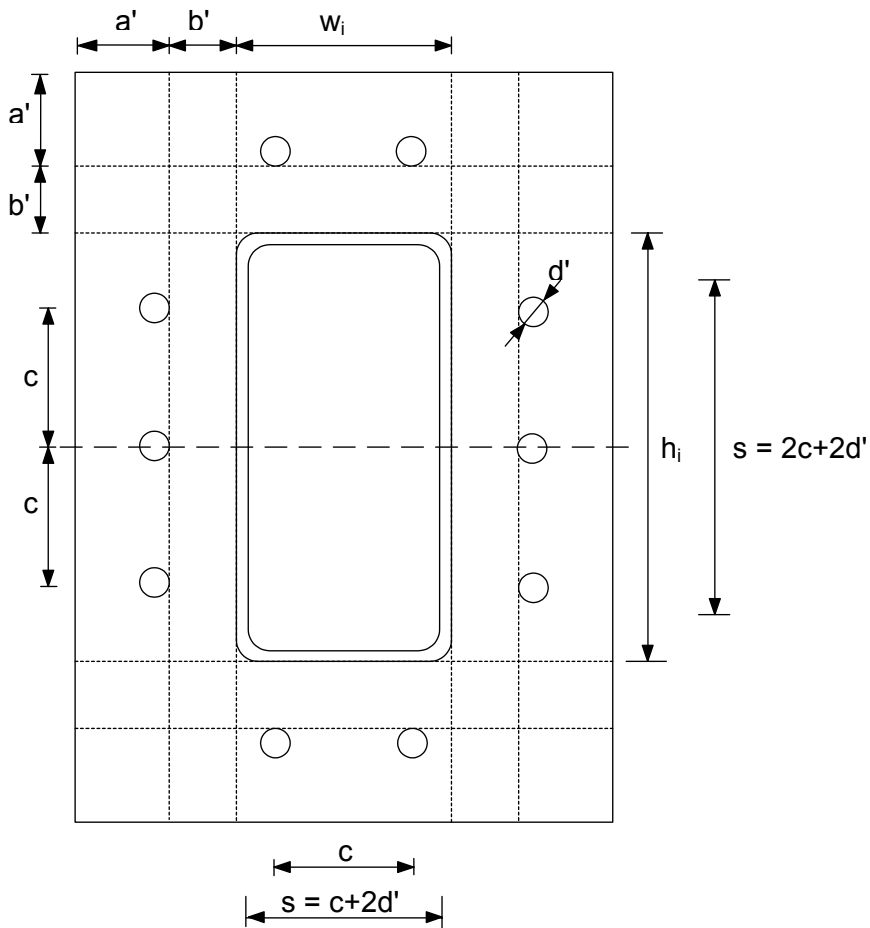


Figure 5.5 Definition of tributary flange-plate width p for flange-plate connections with bolts on all four sides of the connection

Equations 5.13 and 5.14 disregard the influence of the bolt pitch (length "c") for the calculation of the tributary flange-plate width. For connections with bolts on all four sides (see Figure 5.5), the plastic hinges intersect at the corners of the flange-plate. Therefore, it was found that it is not feasible to use the full width of the flange-plate for the calculation of the tributary flange-plate width "p₁" and "p₂". To account for the difference between the model for connections with bolts on two sides and the present bolt layout, a factor "ψ" is introduced:

$$\psi = \begin{cases} \left(\frac{s}{h_i - 3t_i} \sqrt{\frac{b''}{a'}}\right)^{0.25} & \text{for } s \leq h_i - 3t_i \text{ (connection height)} \\ \text{and } \left(\frac{s}{w_i - 3t_i} \sqrt{\frac{b''}{a'}}\right)^{0.25} & \text{for } s \leq w_i - 3t_i \text{ (connection width)} \\ \left(\frac{h_i - 3t_i}{s} \sqrt{\frac{b''}{a'}}\right)^{0.25} & \text{for } s > h_i - 3t_i \text{ (connection height)} \\ \text{and } \left(\frac{w_i - 3t_i}{s} \sqrt{\frac{b''}{a'}}\right)^{0.25} & \text{for } s > w_i - 3t_i \text{ (connection width)} \end{cases} \quad (\text{Equation 5.15})$$

$$\text{With: } s = c(n_s - 1) + 2d' \quad (\text{Equation 5.16})$$

The tributary lengths "p₁" and "p₂" are replaced and given by:

$$p_2' = \begin{cases} \psi \cdot \frac{h_p}{n_s} \\ \psi \cdot \frac{w_p}{n_s} \end{cases} \quad (\text{Equation 5.17})$$

$$p_1' = p_2' - d' \quad (\text{Equation 5.18})$$

The correction factor "ψ" is based on the results of the numerical as well as experimental study. It has been chosen to give good agreement between the predicted failure loads and the results of the numerical and experimental study.

Using the modified values for "a", "b", "p₁" and "p₂" the connection load for each bolt (Equations 5.2 to 5.4) and each failure mechanism now becomes:

Failure mechanism 1:

$$N_{b1} = F_{bu} \quad (\text{Equation 5.2})$$

Failure mechanism 2:

$$N_{b2} = \frac{1}{a'+b''} (F_{bu} \cdot a' + m_y \cdot p_2') \quad (\text{Equation 5.19a})$$

$$\Leftrightarrow N_{b2} = \frac{1}{a'+b''} (F_{bu} \cdot a' + \frac{1}{4} f_{yp} t_p^2 \cdot p_2') \quad (\text{Equation 5.19b})$$

Failure mechanism 3:

$$N_{b3} = \frac{p_1' + p_2'}{b''} m_y \quad (\text{Equation 5.20a})$$

$$\Leftrightarrow N_{b3} = \frac{p_1' + p_2'}{b''} \cdot \frac{1}{4} f_{yp} t_p^2 \quad (\text{Equation 5.20b})$$

Table 5.1 shows the results of the regression analysis for the proposed formula when applied to the connections of the numerical and experimental investigation.

Table 5.1 Results of the regression analysis for the one-dimensional yield line model

	Number of Data Points	Mean N_{ux}/N_u (>1 safe)	Coefficient of Variation (%)	Correlation R^2
<i>FE-Study</i>				
Square Specimens				
4-bolts	18	1.02	3.87	0.99
8-bolts	144	0.98	5.55	0.95
Rectangular Specimens				
10-Bolts	123	1.01	9.33	0.94
All FE-Study	285	1.00	7.57	0.95
<i>Experimental Study</i>				
Square Specimens				
4-bolts	4	1.00	2.64	0.96
8-bolts	10	1.00	5.58	0.92
Rectangular Specimens				
10-Bolts	4	0.94	0.53	1.00
All Experimental Study	18	0.99	5.18	0.94
<i>All</i>	303	1.00	7.46	0.95

5.2.2 Two-Dimensional Yield Line Model

Three failure modes have been studied in the following two-dimensional yield line model:

1. Bolt failure without prying action: The plastic capacity of the flange-plate material is not exhausted before the bolts fail.

$$\sum F_{bu} \leq N_{yp} \quad \Rightarrow \quad N_u = \sum F_{bu}$$

2. Bolt failure with prying action: The plastic capacity of the flange-plate material is exhausted simultaneously with bolt failure.

$$N_{yp} + Q > \sum F_{bu} > N_{yp} \quad \Rightarrow \quad N_u = \sum F_{bu} - Q$$

3. Flange-plate failure: The plastic capacity of the flange-plate material is exhausted without the bolts failing.

$$N_{yp} + Q < \sum F_{bu} \quad \Rightarrow \quad N_u = N_{yp}.$$

In the analysis of the yield line model, a number of simplifications have been made:

- the shape of the hollow section is considered to be rectangular with sharp corners, neglecting the corner radii;
- the full utilisation of the plastic moment along all yield lines is regarded as flange-plate failure; the ultimate strength of the flange-plate material is not considered;
- the edge distance, distance "a", and the distance from bolt line to hollow section face, distance "b", is constant for all sides;
- the distance between bolts parallel to hollow section face, distance "c", is constant for all sides;
- non-plastic states, up until the full development of the plastic hinge along all lines of the yield line pattern, have not been considered;
- the prying force is assumed to be concentrated along the edge of the flange.

Figure 5.6 shows the assumed yield line pattern for a rectangular flange-plate connection. The derivation of the following formulae can be found in Appendix Part I.

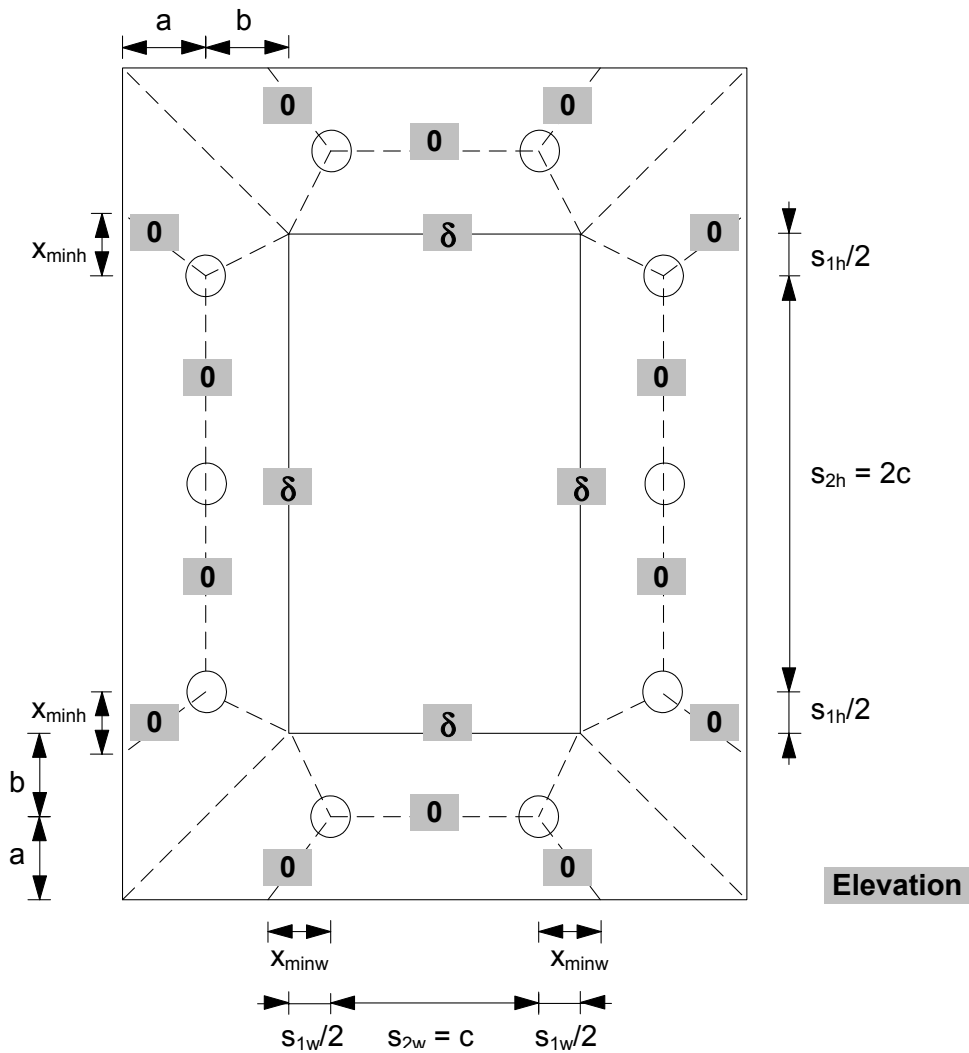


Figure 5.6 Yield line pattern of a rectangular flange-plate connection

Based on the principle of virtual work, the external work should equal the internal work when a virtual displacement is applied, so that the critical collapse load can be calculated. The collapse load depends on the yield line distribution (see Figure 5.6), particularly the lengths "x_{minh}" and "x_{minw}". The lengths "x_{minh}" and "x_{minw}" correspond to the minimum (governing) load for which the flange-plate will reach its yield strength along all yield lines. For a rectangular flange-plate connection they are given by:

$$x_{minh} = \frac{a}{2} \left(\sqrt{\left(1 + \frac{b}{a}\right) \left(\frac{s_{1h}^2}{b^2} - 2 \frac{s_{1h}}{b} + 8\right)} - \frac{s_{1h}}{b} \right) \tag{Equation 5.21a}$$

$$x_{minw} = \frac{a}{2} \left(\sqrt{\left(1 + \frac{b}{a}\right) \left(\frac{s_{1w}^2}{b^2} - 2 \frac{s_{1w}}{b} + 8\right)} - \frac{s_{1w}}{b} \right) \tag{Equation 5.21b}$$

with:

$$s_{1h} = h_i - s_{2h} \quad (\text{Equation 5.22a})$$

$$s_{1w} = w_i - s_{2w} \quad (\text{Equation 5.22b})$$

and,

$$s_{2h} = n_s c \text{ (height, see Figure 5.6)} \quad (\text{Equation 5.23a})$$

$$s_{2w} = n_s c \text{ (width, see Figure 5.6)} \quad (\text{Equation 5.23b})$$

The corresponding critical load N_{yp} (yield strength of the flange-plate) is then:

$$N_{yp} = 8 \left\{ \frac{a}{2b} \sqrt{1 + \frac{b}{a} \left(\sqrt{\frac{s_{1h}^2}{b^2} - 2 \frac{s_{1h}}{b} + 8} + \sqrt{\frac{s_{1w}^2}{b^2} - 2 \frac{s_{1w}}{b} + 8} \right)} + \frac{1}{4} \frac{s_{1h} + s_{1w}}{b} \right. \\ \left. + \frac{1}{2} \frac{s_{2h} + s_{2w}}{b} + \frac{a}{b} \left(1 - \frac{s_{1h} + s_{1w}}{2b} \right) + 1 \right\} m_y \quad (\text{Equation 5.24})$$

with:

$$m_y = \frac{1}{4} t_p^2 f_{yp} \quad (\text{Equation 5.25})$$

The prying force which corresponds to this yield line mechanism is then given by:

$$Q = 2 \left[\frac{3 \left(1 + \left(\frac{x_{\min h}}{a} \right)^2 \right)}{\frac{s_{2h}}{a} + 2 \frac{x_{\min h}}{a}} + \frac{3 \left(1 + \left(\frac{x_{\min w}}{a} \right)^2 \right)}{\frac{s_{2w}}{a} + 2 \frac{x_{\min w}}{a}} + \frac{s_{2h} + s_{2w}}{a} \right] m_y \quad (\text{Equation 5.26})$$

The formulae are also applicable for flange-plate connections with square hollow sections. For square flange-plate connections, the values " s_{1h} " and " s_{1w} " as well as " s_{2h} " and " s_{2w} " are respectively identical. In connections with four bolts only, a value of $s_2 = 0$ has to be used in the preceding equations.

The results of the regression analysis for the two-dimensional yield line model are shown in Table 5.2.

Table 5.2 Results of the regression analysis for the two-dimensional yield line model

	Number of Data Points	Mean N_{ux}/N_u (>1 safe)	Coefficient of Variation (%)	Correlation R^2
<i>FE-Study</i>				
Square Specimens				
4-bolts	18	1.18	10.52	0.95
8-bolts	144	0.97	17.70	0.88
Rectangular Specimens				
10-Bolts	123	0.98	21.61	0.81
All FE-Study	285	0.99	19.68	0.85
<i>Experimental Study</i>				
Square Specimens				
4-bolts	4	1.08	12.71	0.95
8-bolts	10	1.02	15.53	0.59
Rectangular Specimens				
10-Bolts	4	0.92	7.97	0.90
All Experimental Study	18	1.01	14.73	0.78
<i>All</i>	303	0.99	19.41	0.85

5.3 Summary

Two analytical approaches for the calculation of bolted flange-plate connections with square and rectangular hollow sections have been proposed. The first design model, based on a one-dimensional yield line analysis, has better agreement between predicted and measured failure loads than the second design model based on a two-dimensional yield line analysis. The two-dimensional yield line model involves rather complicated formulae that might deter many designers from the application of this method. Therefore, the design method based on the one-dimensional yield line analysis is suggested for the calculation of bolted flange-plate connections. Figure 5.7 shows a flowchart of the proposed calculation method. The validity range for rectangular connections is $0.75 \leq h_p/w_p \leq 1.33$. For connections with a h_p/w_p -ratio not covered by the validity range, a connection with bolts along just the longer side of the connection is recommended.

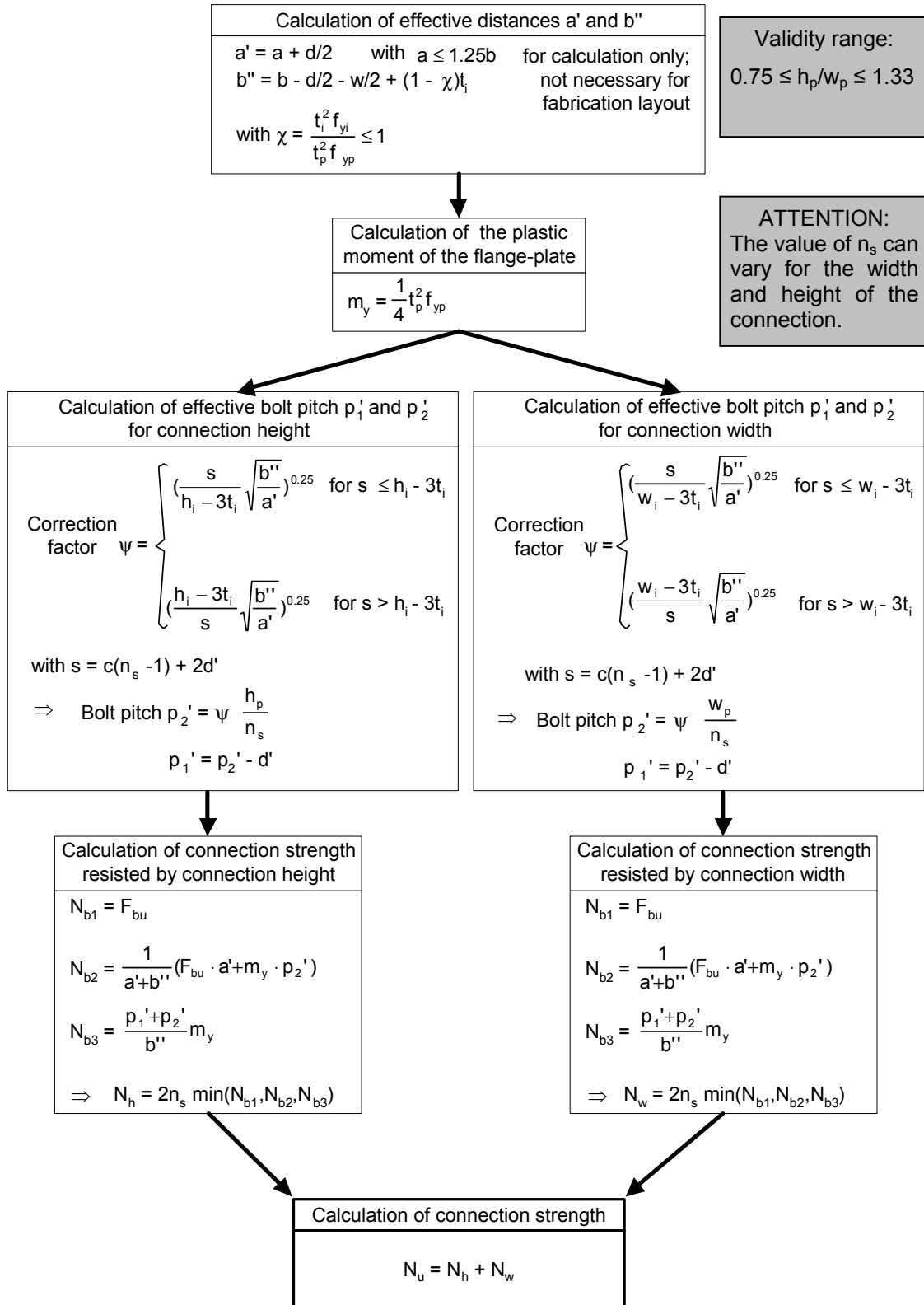


Figure 5.7 Flowchart of the proposed calculation method

PART II HIDDEN JOINT CONNECTIONS

6 *LITERATURE REVIEW*

Hollow sections enable architects to build elegant structures that show the exposed steel. The most typical applications can be found in large-scale buildings such as airport terminals, bridges, arenas or exhibition halls. To span the large dimensions of a roof or bridge structure, trusses are commonly used. Flange-plate as well as gusset plate connections are usually found if it becomes necessary to splice the members of the truss. Standard gusset plate connections (see Figure 6.1) in which the gusset plate is slotted into the hollow section, with the plate protruding out of the slots at the two ends, as well as the flange-plate connections described in Part I, destroy the elegant appearance of the structure. A need for invisible connections arises. Hidden joint connections (see Figure 6.1) represent such an invisible connection. A cover (non-structural) in the shape of the hollow section (see Figure 6.2) hides the bolted gusset plate that protrudes beyond the end of the hollow section. The gusset plates are then completely out of sight. With regard to the fabrication of the connection, in particular the welding inside the hollow section, a single shear connection with only two gusset plates placed slightly eccentric below and above the axis of the hollow section is not only more economical in fabrication than other arrangements, but also easy to erect. A hidden joint free of eccentricity would require three plates; two parallel plates which are fitted into one hollow section and a single central plate which is fitted into the other hollow section. The single plate would then be inserted in between the other two plates during erection. As all welding has to be done from the open ends of the hollow section and the operating room for the welder is restricted to half of the cross sectional area of the hollow section, the number and length of welds should be minimised. Therefore, only a single shear connection with two gusset plates has been considered here.

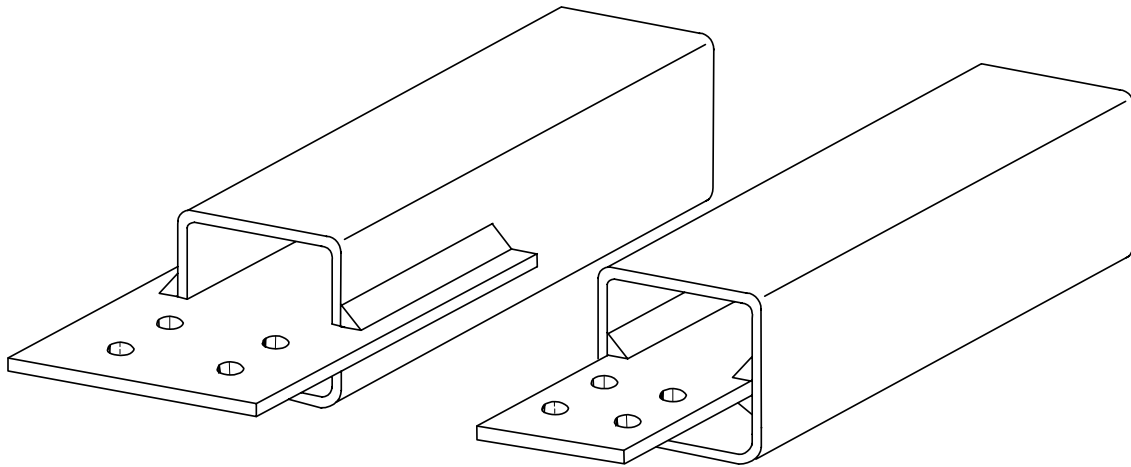


Figure 6.1 Standard gusset plate connection (left) and hidden joint connection (right)

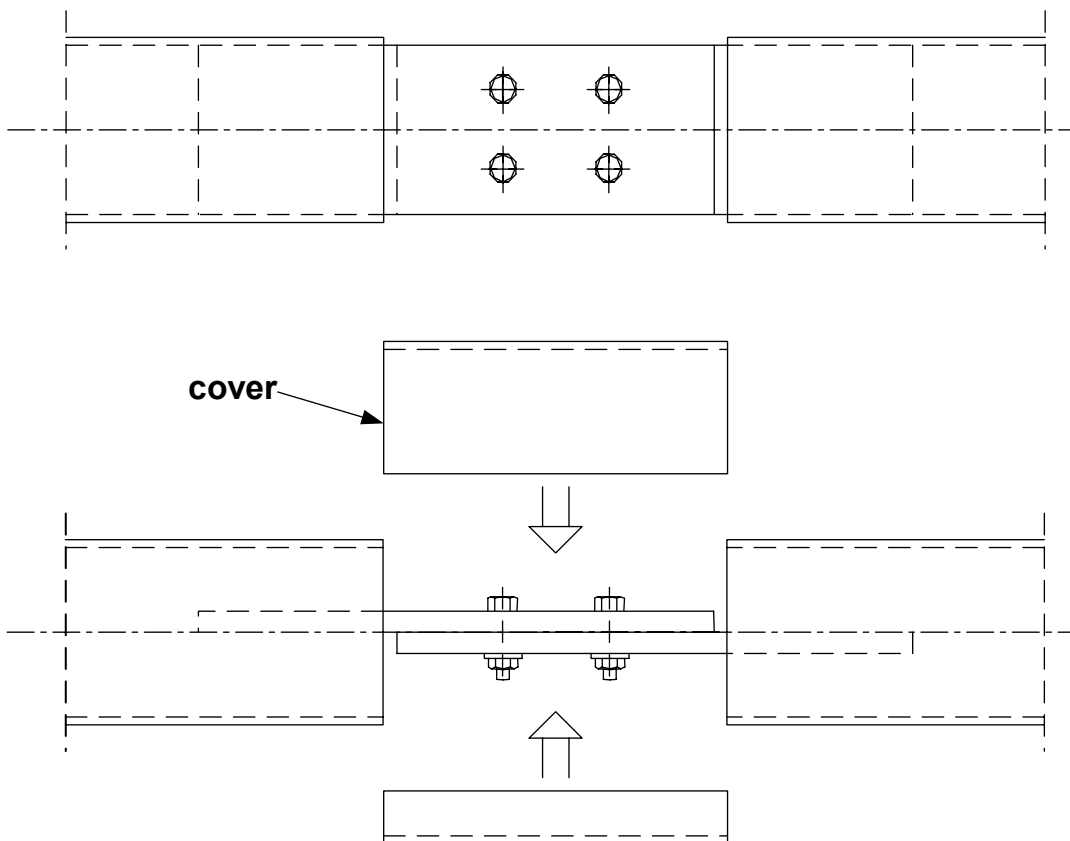


Figure 6.2 Hidden joint connection with cover

Hidden joint connections can potentially fail in various modes and in various components of the connection:

- I. Hollow section
 - a) gross yielding of the hollow section material,
 - b) block shear tear-out along the welds,

- c) shear lag failure due to stress concentrations at the weld end.
- II. Gusset plate
- a) gross yielding of the gusset plate material,
 - b) block shear tear-out along the welds,
 - c) net section failure of the gusset plate,
 - d) shear lag failure of the plate due to stress concentrations at the weld end.
- III. Welds
- a) failure due to shear stresses parallel to the axis of the weld.
- IV. Bolts
- a) failure in single shear,
 - b) bolt bearing failure of the gusset plate.

Most failure modes for this connection type are well known and can be excluded by applying the design rules provided in national steel codes. The least known failure mode is shear lag failure, in particular the rupture of the hollow section due to shear lag. Unfortunately, specific research on hidden joint connections, especially with regard to shear lag of the hollow section, is not published or studied as yet. Supposedly, standard gusset plate connections with slotted hollow sections (see Figure 6.1) have a nearly similar behaviour as hidden joint connections. The following literature review therefore covers predominantly research done on slotted gusset plate connections.

6.1 Shear Lag Failure of the Hollow Section

Shear lag failure occurs if the unconnected circumference of the hollow section is not fully engaged and contributes only in part to the resistance of the member. If the hollow sections are slotted as for standard gusset plate connections, local stress peaks at the slot ends cause initiating cracks that will result in an even earlier failure of the connection. The location of these stress peaks coincides with the heat affected zone caused by the weld between the hollow section and the gusset plate. The local stress peaks due to the slots will not occur in the non-slotted hidden joint connections. As these stress peaks decrease the hollow section capacity, the current design models for shear lag are bound to err on the safe side.

6.1.1 International Specifications

Eurocode 3 [1992], particularly Eurocode 3 Part 1-8 [prEN 1993-1-8, 2002], addresses shear lag failure in bolted connections for angles connected by one leg and other unsymmetrically

connected tension members by giving formulae to calculate the effective net area depending on the connected length. Unfortunately, these design rules are only applicable for bolted connections as the formulae use the bolt hole diameter to determine the reduction factor of the net section (see Table 3.7 in Eurocode 3, Part 1-8 [prEN 1993-1-8, 2002]). For connections with welds, no specific design method is provided in the Eurocode. Shear lag is mentioned in connection with locally introduced shear loads causing bending moments in longitudinally stiffened plated structures. Formulae are given to calculate an effective width used for the buckling analysis of thin gauge members and sheets [Eurocode 3 Part 1-3, prEN 1993-1-3, in prep.] and plated structural elements [Eurocode 3 Part 1-5, prEN 1993-1-5, in prep.]. For axial tension loading, reference is made to the earlier-mentioned formulae for bolted connections of angles connected by one leg and other unsymmetrically connected tension members.

The American specification for structural hollow sections [AISC 2000] uses the concept of "effective net area" which refers to Clause B3-2 in the LRFD specifications for structural steel buildings [AISC 1999]. The design method provided is based on research carried out by Chesson and Munse [1963]. An eccentricity factor "U" is calculated from the connection eccentricity " \bar{x} " (see Figure 6.3) and the welded connection length " L_w ":

$$U = 1 - \frac{\bar{x}}{L_w} \leq 0.9 \quad (\text{Equation 6.1}),$$

$$\text{with: } \bar{x} = \frac{h_i^2 + 2w_i h_i}{4(w_i + h_i)} \quad \text{for rectangular} \quad (\text{Equation 6.2a}),$$

$$\text{and } \bar{x} = \frac{3}{8} h_i \quad \text{for square hollow sections} \quad (\text{Equation 6.2b}).$$

The effective net area is then calculated as:

$$A'_{ne} = A_{ne} \cdot U \quad (\text{Equation 6.3}).$$

As the hollow section in the hidden joint connections is unslotted, the net section " A_{ne} " equals the gross cross sectional area of the RHS, " A_i ". For gusset plate connections with slotted hollow sections (see Figure 6.1), the cross sectional area of the RHS is reduced by the area of the slot ($A_{ne} = A_i - 2t_p \cdot t_i$). In practise, the slot width t_{slot} is usually greater than t_p to allow ease of fabrication, and in such cases $A_{ne} = A_i - 2t_{slot} \cdot t_i$

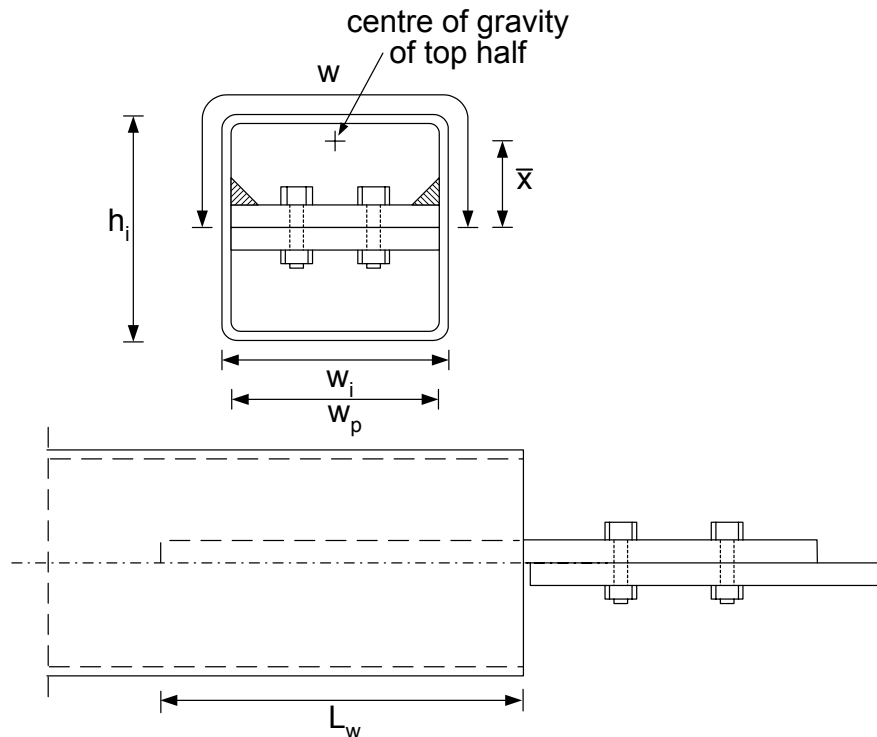


Figure 6.3 Hidden Joint dimensions and symbols

Recently, a general examination of the AISC LRFD shear lag design provision has been given by Kirkham and Miller [2000]. Based on recent studies, it was concluded that the existing design approaches are overly conservative and further research is necessary.

The former Canadian Standard CAN/CSA-S16.1-94 [1994] addresses shear lag in elements connected by a pair of welds parallel to the load by calculating the "effective net area" (Clause 12.3.3) based on an efficiency factor that depends on the ratio between the distance between the welds around the hollow section perimeter " w " and the connection length " L_w ". The distance between the welds for slotted plate hollow section connections is nominally taken as half the hollow section circumference (see Figure 6.3) [Packer and Henderson 1997]. The efficiency factor is:

- 1.0 for $L_w/w \geq 2.0$;
- 0.87 for $2.0 > L_w/w \geq 1.5$;
- 0.75 for $1.5 > L_w/w \geq 1.0$.

L_w/w values smaller than 1.0 are not permitted. In their current design guide for hollow sections, Packer and Henderson [1997] propose an efficiency factor of 0.62 for connections with $0.6 \leq L_w/w < 1.0$ based on the results of an experimental study by Korol et al. [1994]. For values smaller than $L_w/w = 0.6$ shear rupture of the base metal of the hollow section along the weld line is considered to govern.

The current Canadian Standard CAN/CSA-S16-01 [2001] is slightly less conservative than the superseded code of 1994. The efficiency factor according to the new provisions on shear lag (Clause 12.3.3.3) is:

- 1.0 for $L_w/w \geq 2.0$;
- $0.5 + 0.25 L_w/w$ for $2.0 > L_w/w \geq 1.0$;
- $0.75 L_w/w$ for $1.0 > L_w/w$.

The new code allows L_w/w values smaller than 1.0. Compared to the American specifications, the new Canadian specification is more conservative if applying to hollow section connections with L_w/w values smaller than about 1.5.

6.1.2 Recent Research on Shear Lag

Specific research on hidden joint connections, especially with regard to shear lag of the hollow section, is not published or studied as yet. For connections with the gusset plate slotted into the hollow section, only a few studies have been carried out. In an experimental study by British Steel [Swinden Laboratories 1992] on slotted end plate connections for circular, square and rectangular hollow sections, 13 of the 24 specimens failed by shear lag.

The results of an experimental as well as numerical investigation on shear lag failure for slotted circular hollow sections were given by Cheng et al. [1996]. Nine tests on gusset plate connections to CHS tension members were performed. None of the specimens failed by shear lag. However, the experimental and numerical investigation showed that considerable stress concentrations occur at the slot ends. Comparing the results of the study with the Canadian [Cheng et al. 1998] as well as the American specifications [Cheng and Kulak 2000], it is shown that neither code accurately models the behaviour of slotted round tubular (CHS) connections. In contrast to the specifications, Cheng and Kulak [2000] conclude that shear lag failure is not critical for tubular sections if the connection length is longer than 1.3 times the diameter of the circular hollow section and provided that the slot end is welded ($U = 0.76$ with $\bar{x} = d_i/\pi$ for round hollow sections, or $L_w/w = 0.83$ theoretically, but Cheng and Kulak imply that $U = 1.0$ if $L_w > 1.3 d_i$).

A study on shear lag in slotted square and rectangular hollow sections has been performed by Korol et al. [1994]. A total of 18 specimens was tested under tensile loading with seven specimens failing by shear lag. Shear lag failure was characterized by a circumferential tube failure at the beginning of the weld in combination with reduced deformation (sudden failure). The authors concluded that for six of the seven specimens that failed by shear lag, all with $L_w/w \approx 1.0$, the connection capacity was nearly equal to the tensile capacity of the hollow section, $N_u = A_{ne} \cdot f_u$. Only one of the specimens ($L_w/w = 0.61$) failed very prematurely due to

shear lag. For L_w/w -ratios smaller than 0.6, base metal shear resistance of the hollow section governed. The influence of the eccentricity " \bar{x} " on the connection capacity was found to be only minor. Based on the results of the earlier study, Korol [1996] proposed a slightly modified approach for the calculation of the effective shear lag net section area. Instead of using the efficiency factors as given in the Canadian or American specifications, less conservative formulae were provided:

- for $L_w/w \geq 1.2$ (net/gross section failure governs), $\alpha = 1.0$; (Equation 6.4a)
- for $1.2 > L_w/w \geq 0.6$ (shear lag governs),
 $\alpha = 0.4 + 0.5 \cdot L_w/w$ (Equation 6.4b);
- for $L_w/w < 0.6$ block shear tear-out governs.

In contrast to the American specifications, the eccentricity factor "U" is now calculated as follows:

$$U = 1 - 0.4 \frac{\bar{x}}{L_w} \quad (\text{Equation 6.5}).$$

The effective shear lag net section is then:

$$A'_{ne} = A_{ne} \cdot \alpha \cdot U \quad (\text{Equation 6.6}).$$

Table 6.1 compares the strength predictions for shear lag failure (including gross section fracture of the hollow section) of the different calculation methods for the specimens tested by British Steel [Swinden Laboratories 1992], Korol et al. [1994] and Cheng et al. [1996]. Specimens that failed in the gusset plate or bolts or by block shear tear-out of the hollow section along the welds have not been considered here. All methods err on the safe side (mean values larger than 1.0). The formulae by Korol [1996] and by AISC [2000] give better predictions than the more conservative design method by Packer and Henderson [1997]. For connections with very low L_w/w -ratios, the predicted capacity according to the design method by AISC [2000] is too high (unsafe) compared to the test result.

Table 6.1 Comparison of calculation methods

Test Series		N_{ux}/N_u	Korol [1996]	AISC [2000]	Packer and Henderson [1997]
Swinden Laboratories [1992]	6 tests on CHS and 10 tests on RHS connections	Mean	1.14	1.18	1.43
		Coeff. of Var. (%)	8.1	7.4	12.4
Korol et al. [1994]	7 tests on RHS connections	Mean	1.12	1.06	1.53
		Coeff. of Var. (%)	2.4	7.4	12.2
Cheng et al. [1996]	9 tests on CHS connections	Mean	1.25	1.29	1.49
		Coeff. of Var. (%)	6.9	3.3	13.8

7 EXPERIMENTAL INVESTIGATION

7.1 Introduction

The experimental work, which has been carried out within the framework of CIDECT Research Programme 8E, had two main objectives, namely to study the structural strength and possible failure modes of this connection type as well as to establish the technical feasibility of the fabrication (welding). The data from the tests have also been used to verify a finite element model which has been used in a subsequent numerical study.

7.2 Scope of Experimental Programme

The experimental study consisted of six hidden joint connection tests under tensile loading. Hot rolled square S355 J2H hollow structural sections [EN 10210-1 1994], of sizes 200 x 6.3 mm and 200 x 12.5 mm and a nominal yield strength of 355 MPa were used. The gusset plate material was Grade S355 J2G3 [EN 10025 1994] with a nominal yield strength of 355 MPa. The stress-strain curves of the tensile coupon tests can be found in Appendix Part II. The material for the hollow sections with similar dimensions, as well as for the gusset plates with similar thicknesses, each came from a single length. The gusset plate thickness varied between 12 mm and 25 mm. Tables 7.1 and 7.2 show the measured dimensions and material properties of the six specimens. High tensile strength hexagonal fitted bolts of Grade 10.9 [ISO 898-1 1999], size M24 and M30, with a nominal design shear strength ($\gamma_M = 1.25$, single shear plane) of 199 kN and 311 kN respectively have been used throughout. Material tests on the bolts were not carried out as the bolts were not critical elements.

Table 7.1 Measured dimensional properties of test specimens

Specimen	h_i (mm)	t_i (mm)	$A_i^{1)}$ (mm ²)	t_p (mm)	w_p (mm)	L_w (mm)	$a^{2)}$ (mm)	r_{out} (mm)	\bar{x} (mm)	$w^{3)}$ (mm)	n	d (mm)
VK6-2-04	200	6.4	5090	12.5	187	160	8.1	17.5	75.0	400	4	24
VK6-2-06				240		8.3						
VK6-3-04				160		8.2						
VK6-3-06				240		8.3						
VK12-2-04	199	12.4	8940	24.7	174	160	8.1	24	74.6	398	6	30
VK12-2-06						240	8.0					

¹⁾ Measured area obtained by weighing a specific length of hollow section and using a density of 7850 kg/m³ [Eurocode 3 Part 1-2 1995]

²⁾ Measured throat thickness of the fillet weld between hollow section and gusset plate

³⁾ Measured distance between the welds, equals half the hollow section circumference

Table 7.2 Measured material properties of test specimens

	f_y (MPa)	f_u (MPa)	ϵ_{ul} (%) ¹⁾	E (MPa)
Plate				
$t_p = 12$ mm	364.0	525.5	27.6	228000
$t_p = 20$ mm	365.5	538.8	30.0	252258
$t_p = 25$ mm	428.0 ²⁾	567.5 ²⁾	26.0 ²⁾	221500 ²⁾
Hollow Section				
$t_i = 6.5$ mm	385.5	537.5	28.9	242000
$t_i = 12.5$ mm	394.5	536.0	26.4	204000

¹⁾ Measured over a gauge length of 60 mm ($t = 6.5$ mm), 90 mm ($t = 12$ and 12.5 mm), 100 mm ($t = 25$ mm, round coupons with $d_{coupon} = 20$ mm) and 140 mm ($t = 20$ mm)

²⁾ Derived from tensile coupon tests with round coupons

7.3 Testing and Measuring Equipment

All specimens have been tested in a vertical testing frame (see Figure 7.1). The load was applied by a pair of hydraulic cylinders that jacked up a horizontal beam on top of the frame. Load cells which were placed between the hydraulic cylinders and the beam monitored the applied load. Besides the measurements of the load, the strains on the hollow section as well as the gusset plate were monitored by 12 strain gauge rosettes (triaxial, 45°) on each specimen. The exact location of the strain gauges is shown in Figure 7.2.

7.4 Specimen Fabrication and Testing

Special attention has been given to the fabrication of welds. GMAW welding (gas-shielded metal arc welding) was used for all fillet welds. Shielding gas M21, 82% Argon and 18% CO₂, [EN 439 1994] and wire electrodes G4Si1, Ø 1mm, [EN 440 1994] were used throughout. Figure 7.3 shows a close-up of a typical weld. The length of the weld connecting the hollow section and the gusset plate is restricted by the operating space inside the hollow section. It was found that the limit for square hollow sections with $h_i = 200$ mm is roughly 240 mm or 1.2 times the height of the hollow section. A weld length of 1.2 times the height of the hollow section is probably feasible for larger hollow sections as well. In any case, the weld length should not exceed the arm length of the welder for practical considerations.

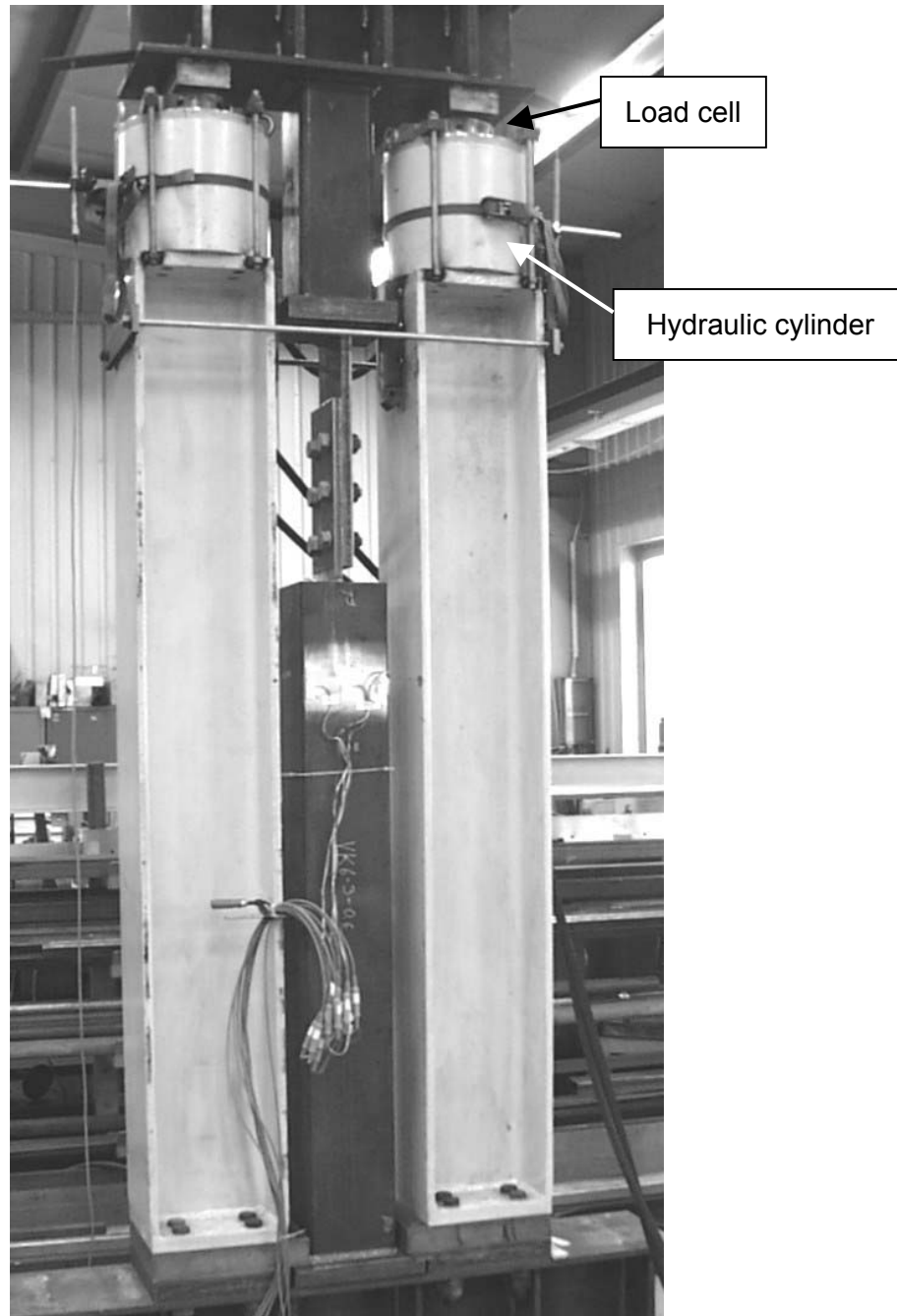


Figure 7.1 Specimen VK6-3-06 in testing frame (typical)

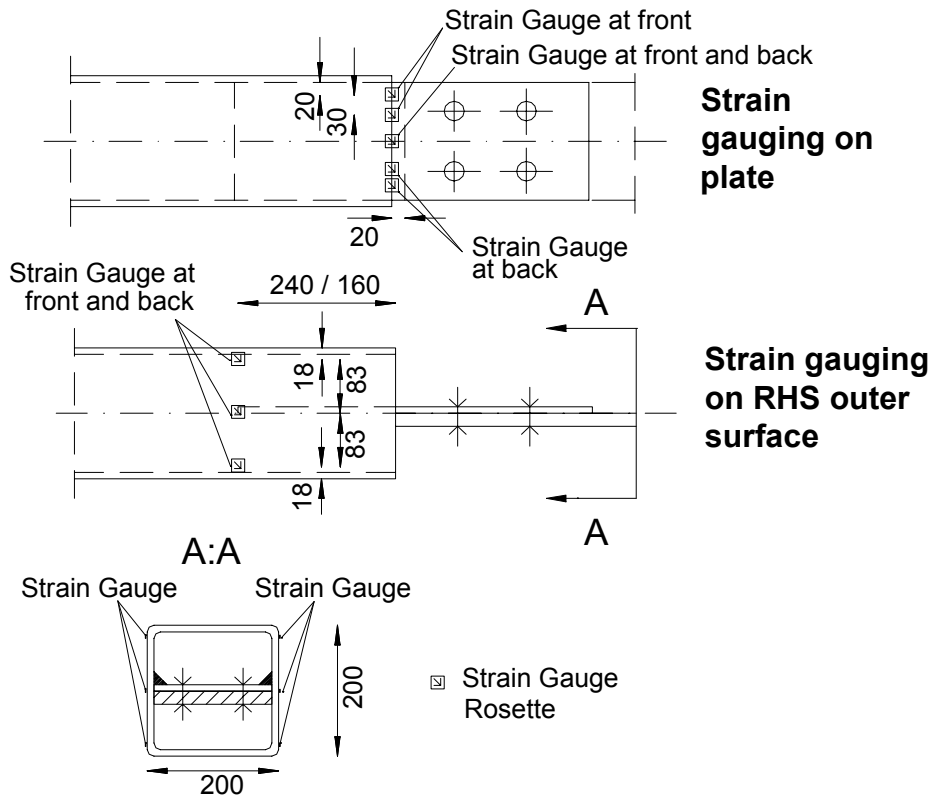


Figure 7.2 Strain gauge positions



Figure 7.3 Typical fillet weld

7.5 Test Results

A total of six specimens were tested. Table 7.3 shows the connection strength as well as the failure mode for each specimen. All specimens except specimen VK6-2-04 with the smallest plate thickness ($t_p = 12.5$ mm) and weld length ($L_w = 160$ mm) failed due to plate tensile failure through the first line of bolts (see Figure 7.4). Specimen VK6-2-04 failed due to shear lag of the plate, yet with plate failure imminent (see Figure 7.5). Bending of the gusset plate (see Figure 7.6) was observed for all specimens. None of the hollow sections or welds showed any signs of failure. The complete results of all strain gauge measurements on the hollow section and gusset plate can be found in the Appendix Part II.

All specimens failed at tensile loads higher than the calculated net section failure load of the gusset plate (at the first line of bolts). The difference between calculated and measured failure loads is between 10% and 16% (see Table 7.3). In tensile coupon tests the stress distribution is constant over the full width of the cross section material and the material is free to neck. The stress distribution in the gusset plates during the specimen tests is not constant. Stress peaks exist around the bolt holes. Due to a restriction of deformation in this area (caused by the remaining material) the stress can increase and initiate "premature" failure.

Table 7.3 Test results

Test	N_{ux} (kN)	N_{up} (kN) ¹⁾	N_{ux}/N_{up}	Failure Mode
VK6-2-04	1003	901	1.11	Shear lag failure of the plate and plate tensile failure imminent
VK6-2-06	990		1.10	Plate tensile failure
VK6-3-04	1646	1481	1.11	Plate tensile failure
VK6-3-06	1632		1.10	Plate tensile failure
VK12-2-04	1808	1574	1.15	Plate tensile failure
VK12-2-06	1828		1.16	Plate tensile failure

¹⁾ N_{up} = predicted net section strength of gusset plate

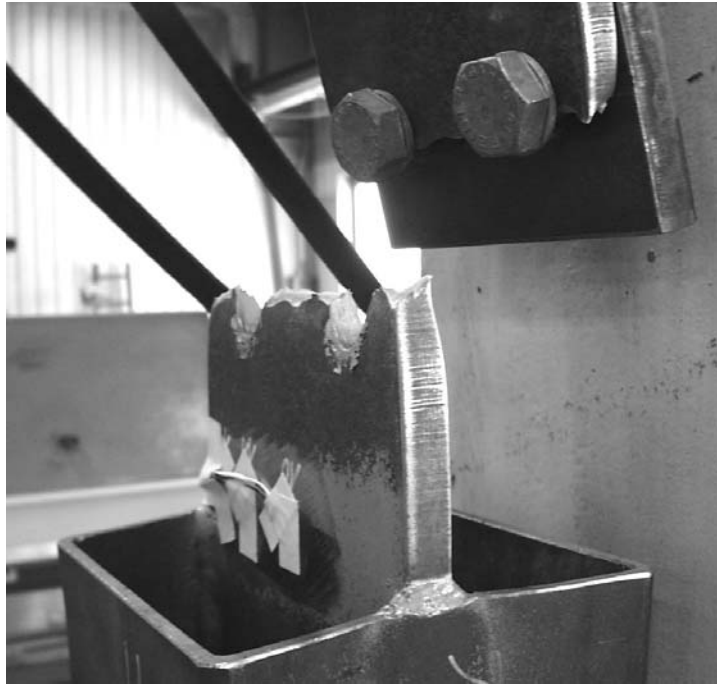


Figure 7.4 Plate tensile failure along the bolt line for specimen VK6-3-04 (typical for all specimens except VK6-2-04)



Figure 7.5 Shear lag failure of the gusset plate for specimen VK6-2-04 (smallest plate thickness $t_p = 12.5$ mm, and weld length, $L_w = 160$ mm)

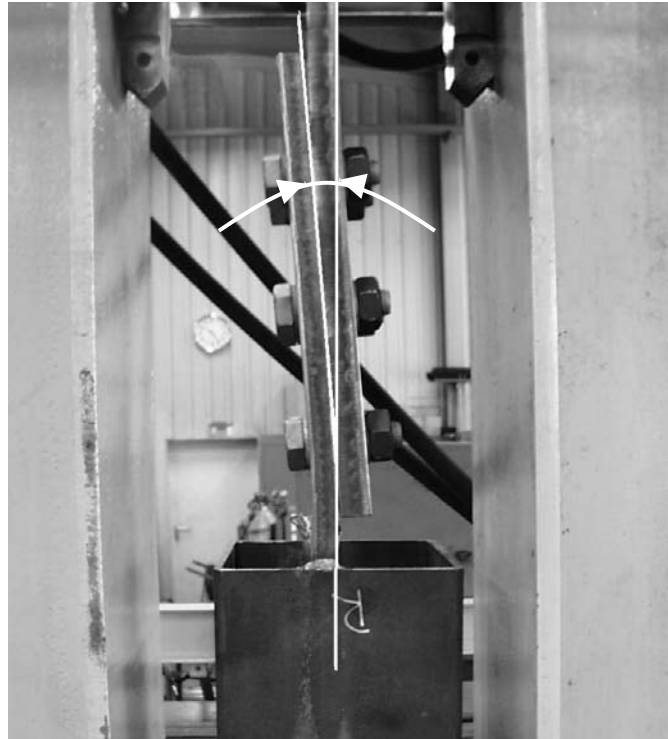


Figure 7.6 Bending in the gusset plate for specimen VK6-3-06 (typical for all specimens)

7.5.1 Results of Strain Gauge Measurements

Figure 7.7 shows the measured strains on the hollow section at a particular cross section during the test for specimen VK6-3-04. The strains are measured along the axis of the hollow section (loading direction). The maximum strain that can be measured by this type of strain gauge is about 5000 to 6000 $\mu\text{m}/\text{m}$ (= 5 to 6 %). As expected, the strain readings of strain gauge 1 (strain gauge at the centre line) are much higher compared to strain readings of strain gauges 2 and 3. The strains at the corner closer to the eccentrically placed gusset plate (strain gauge 2) are also slightly higher than the strains at the corner further away from it (strain gauge 3). Despite the rather high strain readings from the strain gauges of the hollow section, no visible plastic deformation could be reported in the hollow sections after failure of the connection.

Figure 7.8 compares the principal strains and the principal angle for strain gauge 1 (hollow section, centre position) of specimen VK6-3-04. The principal strain angle stays constant at about 6° during the test. The angle between loading direction and principal strain direction is caused by the slight eccentricity of the gusset plate in the single shear connection.

Figure 7.9 compares the strain readings of strain gauge 1 (strain gauge at the centre line) in the longitudinal axis direction for specimens VK6-3-04 and VK6-3-06. The specimens only

vary with regard to the length of the gusset plate inside the hollow section, such that strain gauge 1 for VK6-3-06 is deeper inside the RHS than for VK6-3-04. However, the strain gauge readings for both specimens are still about the same.

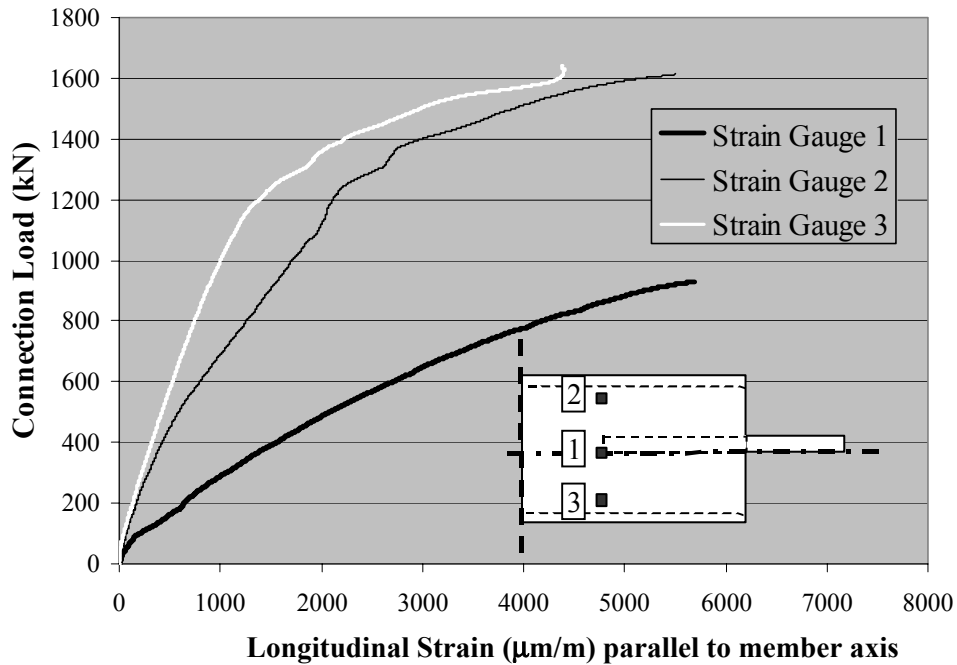


Figure 7.7 Hollow section strain gauge readings (VK6-3-04)

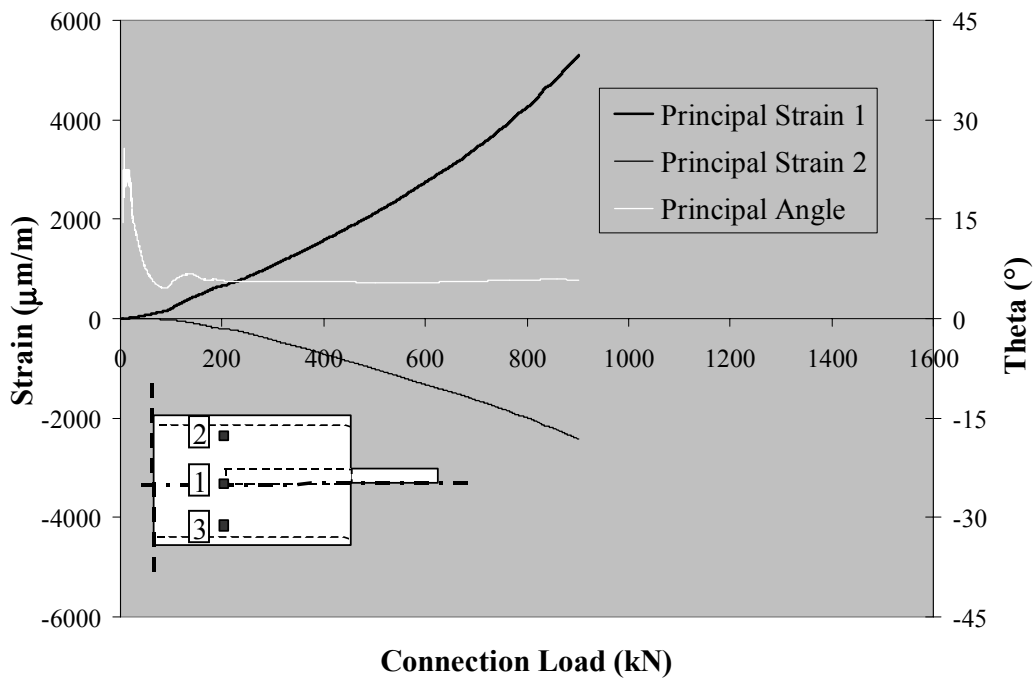


Figure 7.8 Principal strains and principal angle of strain gauge 1 (VK6-3-04)

Figure 7.10 compares the gusset plate strains for specimen VK6-2-04 which failed by shear lag fracture of the plate. The strain readings of the strain gauges on the gusset plate show increasing strains closer to the hollow section (strain gauge 9).

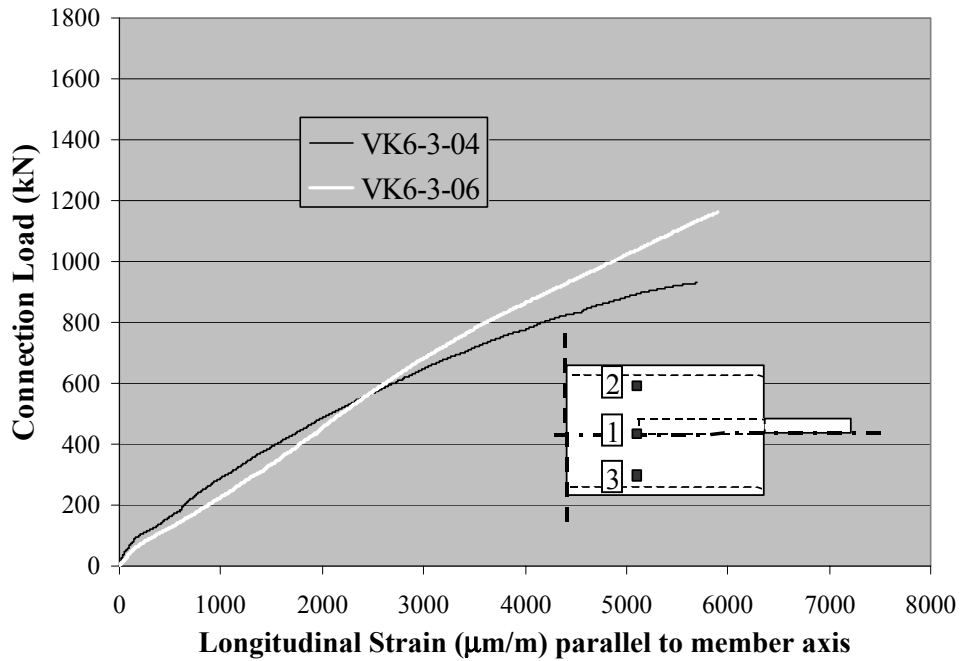


Figure 7.9 Comparison of strain results of strain gauge 1 on hollow section for specimens with varying lengths " L_w "

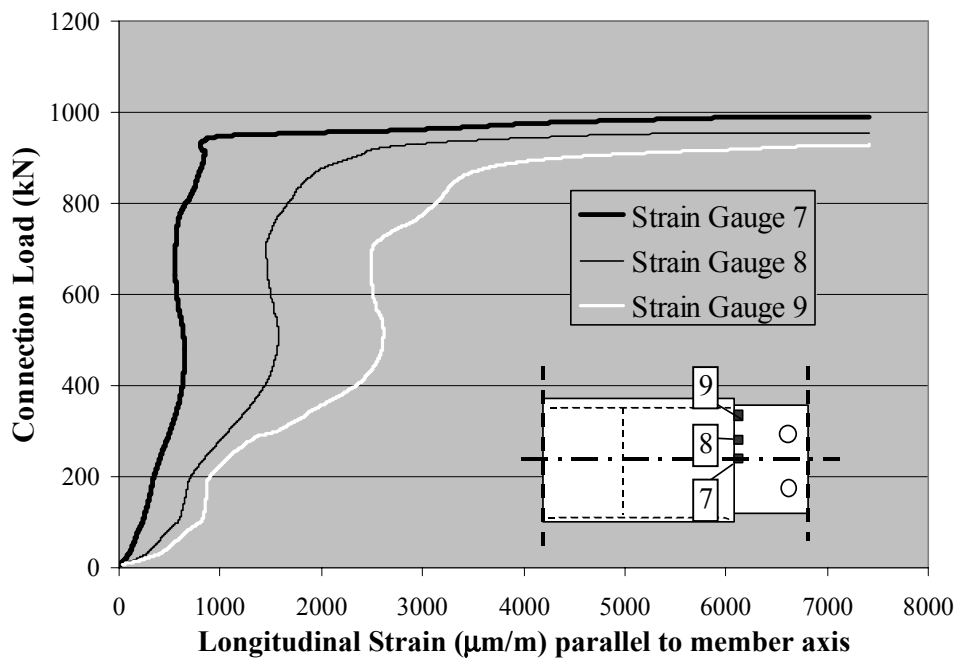


Figure 7.10 Gusset plate strain gauge readings (VK6-2-04)

7.6 General Observations from the Testing Program

The experimental study on six hidden joint connections indicates that shear lag in the hollow section is not critical for such hidden joint connections, within the parameter range of these six experiments. Due to the restricted width of the gusset plates, failure is prone to occur in this component of the connection for all practical cases. The bolt holes decrease the net section of the gusset plates even more. Due to the eccentric placement of the gusset plates along the axis of the connection, bending of the gusset plates was apparent during the test. The use of thicker gusset plates is restricted, as thicker gusset plates which would allow shear failure in the rectangular hollow section decrease the operating room for the welder. Embrittlement and cold cracking provisions require a minimum throat thickness of the fillet weld, e.g. $a \geq \sqrt{\max t} - 0.5 \text{ mm}$ as given in the German steel code DIN 18800-1 [1990]. On the other hand, throat thickness is restricted by the minimum thickness of each component, $a \leq 0.7 \cdot \min t$ [DIN 18800-1 1990] to exclude warping and minimise residual stresses.

The bolt size is a further concern in the design of this connection type. Assuming two bolts across the plate width, the maximum bolt hole size can be calculated from the minimum edge distances, $1.2 d'$, and the bolt spacing, $3 d'$, as given in Eurocode 3 [1992]. The maximum possible size "d" of the bolt holes is therefore $\frac{1}{5.4}$ times the width of the gusset plate.

The results of the experimental test program indicate that shear lag in the hollow section is not likely not to be critical, for all practical cases, provided that the hollow section material is of the same grade, or higher than, the gusset plate material. Net section failure of the gusset plate along the line of bolts is the dominant failure mode. The length of the gusset plate inside the hollow section, length " L_w ", only had a minor influence on the strains recorded by the strain gauges on the hollow section.

8 *VALIDATION OF NUMERICAL MODELS*

A general introduction to numerical studies can be found in Section 3.1. In accordance with the earlier numerical study on bolted flange-plate connections the complete pre- and post-processing as well as the analysis of all finite element models has been carried out using the finite element package ANSYS 5.6 [Swanson Analysis System Inc. 1999].

8.1 *General Consideration*

The following general considerations are made regarding the finite element models for the hidden joint connections, with respect to:

1. Element types;
2. Geometrical and material non-linearities;
3. Solution techniques used for the numerical analysis;
4. Boundary conditions;
5. Element discretisation.

8.1.1 *Element Type used in the Study*

Element type solid45, an 8-noded 3D structural solid element with 3 degrees of freedom per node, has been used for all components of the connection. This linear solid element includes plasticity, large stress and strain capabilities, and stress stiffening. Reduced integration with hourglass control has been applied as the use of full integration is not recommended for linear solid elements [Puthli and van der Vegte 2002].

To verify and establish the choice of this element type, three finite element models of specimen VK12-2-04 have been done. All components in the first model have been modelled using 8-noded, linear solids. The hollow section in the second model was meshed with 20-noded solids while the remaining components used linear solids. Quadratic solid elements (20-noded brick element, solid95) could not be used for all components of the connection, as the number of nodes would have exceeded the maximum number of nodes in the ANSYS version used. The last model consisted of shell elements. Figure 8.1 shows the Load-Displacement curves for all three FE-models of specimen VK12-2-04. The difference between the three models is only marginal. Table 8.1 compares the CPU time of the three models. The FE-model using both linear and quadratic solids requires about five times more time than the models only with linear solids or shell elements. Finally, 8-noded solid elements have been chosen for the

finite element study as the welds can be discretized more accurately with solid than with shell elements.

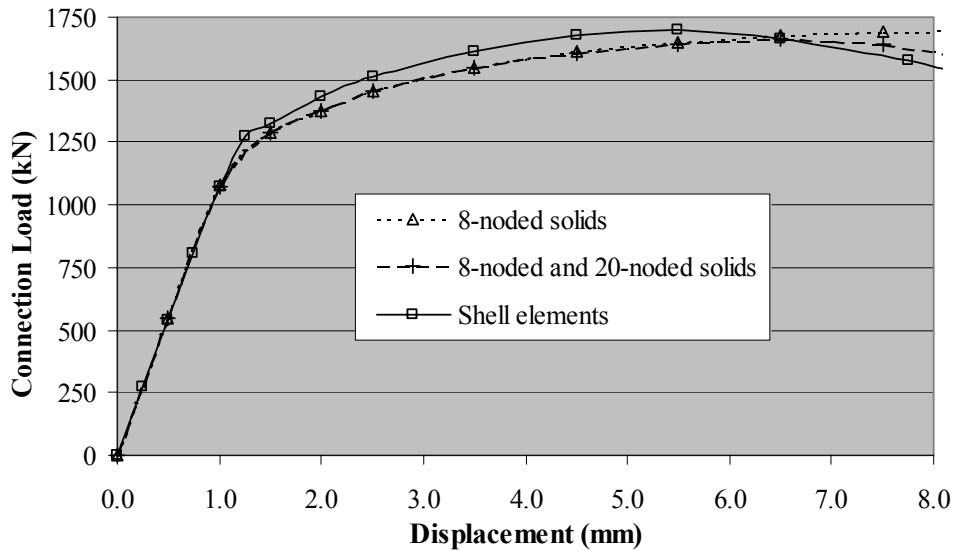


Figure 8.1 Load-Displacement curve of specimen VK12-2-04

Table 8.1 CPU Time for the different models of specimen VK12-2-04

FE-Model	CPU-time (min.)	# of nodes	# of elements
8-noded solids	31.1	9858	7074
8-noded and 20-noded solids	179.2	19389	7074
Shell elements	25.0	2768	2675

8.1.2 Geometrical and Material Non-Linearities

The element type (solid45) used allows "large strains". Strains are referred to as "large" if they are no longer infinitesimal (they are finite). Shape changes (e.g., area, thickness, etc.) are then taken into account. Deflections and rotations can therefore be arbitrarily large.

The material properties were input as a multi-linear curve with the engineering stress and strain converted into the true stress and strain values (see Figure 8.2). A closer description of the relationship between true and engineering stress and strain can be found in chapter 3.3.2. To check the material input, tensile coupons were modelled with finite elements and the Load-Displacement curves of the FE-models compared to the data from the tensile coupon tests of the specimen material (see Figure 8.3). With these tensile coupon FE models the maximum equivalent plastic strain for rupture of the material was also determined. Elements which exceed this equivalent plastic strain limit are assumed to have cracked. If any integration point

in an element during the analysis of the hidden joint connections reaches the equivalent plastic strain, the stiffness of this element is drastically reduced in the following load steps to simulate the "loss" of this element.

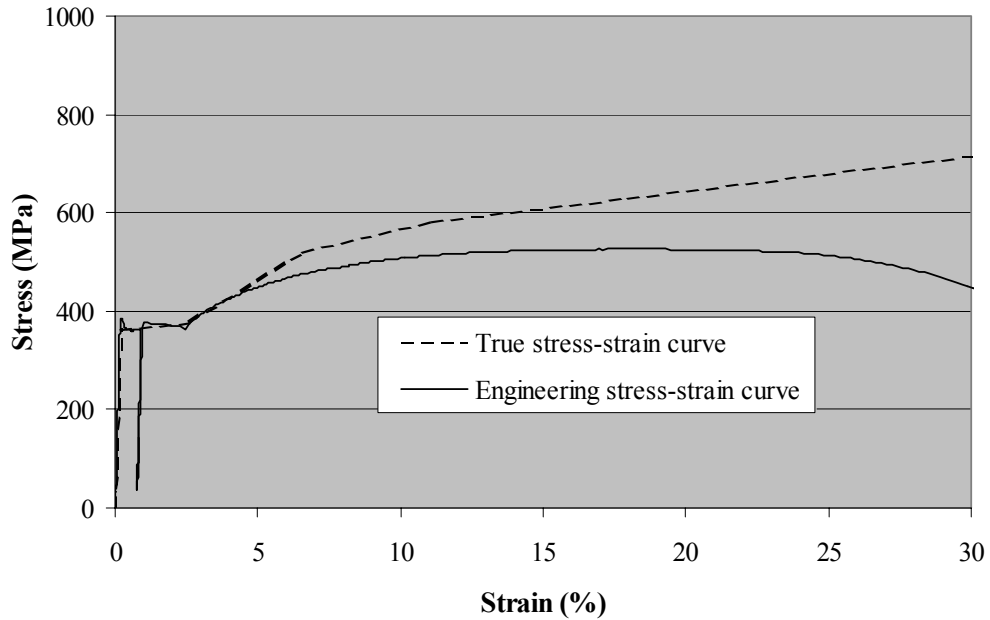


Figure 8.2 Engineering and true stress-strain curves

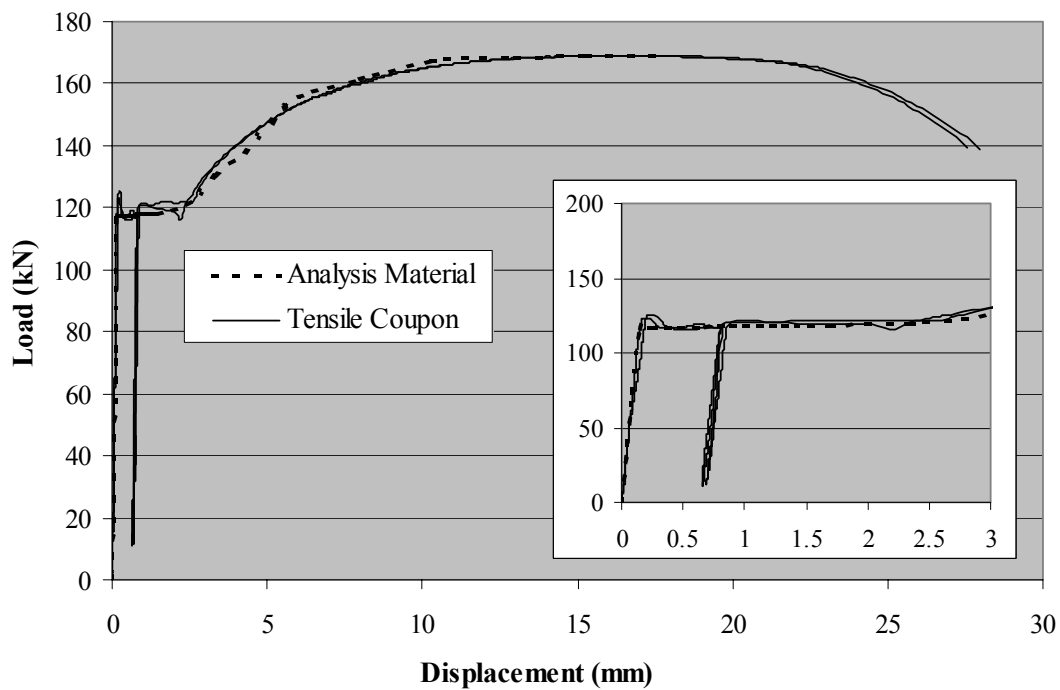


Figure 8.3 Load-Displacement graph of tensile coupon

8.1.3 Solution Techniques used in the Study

The solver in the study is a frontal direct equation solver. The solution has been carried out in multiple load steps. The load is applied by displacement (see following Chapter) of the nodes at the end of the hollow section away from the vicinity of the connection. In the elastic region of the test, the increase in load is very large for small changes in displacement. On the other hand, a smaller increase or decrease in load takes place once plasticity occurs, due to loss of stiffness. To account for this behaviour the displacement increments are chosen to be very small for the first few load steps and to increase in the plastic regions. After each load step, the solver has been exited and specific results (load, displacement, strains at strain gauge locations) have been written to a list file. In addition, the equivalent plastic strain was determined for each element of the connection and compared to the strain limit. The stiffness of each element that exceeded the strain limit was reduced drastically to simulate a crack in the element (see preceding Chapter). The analysis was then restarted using the restart option which employs the deformed model for further analysis.

8.1.4 Discretization and Boundary Conditions

Due to the eccentricity of the gusset plate, the connection possesses only a single plane of symmetry. Therefore, only half of the specimen has been modelled (see Figure 8.4). As failure of the bolts was not of interest in the study, the bolts were not discretised and the finite element model ended at the first line of bolts. The welds were fully modelled. Figure 8.5 shows the gap between the gusset plate and the hollow section, assuming that the fillet welds have no penetration into the gusset plate. The gap was modelled to prohibit any direct stress transfer between the gusset plate and the hollow section.

Exact measurements of the wall thickness of the hollow sections in the experimental study were made in the corners as well as in the flat areas. It was found that the thickness varied up to 17% between the thicker corners and the flat part of the hot-formed hollow section. These changes in thickness have been incorporated into the calibration model of the hollow section.

The boundary conditions are shown in Figure 8.6. Symmetry boundary conditions have been employed along the plane of symmetry (translations of the solid elements at the planes of symmetry of the plate and the hollow section are fixed normal to the plane of symmetry) and the nodes at the gusset plate end are also fixed. The specimens were loaded by displacing the nodes at the end of the hollow section.

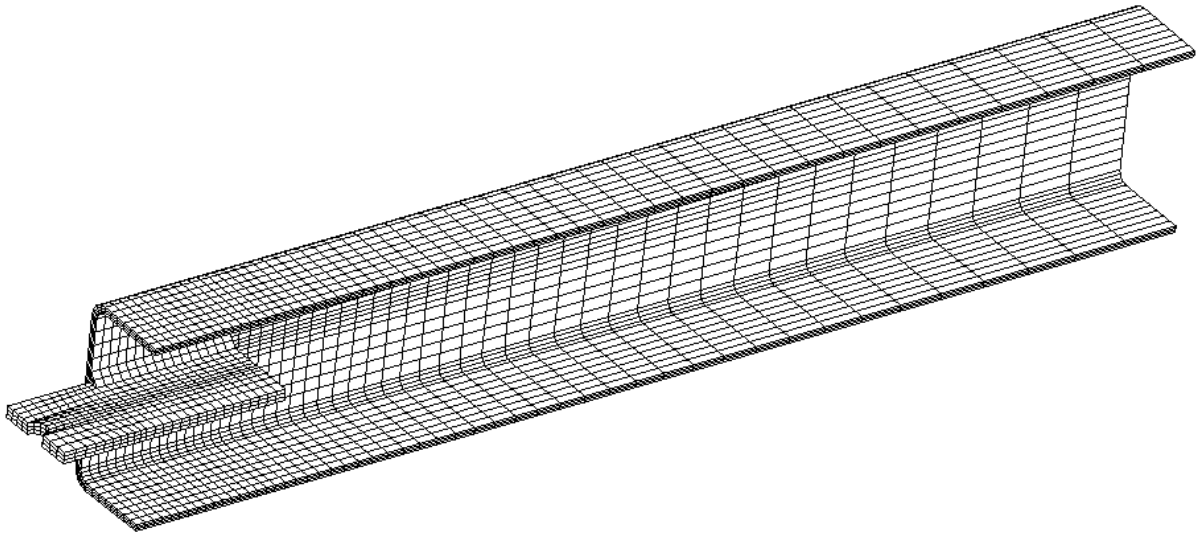


Figure 8.4 FE-Model of specimen VK6-2-04

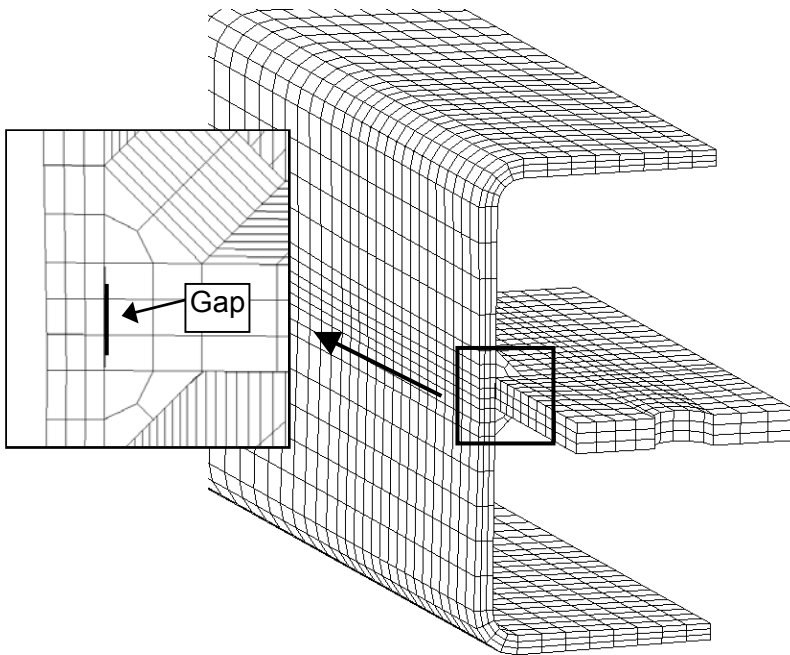


Figure 8.5 Gap between hollow section and plate

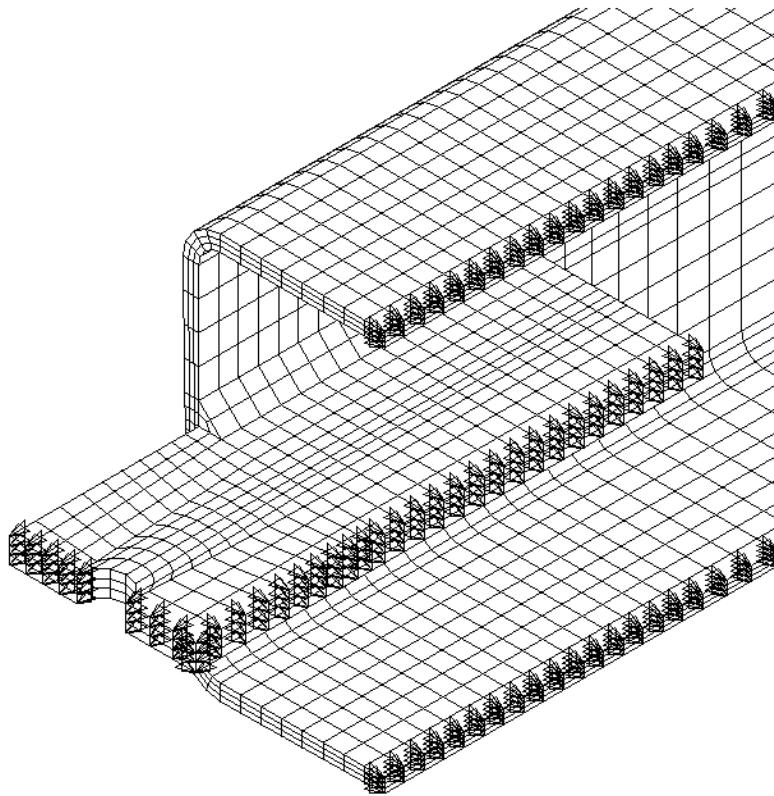


Figure 8.6 Boundary conditions

8.2 Validation of the Numerical Models with the Experimental Results

Table 8.2 shows the comparison of maximum loads for the six tested specimens. Generally, the finite element models have slightly lower capacity than the tested specimens (mean of 0.96). Failure occurs at the first line of bolts in the gusset plate. In the FE-model this location is restricted by its boundary conditions. This can cause slight errors. In addition, any load which has been transferred by friction between the gusset plates in the test is not accounted for in the numerical model. A full representation of the gusset plate and bolts (including contact and friction) would have meant excessive costs in analysis time. As the main area of investigation of the numerical research lay in the study of the hollow section, the error in these components was neglected.

Figure 8.7 compares the strain gauge readings (strains parallel to member axis, in loading direction) on the hollow section of connection VK6-3-04 in the test and the numerical study for two load stages. Specimen VK6-3-04 has the biggest plate to hollow section wall thickness ratio, t_p/t_f -ratio of 3, and the smallest weld length, $L_w = 160$ mm, thus having the highest longitudinal strains in the hollow section of all specimens. The result for the central

strain gauge ($\Delta_y = 0$) at 1072 kN has been linearly extrapolated to about 7800 $\mu\text{m}/\text{m}$, from earlier load stages as the readings of the strain gauges stopped at about 6500 $\mu\text{m}/\text{m}$. The comparison for the strain of the gusset plate is shown in Figure 8.8. Therefore, good agreement is observed between the results of the numerical and experimental study can be found for the hollow section and reasonable agreement for the gusset plate at higher loads. The less favourable results for the gusset plate are probably caused by the vicinity of the gusset plate end in the FE-model (see Figure 8.6).

Table 8.2 Comparison between test and numerical results

Specimen	t_i (mm)	t_p (mm)	\bar{x}/L_W (mm)	Test N_{ux} (kN)	FE-Model N_{uFE} (kN)	N_{uFE}/N_{ux}
VK6-2-04	6.4	12.5	0.40	1003	980	0.98
VK6-2-06			0.60	990	981	0.99
VK6-3-04		20.0	0.40	1646	1571	0.95
VK6-3-06			0.60	1632	1585	0.97
VK12-2-04	12.4	24.7	0.40	1808	1706	0.94
VK12-2-06			0.60	1828	1708	0.93
Mean						0.96
Coefficient of variation (%)						2.25

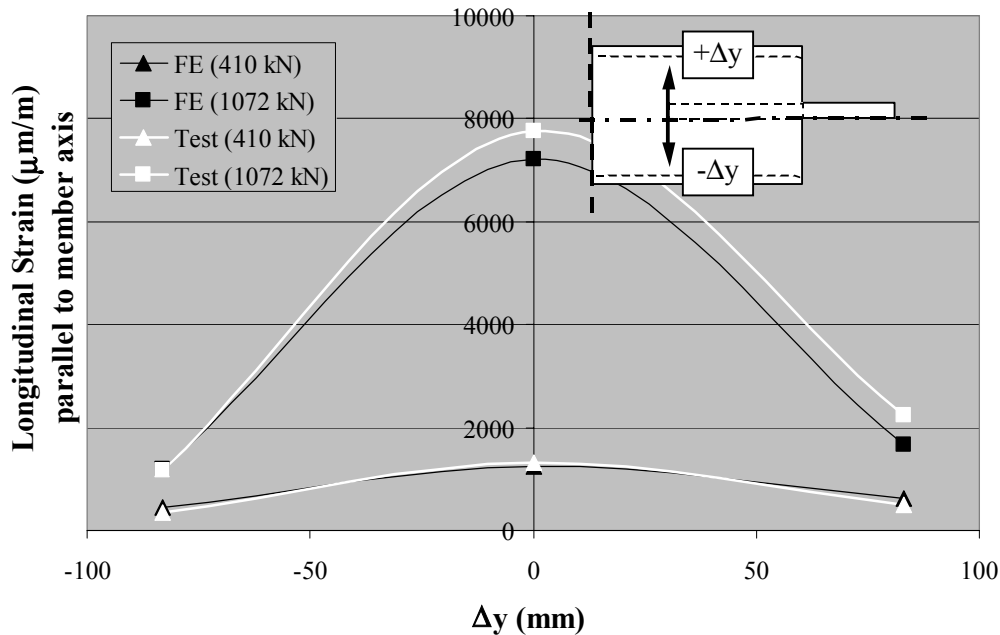


Figure 8.7 Strain distribution on hollow section side wall, specimen VK6-3-04

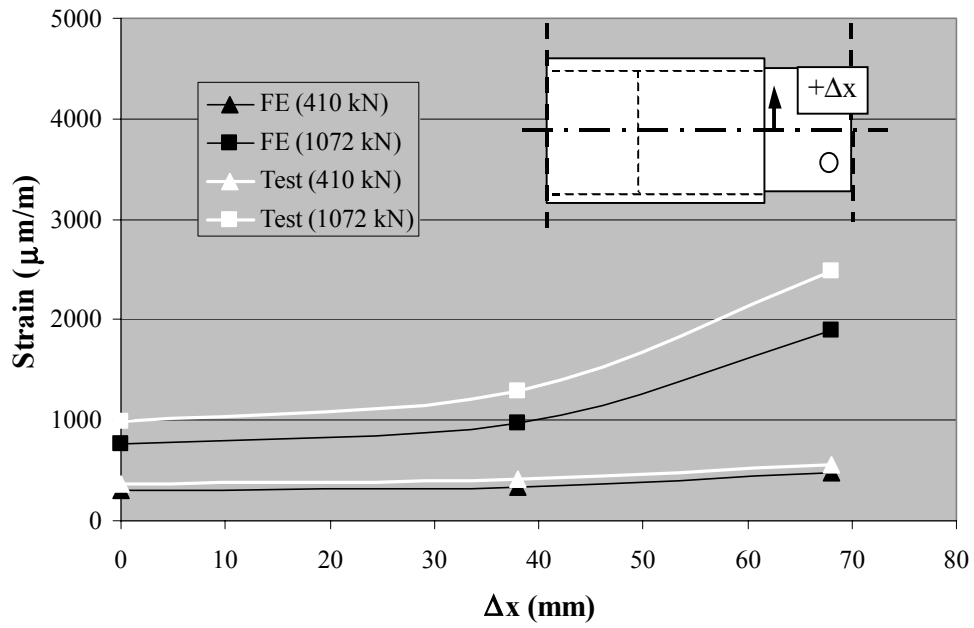


Figure 8.8 Strain distribution on gusset plate at hollow section end, specimen VK6-3-04

9 *NUMERICAL STUDY*

9.1 Numerical Model

The numerical model that has been verified by the results of the experimental study can be summarized as follows:

- 8-noded solid elements were used for all parts of the connection.
- Symmetry of the connection was taken into account by modelling only a half of the connection and applying suitable boundary conditions. Displacement controlled loading conditions were simulated by applying axial displacements to the nodes of the hollow section end.
- Bolts were not discretized and the finite element model ended at the first line of bolts.
- Nominal dimensions of the members were used for the parameter study. The square hollow sections are hot rolled 200 x 6.5 mm and the rectangular hollow sections are either 300 x 200 x 6.5 mm or 400 x 200 x 6.5 mm hollow sections all with an outside corner radius of 10 mm [EN10210-2 1997] (see Table 10.1 in Chapter 10.2). The gusset plate thickness $t_p = 20$ mm relates to about three times the hollow section thickness. The gusset plate width of 187 mm is determined by the width and thickness of the hollow section.
- The hollow section steel grade was S235 with a yield strength of 235 MPa and an ultimate strength of 340 MPa [EN 10210-1 1994]. The steel grade of the gusset plate and welds was chosen to be S355 with a yield strength of 355 MPa and an ultimate strength of 490 MPa [EN 10025 1990]. To exclude any failure in the gusset plate or welds, the plate and weld strength was increased ($f_y = 600$ MPa, $f_u = 800$ MPa) for some models.

To relate the capacity of the hidden joint connection with the capacity of the steel tension member, one square and two rectangular control tubes were modelled and calculated. The control tubes have the same dimensions and are meshed in the same way as the hollow sections in the parametric study except that there is no plate or welding present. Figure 9.1 shows the Load-Displacement graph of the square control tube. The cross sectional area of the square control tube ($t_i = 6.5$ mm) is $A_i = 4872$ mm² resulting in a calculated yield strength of 1145 kN and a tensile strength of 1656 kN.

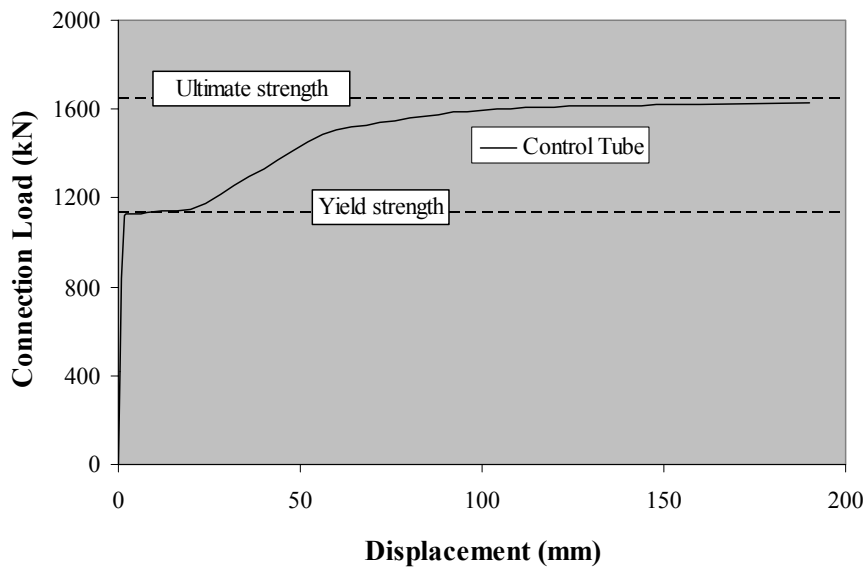


Figure 9.1 Load-Displacement graph of square control tube

9.2 Scope of Numerical Study

The design models in the current codes address shear lag by calculating efficiency factors based on either the ratio of connecting length " L_w " to " w ", the distance between the welds measured around the hollow section perimeter (Clause 12.3.3 in CAN/CSA-S16.1-94 [1994]), or based on the ratio of connecting length " L_w " to eccentricity " \bar{x} ", the vertical distance between the welds and the centre of gravity of the connected part (Clause B3-2 in the American LRFD specification for structural steel buildings [AISC 1999]). Figure 9.2 shows the respective dimensions.

To study the ratio of " L_w " to " w " and the ratio of " L_w " to " \bar{x} ", nine hidden joint connections for square hollow sections ($w_i/h_i = 1.00$) and another 10 connections for rectangular hollow sections ($w_i/h_i = 0.50$ and 0.67) have been modelled. In contrast to the experimental study, it was possible to study connection lengths " L_w " greater than 1.2 times the height of the hollow section. Due to the slight eccentricity of the gusset plate, the length " w " as well as the eccentricity " \bar{x} " differ between the top and bottom side of the hollow section. Choosing the more critical side for the further study, " w " and " \bar{x} " can be calculated as $w = h_i + w_i$ and

$$\bar{x} = \frac{h_i^2 + 2w_i h_i}{4(w_i + h_i)}, \text{ respectively.}$$

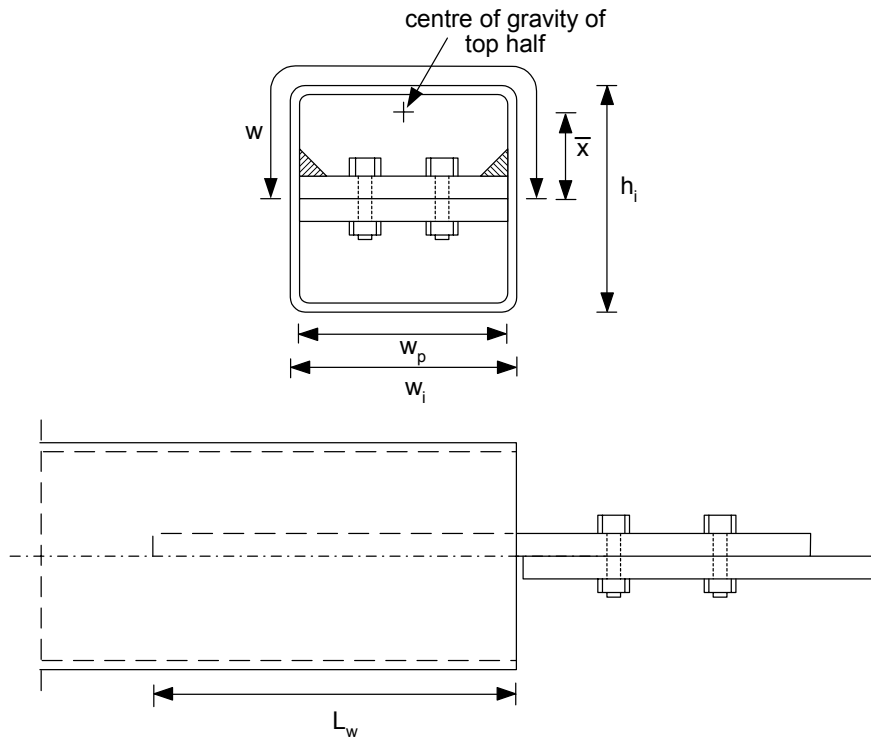


Figure 9.2 Critical dimensions for shear lag of the hollow section

The scope of the numerical study was thus:

- L_w/w -ratio of 0.40 to 1.20;
- \bar{x}/L_w -ratio of 0.10 to 0.47;
- w_i/h_i -ratio of 0.50, 0.67 and 1.00.

9.3 Numerical Results and Observations

9.3.1 Square Hidden Joint Connections

Table 9.1 shows the results of the numerical study on square hidden joint connections. The ratio of connection strength to ultimate strength of the hollow section varies between 63% and 96%. Generally, an increase in connection length " L_w " results in an increase in connection strength. For connections with high L_w/w -ratios ($L_w/w \geq 1.0$) only marginal differences exist between the strength of the hidden joint connection and the ultimate strength of the pure tension member (control tube).

Table 9.1 Results of square connections ($w_i/h_i = 1.00$)

Connection	Properties							Parameters			Results		
	w_i (mm)	h_i (mm)	L_w (mm)	w (mm)	\bar{x} (mm)	N_{yi} (kN)	N_{ui} (kN)	$\frac{w_i}{h_i}$	$\frac{L_w}{w}$	\bar{x} L_w	N_{uFE} (kN)	$\frac{N_{uFE}}{N_{yi}}$	$\frac{N_{uFE}}{N_{ui}}$
P6_3_04	200	200	160	400	75.0	1144	1656	1.00	0.40	0.47	1049	0.92	0.63
P6_3_05			200						0.50	0.38	1243	1.09	0.75
P6_3_06			240						0.60	0.31	1397	1.22	0.84
P6_3_07			280						0.70	0.27	1513	1.32	0.91
P6_3_08			320						0.80	0.23	1559	1.36	0.94
P6_3_09			360						0.90	0.21	1575	1.38	0.95
P6_3_10			400						1.00	0.19	1587	1.39	0.96
P6_3_11			440						1.10	0.17	1590	1.39	0.96
P6_3_12			480						1.20	0.16	1590	1.39	0.96

The load-deformation behaviour of the hidden joint connections depends on the connection length (see Figure 9.3). Hidden joint connections with a low L_w/w -ratio have less deformation capacity. The connections with L_w/w -ratios smaller than or equal to 0.67 fail suddenly by block shear tear-out. The connections failing by shear lag all reach the yield plateau of the hollow section in contrast to the connections failing by block shear tear-out. The connections with L_w/w -ratios greater than or equal to 1.0 show a load-deformation behaviour very similar to that of the hollow section (control tube). However, all connections possess the same initial stiffness.

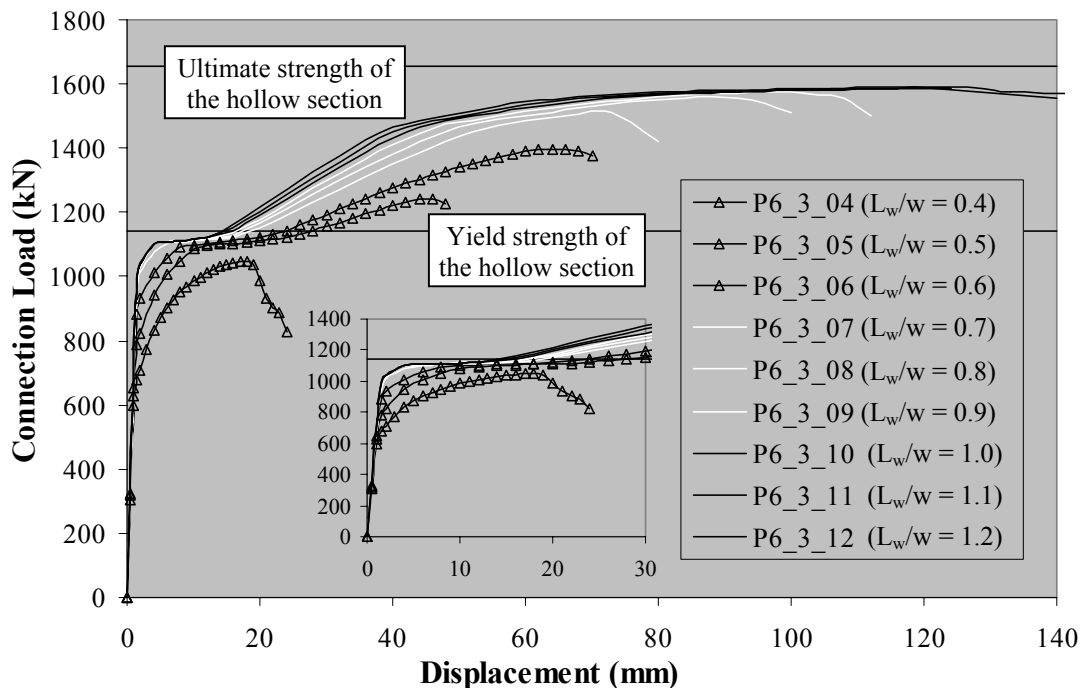
**Figure 9.3 Load-Displacement Graph of square hidden joint connections**

Figure 9.4 shows the influence of L_w/w -ratio on the connection capacity. The white dotted line is a bilinear approximation of the results from the FE-Analyses. In an earlier study on slotted hollow sections by Korol [1996], block shear tear-out of the base metal along the weld governed for L_w/w -ratios smaller than 0.6, which roughly compares to the 0.67 value found in this numerical study (dashed line). For connection lengths greater than 1.2 times the distance between the welds ($L_w/w = 1.2$), influence of shear lag becomes negligible. Figures 9.5 to 9.8 show the equivalent plastic strain distribution of the hollow section at failure load for connections with varying L_w/w -ratios. A full plastification along the welds can be seen for low L_w/w -ratios, $L_w/w = 0.4$ and 0.6 . For $L_w/w = 0.8$, the equivalent plastic strains are concentrated locally around the perimeter at the cross-section where the connection ends, which initiates rupture due to shear lag. The hollow section in the connection with $L_w/w = 1.0$ shows these high strains over the whole length (gross yielding/plastifications). These findings agree with the behaviour of the Load-Displacement curves (see Figure 9.3).

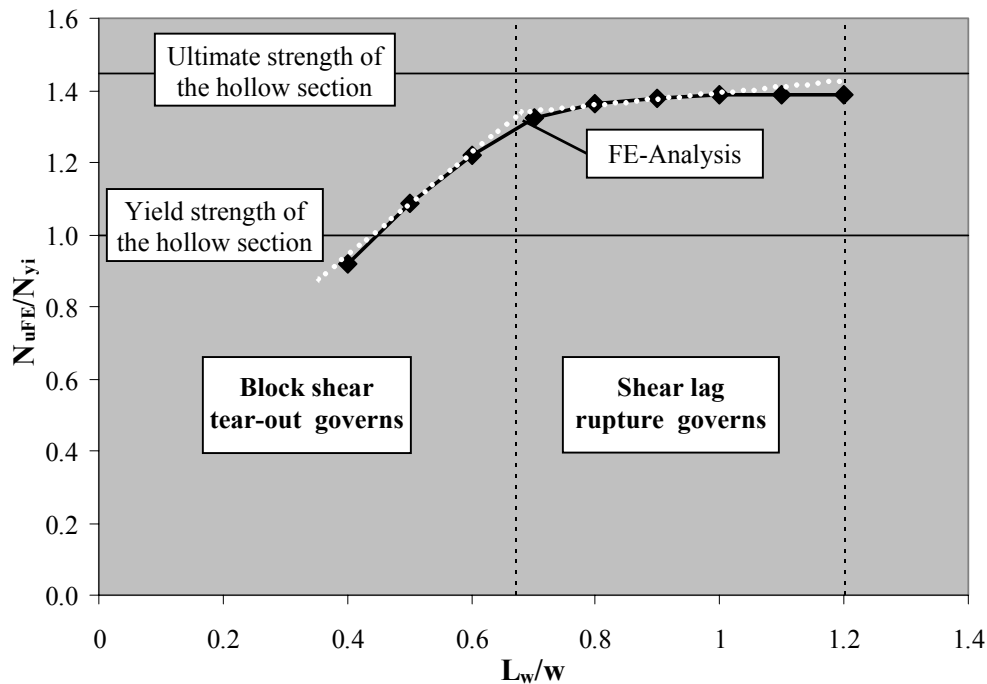


Figure 9.4 Influence of L_w/w -ratio on connection capacity

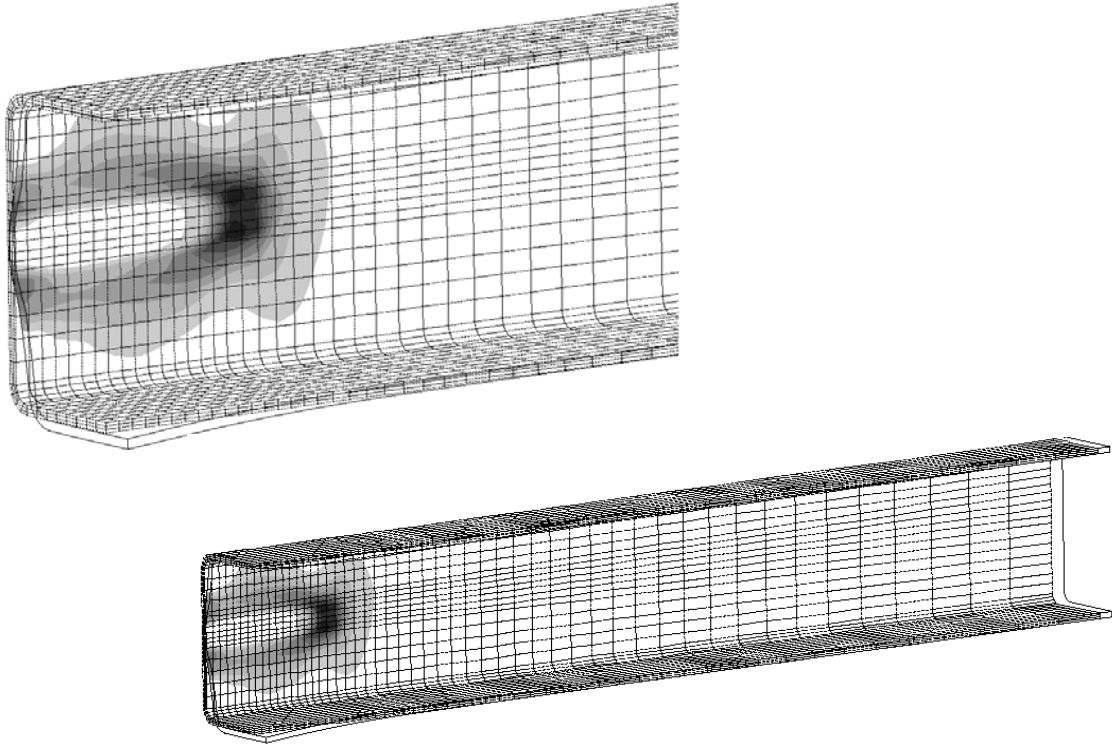


Figure 9.5 Equivalent plastic strains at failure for the connection with $L_w/w = 0.4$

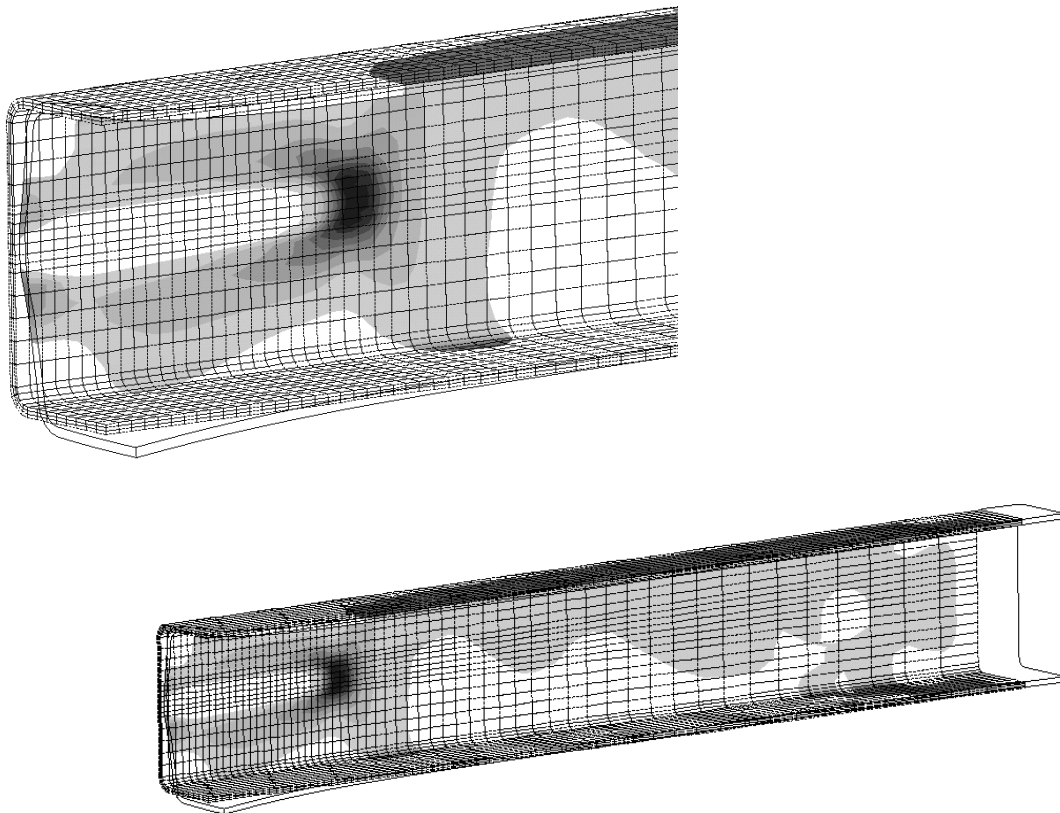


Figure 9.6 Equivalent plastic strains at failure for the connection with $L_w/w = 0.6$

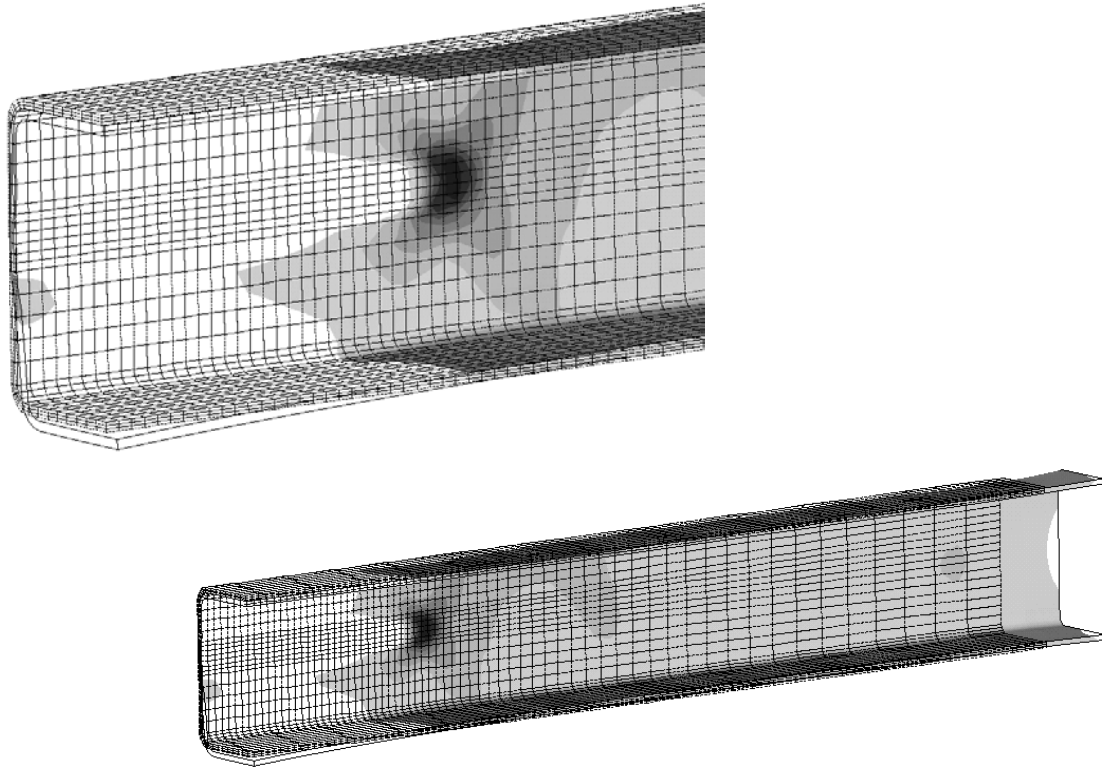


Figure 9.7 Equivalent plastic strains at failure for the connection with $L_w/w = 0.8$

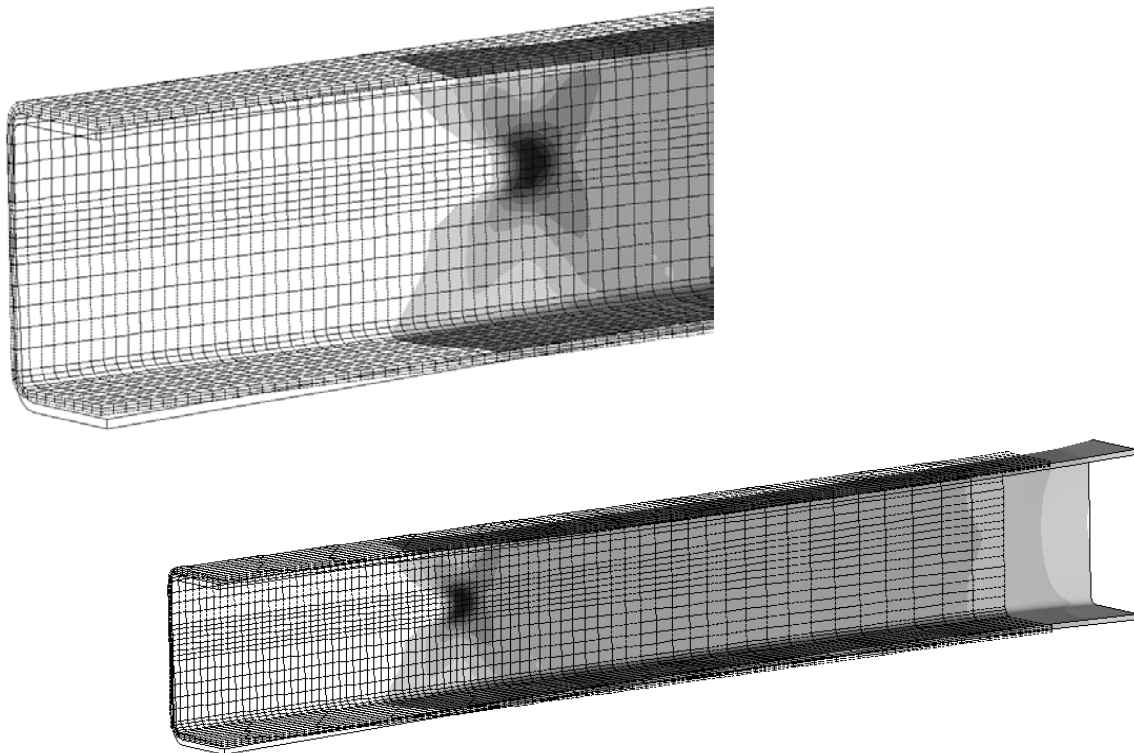


Figure 9.8 Equivalent plastic strains at failure for the connection with $L_w/w = 1.0$

9.3.2 Rectangular Hidden Joint Connections

The results of the rectangular hidden joint connections with a width to height ratio of the hollow section (w_i/h_i -ratio) of 0.67 and 0.50 are shown in Tables 9.2 and 9.3 respectively. As with the results of the square hidden joint connections, the ratio of connection strength to yield or ultimate strength of the hollow section varies considerably (81% to 136% or 56% to 94% respectively). The connection with the lowest strength ratio N_{uFE}/N_{yi} is connection R20_3_04 with a w_i/h_i -ratio of 0.5 and a L_w/w -ratio (connection length to distance between the welds) of 0.4. The highest strength ratio N_{uFE}/N_{yi} is attained by connection R15_3_12 with a w_i/h_i -ratio of 0.67 and a L_w/w -ratio of 1.2.

Table 9.2 Results of rectangular connections with $w_i/h_i = 0.67$

Connection	Properties							Parameters			Results		
	w_i (mm)	h_i (mm)	L_w (mm)	w (mm)	\bar{x} (mm)	N_{yi} (kN)	N_{ui} (kN)	$\frac{w_i}{h_i}$	$\frac{L_w}{w}$	\bar{x} L_w	N_{uFE} (kN)	$\frac{N_{uFE}}{N_{yi}}$	$\frac{N_{uFE}}{N_{ui}}$
R15_3_04	200	300	200	500	80.0	1450	2098	0.67	0.40	0.40	1236	0.85	0.59
R15_3_06			300						0.60	0.27	1636	1.13	0.78
R15_3_08			400						0.80	0.20	1868	1.29	0.89
R15_3_10			500						1.00	0.16	1961	1.35	0.93
R15_3_12			600						1.20	0.13	1979	1.36	0.94

Table 9.3 Results of rectangular connections with $w_i/h_i = 0.50$

Connection	Properties							Parameters			Results		
	w_i (mm)	h_i (mm)	L_w (mm)	w (mm)	\bar{x} (mm)	N_{yi} (kN)	N_{ui} (kN)	$\frac{w_i}{h_i}$	$\frac{L_w}{w}$	\bar{x} L_w	N_{uFE} (kN)	$\frac{N_{uFE}}{N_{yi}}$	$\frac{N_{uFE}}{N_{ui}}$
R20_3_04	200	400	240	600	83.3	1756	2540	0.50	0.40	0.35	1429	0.81	0.56
R20_3_06			360						0.60	0.23	1865	1.06	0.73
R20_3_08			480						0.80	0.17	2173	1.24	0.86
R20_3_10			600						1.00	0.14	2309	1.31	0.91
R20_3_12			720						1.20	0.12	2342	1.33	0.92

The load-displacement curves of the rectangular hidden joint connections (see Figures 9.9 and 9.10) resemble the respective curves for the square hidden joint connections (see Figure 9.3). The initial stiffness of the connections is similar regardless of the connection length " L_w ". Connections failing in block shear tear-out ($L_w/w < 0.67$) do not reach the yield plateau of the hollow section but start to yield early and fail suddenly. The connections failing in shear lag reach the yield plateau of the hollow section but break before reaching the ultimate strength of the hollow section. The connections with an L_w/w -ratio of 1.0 or higher show a deformation behaviour similar to that of the hollow section.

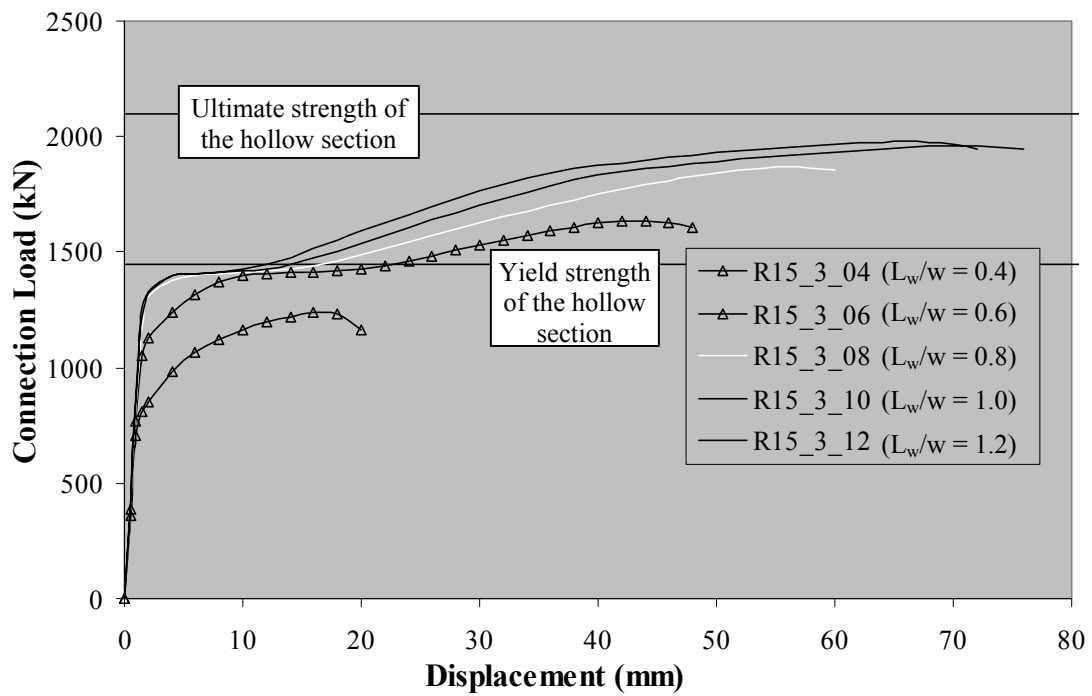


Figure 9.9 Load-Displacement Graph of rectangular hidden joint connections with $w_i/h_i = 0.67$

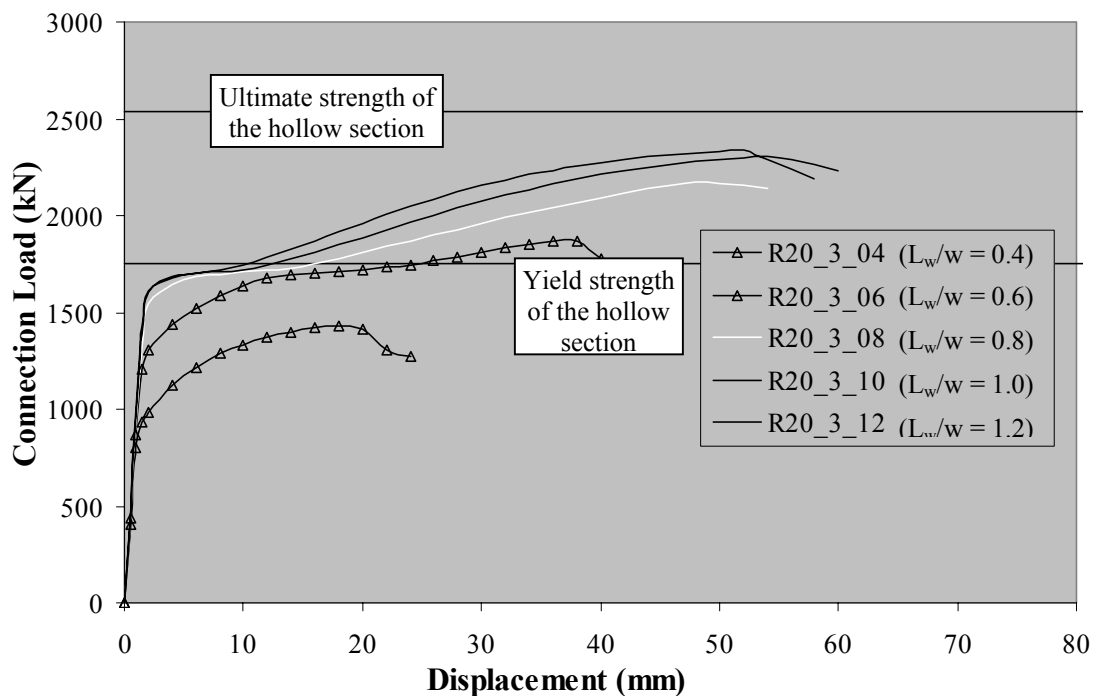


Figure 9.10 Load-Displacement Graph of rectangular hidden joint connections with $w_i/h_i = 0.50$

Figure 9.11 compares the different existing design methods with the results of the numerical analysis. In accord with the comparison between existing experimental results of slotted gusset plate connections and the predictions by different design methods (see Section 6.1.2), Korol [1996] again gives the best predictions. While Korol suggests that shear lag is critical for L_w/w -ratios greater than or equal to 0.6, the results of this numerical study suggest that the lower bound for shear lag is roughly 0.67.

The design method by Packer and Henderson [2002] seems to be overly conservative. Comparing the results of connections with the same L_w/w -ratio but varying w_i/h_i -ratios, the design method provided by AISC [2000] predicts the most favourable results for connections with a lower w_i/h_i -ratio. Generally, all design methods err on the safe side. All design methods have been developed for gusset plate connections with slotted hollow sections. High stresses occur at the end of the slot inside the hollow section and can cause an initiating crack which will lead to an early failure of the connection.

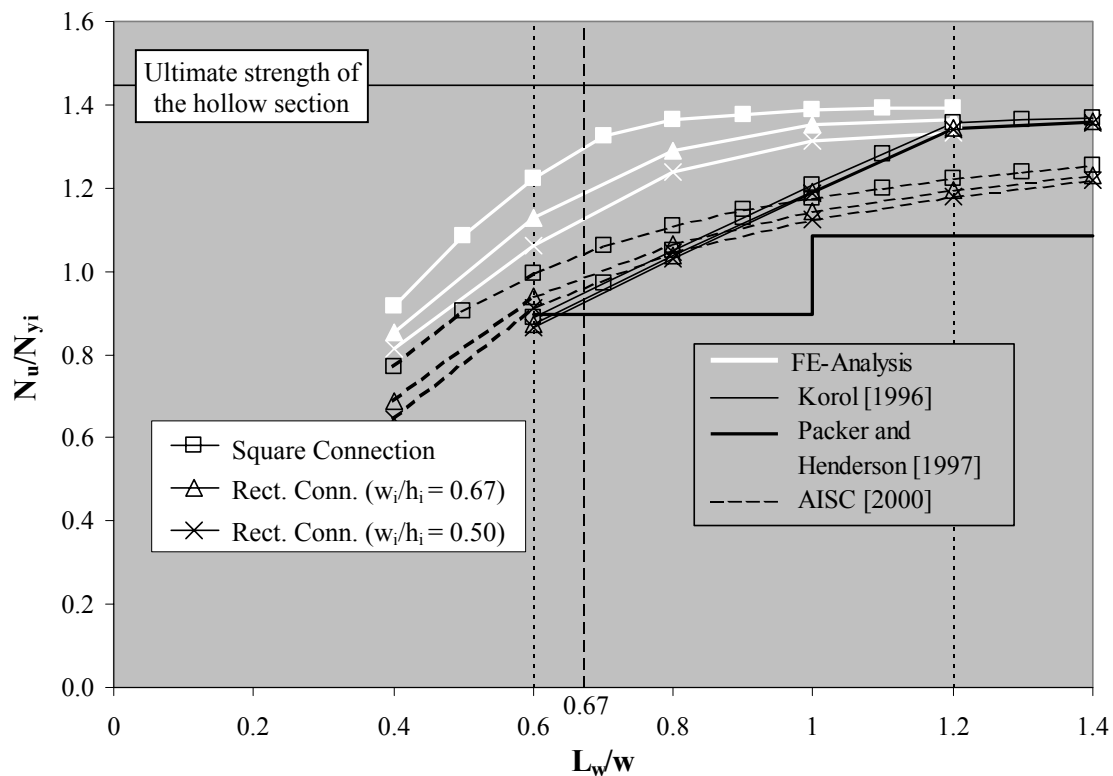


Figure 9.11 Influence of L_w/w -ratio on connection capacity

10 ANALYTICAL STUDY AND SOLUTIONS

10.1 Introduction

Shear lag in hollow sections occurs if the unconnected parts of the hollow section circumference are not fully engaged and contribute only in part to the resistance of the member. Failure in the hollow section is caused by the stress concentrations at the end of the weld between the hollow section and the gusset plate. Figure 10.1 shows the location of these stress concentrations.

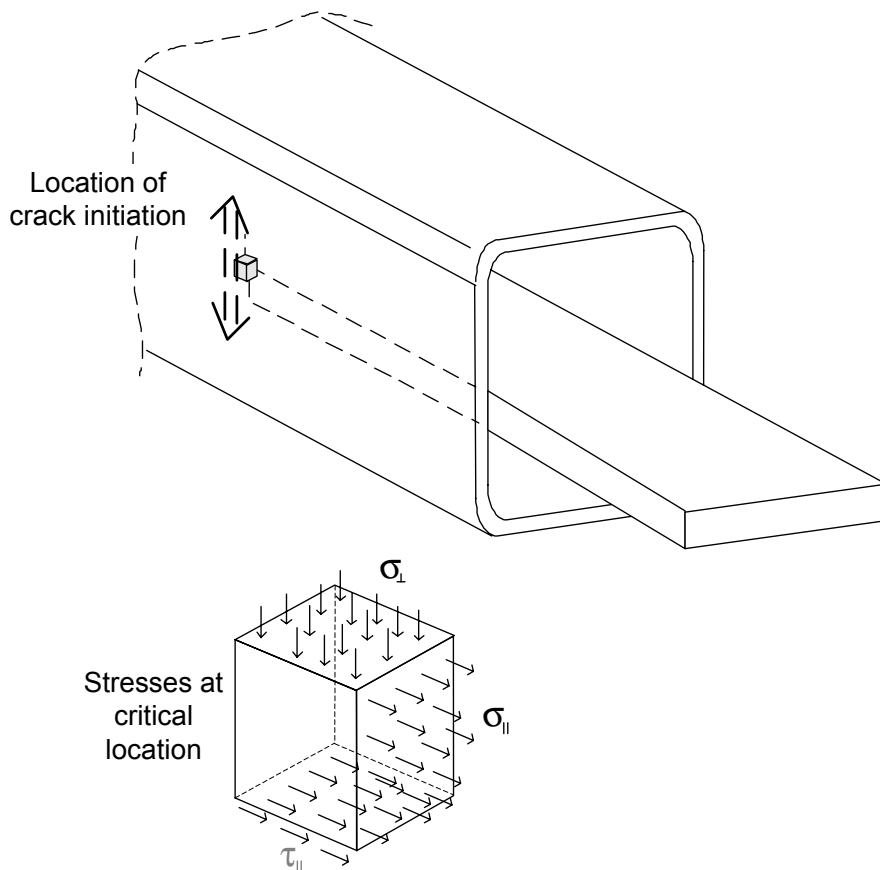


Figure 10.1 Stresses at critical location (crack initiation)

At the critical cross section, two axial and one shear stress can be distinguished in the plane of the hollow section web:

- σ_{\parallel} caused by the tensile loading of the web;
- σ_{\perp} caused by the eccentricity of the load in the flanges;
- τ_{\parallel} caused by the shear stress between hollow section and weld/plate.

Using these stresses an equivalent stress " σ_e " can be calculated as follows:

$$\sigma_e = \sqrt{\sigma_{||}^2 - \sigma_{||}\sigma_{\perp} + \sigma_{\perp}^2 + 3\tau^2} \quad (\text{Equation 10.1}).$$

10.2 Determination of $\sigma_{||}$, σ_{\perp} and τ

A simple idealisation is used for the following formulations. The stresses in the top and bottom chord can be substituted by two forces along the top and bottom of the web (see Figure 10.2). The magnitude of these forces equals the load transferred by the top and bottom flange and can be calculated as follows:

$$N_{\text{flange}} = \frac{N}{2} \cdot \frac{w - 2a}{w} \quad (\text{Equation 10.2}),$$

with

$$a = \frac{h_i}{2} - r_{\text{out}} \quad (\text{Equation 10.3}).$$

The outside corner radii of hollow sections generally depend on the wall thickness as well as the forming process (hot rolled versus cold formed). Table 10.1 shows the outside corner radii used for design according to EN 10210-2 [1997] and EN 10219-2 [1997].

Table 10.1 Outside corner radii of hollow sections according to European Standards

Hollow section wall thickness t_i	Hot-rolled hollow sections [EN10210-2 1997]	Cold-formed hollow sections [EN10219-2 1997]
$t_i \leq 6 \text{ mm}$	$r_{\text{out}} = 1.5 t_i$	$r_{\text{out}} = 2.0 t_i$
$6 \text{ mm} < t_i \leq 10 \text{ mm}$		$r_{\text{out}} = 2.5 t_i$
$t_i > 10 \text{ mm}$		$r_{\text{out}} = 3.0 t_i$

The load transferred in the web is:

$$N_{\text{web}} = \frac{N}{2} \cdot \frac{2a}{w} = N \frac{a}{w} \quad (\text{Equation 10.4}).$$

For simplicity, it is assumed in the analytical model, that N_{flange} acts at the extremities of the web before the tangent of the corner radius.

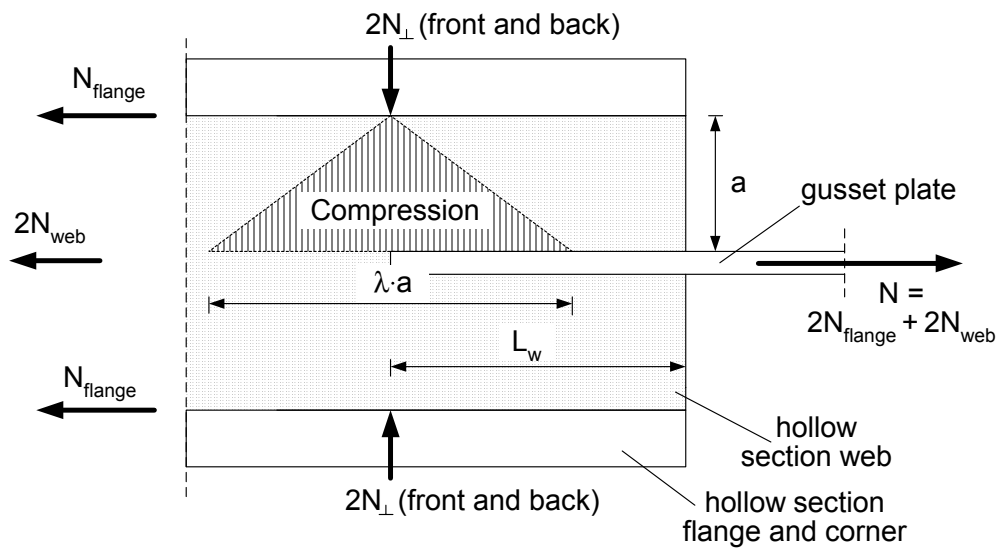


Figure 10.2 Side view of the gusset plate connection

Due to the eccentricity of the load in the top and bottom flange, a moment exists which causes compressive stresses normal to the member loading in the web at the beginning of the connection and tensile stresses at the hollow section opening (see Figure 10.2). Depending on the height of the web, "a", and the length of the connection, "L_w", the compressive force at the beginning of the weld is:

$$N_{\perp} = \frac{N_{\text{flange}}}{2} \cdot \frac{a}{L_w} \quad (\text{Equation 10.5}).$$

The stress at the critical cross section can now be calculated on the basis of the above assumptions. The parallel stress in the critical area of the hollow section is assessed as follows:

$$\sigma_{\parallel} = \frac{N_{\text{web}}}{A_{\text{web}}} = \frac{N}{A_i} \quad (\text{tension}) \quad (\text{Equation 10.6}).$$

The stresses normal to the hollow section axis are caused by the eccentricity of the forces in the flange.

$$\sigma_{\perp} = \frac{N_{\perp}}{t_i \cdot \lambda a} = \frac{N_{\text{flange}} a}{2L_w} \cdot \frac{1}{t_i \lambda a} = \frac{N}{4} \cdot \frac{w - 2a}{w} \cdot \frac{1}{L_w t_i \lambda} \quad (\text{compression}) \quad (\text{Equation 10.7})$$

with $t_i \approx \frac{A_i}{2w}$ Equation 10.7 becomes:

$$\sigma_{\perp} = \frac{N}{A_i} \cdot \frac{1}{2\lambda} \cdot \frac{w - 2a}{L_w} \quad (\text{compression}) \quad (\text{Equation 10.8})$$

The shear plane is assumed to be in the hollow section wall running parallel to the weld. The shear stresses due to the force in the flanges is not supposed to act at the critical location.

Thus, the force causing the shear loads at the critical location equals the load transferred in the web. The shear stresses caused by the load transfer of the force in the web to the gusset plate are estimated as follows:

$$\tau = \frac{N_{web}}{t_i 2L_w} = N \frac{a}{w} \frac{1}{t_i 2L_w} = \frac{N}{A_i} \cdot \frac{a}{L_w} \quad (\text{Equation 10.9})$$

Inserting $\sigma_{||}$, σ_{\perp} and τ into Equation 10.1, the equivalent stress " σ_e " becomes:

$$\begin{aligned} \sigma_e &= \sqrt{\sigma_{||}^2 - \sigma_{||}\sigma_{\perp} + \sigma_{\perp}^2 + 3\tau^2} \\ &= \frac{N}{A_i} \sqrt{1^2 - 1 \cdot \left(-\frac{1}{2\lambda} \frac{w-2a}{L_w}\right) + \left(-\frac{1}{2\lambda} \frac{w-2a}{L_w}\right)^2 + 3\left(\frac{a}{L_w}\right)^2} \\ &= \frac{N}{A_i} \sqrt{1 + \frac{1}{2\lambda} \frac{w-2a}{L_w} + \frac{1}{4\lambda^2} \left(\frac{w-2a}{L_w}\right)^2 + 3\left(\frac{a}{L_w}\right)^2} \end{aligned} \quad (\text{Equation 10.10})$$

If the equivalent stress reaches ultimate stress the connection fails. Setting " σ_e " equal to the ultimate tensile stress of the hollow section material, " f_{ui} ", the ultimate connection load for shear lag of the hollow section can be calculated:

$$N_u = f_{ui} A_i \frac{1}{\sqrt{1 + \frac{1}{2\lambda} \frac{w-2a}{L_w} + \frac{1}{4\lambda^2} \left(\frac{w-2a}{L_w}\right)^2 + 3\left(\frac{a}{L_w}\right)^2}} \quad (\text{Equation 10.11})$$

In accordance with the earlier introduced design provisions for shear lag, the efficiency factor " α " for determining the net section area for shear lag becomes:

$$\alpha = \frac{1}{\sqrt{1 + \frac{1}{2\lambda} \frac{w-2a}{L_w} + \frac{1}{4\lambda^2} \left(\frac{w-2a}{L_w}\right)^2 + 3\left(\frac{a}{L_w}\right)^2}} \quad (\text{Equation 10.12})$$

Based on the results of the numerical results a value of $\lambda = 5$ (equivalent to a slope of 1:2.5, which is commonly used for load dispersion at the plastic state) has given good agreement between the results of the numerical study. Table 10.2 compares the results of the numerical study with the strength predictions of the newly proposed design method. In accordance with the numerical study, the range of validity for the proposed design method is $0.67 < \frac{L_w}{w} < 1.2$.

Applying this formula to the gusset plate connections tested in earlier studies [Swinden Laboratories 1992, Korol et al. 1994], good agreement is also found (see Table 10.2).

Table 10.2 Comparison of calculation methods

Test Series	N_{ux}/N_u	Equation 10.12 using $\lambda = 5$	Korol [1996]	AISC [2000]	Packer and Henderson [1997]
Numerical Study	Mean N_{ux}/N_u (>1 safe)	1.03	1.21	1.15	1.33
	Coeff. of Var. (%)	2.1	15.7	9.1	11.0
	Correlation R^2	0.99	0.91	0.96	0.95
Swinden Laboratories [1992]	Mean N_{ux}/N_u (>1 safe)	1.02	1.14	1.18	1.43
	Coeff. of Var. (%)	7.2	8.1	7.4	12.4
	Correlation R^2	0.98	0.97	0.98	0.95
Korol et al. [1994]	Mean N_{ux}/N_u (>1 safe)	1.04	1.12	1.06	1.53
	Coeff. of Var. (%)	6.4	2.4	7.4	12.2
	Correlation R^2	0.89	0.98	0.91	0.75

Using a value of $\lambda = 5$ and introducing the coefficient " ω " into Equation 10.12 the coefficient for shear lag net section failure becomes:

$$\alpha = \frac{1}{\sqrt{1 + \frac{1}{10}\omega + \frac{1}{100}\omega^2 + 3\left(\frac{a}{L_w}\right)^2}} \quad (\text{Equation 10.13})$$

with:

$$\omega = \frac{w - 2a}{L_w} \quad (\text{Equation 10.14})$$

10.3 Summary

A semi-empirical design method has been developed. The correlation between the connection strengths predicted by the new design formulae and the results of the numerical study is very good. Unfortunately, specific tests on hidden joint connections to verify the new design method do not exist, since the connections tested as part of this study did not fail in shear lag of the hollow section. Applying the new design method to gusset plate connections with slotted hollow sections, reasonable agreement is also obtained between the load prediction and test results. This finding supports the assumption that only a small difference exists between the shear lag behaviour of the hollow section for hidden joint connections and gusset plate connections with slotted hollow sections.

Figure 10.3 shows a flowchart of the suggested new design method for the calculation of shear lag in hidden joint connections.

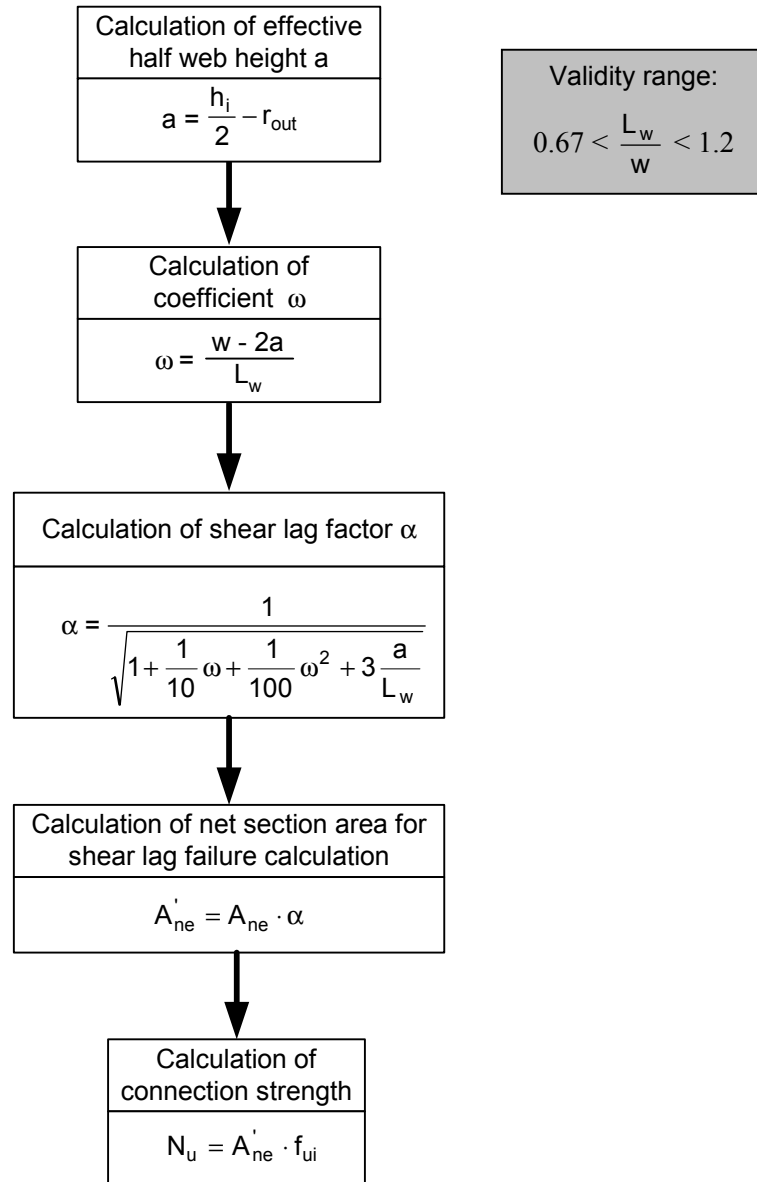


Figure 10.3 Flowchart of the proposed calculation method

CONCLUSIONS AND RECOMMENDATIONS

The presented work covers two types of bolted connections for rectangular hollow sections under tensile loading. The first connection type, the bolted flange-plate connection, has been studied with respect to prying action failure while the second connection type, the hidden joint connection, was studied with respect to shear lag in the hollow section. For each connection type, an experimental, parametric (numerical) and analytical study has been carried out.

Bolted Flange-Plate Connections

Prying forces occur when deforming flange-plates lever against each other. These forces add to the initial bolt forces caused by the member loading on the splice. So far, the unpredictability of the prying forces has been the main obstacle in the use of this connection type.

The experimental study comprised of 20 square and rectangular bolted flange-plate connections with the bolts placed on all four sides of the hollow section. The connections varied in their flange-plate thickness as well as their bolt layout. The experimental study demonstrated that prying can very seriously decrease the capacity of square and rectangular bolted flange-plate connections. Prying ratios (ratio of prying forces to connection loading) of over 30% and 40% for square and rectangular connections respectively occurred during testing, which equals a loss of about 23% and 28% in connection capacity compared to a similar connection not affected by prying. The tests showed that the main geometrical parameter influencing the connection capacity is the flange-plate thickness " t_p ". The bolt layout can be optimised by placing the bolts as close to the hollow section as possible (small value of " b ") as well as keeping the distance between bolts on one side of the connection, distance " c " or bolt pitch, small. For certain bolt layouts (square connections with bolt layout S'8 and rectangular connections, see Table 2.1 in Chapter 2), the even distribution of the connection load on all bolts is not guaranteed. The higher stress in some bolts causes them to rupture before the remaining bolts are fully utilised. After rupture of the initially overstressed bolts, the remaining bolts are not able to compensate for the missing bolts, resulting in the failure of the connection. A further finding of the experimental study was that the fillet weld between hollow section and flange-plate acted as a stiffening element for the flange-plate. The lever arm between the forces in the bolts and the hollow section decreases with an increase in fillet weld size as the yield line along the outer hollow section wall is shifted towards the bolt line. To study the influence of the fillet weld on prying, the numerical study considered flange-plate connections with fillet welds as well as butt welds. In the direct comparison of models with fillet weld and butt weld,

the increase in capacity due to the fillet weld could be quantified; a shift of the inner yield line towards the bolt line of half the weld leg size was established. The numerical study also allowed a closer study of the flange-plate thickness and the parameters describing the bolt layout with respect to their influence on the connection capacity. The findings on each parameter were included into a semi-analytical model which is based on a one-dimensional yield line model. The one-dimensional yield line model is currently used by the design methods for bolted flange-plate connections with bolts on two sides of the hollow section, which can be found in the AISC HSS Connections Manual [1997] for example. The design model is now transferred to connections where the bolts are placed on all four sides. To account for the difference between these connections, certain modifications with respect to the bolt pitch have been made. In addition, the influence of the fillet weld is now also considered in the calculation of the connection capacity. In addition to the one-dimensional yield line model, a two-dimensional yield line model has been developed. Unfortunately, the formulae derived from the two-dimensional yield line model are less descriptive and more complicated. The strength predictions are also less accurate than the results of the one-dimensional yield line model.

Based on these findings for connections with bolts on all four sides of the hollow section, it is reasonable to assume that the fillet weld can also increase the capacity in connections where the bolts are placed on two sides only. Future design formulae for this connection type could consider incorporating the fillet weld size to allow a more efficient design.

Hidden Joint Connections

Shear lag in hollow sections occurs if the unconnected parts of the hollow section circumference are not fully engaged and contribute only in part to the resistance of the member. In gusset plate connections, the gusset plate is welded to the relatively more flexible side walls (web) of the hollow section. If the connection is highly stressed, a crack may eventually initiate in the hollow section web at the beginning of the weld between hollow section and gusset plate. The crack will continue circumferentially around the hollow section resulting in a sudden failure of the section/splice.

In contrast to the more common gusset plate connections where the gusset plate protrudes beyond the width of the slotted member, the gusset plate of the hidden joint connection is fitted into the inside width of the unslotted hollow section. After bolting of the gusset plates, a cover is placed over the part of the gusset plates that extends outside of the hollow section. Only a small test series on hidden joint connections has been carried out.

Unfortunately, the studied failure mode of shear lag in the hollow section could not be obtained. Failure of the tested connections occurred by rupture of the gusset plates. However, the experimental study still gave valuable insights into the fabrication problems, in particular with regard to welding between the hollow section and the gusset plate. All welding has to be done from the open ends of the hollow section and the operating room for the welder is restricted to half of the cross sectional area of the hollow section as the connection is designed to be invisible from the outside. It was found that the maximum weld length possible inside the square hollow section is roughly 1.2 times the height of the section (or the arm length of the welder). Due to the large number of strain gauges applied to the hollow section as well as the gusset plate, the tests could be used to verify a numerical model which was then used for further parametric studies. Based on experience from studies on gusset plate connections with slotted hollow sections, the governing parameters were found to be the ratio of weld length " L_w " to the length between the welds around the circumference of the hollow section " w ", as well as ratio of eccentricity of the top or bottom half of the hollow section " \bar{x} " to the weld length " L_w ". The numerical study consisted of connections with square ($h_i/w_i = 1.00$) and rectangular hollow sections ($h_i/w_i = 1.5$ and 2). The weld length varied between 0.4 and 1.2 times the length between the welds measured circumferentially along the hollow section. It was found that shear lag failure is critical only for connections with $0.67 < L_w/w < 1.2$; for smaller connection/weld lengths, block shear tear-out along the weld will govern, whereas the hollow section will fail by gross cross section ultimate strength in connections with $L_w/w \geq 1.2$ (connection has not failed but the member itself). The analytical study concentrated on the critical location in the hollow section web at the beginning of the weld between the hollow section and the gusset plate. The parallel, normal and shear stresses of the critical location have been assessed and are used to calculate an equivalent stress. Comparing the equivalent stress with the ultimate stress of the hollow section material, the connection capacity for shear lag failure of the hollow section can be calculated. The derived formula compares very well to the results of the numerical study. A comparison with a limited number of gusset plate connections with slotted hollow sections from earlier studies also resulted in reasonable results.

Experimental data on hidden joint connections (especially for rectangular hollow sections) as well as gusset plate connections with slotted hollow sections is still very limited; further research is desirable. Gusset plate connections with slotted hollow sections are generally easier and thus cheaper to fabricate. Also, the range for the parameters is increased, since the connection length " L_w " is not restricted by fabrication limits. Due to the similarity between the two connection types, future studies should therefore concentrate on gusset plate connections with slotted hollow sections.

REFERENCES

- AISC. 1997. Hollow structural sections connections manual. American Institute of Steel Construction, Chicago, U.S.A.
- AISC. 1999. Load and resistance factor design specification for structural steel buildings. American Institute of Steel Construction, Chicago, U.S.A.
- AISC. 2000. Load and resistance factor design specification for steel hollow structural sections. American Institute of Steel Construction, Chicago, U.S.A.
- AISC. 2001. Manual of steel construction – Load and resistance factor design. 3rd ed. American Institute of Steel Construction, Chicago, U.S.A.
- ANSI. 1999. Square and hex bolts and screws inch series. ANSI B18.2.1. American National Standards Institute, New York, U.S.A.
- ASME. 2001. Unified inch screw threads (UN & UNR thread form). ASME B1.1. American Society of Mechanical Engineers, New York, U.S.A.
- ASTM. 1997a. Standard specification for structural bolts, steel, heat treated, 120/105 ksi minimum tensile strength. ASTM A325-97. American Society for Testing and Materials, West Conshohocken, U.S.A.
- ASTM. 1997b. Standard specification for heat-treated steel structural bolts, 150 ksi minimum tensile strength. ASTM A490-97. American Society for Testing and Materials, West Conshohocken, U.S.A.
- Bickford, J.H. 1995. An introduction to the design and behavior of bolted joints. 3rd ed. Marcel Dekker, Inc., New York, U.S.A.
- Birkemoe, P.C. 1989. Installation tension of high strength bolts in connections with out-of-flat plates. Publication, IABSE International Colloquium on Bolted and Special Structural Joints, Moscow, U.S.S.R.
- Birkemoe, P.C., and Packer, J.A. 1986. Ultimate strength design of bolted tubular tension connections. Proceedings, Steel Structures - Recent Research Advances and their Application to Design, Budva, Yugoslavia, pp. 153-168.
- Cao, J.J. and Bell, A.J. 1994. Finite element analysis of circular flange joints under tension forces. Proceedings of the 9th UK ABAQUS User Group Conference, Exeter College, Oxford, U.K.
- Cao, J.J., Packer, J.A. and Du, S. 2000. Finite element modelling of bolted flange connections. Proceedings, 7th International Symposium on Structural Failure and Plasticity, Melbourne, Australia, pp. 473-478.

- Caravaggio, A. 1988. Tests on steel roof joints for Toronto SkyDome. Master of Applied Science thesis, University of Toronto, Canada.
- Cheng, J.J.R., Kulak, G.L., and Khoo, H. 1996. Shear lag effect in slotted tubular tension members. Proceedings, 1st Structural Specialty Conference, Edmonton, Canada, pp. 1103-1114.
- Cheng, J.J.R., Kulak, G.L., and Khoo, H. 1998. Strength of slotted tubular tension members. Canadian Journal of Civil Engineering, Vol.25, pp. 982-991.
- Cheng, J.J.R., and Kulak, G.L. 2000. Gusset plate connection to round HSS tension members. Engineering Journal, American Institute of Steel Construction, 4th Quarter, pp. 133-139.
- Chesson E., Jr., and Munse, W.H. 1963. Riveted and bolted joints: Truss type tensile connections. Journal of the Structural Division, American Society of Civil Engineers, Vol. 89 No.1, pp. 67-106.
- CISC. 2000. Handbook of steel construction. 7th ed. Canadian Institute of Steel Construction, Toronto, Canada.
- CSA. 1992. Structural Quality Steels, CAN/CSA-G40.21-M92. Canadian Standards Association, Toronto, Canada.
- CSA. 1994. Limit States Design of Steel Structures, CAN/CSA-S16.1-94. (superseded) Canadian Standards Association, Toronto, Canada.
- CSA. 2001. Limit States Design of Steel Structures, CAN/CSA-S16-01. Canadian Standards Association, Toronto, Canada.
- DIN 18800. 1990. Stahlbauten; Bemessung und Konstruktion. (DIN 18 800 Structural steelwork; design and construction), Deutsches Institut für Normung, Berlin, Germany.
- DIN 18808 (10.84). 1984. Stahlbauten - Tragwerke aus Hohlprofilen unter vorwiegend ruhender Beanspruchung (DIN 18 808 (10.84) Steel structures – Load bearing structures out of HSS under predominantly static loading) Deutsches Institut für Normung, Berlin, Germany.
- EN 439. 1994. Welding consumables - Shielding gases for arc welding and cutting.
- EN 440. 1994. Welding consumables - Wire electrodes and deposits for gas-shielded metal arc welding of non-alloy and fine grain steels - Classification.
- EN 10025. 1990. Hot rolled products of non-alloy structural steels; technical delivery conditions (includes amendment A1: 1993).
- EN 10027-1. 1992. Designation systems for steels; steel names and principal symbols.

- EN 10210-1. 1994. Hot finished structural hollow sections of non-alloy and fine grain structural steels - Part 1: Technical delivery requirements.
- EN 10210-2. 1997. Hot finished structural hollow sections of non-alloy and fine grain structural steels - Part 2: Tolerances, dimensions and sectional properties.
- EN 10219-1. 1997. Cold formed welded structural hollow sections of non-alloy and fine grain steels - Part 1: Technical delivery requirements.
- EN 10219-2. 1997. Cold formed welded structural hollow sections of non-alloy and fine grain steels - Part 2: Tolerances, dimensions and sectional properties.
- ENV 1090-1. 1996. Execution of steel structures - Part 1: General rules and rules for buildings.
- Eurocode. 2002. Basis of structural design; EN 1990.
- Eurocode 3. 1992. Design of steel structures - General rules - Part 1-1: General rules and rules for buildings; ENV 1993-1-1.
- Eurocode 3. 1995. Design of steel structures - General rules - Part 1-2: Structural fire design; ENV 1993-1-2.
- Eurocode 3. forthcoming. Design of steel structures - General rules - Part 1-3: Supplementary rules for cold formed thin gauge members and sheeting; prEN 1993-1-3 (Draft, April 2002).
- Eurocode 3. forthcoming. Design of steel structures - General rules - Part 1-5: Supplementary rules for planar plated structures without transverse loading; prEN 1993-1-5 (Draft, August 2002).
- Eurocode 3. 2002. Design of steel structures - General rules - Part 1-8: Design of joints; prEN 1993-1-8.
- Herion, S. 1994. Räumliche K-Knoten aus Rechteckhohlprofilen. Ph.D. thesis, University of Karlsruhe, Germany.
- IBK. 1996. Trag und Verformungsverhalten von auf Zug beanspruchten Schrauben. IBK Bericht Nr. 217, Institut für Baustatik und Konstruktion, Eidgenössische Technische Hochschule (ETH) Zürich, Switzerland.
- Igarashi, S., Wakiyama, K., Matsumoto, T. and Murase, Y. 1985. Limit design of high strength bolted tube flange joint - Parts 1 and 2. Journal of Structural and Construction Engineering Transactions AIJ, Department of Architecture Reports, University of Osaka, Japan.
- IIW 1989. Design recommendations for hollow section joints – predominantly statically loaded. 2nd ed., IIW Doc. XV-701-89, International Institute of Welding Annual Assembly, Helsinki, Finland.

- ISO 898-1. 1999. Mechanical properties of fasteners made of carbon steel and alloy steel - Part 1: Bolts, screws and studs.
- Kato, B. and Mukai, A. 1982. Bolted tension flanges joining square hollow section members. CIDECT Program 8B Report, University of Tokyo, Japan.
- Kato, B. and Mukai, A. 1985. Bolted tension flanges joining square hollow section members- Supplement: Bolted at two sides of flange. CIDECT Program 8C Report No. 8C-85/10-E, University of Tokyo, Japan.
- Kirkham, W.J., and Miller, T.H. 2000. Examination of AISC LRFD shear lag design provisions. Engineering Journal, American Institute of Steel Construction, Vol.37, 3rd Quarter, pp. 83-98.
- Korol, R.M., Mirza, F.A., and Mirza, M.Y. 1994. Investigation of shear lag in slotted HSS tension members. Proceedings, 6th International Symposium on Tubular Structures, Melbourne, Australia, pp. 473-482.
- Korol, R.M. 1996. Shear lag in slotted HSS tension members. Canadian Journal of Civil Engineering, Vol. 23, pp. 1350-1354.
- Krautkrämer, J. and Krautkrämer, H. 1990. Ultrasonic testing of materials. 4th ed. Springer-Verlag, Berlin, Germany.
- Kulak, G.L., Fisher, J.W. and Struik, J.H.A. 1987. Guide to design criteria for bolted and riveted joints. 2nd ed. John Wiley & Sons, New York, U.S.A.
- Kulak, G.L. and Birkemoe, P.C. 1993. Field studies of bolt pretension. Journal of Constructional Steel Research, Vol. 25, pp. 95-105.
- Lu, L.H., Winkel, G.D. de, Yu, Y. and Wardenier J. 1994. Ultimate deformation limit for tubular joints. Tubular Structures VI. Proceedings of the 6th International Symposium on Tubular Structures, Melbourne, Australia, pp.457-464.
- Lu, L.H. 1997. The static strength of I-beam to rectangular hollow section column connections. Ph.D. thesis, Delft University of Technology, the Netherlands.
- Mang, F. 1980. Investigation of standard bolted flange connections for circular and rectangular hollow sections. Final report, CIDECT Program 8A Report, University of Karlsruhe, Germany.
- Packer, J.A., Bruno, L. and Birkemoe, P.C. 1989. Limit analysis of bolted RHS flange plate joints. Journal of Structural Engineering, American Society of Civil Engineers, 115 (9), pp. 2226-2242.
- Packer, J. A., Wardenier, J., Kurobane, Y., Dutta, D. and Yeomans, N. 1992. Design guide for rectangular hollow section (RHS) joints under predominantly static loading. CIDECT (ed.) and Verlag TÜV Rheinland, Köln, Germany.

- Packer, J. A. and Henderson, J. E. 1997. Hollow structural section connections and trusses - A design guide. 2nd ed., Canadian Institute of Steel Construction, Toronto, Canada.
- Puthli, R. S. and Vegte, G. J. van der. 2002. An overview of finite element strategies for predicting the static strength of tubular connections. Proceedings, International Workshop on Tubular Connections: The Way ahead, University of Kumamoto, Japan.
- POWER-DYNE. 1997. Quick reference guide & user's guide. BIDWELL Industrial Group, Inc., Middletown, U.S.A.
- Rockey, K.C. and Griffiths, D.W. 1970. The behaviour of bolted flanged joints in tension. Proceedings of the Conference on Joints in Structures, University of Sheffield, U.K.
- Romeijn, A. 1994. Stress and strain concentration factors of welded multiplanar tubular joints. Ph.D. thesis, Delft University of Technology, the Netherlands.
- Schaumann, P. and Kleineidam, P. 2002. Global structural behaviour of ring flange joints. Proceedings of NAFEMS seminar: Modelling of Assemblies and Joints for FE Analyses, Wiesbaden, Germany.
- STELCO. 1981. Hollow structural sections - design manual for connections. 2nd ed. Stelco Inc., Hamilton, Canada.
- Struik, J.H.A. and de Back, J. 1969. Tests on bolted T-stubs with respect to a bolted beam-to-column connection. Stevin Laboratory Report 6-69-13, Delft University of Technology, the Netherlands.
- Swanson Analysis System Inc. 1999. ANSYS Release 5.6, Houston, U.S.A.
- Swinden Laboratories. 1992. Slotted end plate connections. Report No. SL/HED/TN/22/-/92/D. British Steel Technical, Rotherham, U.K.
- Syam, A.A., and Chapman, B.G. 1996. Design of structural steel hollow section connections. Vol. 1: Design Models. Australian Institute of Steel Construction, Sydney, Australia.
- Timoshenko, S. and Woinowsky-Krieger. 1959. Theory of plates and shells. 2nd ed. McGraw Hill.
- Vegte, G. J. van der. 1995. The static strength of uniplanar and multiplanar T-and X-joints. Ph.D. thesis, Delft University of Technology, the Netherlands.
- Wardenier, J. 1982. Hollow section joints. Delft University Press, the Netherlands.
- Wardenier, J., Kurobane, Y., Packer, J. A., Dutta, D. and Yeomans, N. 1991. Design guide for circular hollow section (CHS) joints under predominantly static loading. CIDECT (ed.) and Verlag TÜV Rheinland, Köln, Germany.

- Wheeler, A. T., Clarke M. J. and Hancock, G. J. 2000. FE Modeling of four-bolt, tubular moment end-plate connections. *Journal of Structural Engineering, American Society of Civil Engineers*, 126 (7), pp. 816-822.
- Willibald, S., Packer, J.A. and Puthli, R.S. 2000. Bolted connections for RHS tension members. Final report, CIDECT Program 8D-10/00 + 8E-11/00 Report, University of Toronto, Canada.
- Willibald, S., Puthli, R.S. and Packer, J.A. 2001. Experimentelle Studie zu geschraubten Kopfplattenverbindungen für Quadrathohlprofile. *Stahlbau, Ernst und Sohn Verlag*, Vol. 03.01, pp. 183-192.
- Willibald, S., Packer, J.A. and Puthli, R.S. 2002. Experimental study of bolted HSS flange-plate connections in axial tension. *Journal of Structural Engineering, American Society of Civil Engineers*, 128 (3), pp. 328-336.
- Willibald, S., Packer, J.A. and Puthli, R.S. 2003. Design recommendations for bolted rectangular HSS flange-plate connections in axial tension. *Engineering Journal, American Institute of Steel Construction*, Vol. 40, 1st Quarter, pp. 15-24.
- Wingerde, A.M. van. 1992. The fatigue behaviour of T-and X-joints made of square hollow sections. Ph.D. thesis, Delft University of Technology, the Netherlands.
- Winkel, G.D. de. 1998. The static strength of I-beam to circular hollow section column connections. Ph.D. thesis, Delft University of Technology, the Netherlands.
- Yu, Y. 1997. The static strength of uniplanar and multiplanar connections in rectangular hollow sections. Ph.D. thesis, Delft University of Technology, the Netherlands.

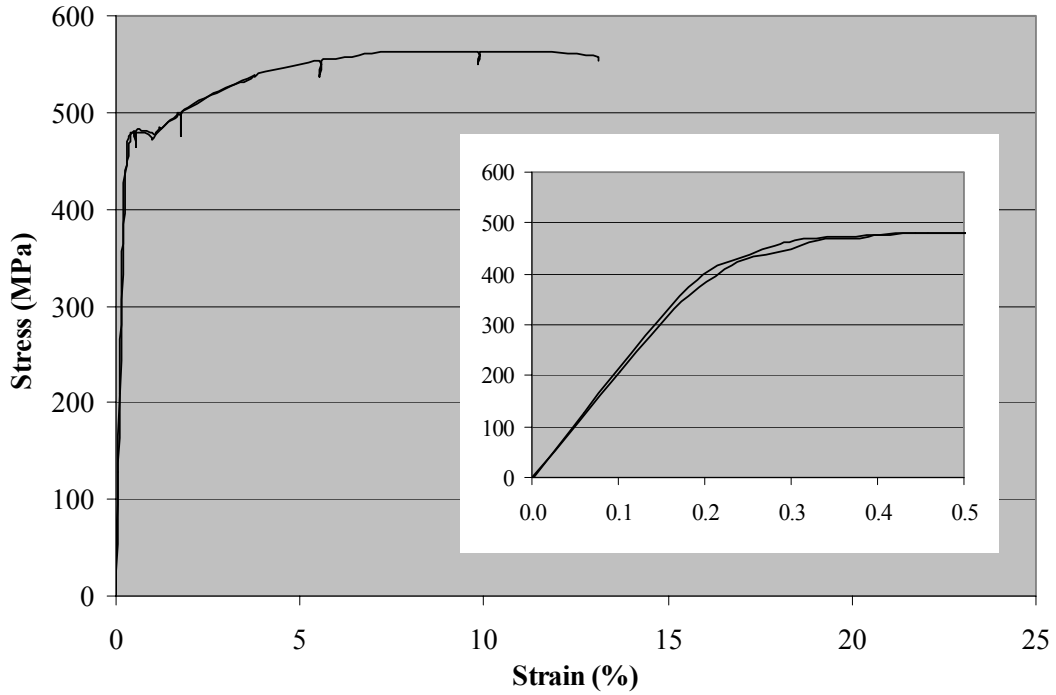
APPENDIX PART I

Experimental Study	I-2
Tensile Coupon Tests	I-2
Square Hollow Section (152 x 9.5 mm)	I-2
Rectangular Hollow Section (254 x 152 x 8 mm)	I-2
Flange-plate ($t_p = 12$ mm)	I-3
Flange-plate ($t_p = 16$ mm, Test Series 1)	I-3
Flange-plate ($t_p = 16$ mm, Test Series 2)	I-4
Flange-plate ($t_p = 20$ mm)	I-4
Connection Load versus average LVDT Displacement Curves and Test Results	I-5
Square Flange-plate Connections with four Bolts	I-5
Square Flange-plate Connections with eight Bolts	I-7
Rectangular Flange-plate Connections with ten Bolts	I-10
Numerical Study	I-11
Connection Load versus Displacement Curves and Numerical Results	I-11
Load-Deformation Curves of Square Connections with eight Bolts	I-11
Load-Deformation Curves of Square Connections with eight Bolts	I-13
Load-Deformation Curves of Rectangular Connections with ten Bolts	I-22
Analytical Study	I-31
One-Dimensional Yield Line Model	I-31
Two-Dimensional Yield Line Model	I-33

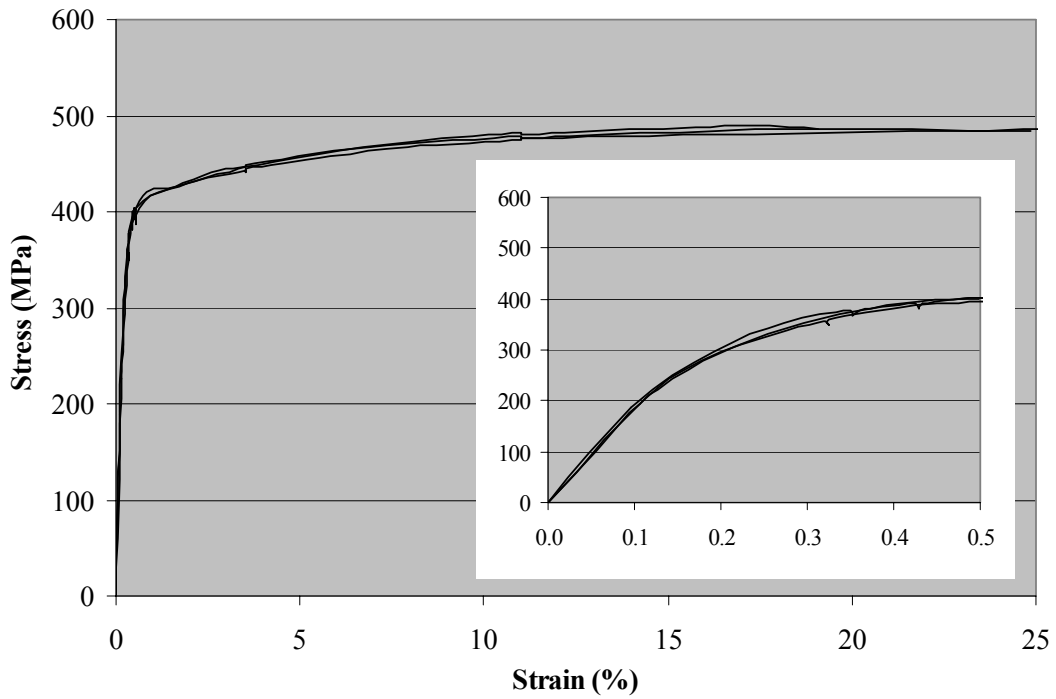
Experimental Study

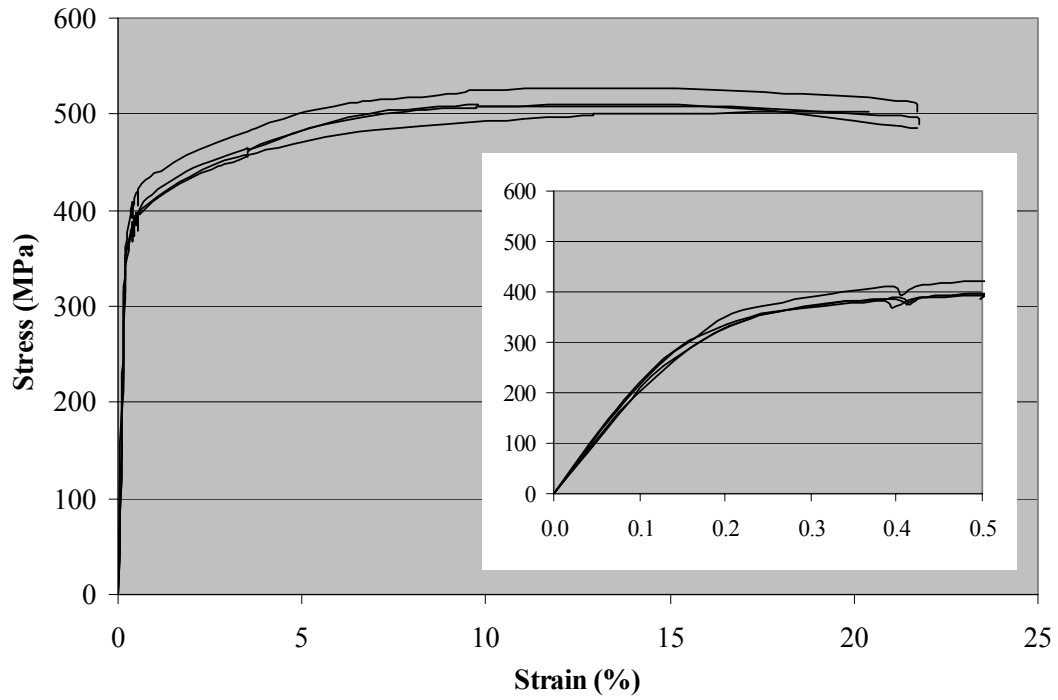
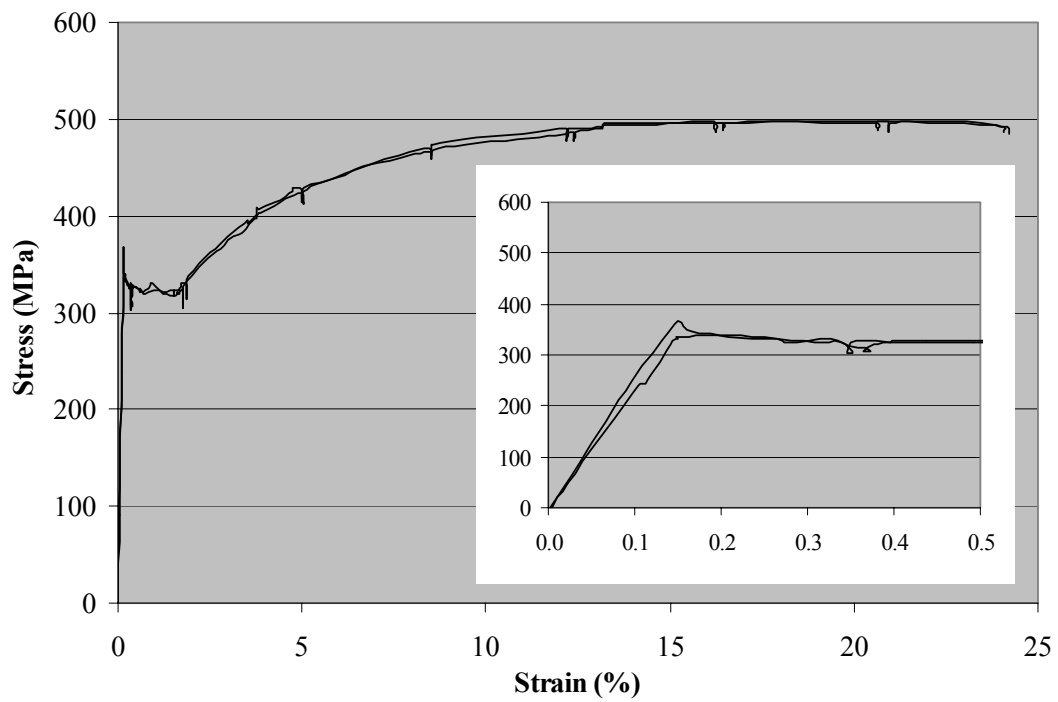
Tensile Coupon Tests

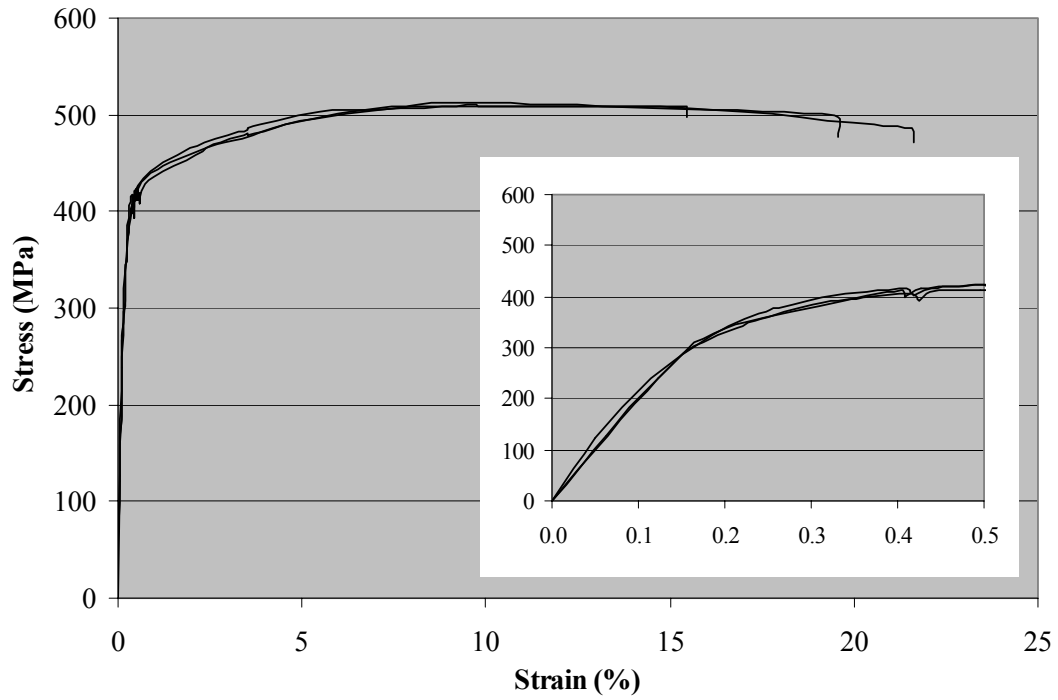
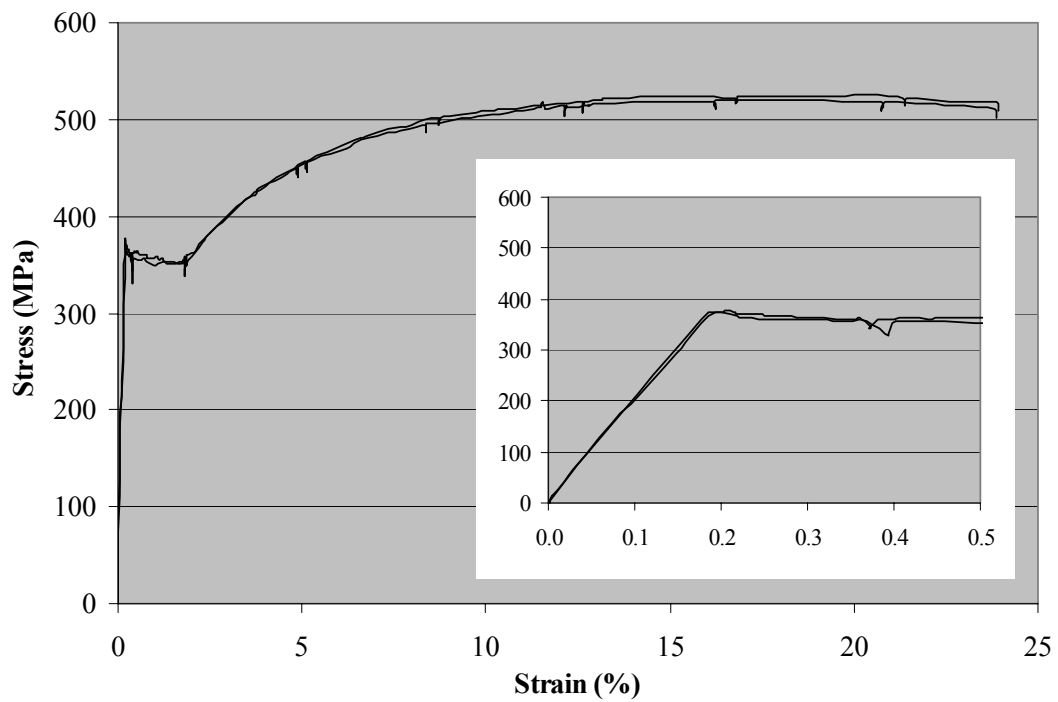
Square Hollow Section (152 x 9.5 mm)



Rectangular Hollow Section (254 x 152 x 8 mm)



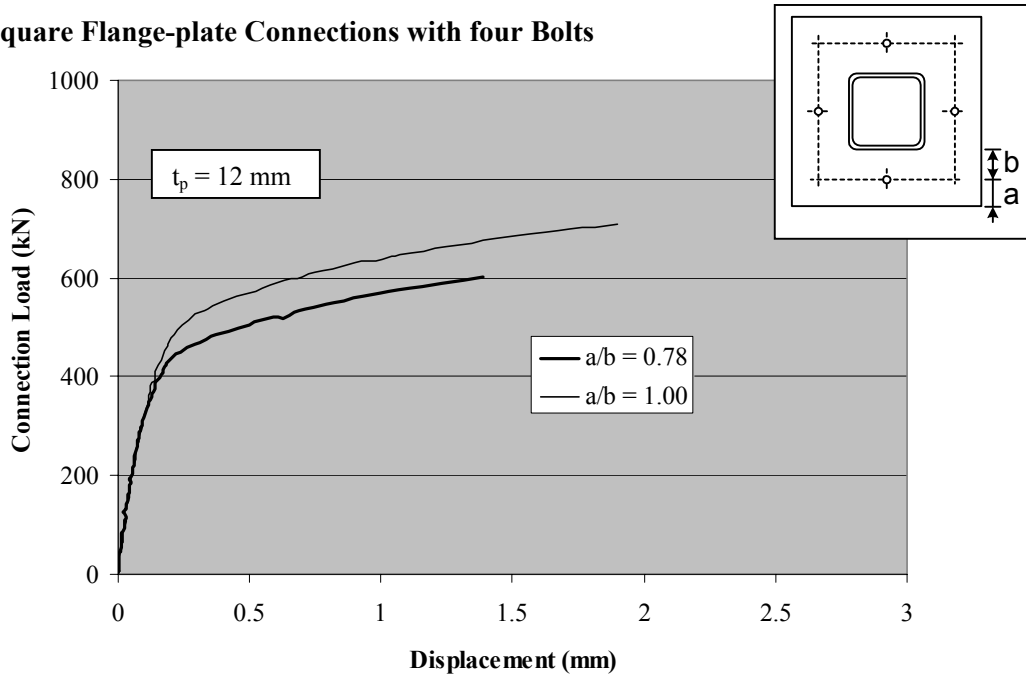
Flange-plate ($t_p = 12$ mm)**Flange-plate ($t_p = 16$ mm, Test Series 1)**

Flange-plate ($t_p = 16$ mm, Test Series 2)**Flange-plate ($t_p = 20$ mm)**

Connection Load versus average LVDT Displacement Curves

The displacement was measured over a distance of 65 mm (distance between the positioning screws of the top and bottom LVDT mounts, see Figure 2.10). The average displacement of all four LVDTs for each specimen is shown.

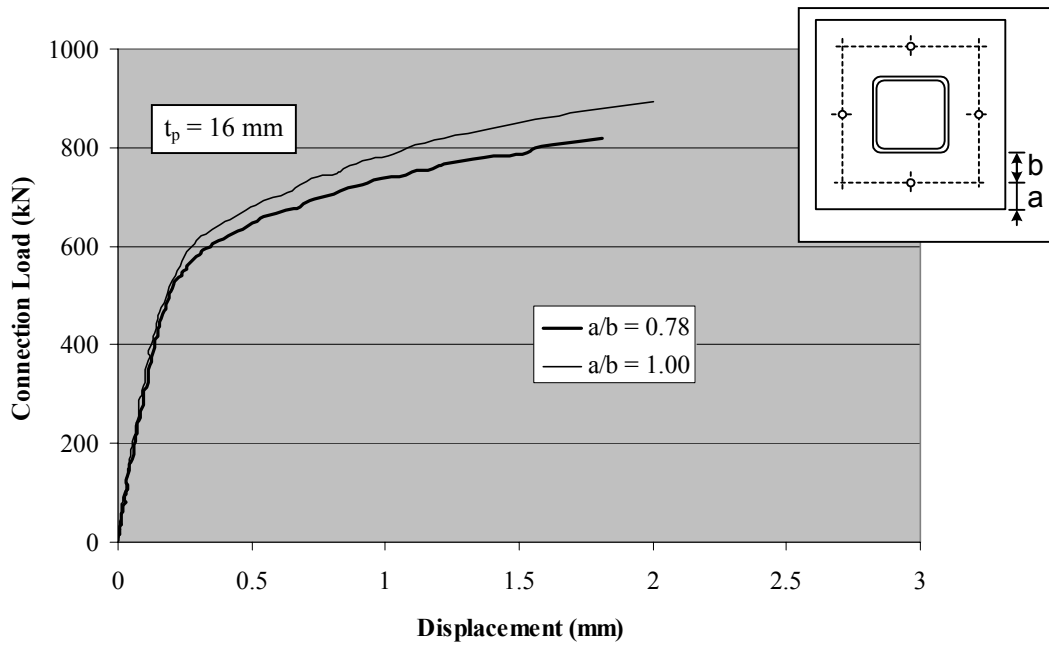
Square Flange-plate Connections with four Bolts



Connection	Properties					Results	
	n	a (mm)	b (mm)	t_p (mm)	Bolt strength F_{bu} (kN)	Connection strength N_{ux} (kN)	Prying ratio $\beta_{ux}^{1)}$ (%)
S4-3	4	35	45	12	256	792	29.3
S4-1		40	40			847	20.9

$$1) \beta_{ux} = \frac{n \cdot F_{bu} - N_{ux}}{N_{ux}}$$

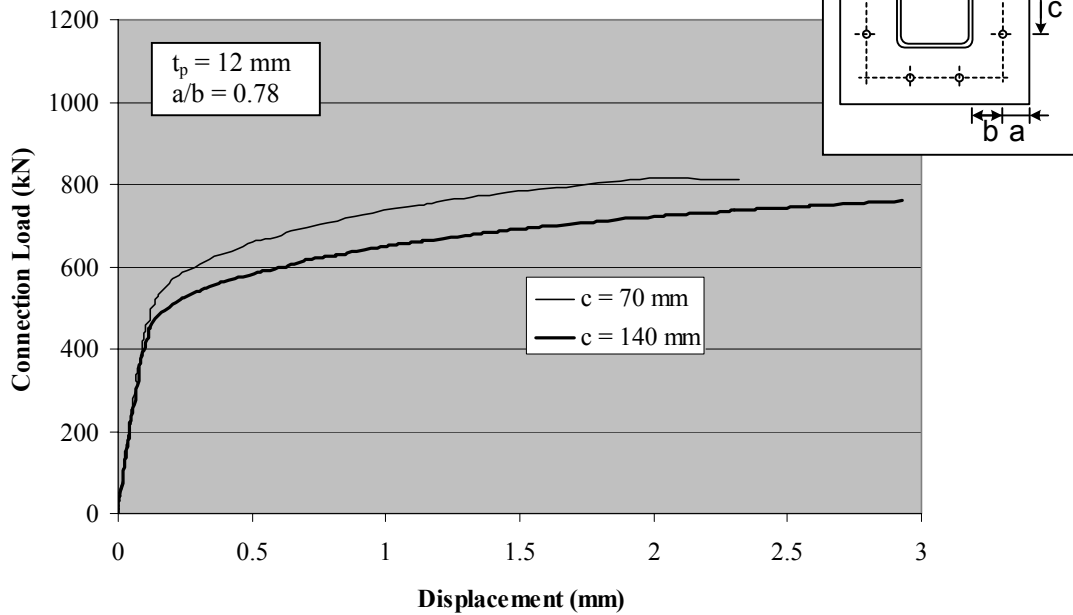
Square Flange-plate Connections with four Bolts (contd.)



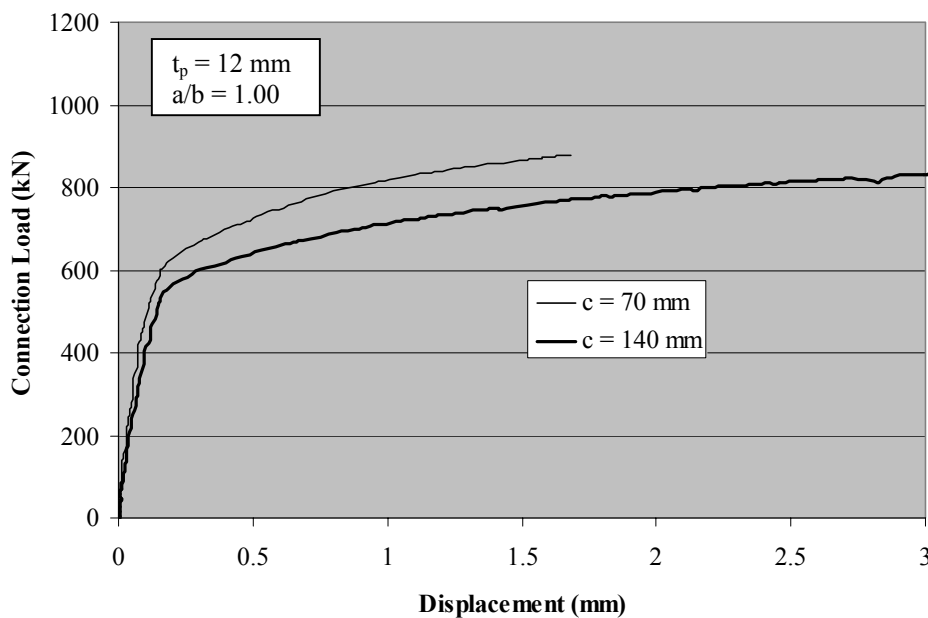
Connection	Properties					Results	
	n	a (mm)	b (mm)	t_p (mm)	Bolt strength F_{bu} (kN)	Connection strength N_{ux} (kN)	Prying ratio $\beta_{ux}^{1)}$ (%)
S4-4	4	35	45	16	247	910	8.8
S4-2		40	40			955	3.7

$$1) \beta_{ux} = \frac{n \cdot F_{bu} - N_{ux}}{N_{ux}}$$

Square Flange-plate Connections with eight Bolts



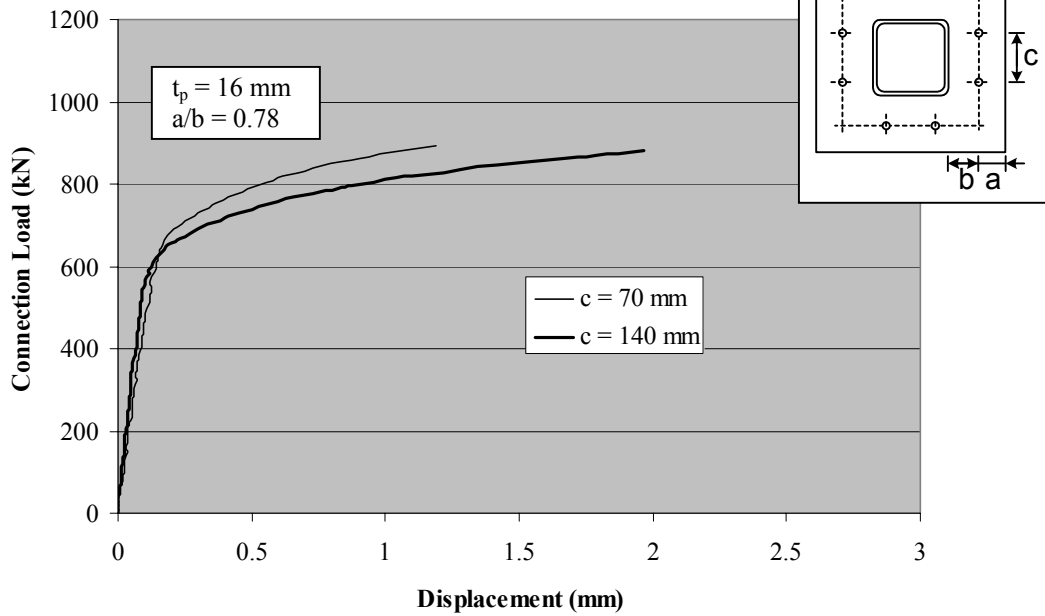
Connection	Properties						Results	
	n	a (mm)	b (mm)	c (mm)	t _p (mm)	Bolt strength F _{bu} (kN)	Connection strength N _{ux} (kN)	Prying ratio β _{ux} ¹⁾ (%)
S8-9	8	35	45	70	12	138	881	25.2
S8-7				140			843	30.9



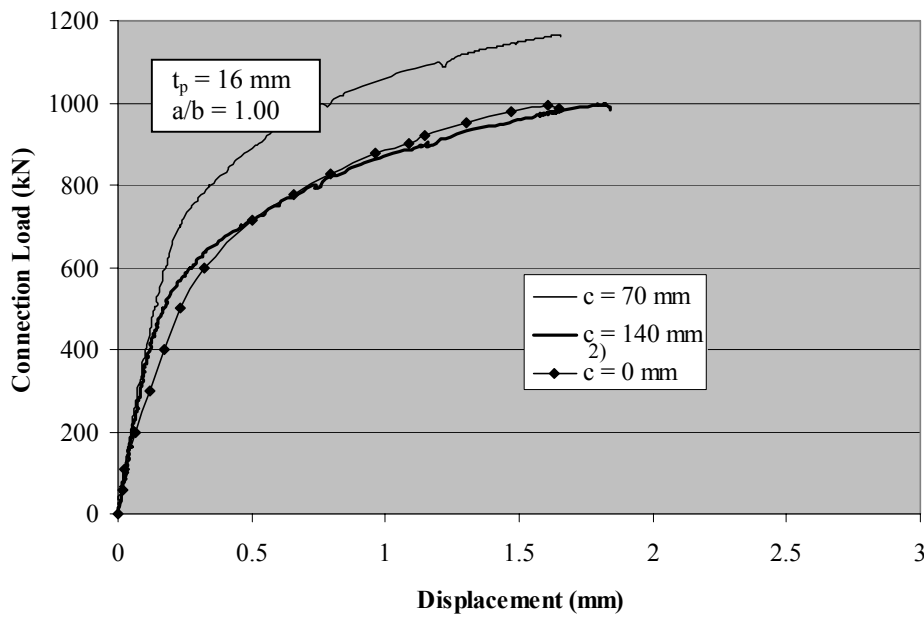
Connection	Properties						Results	
	n	a (mm)	b (mm)	c (mm)	t _p (mm)	Bolt strength F _{bu} (kN)	Connection strength N _{ux} (kN)	Prying ratio β _{ux} ¹⁾ (%)
S8-6	8	40	40	70	12	138	946	16.6
S8-5				140			903	22.2

$$1) \beta_{ux} = \frac{n \cdot F_{bu} - N_{ux}}{N_{ux}}$$

Square Flange-plate Connections with eight Bolts (contd.)



		Properties				Results		
Connection	n	a (mm)	b (mm)	c (mm)	t _p (mm)	Bolt strength F _{bu} (kN)	Connection strength N _{ux} (kN)	Prying ratio β _{ux} ¹⁾ (%)
S8-10	8	35	45	70	16	134	1019	5.4
S8-8				140			946	13.5

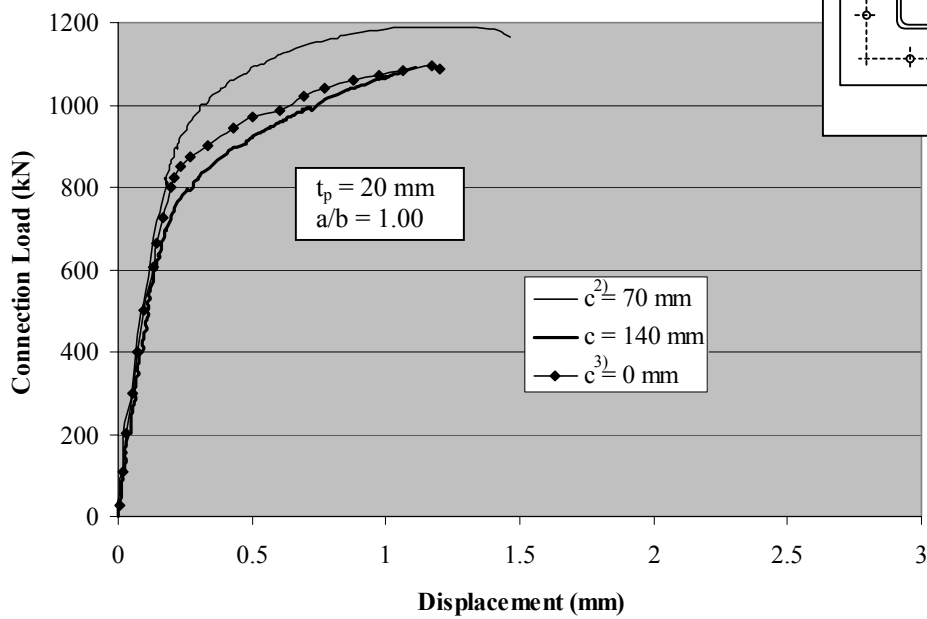


		Properties				Results		
Connection	n	a (mm)	b (mm)	c (mm)	t _p (mm)	Bolt strength F _{bu} (kN)	Connection strength N _{ux} (kN)	Prying ratio β _{ux} ¹⁾ (%)
S8-3	8	40	40	70	16	160	1240	3.4
S8-1				140			1108	15.7
S'8-1				0 ²⁾			1049	22.2

$$1) \beta_{ux} = \frac{n \cdot F_{bu} - N_{ux}}{N_{ux}}$$

2) Specimen with bolt layout S'8. Bolts are placed in the corner and the middle of the flange-plate.

Square Flange-plate Connections with eight Bolts (contd.)



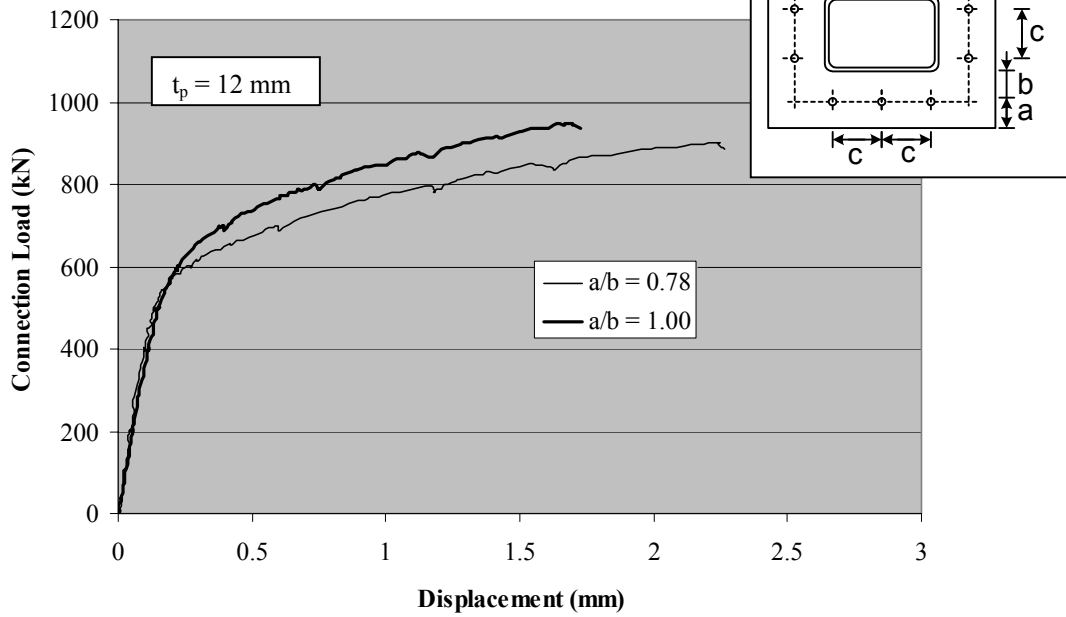
Connection	Properties					Results		
	n	a (mm)	b (mm)	c (mm)	t_p (mm)	Bolt strength F_{bu} (kN)	Connection strength N_{ux} (kN)	Prying ratio $\beta_{ux}^{1)}$ (%)
S8-4	8	40	40	70 ²⁾	20	152	1190	2.1
S8-2				140			1162	4.5
S'8-2				0 ³⁾			1141	6.4

$$1) \beta_{ux} = \frac{n \cdot F_{bu} - N_{ux}}{N_{ux}}$$

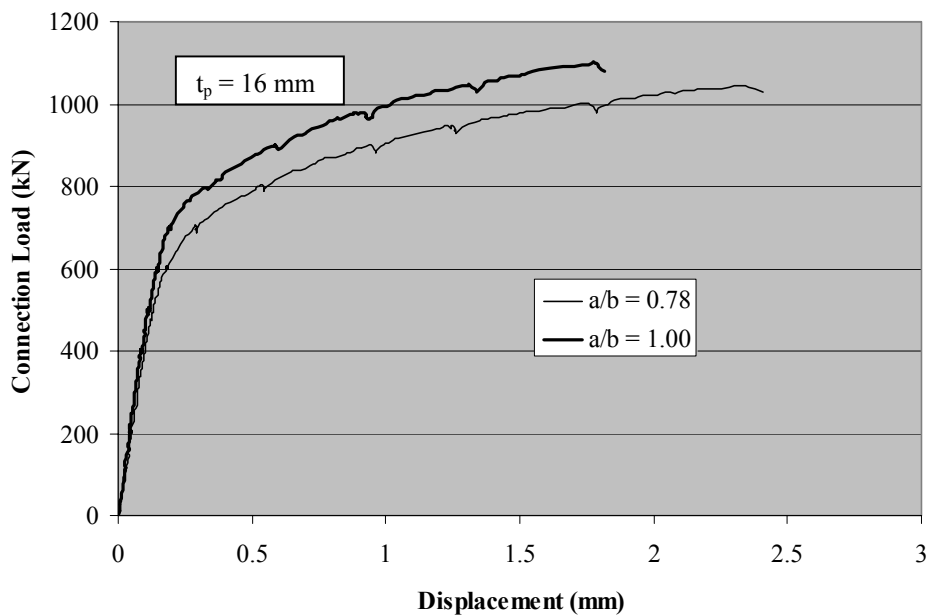
2) Due to installation of strain gauges the displacement was only measured over a distance of 57 mm.

3) Specimen with bolt layout S'8. Bolts are placed in the corner and the middle of the flange-plate.

Rectangular Flange-plate Connections with ten Bolts



Connection	Properties						Results	
	n	a (mm)	b (mm)	c (mm)	t_p (mm)	Bolt strength F_{bu} (kN)	Connection strength N_{ux} (kN)	Prying ratio $\beta_{ux}^{1)}$ (%)
R10-1	10	35	45	110	12	146	1030	41.7
R10-3		40	40				1105	32.1



Connection	Properties						Results	
	n	a (mm)	b (mm)	c (mm)	t_p (mm)	Bolt strength F_{bu} (kN)	Connection strength N_{ux} (kN)	Prying ratio $\beta_{ux}^{1)}$ (%)
R10-2	10	35	45	110	16	141	1153	22.2
R10-4		40	40				1240	13.6

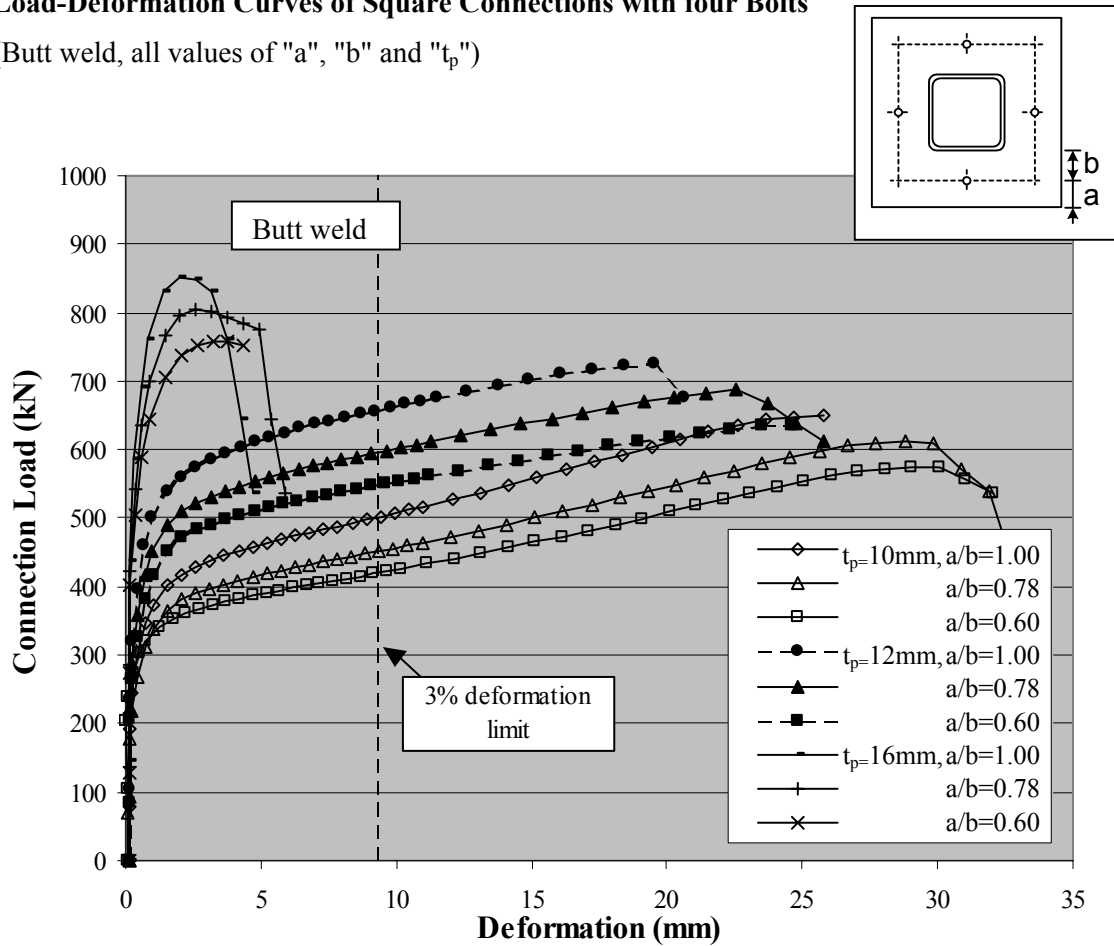
$$1) \beta_{ux} = \frac{n \cdot F_{bu} - N_{ux}}{N_{ux}}$$

Numerical Study

Connection Load versus Displacement Curves

Load-Deformation Curves of Square Connections with four Bolts

(Butt weld, all values of "a", "b" and "t_p")



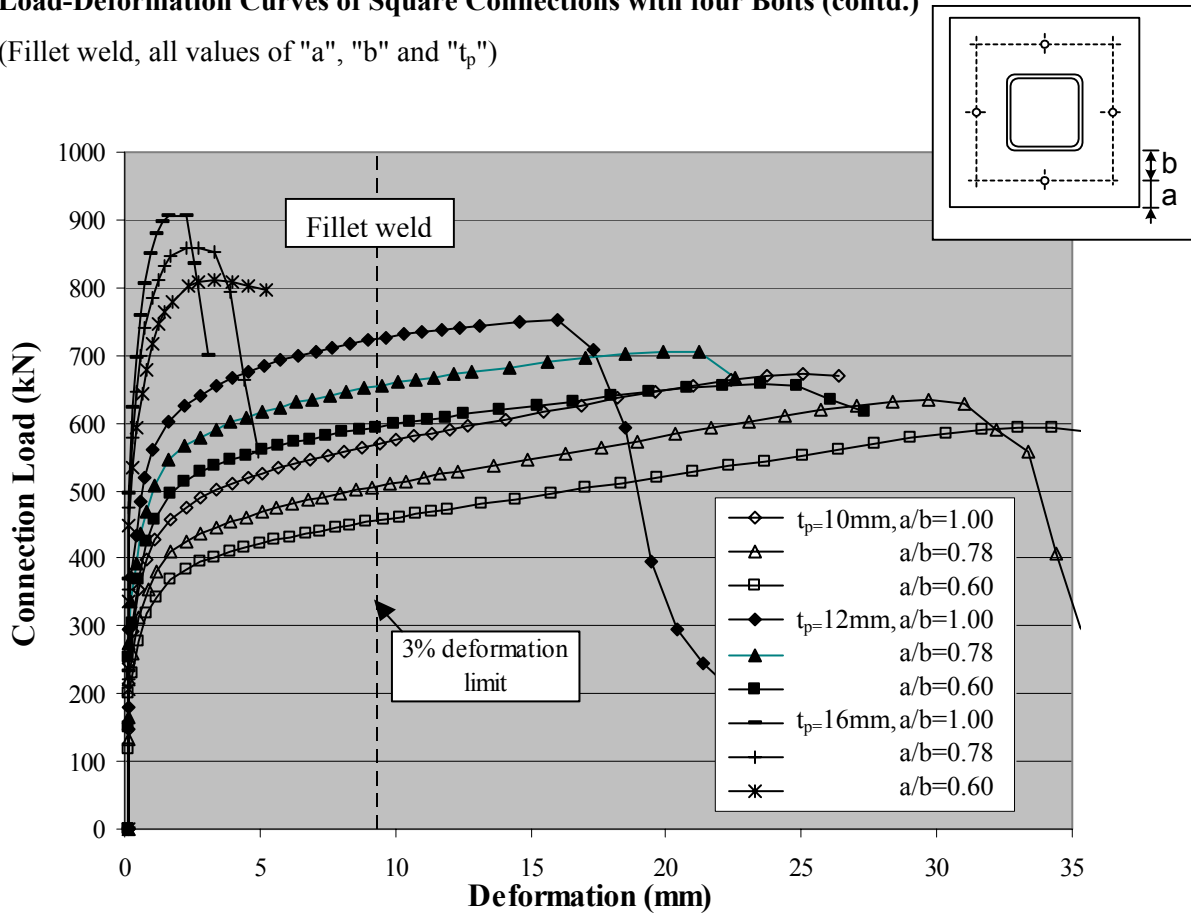
Connection	Properties					Results			
	n	a (mm)	b (mm)	t _p (mm)	Bolt strength F _{bu} (kN)	Connection strength N _{uFE} (kN)	Prying ratio β _{uFE} ¹⁾ (%)		
NW 10 50	4	30	50	10	250	420	138.0		
NW 10 45		35	45			451	121.3		
NW 10 40		40	40			501	99.3		
NW 12 50		30	50	12		248	549	80.4	
NW 12 45		35	45				596	66.1	
NW 12 40		40	40				658	50.5	
NW 16 50		30	50	16			245	757	29.5
NW 16 45		35	45					806	21.7
NW 16 40		40	40					852	15.1

Butt weld

$$1) \beta_{ux} = \frac{n \cdot F_{bu} - N_{uFE}}{N_{uFE}}$$

Load-Deformation Curves of Square Connections with four Bolts (contd.)

(Fillet weld, all values of "a", "b" and "t_p")



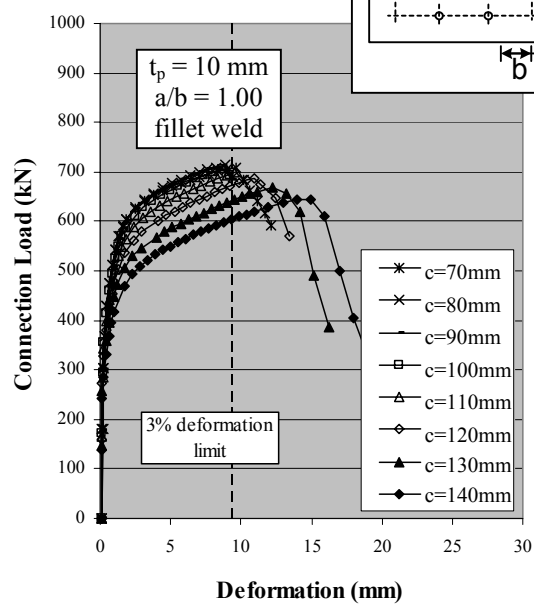
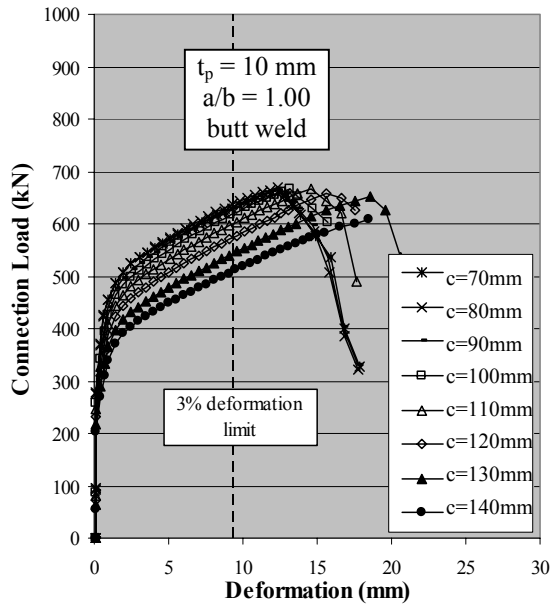
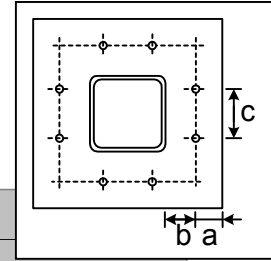
Connection	Properties				Results		
	n	a (mm)	b (mm)	t _p (mm)	Bolt strength F _{bu} (kN)	Connection strength N _{uFE} (kN)	Prying ratio β _{uFE} ¹⁾ (%)
W 10 50	4	30	50	10	250	455	119.3
W 10 45		35	45			506	97.3
W 10 40		40	40			568	75.9
W 12 50		30	50	12	248	594	66.6
W 12 45		35	45			654	51.3
W 12 40		40	40			724	36.7
W 16 50		30	50	16	245	812	20.7
W 16 45		35	45			860	14.0
W 16 40		40	40			905	8.3

Fillet weld

$$1) \beta_{uFE} = \frac{n \cdot F_{bu} - N_{uFE}}{N_{uFE}}$$

Load-Deformation Curves of Square Connections with eight Bolts

(a = 40 mm, b = 40 mm, t_p = 10 mm)



Connection	Properties						Results	
	n	a (mm)	b (mm)	c (mm)	t _p (mm)	Bolt strength F _{bu} (kN)	Connection strength N _{uFE} (kN)	Prying ratio β _{uFE} ¹⁾ (%)
NW10 40 140	8	40	40	140	10	126	509	98.5
NW10 40 130				130			543	86.2
NW10 40 120				120			573	76.3
NW10 40 110				110			599	68.7
NW10 40 100				100			619	63.2
NW10 40 90				90			632	59.9
NW10 40 80				80			637	58.6
NW10 40 70				70			630	60.5

Butt weld

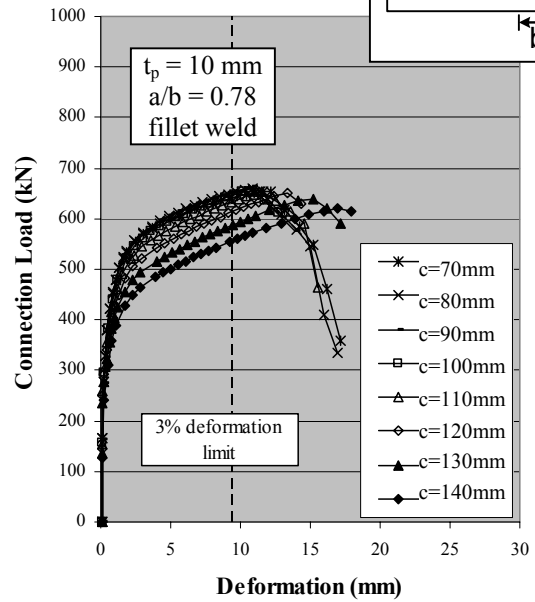
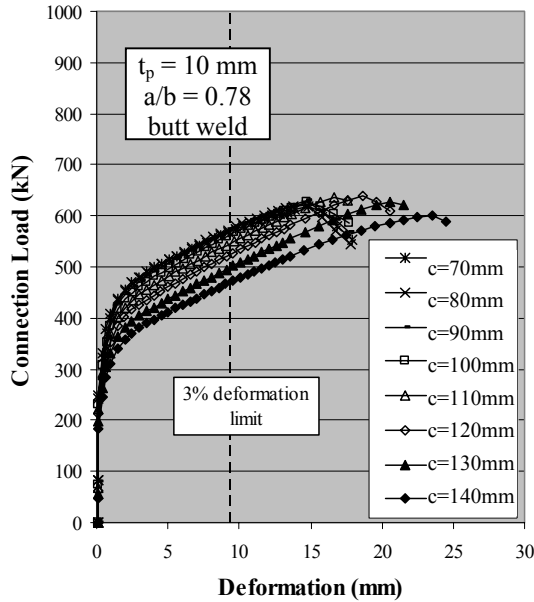
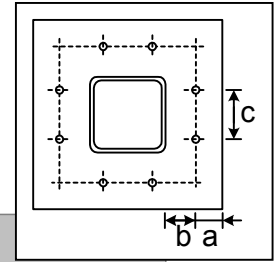
Connection	Properties						Results	
	n	a (mm)	b (mm)	c (mm)	t _p (mm)	Bolt strength F _{bu} (kN)	Connection strength N _{uFE} (kN)	Prying ratio β _{uFE} ¹⁾ (%)
W10 40 140	8	40	40	140	10	126	604	67.4
W10 40 130				130			641	57.7
W10 40 120				120			672	50.4
W10 40 110				110			696	45.2
W10 40 100				100			705	43.3
W10 40 90				90			710	42.3
W10 40 80				80			715	41.4
W10 40 70				70			708	42.7

Fillet weld

$$1) \beta_{uFE} = \frac{n \cdot F_{bu} - N_{uFE}}{N_{uFE}}$$

Load-Deformation Curves of Square Connections with eight Bolts (contd.)

(a = 35 mm, b = 45 mm, t_p = 10 mm)



Connection	Properties					Results		
	n	a (mm)	b (mm)	c (mm)	t _p (mm)	Bolt strength F _{bu} (kN)	Connection strength N _{uFE} (kN)	Prying ratio β _{uFE} ¹⁾ (%)
NW10 45 140	8	35	45	140	10	126	469	115.3
NW10 45 130				130			498	102.9
NW10 45 120				120			524	92.9
NW10 45 110				110			545	85.3
NW10 45 100				100			562	79.8
NW10 45 90				90			572	76.7
NW10 45 80				80			574	76.2
NW10 45 70				70			568	77.8

Butt weld

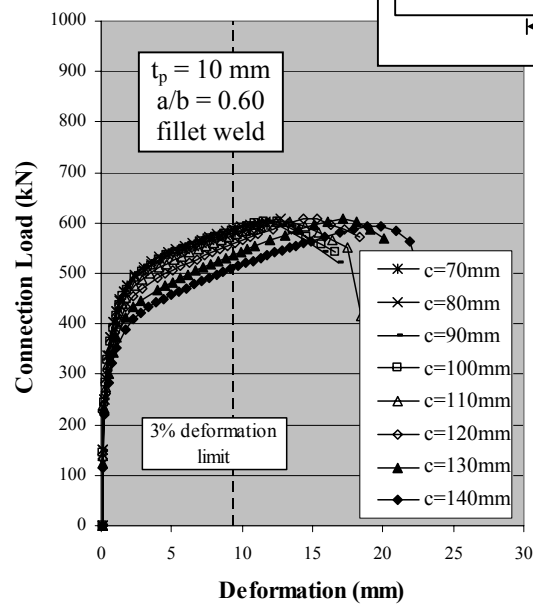
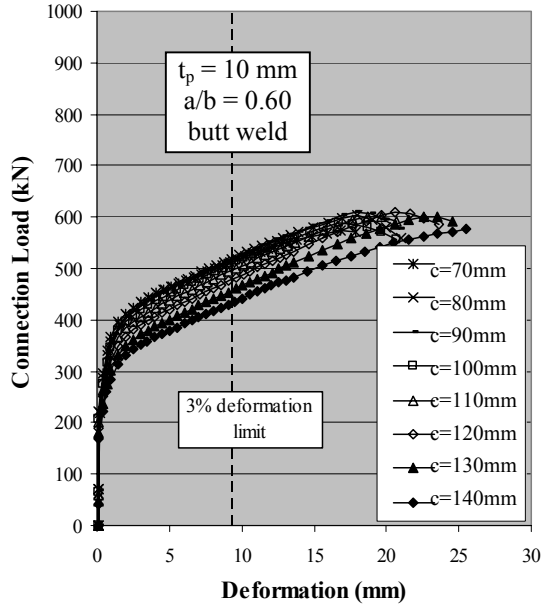
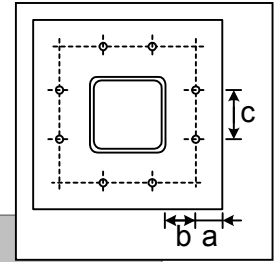
Connection	Properties					Results		
	n	a (mm)	b (mm)	c (mm)	t _p (mm)	Bolt strength F _{bu} (kN)	Connection strength N _{uFE} (kN)	Prying ratio β _{uFE} ¹⁾ (%)
W10 45 140	8	35	45	140	10	126	554	82.3
W10 45 130				130			586	72.4
W10 45 120				120			612	65.0
W10 45 110				110			632	59.8
W10 45 100				100			645	56.6
W10 45 90				90			651	55.1
W10 45 80				80			650	55.5
W10 45 70				70			641	57.7

Fillet weld

$$1) \beta_{uFE} = \frac{n \cdot F_{bu} - N_{uFE}}{N_{uFE}}$$

Load-Deformation Curves of Square Connections with eight Bolts (contd.)

(a = 30 mm, b = 50 mm, t_p = 10 mm)



Connection	Properties					Results		
	n	a (mm)	b (mm)	c (mm)	t _p (mm)	Bolt strength F _{bu} (kN)	Connection strength N _{uFE} (kN)	Prying ratio β _{uFE} ¹⁾ (%)
NW10_50_140	8	30	50	140	10	126	433	133.4
NW10_50_130				130			457	121.1
NW10_50_120				120			478	111.2
NW10_50_110				110			496	103.6
NW10_50_100				100			509	98.3
NW10_50_90				90			517	95.3
NW10_50_80				80			519	94.7
NW10_50_70				70			514	96.7

Butt weld

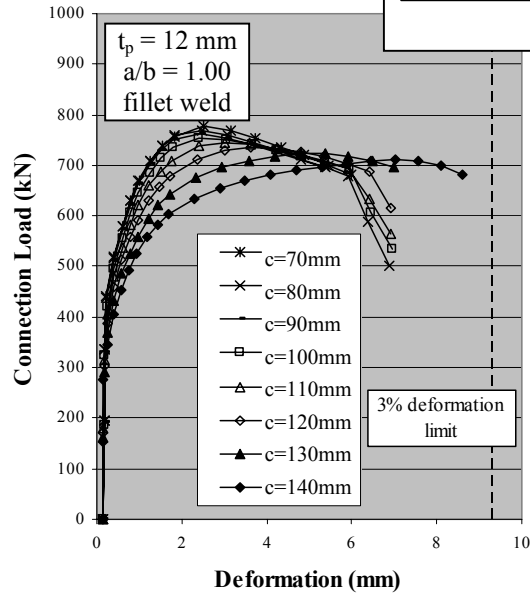
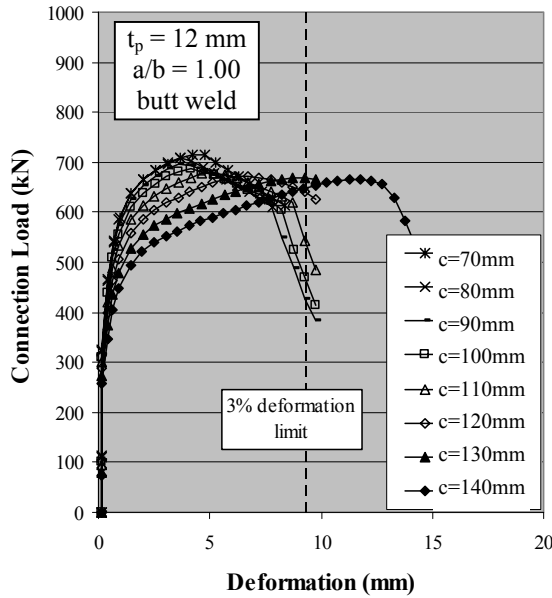
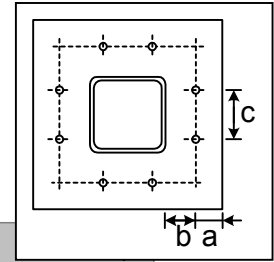
Connection	Properties					Results		
	n	a (mm)	b (mm)	c (mm)	t _p (mm)	Bolt strength F _{bu} (kN)	Connection strength N _{uFE} (kN)	Prying ratio β _{uFE} ¹⁾ (%)
W10_50_140	8	30	50	140	10	126	508	98.8
W10_50_130				130			536	88.5
W10_50_120				120			558	81.2
W10_50_110				110			574	76.0
W10_50_100				100			584	72.9
W10_50_90				90			589	71.4
W10_50_80				80			587	72.2
W10_50_70				70			579	74.5

Fillet weld

$$1) \beta_{uFE} = \frac{n \cdot F_{bu} - N_{uFE}}{N_{uFE}}$$

Load-Deformation Curves of Square Connections with eight Bolts (contd.)

(a = 40 mm, b = 40 mm, t_p = 12 mm)



Connection	Properties					Results		
	n	a (mm)	b (mm)	c (mm)	t _p (mm)	Bolt strength F _{bu} (kN)	Connection strength N _{uFE} (kN)	Prying ratio β _{uFE} ¹⁾ (%)
NW12 40 140	8	40	40	140	12	126	648	55.3
NW12 40 130				130			669	50.2
NW12 40 120				120			672	49.7
NW12 40 110				110			678	48.3
NW12 40 100				100			687	46.5
NW12 40 90				90			696	44.5
NW12 40 80				80			708	42.1
NW12 40 70				70			716	40.5

Butt weld

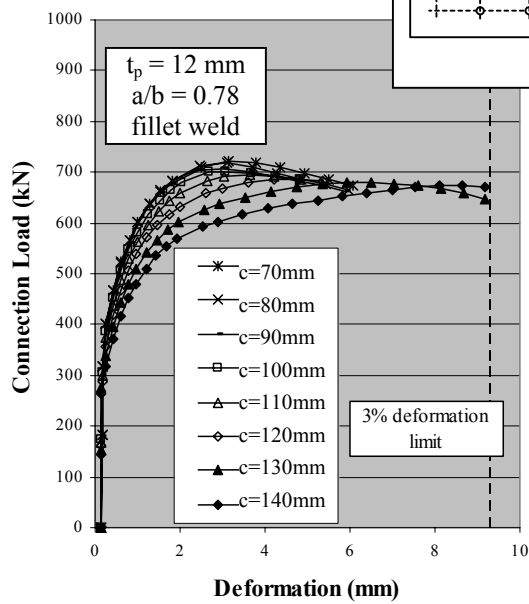
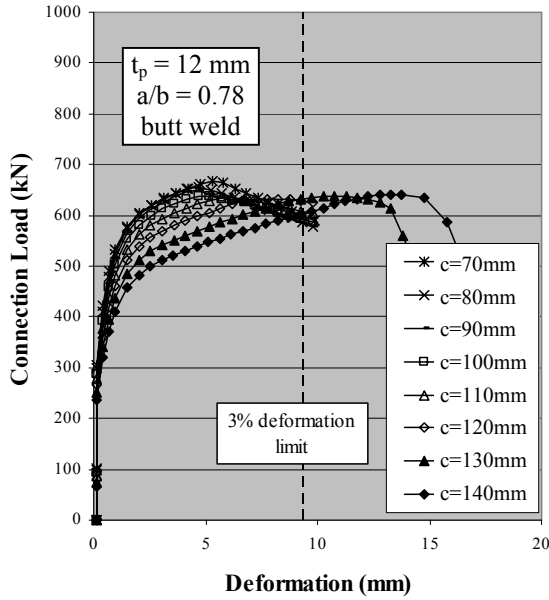
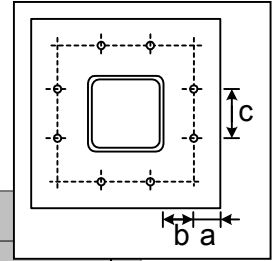
Connection	Properties					Results		
	n	a (mm)	b (mm)	c (mm)	t _p (mm)	Bolt strength F _{bu} (kN)	Connection strength N _{uFE} (kN)	Prying ratio β _{uFE} ¹⁾ (%)
W12 40 140	8	40	40	140	12	126	711	41.5
W12 40 130				130			724	39.0
W12 40 120				120			735	36.8
W12 40 110				110			746	34.8
W12 40 100				100			754	33.3
W12 40 90				90			762	31.9
W12 40 80				80			770	30.7
W12 40 70				70			778	29.3

Fillet weld

$$1) \beta_{uFE} = \frac{n \cdot F_{bu} - N_{uFE}}{N_{uFE}}$$

Load-Deformation Curves of Square Connections with eight Bolts (contd.)

(a = 35 mm, b = 45 mm, t_p = 12 mm)



Connection	Properties					Results		
	n	a (mm)	b (mm)	c (mm)	t _p (mm)	Bolt strength F _{bu} (kN)	Connection strength N _{uFE} (kN)	Prying ratio β _{uFE} ¹⁾ (%)
NW12 45 140	8	35	45	140	12	126	603	66.6
NW12 45 130				130			632	59.0
NW12 45 120				120			633	58.9
NW12 45 110				110			634	58.6
NW12 45 100				100			639	57.3
NW12 45 90				90			648	55.1
NW12 45 80				80			657	53.1
NW12 45 70				70			667	50.8

Butt weld

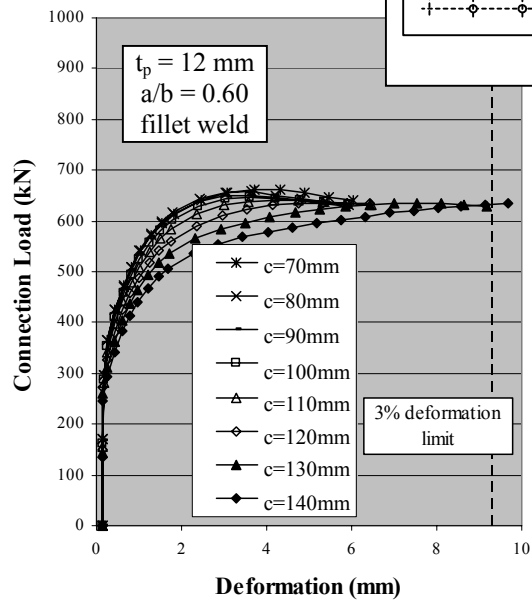
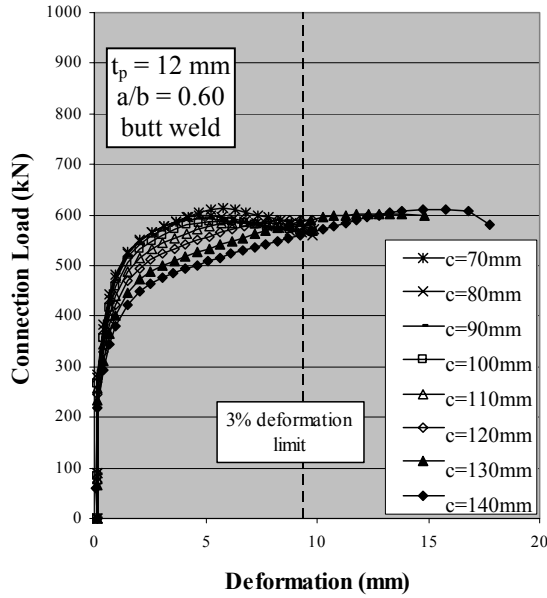
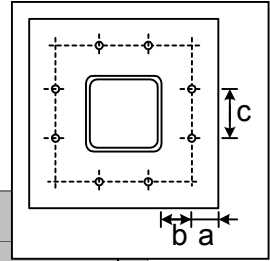
Connection	Properties					Results		
	n	a (mm)	b (mm)	c (mm)	t _p (mm)	Bolt strength F _{bu} (kN)	Connection strength N _{uFE} (kN)	Prying ratio β _{uFE} ¹⁾ (%)
W12 45 140	8	35	45	140	12	126	674	49.3
W12 45 130				130			680	47.9
W12 45 120				120			686	46.6
W12 45 110				110			694	44.9
W12 45 100				100			701	43.4
W12 45 90				90			707	42.3
W12 45 80				80			718	40.0
W12 45 70				70			722	39.2

Fillet weld

$$1) \beta_{uFE} = \frac{n \cdot F_{bu} - N_{uFE}}{N_{uFE}}$$

Load-Deformation Curves of Square Connections with eight Bolts (contd.)

(a = 30 mm, b = 50 mm, t_p = 12 mm)



Connection	Properties					Results		
	n	a (mm)	b (mm)	c (mm)	t _p (mm)	Bolt strength F _{bu} (kN)	Connection strength N _{uFE} (kN)	Prying ratio β _{uFE} ¹⁾ (%)
NW12 50 140	8	30	50	140	12	126	561	79.1
NW12 50 130				130			587	71.4
NW12 50 120				120			590	70.5
NW12 50 110				110			586	71.6
NW12 50 100				100			588	71.0
NW12 50 90				90			593	69.5
NW12 50 80				80			600	67.6
NW12 50 70				70			613	63.9

Butt weld

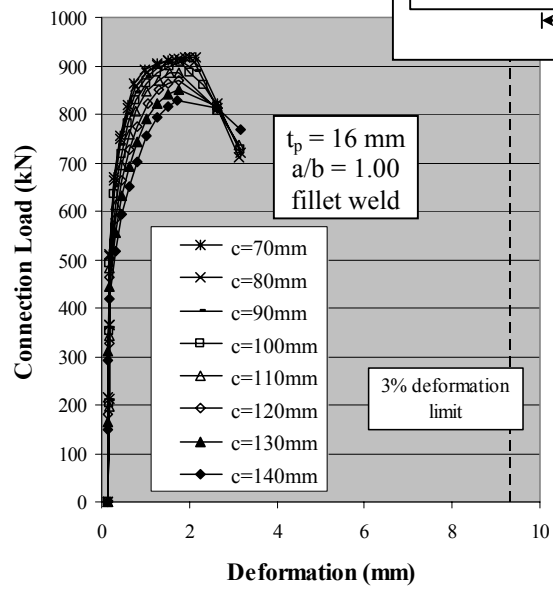
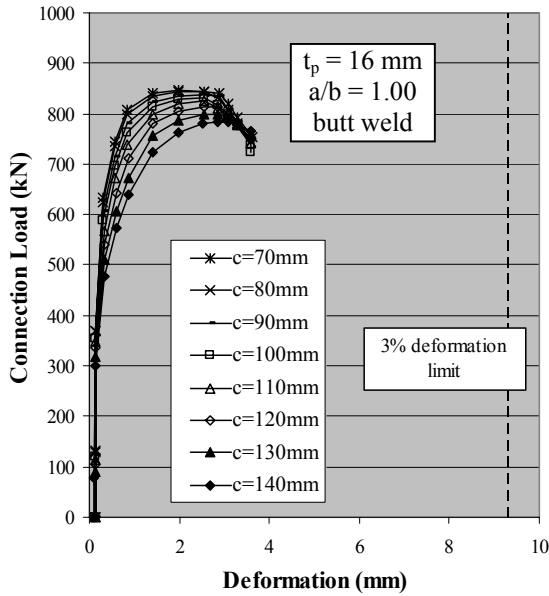
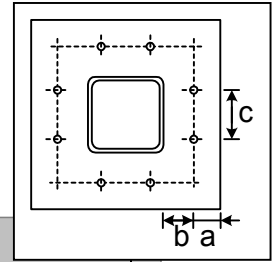
Connection	Properties					Results		
	n	a (mm)	b (mm)	c (mm)	t _p (mm)	Bolt strength F _{bu} (kN)	Connection strength N _{uFE} (kN)	Prying ratio β _{uFE} ¹⁾ (%)
W12 50 140	8	30	50	140	12	126	633	58.9
W12 50 130				130			634	58.5
W12 50 120				120			636	58.1
W12 50 110				110			640	57.1
W12 50 100				100			645	55.8
W12 50 90				90			649	54.9
W12 50 80				80			658	52.8
W12 50 70				70			663	51.8

Fillet weld

$$1) \beta_{uFE} = \frac{n \cdot F_{bu} - N_{uFE}}{N_{uFE}}$$

Load-Deformation Curves of Square Connections with eight Bolts (contd.)

(a = 40 mm, b = 40 mm, t_p = 16 mm)



Connection	Properties						Results	
	n	a (mm)	b (mm)	c (mm)	t _p (mm)	Bolt strength F _{bu} (kN)	Connection strength N _{uFE} (kN)	Prying ratio β _{uFE} ¹⁾ (%)
NW16_40_140	8	40	40	140	16	125	785	27.8
NW16_40_130				130			800	25.4
NW16_40_120				120			813	23.3
NW16_40_110				110			825	21.7
NW16_40_100				100			833	20.4
NW16_40_90				90			838	19.7
NW16_40_80				80			843	18.9
NW16_40_70				70			847	18.5

Butt weld

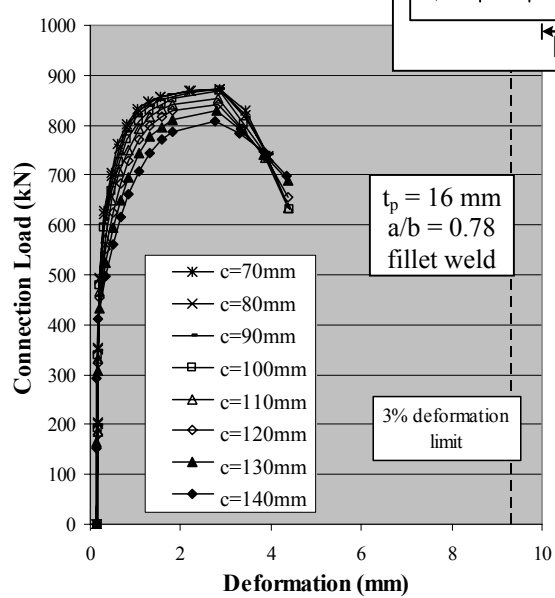
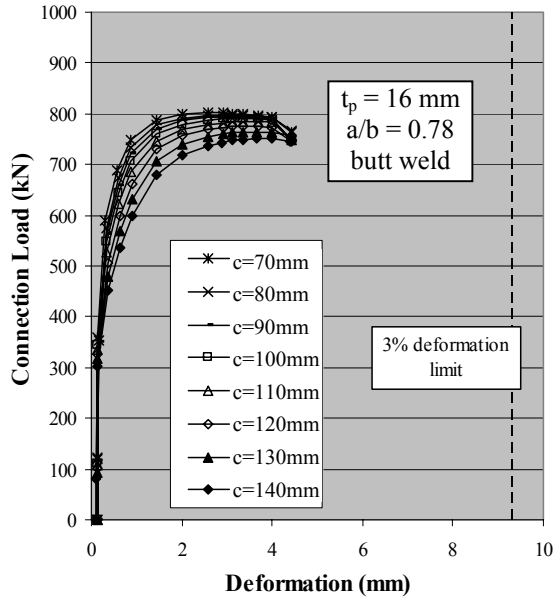
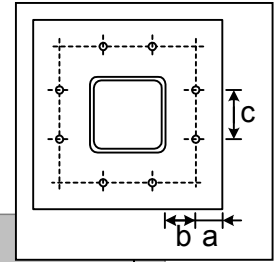
Connection	Properties						Results	
	n	a (mm)	b (mm)	c (mm)	t _p (mm)	Bolt strength F _{bu} (kN)	Connection strength N _{uFE} (kN)	Prying ratio β _{uFE} ¹⁾ (%)
W16_40_140	8	40	40	140	16	125	828	21.1
W16_40_130				130			851	17.9
W16_40_120				120			871	15.2
W16_40_110				110			885	13.4
W16_40_100				100			907	10.6
W16_40_90				90			912	10.0
W16_40_80				80			915	9.6
W16_40_70				70			919	9.2

Fillet weld

$$^1) \beta_{uFE} = \frac{n \cdot F_{bu} - N_{uFE}}{N_{uFE}}$$

Load-Deformation Curves of Square Connections with eight Bolts (contd.)

(a = 35 mm, b = 45 mm, t_p = 16 mm)



Connection	Properties					Results		
	n	a (mm)	b (mm)	c (mm)	t _p (mm)	Bolt strength F _{bu} (kN)	Connection strength N _{uFE} (kN)	Prying ratio β _{uFE} ¹⁾ (%)
NW16 45 140	8	35	45	140	16	125	751	33.5
NW16 45 130				130			764	31.3
NW16 45 120				120			775	29.4
NW16 45 110				110			784	27.9
NW16 45 100				100			790	26.9
NW16 45 90				90			794	26.3
NW16 45 80				80			797	25.9
NW16 45 70				70			802	25.2

Butt weld

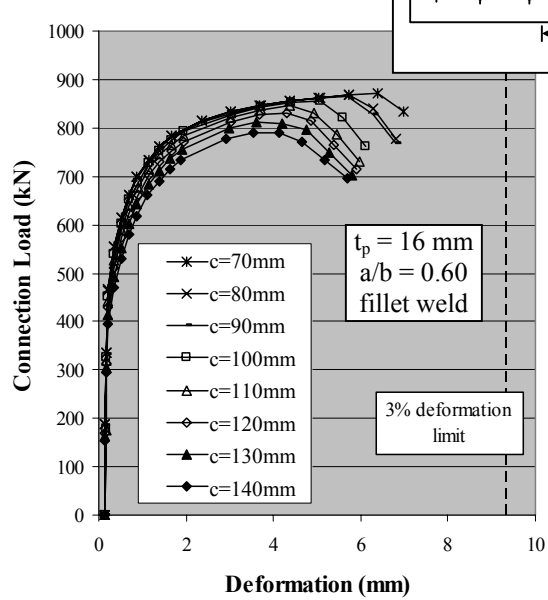
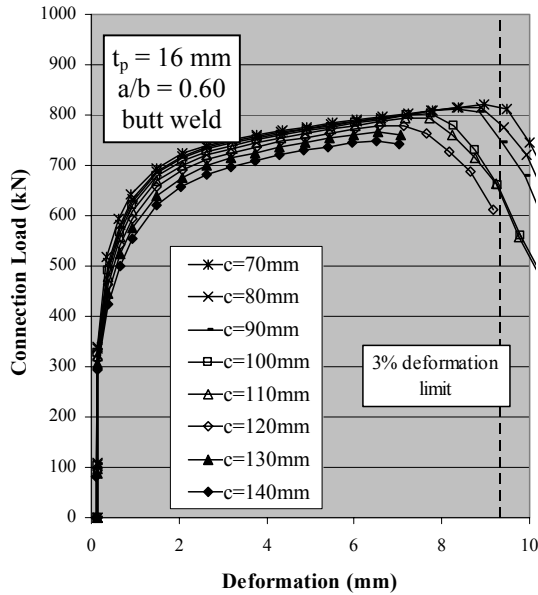
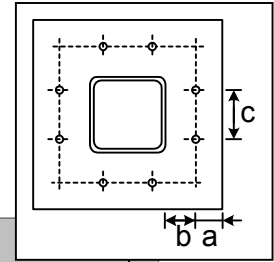
Connection	Properties					Results		
	n	a (mm)	b (mm)	c (mm)	t _p (mm)	Bolt strength F _{bu} (kN)	Connection strength N _{uFE} (kN)	Prying ratio β _{uFE} ¹⁾ (%)
W16 45 140	8	35	45	140	16	125	809	24.0
W16 45 130				130			831	20.8
W16 45 120				120			841	19.3
W16 45 110				110			853	17.6
W16 45 100				100			868	15.6
W16 45 90				90			872	15.1
W16 45 80				80			872	15.0
W16 45 70				70			872	15.0

Fillet weld

$$1) \beta_{uFE} = \frac{n \cdot F_{bu} - N_{uFE}}{N_{uFE}}$$

Load-Deformation Curves of Square Connections with eight Bolts (contd.)

(a = 30 mm, b = 50 mm, t_p = 16 mm)



Connection	Properties						Results	
	n	a (mm)	b (mm)	c (mm)	t _p (mm)	Bolt strength F _{bu} (kN)	Connection strength N _{uFE} (kN)	Prying ratio β _{uFE} ¹⁾ (%)
NW16_50_140	8	30	50	140	16	125	749	34.0
NW16_50_130				130			766	30.9
NW16_50_120				120			780	28.6
NW16_50_110				110			794	26.3
NW16_50_100				100			802	25.1
NW16_50_90				90			811	23.7
NW16_50_80				80			816	22.9
NW16_50_70				70			820	22.3

Butt weld

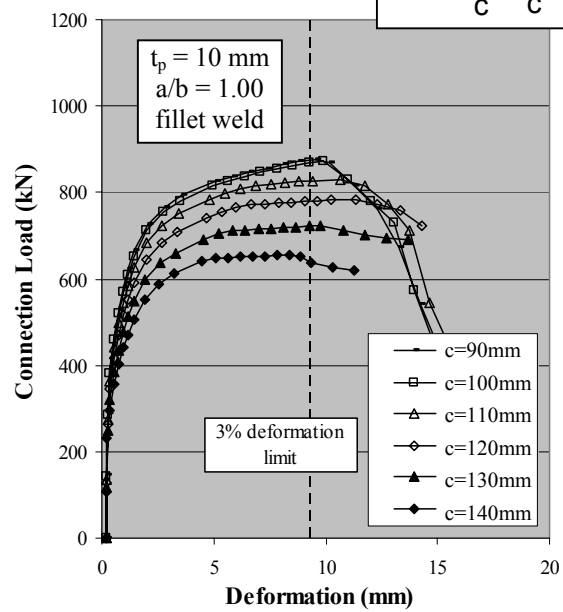
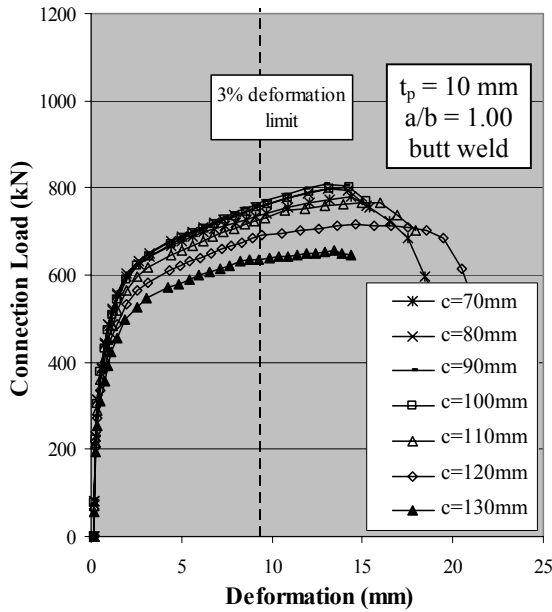
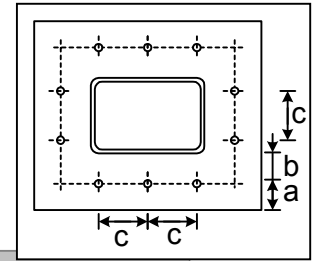
Connection	Properties						Results	
	n	a (mm)	b (mm)	c (mm)	t _p (mm)	Bolt strength F _{bu} (kN)	Connection strength N _{uFE} (kN)	Prying ratio β _{uFE} ¹⁾ (%)
W16_50_140	8	30	50	140	16	125	790	27.0
W16_50_130				130			811	23.7
W16_50_120				120			829	21.0
W16_50_110				110			845	18.7
W16_50_100				100			854	17.4
W16_50_90				90			865	16.0
W16_50_80				80			869	15.4
W16_50_70				70			872	15.1

Fillet weld

$$1) \beta_{uFE} = \frac{n \cdot F_{bu} - N_{uFE}}{N_{uFE}}$$

Load-Deformation Curves of Rectangular Connections with ten Bolts

(a = 40 mm, b = 40 mm, t_p = 10 mm)



Connection	Properties					Bolt strength F _{bu} (kN)	Results	
	n	a (mm)	b (mm)	c (mm)	t _p (mm)		Connection strength N _{uFE} (kN)	Prying ratio β _{uFE} ¹⁾ (%)
RNW10 40 130	10	40	40	130	10	126	636	98.7
RNW10 40 120				120			689	83.2
RNW10 40 110				110			728	73.6
RNW10 40 100				100			756	67.1
RNW10 40 90				90			764	65.3
RNW10 40 80				80			757	66.9
RNW10 40 70				70			738	71.2

Butt weld

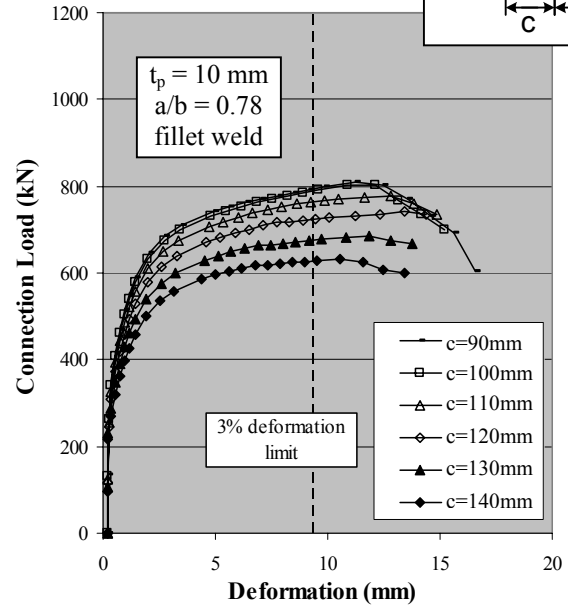
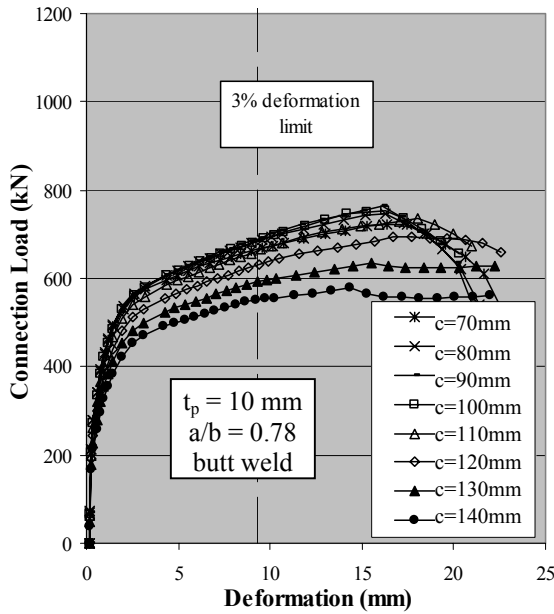
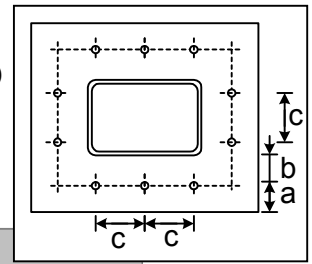
Connection	Properties					Bolt strength F _{bu} (kN)	Results	
	n	a (mm)	b (mm)	c (mm)	t _p (mm)		Connection strength N _{uFE} (kN)	Prying ratio β _{uFE} ¹⁾ (%)
RW10 40 140	10	40	40	140	10	126	655	92.9
RW10 40 130				130			722	75.0
RW10 40 120				120			780	61.9
RW10 40 110				110			826	52.9
RW10 40 100				100			870	45.2
RW10 40 90				90			874	44.6

Fillet weld

$$1) \beta_{uFE} = \frac{n \cdot F_{bu} - N_{uFE}}{N_{uFE}}$$

Load-Deformation Curves of Rectangular Connections with ten Bolts (contd.)

(a = 35 mm, b = 45 mm, t_p = 10 mm)



Connection	Properties					Bolt strength F _{bu} (kN)	Results	
	n	a (mm)	b (mm)	c (mm)	t _p (mm)		Connection strength N _{uFE} (kN)	Prying ratio β _{uFE} ¹⁾ (%)
RNW10 45 140	10	35	45	140	10	126	551	129.2
RNW10 45 130				130			592	113.2
RNW10 45 120				120			630	100.5
RNW10 45 110				110			662	90.8
RNW10 45 100				100			685	84.4
RNW10 45 90				90			690	83.1
RNW10 45 80				80			683	84.9
RNW10 45 70				70			665	89.8

Butt weld

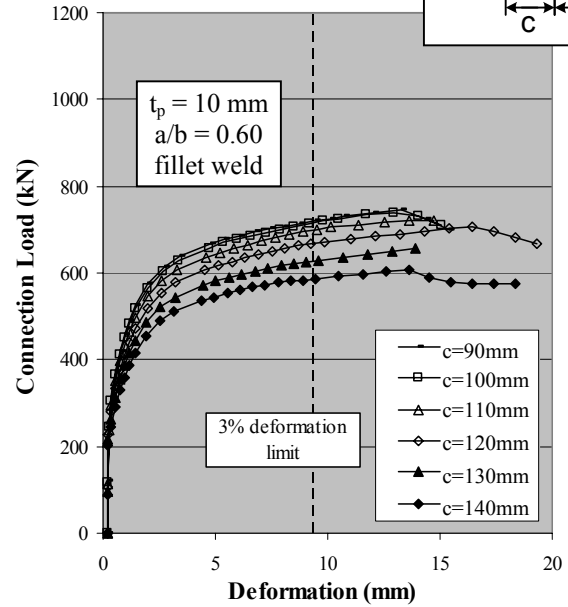
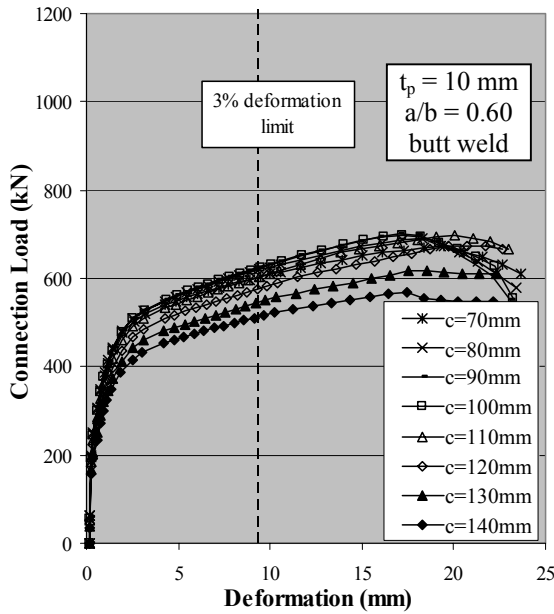
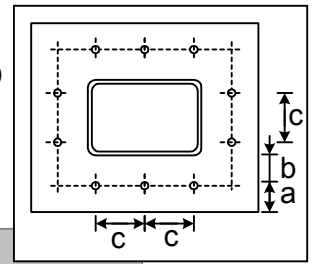
Connection	Properties					Bolt strength F _{bu} (kN)	Results	
	n	a (mm)	b (mm)	c (mm)	t _p (mm)		Connection strength N _{uFE} (kN)	Prying ratio β _{uFE} ¹⁾ (%)
RW10 45 140	10	35	45	140	10	126	627	101.5
RW10 45 130				130			674	87.3
RW10 45 120				120			723	74.8
RW10 45 110				110			765	65.2
RW10 45 100				100			788	60.3
RW10 45 90				90			793	59.3

Fillet weld

$$1) \beta_{uFE} = \frac{n \cdot F_{bu} - N_{uFE}}{N_{uFE}}$$

Load-Deformation Curves of Rectangular Connections with ten Bolts (contd.)

(a = 30 mm, b = 50 mm, t_p = 10 mm)



Connection	Properties						Results	
	n	a (mm)	b (mm)	c (mm)	t _p (mm)	Bolt strength F _{bu} (kN)	Connection strength N _{uFE} (kN)	Prying ratio β _{uFE} ¹⁾ (%)
RNW10_50_140	10	30	50	140	10	126	513	146.4
RNW10_50_130				130			545	131.8
RNW10_50_120				120			576	119.2
RNW10_50_110				110			603	109.4
RNW10_50_100				100			622	103.1
RNW10_50_90				90			624	102.4
RNW10_50_80				80			618	104.4
RNW10_50_70				70			602	109.7

Butt weld

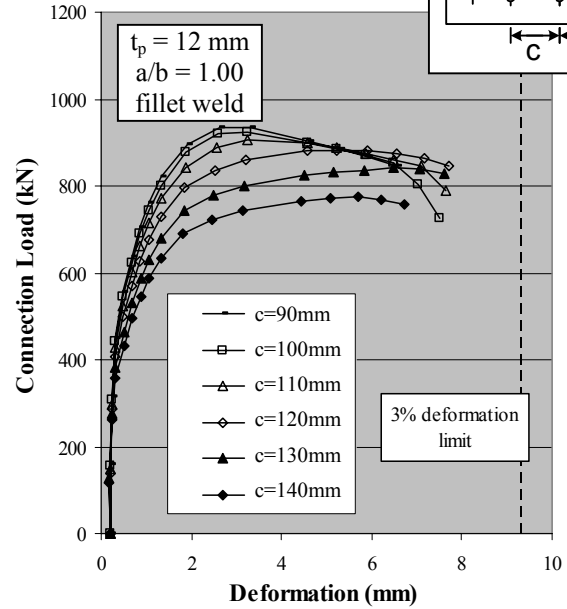
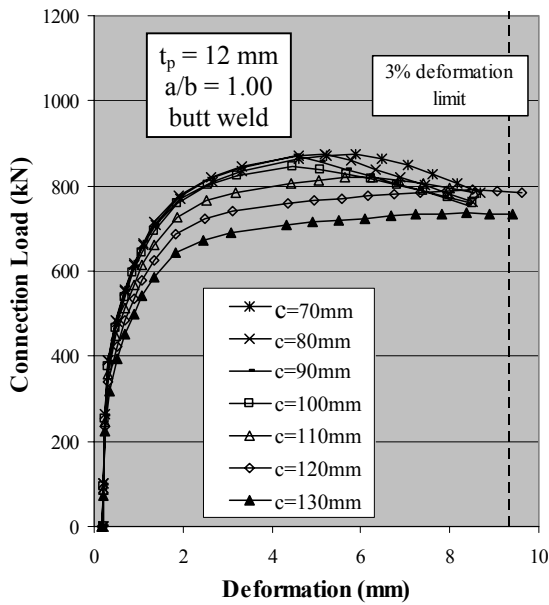
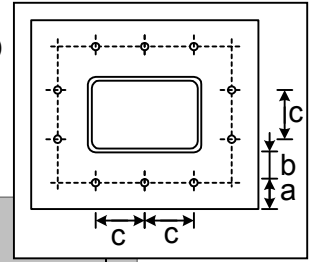
Connection	Properties						Results	
	n	a (mm)	b (mm)	c (mm)	t _p (mm)	Bolt strength F _{bu} (kN)	Connection strength N _{uFE} (kN)	Prying ratio β _{uFE} ¹⁾ (%)
RW10_50_140	10	30	50	140	10	126	586	115.7
RW10_50_130				130			627	101.5
RW10_50_120				120			668	89.2
RW10_50_110				110			698	80.9
RW10_50_100				100			715	76.8
RW10_50_90				90			718	75.9

Fillet weld

$$1) \beta_{uFE} = \frac{n \cdot F_{bu} - N_{uFE}}{N_{uFE}}$$

Load-Deformation Curves of Rectangular Connections with ten Bolts (contd.)

(a = 40 mm, b = 40 mm, t_p = 12 mm)



Connection	Properties					Bolt strength F _{bu} (kN)	Results	
	n	a (mm)	b (mm)	c (mm)	t _p (mm)		Connection strength N _{uFE} (kN)	Prying ratio β _{uFE} ¹⁾ (%)
RNW12 40 130	10	40	40	130	12	126	737	70.7
RNW12 40 120				120			791	58.9
RNW12 40 110				110			819	53.5
RNW12 40 100				100			845	48.8
RNW12 40 90				90			870	44.5
RNW12 40 80				80			874	43.8
RNW12 40 70				70			875	43.7

Butt weld

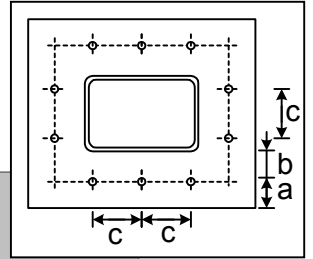
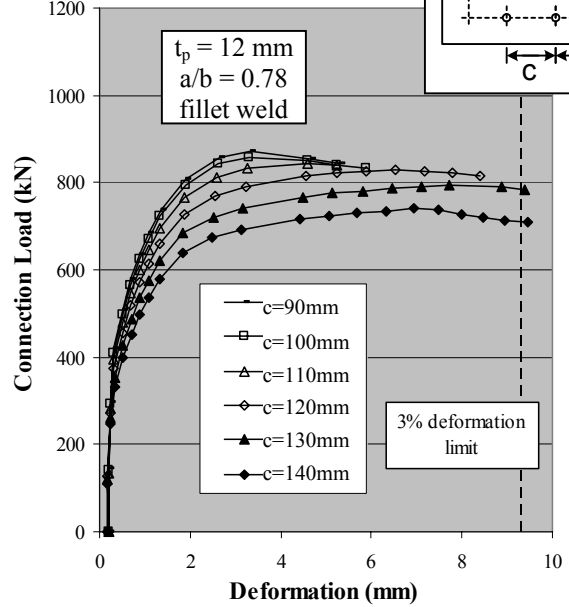
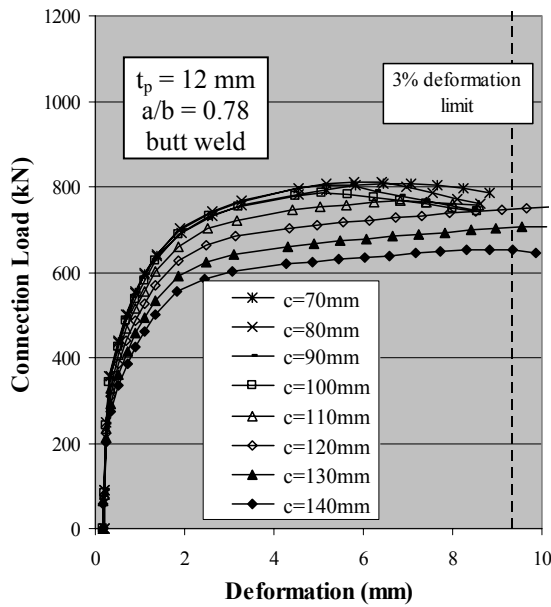
Connection	Properties					Bolt strength F _{bu} (kN)	Results	
	n	a (mm)	b (mm)	c (mm)	t _p (mm)		Connection strength N _{uFE} (kN)	Prying ratio β _{uFE} ¹⁾ (%)
RW12 40 140	10	40	40	140	12	126	776	62.0
RW12 40 130				130			841	49.5
RW12 40 120				120			883	42.4
RW12 40 110				110			905	38.9
RW12 40 100				100			923	36.1
RW12 40 90				90			936	34.3

Fillet weld

$$1) \beta_{uFE} = \frac{n \cdot F_{bu} - N_{uFE}}{N_{uFE}}$$

Load-Deformation Curves of Rectangular Connections with ten Bolts (contd.)

(a = 35 mm, b = 45 mm, t_p = 12 mm)



Connection	Properties					Bolt strength F _{bu} (kN)	Results	
	n	a (mm)	b (mm)	c (mm)	t _p (mm)		Connection strength N _{uFE} (kN)	Prying ratio β _{uFE} ¹⁾ (%)
RNW12 45 140	10	35	45	140	12	126	654	92.3
RNW12 45 130				130			704	78.5
RNW12 45 120				120			747	68.2
RNW12 45 110				110			766	64.1
RNW12 45 100				100			784	60.3
RNW12 45 90				90			803	56.4
RNW12 45 80				80			812	54.9
RNW12 45 70				70			809	55.4

Butt weld

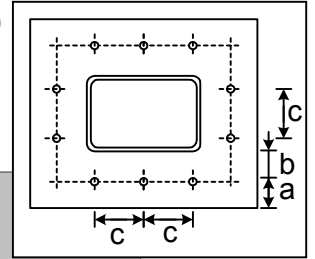
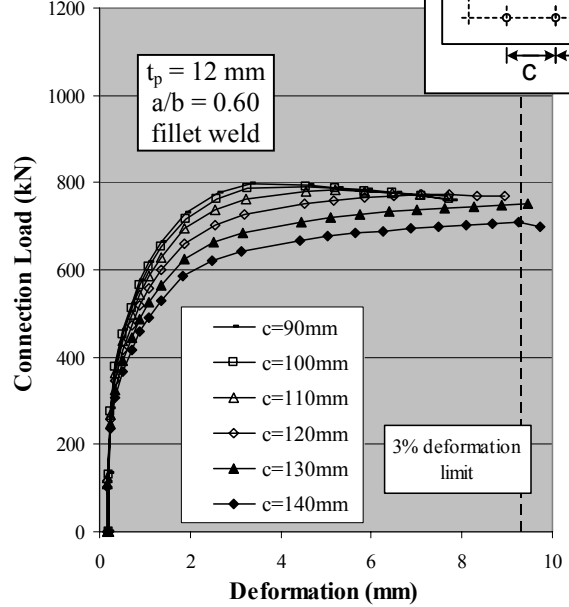
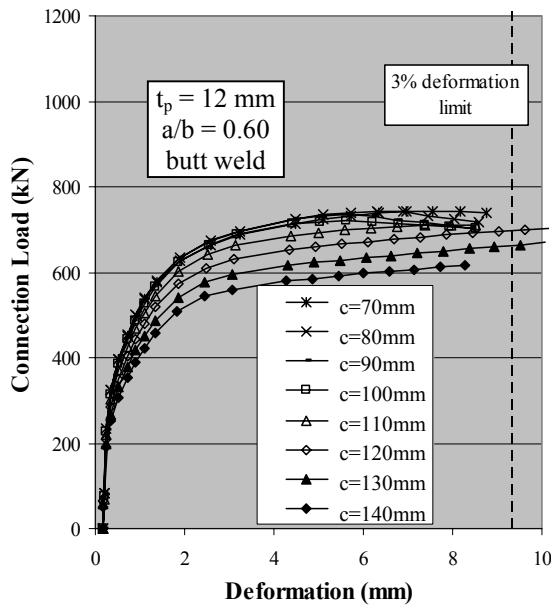
Connection	Properties					Bolt strength F _{bu} (kN)	Results	
	n	a (mm)	b (mm)	c (mm)	t _p (mm)		Connection strength N _{uFE} (kN)	Prying ratio β _{uFE} ¹⁾ (%)
RW12 45 140	10	35	45	140	12	126	740	69.9
RW12 45 130				130			794	58.3
RW12 45 120				120			828	51.8
RW12 45 110				110			844	48.9
RW12 45 100				100			859	46.3
RW12 45 90				90			870	44.4

Fillet weld

$$1) \beta_{uFE} = \frac{n \cdot F_{bu} - N_{uFE}}{N_{uFE}}$$

Load-Deformation Curves of Rectangular Connections with ten Bolts (contd.)

(a = 30 mm, b = 50 mm, t_p = 12 mm)



Connection	Properties					Bolt strength F _{bu} (kN)	Results	
	n	a (mm)	b (mm)	c (mm)	t _p (mm)		Connection strength N _{uFE} (kN)	Prying ratio β _{uFE} ¹⁾ (%)
RNW12_50_140	10	30	50	140	12	126	616	104.0
RNW12_50_130				130			663	89.7
RNW12_50_120				120			698	80.1
RNW12_50_110				110			710	77.0
RNW12_50_100				100			720	74.5
RNW12_50_90				90			735	71.0
RNW12_50_80				80			743	69.2
RNW12_50_70				70			743	69.1

Butt weld

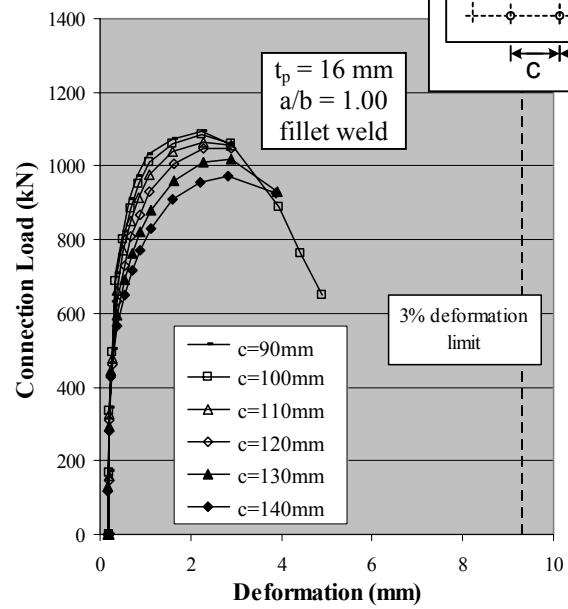
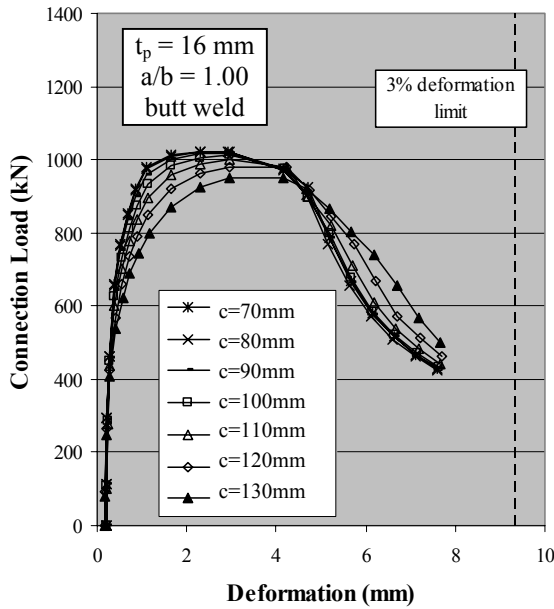
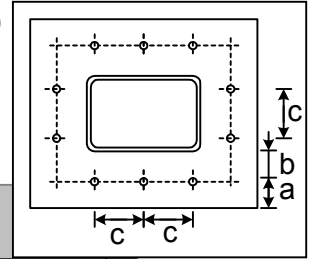
Connection	Properties					Bolt strength F _{bu} (kN)	Results	
	n	a (mm)	b (mm)	c (mm)	t _p (mm)		Connection strength N _{uFE} (kN)	Prying ratio β _{uFE} ¹⁾ (%)
RW12_50_140	10	30	50	140	12	126	708	77.5
RW12_50_130				130			752	67.1
RW12_50_120				120			772	62.8
RW12_50_110				110			782	60.7
RW12_50_100				100			790	59.2
RW12_50_90				90			870	44.4

Fillet weld

$$1) \beta_{uFE} = \frac{n \cdot F_{bu} - N_{uFE}}{N_{uFE}}$$

Load-Deformation Curves of Rectangular Connections with ten Bolts (contd.)

(a = 40 mm, b = 40 mm, t_p = 16 mm)



Connection	Properties					Bolt strength F _{bu} (kN)	Results	
	n	a (mm)	b (mm)	c (mm)	t _p (mm)		Connection strength N _{uFE} (kN)	Prying ratio β _{uFE} ¹⁾ (%)
RNW16 40 130	10	40	40	130	16	125	951	31.9
RNW16 40 120				120			981	27.8
RNW16 40 110				110			1001	25.2
RNW16 40 100				100			1014	23.7
RNW16 40 90				90			1019	23.0
RNW16 40 80				80			1022	22.7
RNW16 40 70				70			1024	22.5

Butt weld

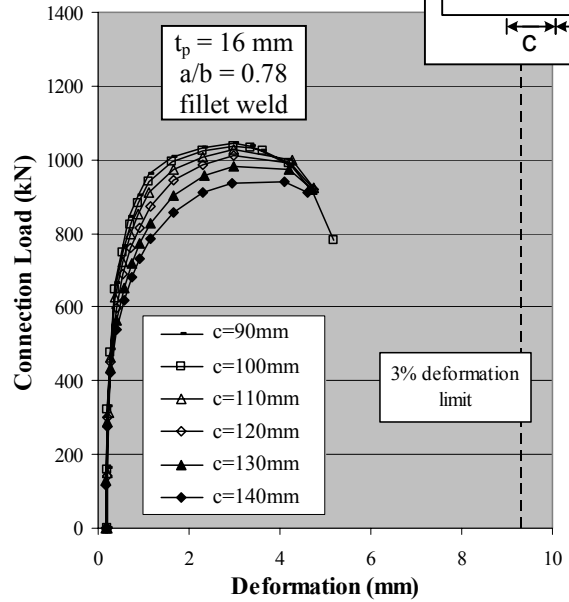
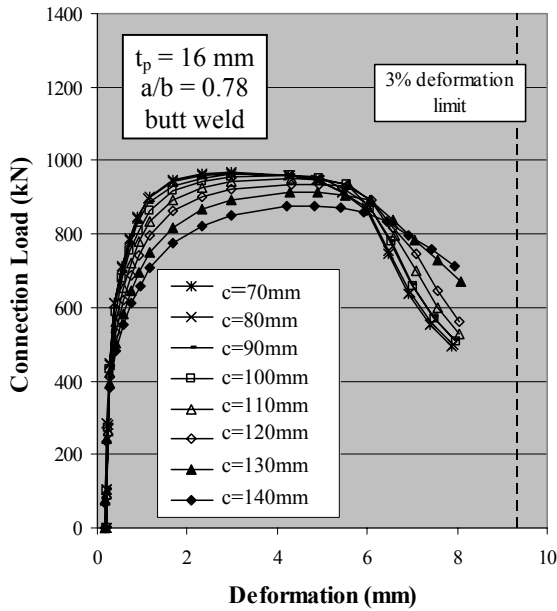
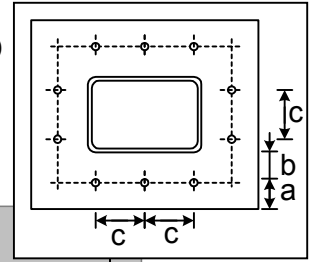
Connection	Properties					Bolt strength F _{bu} (kN)	Results	
	n	a (mm)	b (mm)	c (mm)	t _p (mm)		Connection strength N _{uFE} (kN)	Prying ratio β _{uFE} ¹⁾ (%)
RW16 40 140	10	40	40	140	16	125	973	28.9
RW16 40 130				130			1020	22.9
RW16 40 120				120			1049	19.6
RW16 40 110				110			1066	17.7
RW16 40 100				100			1087	15.4
RW16 40 90				90			1094	14.7

Fillet weld

$$1) \beta_{uFE} = \frac{n \cdot F_{bu} - N_{uFE}}{N_{uFE}}$$

Load-Deformation Curves of Rectangular Connections with ten Bolts (contd.)

(a = 35 mm, b = 45 mm, t_p = 16 mm)



Connection	Properties					Bolt strength F _{bu} (kN)	Results	
	n	a (mm)	b (mm)	c (mm)	t _p (mm)		Connection strength N _{uFE} (kN)	Prying ratio β _{uFE} ¹⁾ (%)
RNW16 45 140	10	35	45	140	16	125	876	43.1
RNW16 45 130				130			915	37.0
RNW16 45 120				120			936	33.9
RNW16 45 110				110			950	32.0
RNW16 45 100				100			958	30.9
RNW16 45 90				90			962	30.3
RNW16 45 80				80			966	29.8
RNW16 45 70				70			967	29.7

Butt weld

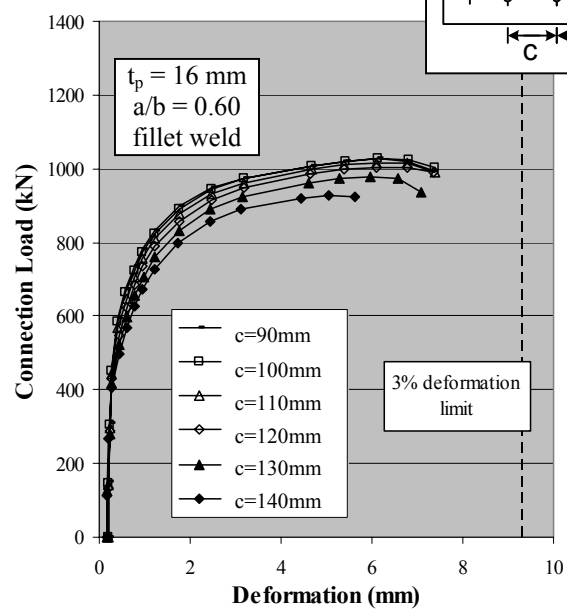
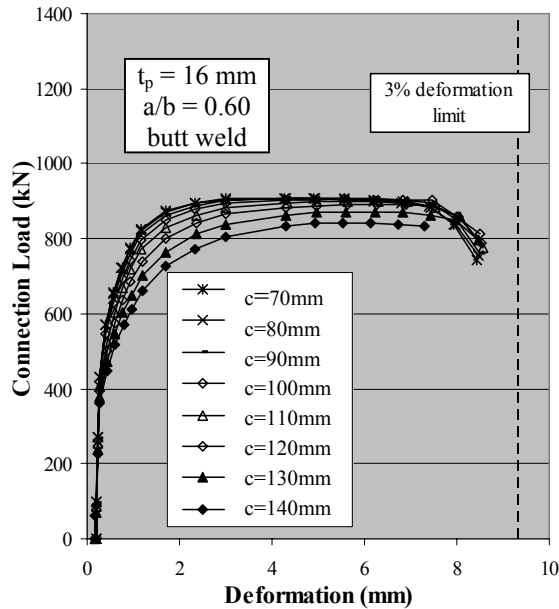
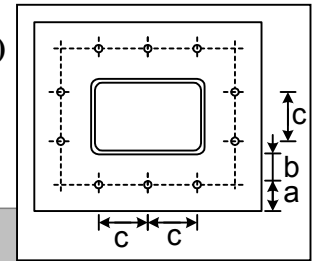
Connection	Properties					Bolt strength F _{bu} (kN)	Results	
	n	a (mm)	b (mm)	c (mm)	t _p (mm)		Connection strength N _{uFE} (kN)	Prying ratio β _{uFE} ¹⁾ (%)
RW16 45 140	10	35	45	140	16	125	941	33.2
RW16 45 130				130			983	27.5
RW16 45 120				120			1009	24.2
RW16 45 110				110			1027	22.1
RW16 45 100				100			1038	20.8
RW16 45 90				90			870	44.4

Fillet weld

$$^1) \beta_{uFE} = \frac{n \cdot F_{bu} - N_{uFE}}{N_{uFE}}$$

Load-Deformation Curves of Rectangular Connections with ten Bolts (contd.)

(a = 30 mm, b = 50 mm, t_p = 16 mm)



Connection	Properties					Results		
	n	a (mm)	b (mm)	c (mm)	t _p (mm)	Bolt strength F _{bu} (kN)	Connection strength N _{uFE} (kN)	Prying ratio β _{uFE} ¹⁾ (%)
RNW16_50_140	10	30	50	140	16	125	842	48.9
RNW16_50_130				130			872	43.8
RNW16_50_120				120			891	40.7
RNW16_50_110				110			901	39.2
RNW16_50_100				100			905	38.5
RNW16_50_90				90			908	38.1
RNW16_50_80				80			909	37.9
RNW16_50_70				70			909	38.0

Butt weld

Connection	Properties					Results		
	n	a (mm)	b (mm)	c (mm)	t _p (mm)	Bolt strength F _{bu} (kN)	Connection strength N _{uFE} (kN)	Prying ratio β _{uFE} ¹⁾ (%)
RW16_50_140	10	30	50	140	16	125	927	35.3
RW16_50_130				130			978	28.2
RW16_50_120				120			1005	24.8
RW16_50_110				110			1016	23.4
RW16_50_100				100			1028	21.9
RW16_50_90				90			1028	22.0

Fillet weld

$$^1) \beta_{uFE} = \frac{n \cdot F_{bu} - N_{uFE}}{N_{uFE}}$$

Analytical Study

One-Dimensional Yield Line Model

Equation 5.3

$$\sum M_2 - m_y p_2 = Q_b(a+b) - (N_b + Q_b) b \quad (1)$$

with:

$$\begin{aligned} N_b + Q_b &= F_{bu} & (2) \\ \Leftrightarrow Q_b &= F_{bu} - N_b \end{aligned}$$

(2) in (1):

$$\begin{aligned} -m_y p_2 &= (F_{bu} - N_b)(a+b) - F_{bu} b \\ \Leftrightarrow N_b(a+b) &= (F_{bu} a + m_y p_2) \\ \Leftrightarrow N_b &= \frac{1}{a+b} (F_{bu} a + m_y p_2) \end{aligned}$$

Equation 5.4

$$\sum M_1 - m_y p_1 = Q_b a \quad (1)$$

$$\Leftrightarrow Q_b = \frac{1}{a} m_y p_1$$

$$\sum M_2 - m_y p_2 = Q_b(a+b) - (N_b + Q_b) b \quad (2)$$

(1) in (2):

$$\begin{aligned} -m_y p_2 &= \frac{1}{a} m_y p_1 (a+b) - (N_b + \frac{1}{a} m_y p_1) b \\ \Leftrightarrow N_b b &= m_y p_1 + m_y p_2 \\ \Leftrightarrow N_b &= \frac{p_1 + p_2}{b} m_y \end{aligned}$$

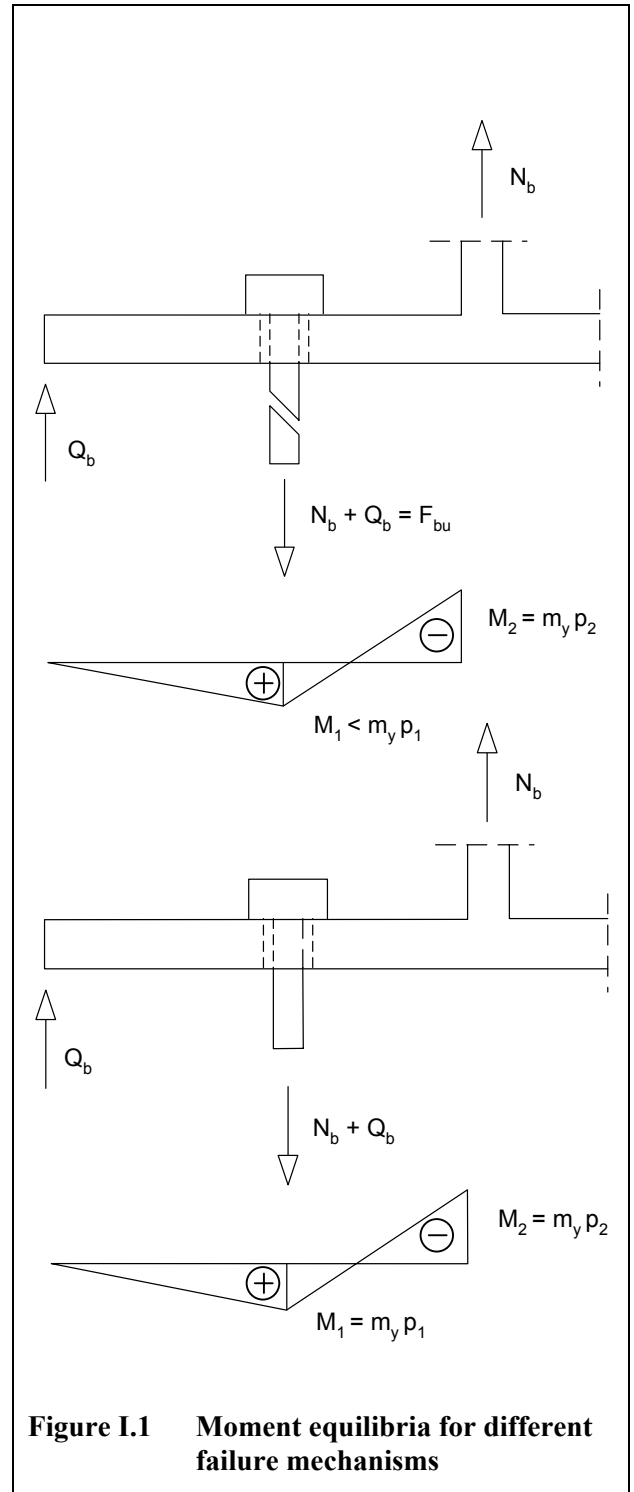


Figure I.1 Moment equilibria for different failure mechanisms

Equation 5.8

For $t_p = t_{q2}$ the connection strength due to Failure mechanism 2 (Equation 5.3b) equals the connection strength due to Failure mechanism 3 (Equation 5.4b), thus:

$$\begin{aligned} \frac{1}{a+b} (F_{bu} \cdot a + \frac{1}{4} F_{yp} t_{q2}^2 \cdot p_2) &= \frac{p_1 + p_2}{b} \cdot \frac{1}{4} F_{yp} t_{q2}^2 \\ \Leftrightarrow \left(\frac{p_2}{a+b} - \frac{p_1 + p_2}{b} \right) \frac{1}{4} F_{yp} t_{q2}^2 &= -\frac{1}{a+b} F_{bu} \cdot a \\ \Leftrightarrow (p_2 b - (p_1 + p_2)(a+b)) \frac{1}{4} F_{yp} t_{q2}^2 &= -F_{bu} \cdot a \cdot b \\ \Leftrightarrow ((p_1 + p_2)a + p_1 b) \frac{1}{4} F_{yp} t_{q2}^2 &= F_{bu} \cdot a \cdot b \\ \Leftrightarrow \left(\frac{p_1 + p_2}{b} + \frac{p_1}{a} \right) \frac{1}{4} F_{yp} t_{q2}^2 &= F_{bu} \\ \Leftrightarrow t_{q2} &= \sqrt{\frac{4F_{bu}}{\left(\frac{p_1 + p_2}{b} + \frac{p_1}{a} \right) F_{yp}}} \end{aligned}$$

Two-Dimensional Yield Line Model

Analysis of yield line mechanism

Assuming a virtual displacement δ the internal and external work of the yield line mechanism as shown in Figure A.2 is calculated based on varying lengths x_h and x_w . The lengths x_{minh} and x_{minw} then correspond to the minimum failure load $P(x_{minh}, x_{minw})$.

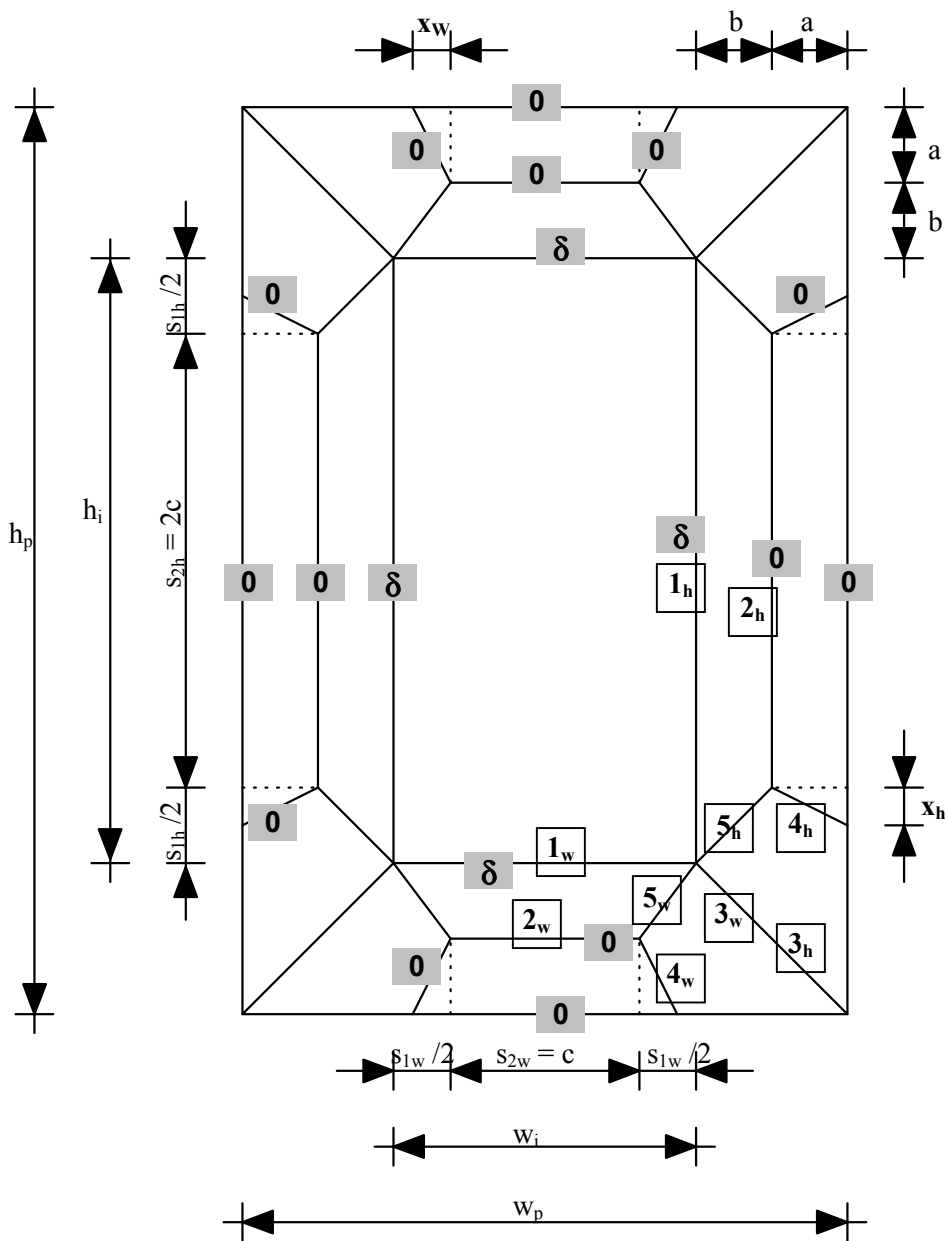


Figure I.2 Symbols

External work:

$$W_{\text{ext}} = N \cdot \delta$$

Internal work:

$$W_{\text{int}} = \sum W_{\text{int},i} \text{ with } W_{\text{int},i} \text{ being the internal work done by segment } i$$

Segment 1

$$W_{\text{int},1} = W_{\text{int},1h} + W_{\text{int},1w} = [2(s_{1h} + s_{2h}) \theta_{1h} + 2(s_{1w} + s_{2w}) \theta_{1w}] m_y$$

$$\text{with } \theta_{1h} = \theta_{1w} = \frac{\delta}{b}$$

$$\Rightarrow W_{\text{int},1} = [2(s_{1h} + s_{2h}) + 2(s_{1w} + s_{2w})] \frac{\delta}{b} m_y$$

Segment 2

$$W_{\text{int},2} = W_{\text{int},2h} + W_{\text{int},2w} = [2 s_{2h} \theta_{2h} + 2 s_{2w} \theta_{2w}] m_y$$

$$\text{with } \theta_{2h} = \theta_{2w} = \frac{\delta}{b}$$

$$\Rightarrow W_{\text{int},2} = [2 s_{2h} + 2 s_{2w}] \frac{\delta}{b} m_y$$

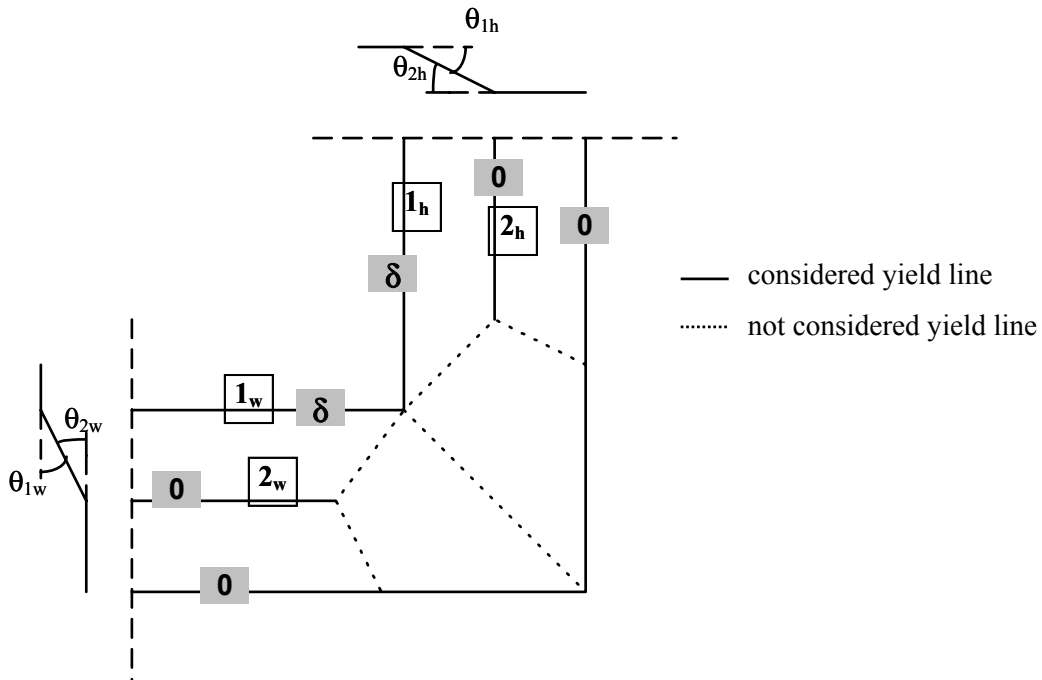


Figure I.3 Angles θ_{1h} , θ_{1w} and θ_{2h} , θ_{2w}

Segment 3

$$W_{\text{int},3} = W_{\text{int},3h} + W_{\text{int},3w} = [4 l_3 \theta_{3h} + 4 l_3 \theta_{3w}] m_y$$

$$\text{with } l_3 = \sqrt{2} (a+b)$$

$$\text{and } \theta_{3h} = \frac{\delta}{l'_h}, \theta_{3w} = \frac{\delta}{l'_w}$$

Looking at segment 3_w:

$$y_1 + y_2 = \sqrt{2} a \quad \text{and} \quad \frac{y_1}{y_2} = \frac{x_w + a + b - s_{1w}/2}{s_{1w}/2 - b}$$

$$\Rightarrow y_2 = \sqrt{2} a \left(\frac{s_{1w}/2 - b}{x_w + a} \right)$$

$$l'_w = \sqrt{2} b + y_2$$

$$\Rightarrow l'_w = \frac{1}{\sqrt{2}} \frac{2bx_w + as_{1w}}{x_w + a}$$

$$\Rightarrow \theta_{3w} = \frac{\delta}{l'_w} = \sqrt{2} \frac{x_w + a}{2bx_w + as_{1w}} \delta$$

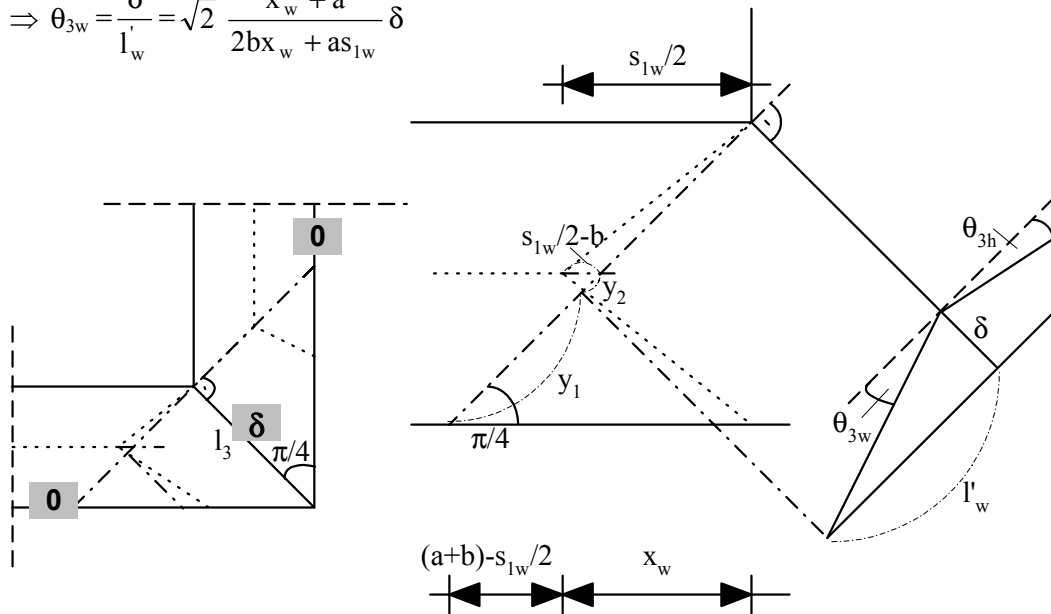


Figure I.4 Angles θ_{3w} , θ_{3h} and lengths l'_w , y_1 and y_2

Calculating θ_{3h} accordingly, the internal work done by segment 3 is:

$$W_{\text{int},3} = 8(a+b) \left[\frac{x_h + a}{2bx_h + as_{1h}} + \frac{x_w + a}{2bx_w + as_{1w}} \right] \delta m_y$$

Segment 4

$$W_{\text{int},4} = W_{\text{int},4h} + W_{\text{int},4w} = 4(l_{4h} \theta_{4h} + l_{4w} \theta_{4w}) m_y$$

$$\text{with } \theta_{4h} = \frac{\delta}{l_h''}, \theta_{4w} = \frac{\delta}{l_w''}$$

Looking at segment 4_w:

$$z_1 + z_2 = a \quad \text{and} \quad \frac{z_2}{z_1} = \frac{s_{1w}/2}{x_w - s_{1w}/2}$$

$$\Rightarrow z_2 = \frac{a}{x_w} s_{1w}/2$$

$$\frac{l_w''}{b + z_2} = \frac{x_w}{l_{4w}}$$

$$\Rightarrow l_w'' = \frac{1}{l_{4w}} (bx_w + as_{1w}/2)$$

$$\Rightarrow \theta_{4w} = l_{4w} \frac{1}{bx_w + as_{1w}/2} \delta$$

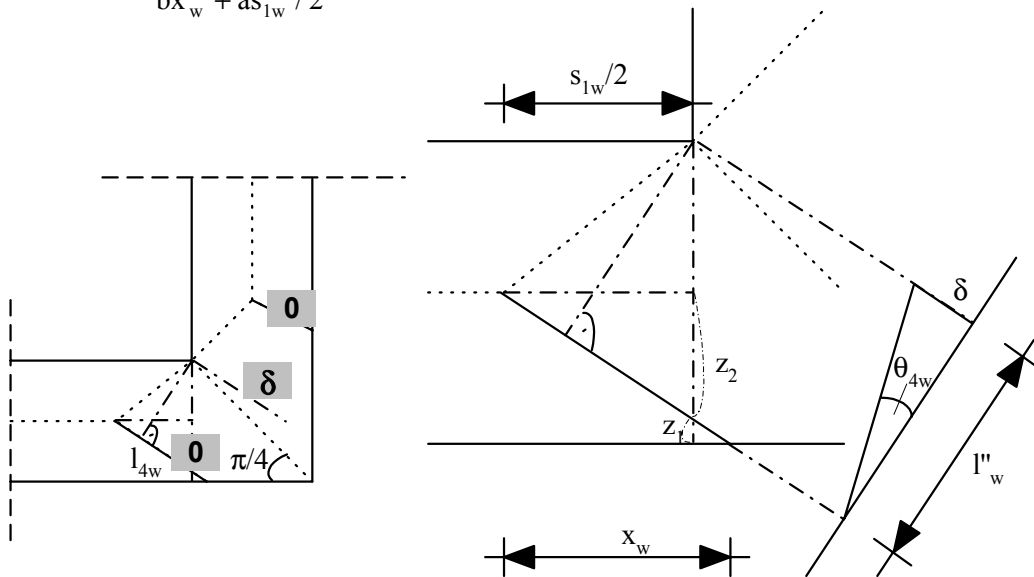


Figure I.5 Angle θ_{4w} and lengths l_w'' , z_1 and z_2

Calculating θ_{4h} accordingly, the internal work done by segment 4 is:

$$W_{\text{int},4} = 4 \left(l_{4h}^2 \frac{1}{bx_h + as_{1h}/2} + l_{4w}^2 \frac{1}{bx_w + as_{1w}/2} \right) \delta m_y$$

$$\text{with } l_{4h}^2 = a^2 + x_h^2 \quad \text{and} \quad l_{4w}^2 = a^2 + x_w^2$$

$$\Rightarrow W_{\text{int},4} = 4 \left(\frac{a^2 + x_h^2}{bx_h + as_{1h}/2} + \frac{a^2 + x_w^2}{bx_w + as_{1w}/2} \right) \delta m_y$$

Segment 5

$$W_{int,5} = W_{int,5h} + W_{int,5w} = 4(l_{5h} \theta_{5h} + l_{5w} \theta_{5w}) m_y$$

Looking at segment 5_w :

$$\theta_{5w} = \frac{\delta - \delta'}{q_1} - \frac{\delta'}{q_2} \quad \text{with} \quad \frac{\delta'}{\delta} = \frac{r_1}{l_{5w}}$$

$$\Rightarrow \theta_{5w} = \left(\frac{1}{q_1} \left(1 - \frac{r_1}{l_{5w}} \right) - \frac{1}{q_2} \frac{r_1}{l_{5w}} \right) \delta$$

solving for r₁, q₁ and q₂ :

$$\frac{r_1}{b} = \frac{b}{l_{5w}} \quad \Rightarrow \quad r_1 = \frac{b^2}{l_{5w}} \quad \Rightarrow \quad \frac{r_1}{l_{5w}} = \left(\frac{b}{l_{5w}} \right)^2$$

$$\frac{q_1}{b} = \frac{s_1/2}{l_{5w}} \quad \Rightarrow \quad q_1 = s_1/2 \frac{b}{l_{5w}}$$

$$\frac{q_2}{r_1} = \frac{l''}{\sqrt{l_{5w}^2 - l''^2}} \quad \Rightarrow \quad q_2 = \frac{l''}{\sqrt{l_{5w}^2 - l''^2}} \frac{b^2}{l_{5w}}$$

using the equations

$$l_{5w}^2 = (s_{1w}/2)^2 + b^2 \quad \text{and} \quad l_w''^2 = \frac{(bx_w + as_{1w}/2)^2}{a^2 + x_w^2} \quad (\text{see Segment 4})$$

$$\Rightarrow \theta_{5w} = \frac{1}{l_{5w}} \frac{a(s_{1w}^2 + 4b^2)}{2b(2bx_w + as_{1w})} \delta$$

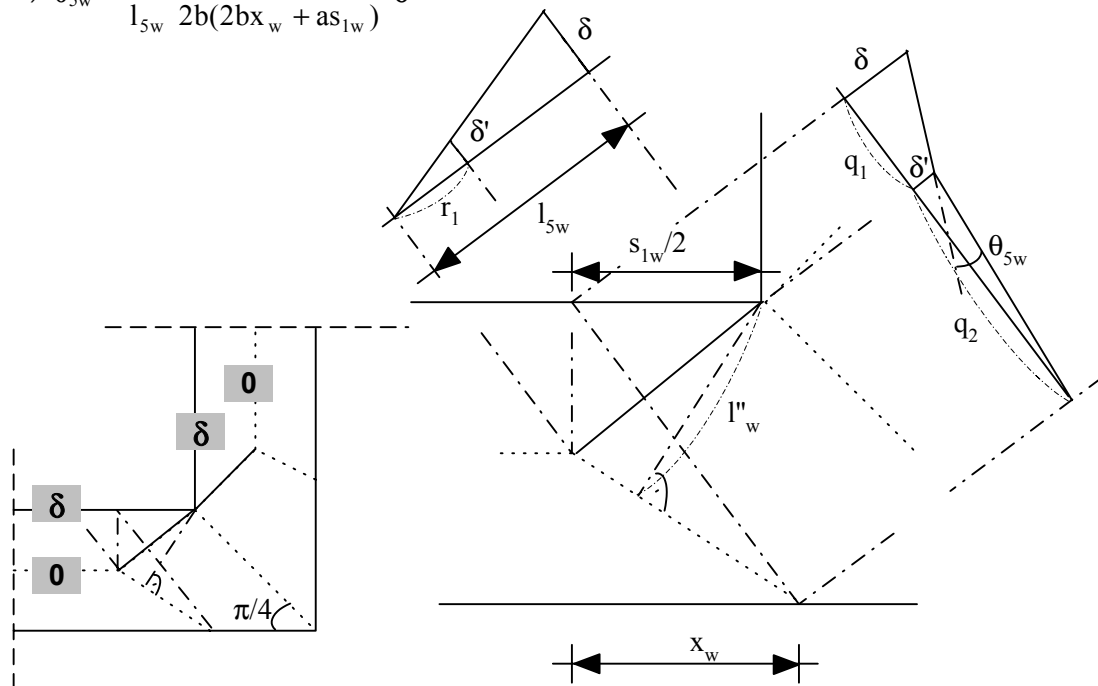


Figure I.6 Angle θ_{5w} , l''_w , lengths r_1 , q_1 and q_2 and displacement δ'

Calculating θ_{5h} accordingly, the internal work done by segment 5 is:

$$W_{int,5} = 4 \left(\frac{a(s_{1h}^2 + 4b^2)}{2b(2bx_h + as_{1h})} + \frac{a(s_{1w}^2 + 4b^2)}{2b(2bx_w + as_{1w})} \right) \delta m_y$$

The internal work done by the flange-plate is depending on the variables x_h and x_w (yield line pattern) and equals the sum of all segments:

$$W_{int}(x_h, x_w) = W_{int,1} + W_{int,2} + W_{int,3} + W_{int,4} + W_{int,5}$$

By equating the internal and external work the ultimate load for the yield line mechanism is found:

$$N(x_h, x_w) = 2 \left\{ \frac{s_{1h} + s_{1w} + 2(s_{2h} + s_{2w})}{b} + \frac{4b[x_h^2 + (a+b)x_h] + a[s_{1h}^2 + 8ab + 8b^2]}{b(2bx_h + as_{1h})} \right. \\ \left. + \frac{4b[x_w^2 + (a+b)x_w] + a[s_{1w}^2 + 8ab + 8b^2]}{b(2bx_w + as_{1w})} \right\} m_y$$

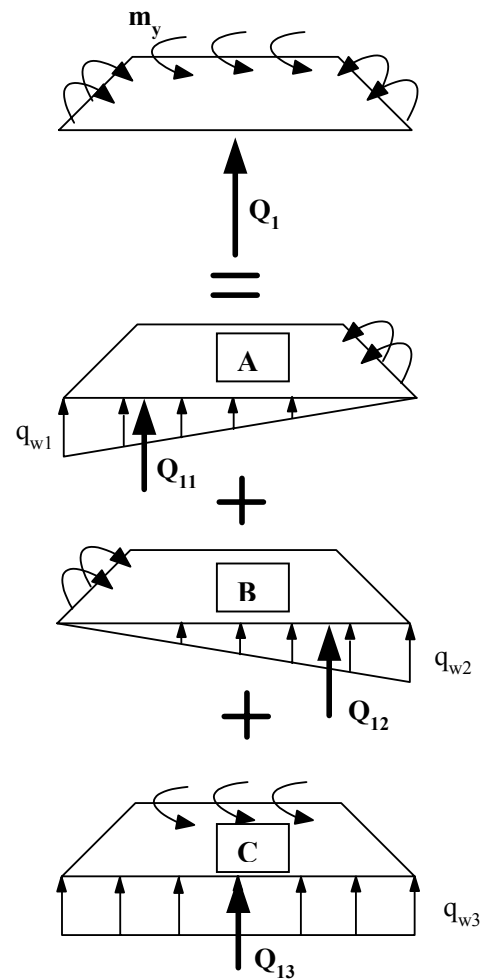
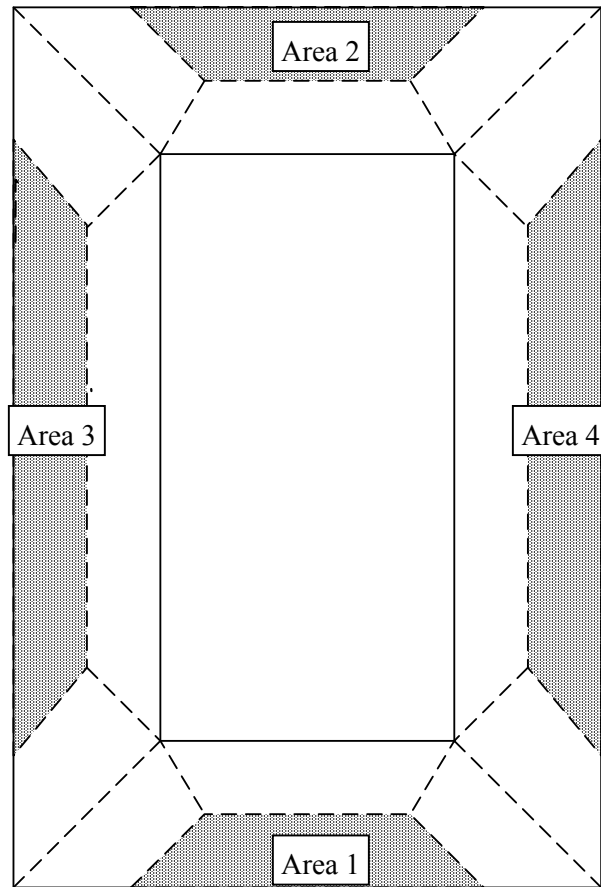
The governing yield line pattern is the pattern caused by the minimum ultimate load. As x_h and x_w are independent variables the lengths x_{minh} and x_{minw} corresponding to the minimum collapse load can be found by the operation $\frac{\partial N}{\partial x_h} = 0$ and $\frac{\partial N}{\partial x_w} = 0$. The lengths x_{minh} and x_{minw} corresponding to the minimum collapse load are then:

$$x_{minh} = \frac{a}{2} \left(\sqrt{\left(1 + \frac{b}{a}\right) \left(\frac{s_{1h}^2}{b^2} - 2\frac{s_{1h}}{b} + 8\right)} - \frac{s_{1h}}{b} \right)$$

$$\text{and } x_{minw} = \frac{a}{2} \left(\sqrt{\left(1 + \frac{b}{a}\right) \left(\frac{s_{1w}^2}{b^2} - 2\frac{s_{1w}}{b} + 8\right)} - \frac{s_{1w}}{b} \right).$$

Introducing the lengths x_{minh} and x_{minw} into the expression for N , the corresponding critical load N_{yp} becomes:

$$N_{yp} = 8 \left\{ \frac{a}{2b} \sqrt{1 + \frac{b}{a}} \left(\sqrt{\frac{s_{1h}^2}{b^2} - 2\frac{s_{1h}}{b} + 8} + \sqrt{\frac{s_{1w}^2}{b^2} - 2\frac{s_{1w}}{b} + 8} \right) + \frac{1}{4} \frac{s_{1h} + s_{1w}}{b} \right. \\ \left. + \frac{1}{2} \frac{s_{2h} + s_{2w}}{b} + \frac{a}{b} \left(1 - \frac{s_{1h} + s_{1w}}{2b}\right) + 1 \right\} m_y$$

Calculation of the prying force**Figure I.7 Linear distributed prying force**

Assuming the prying force is acting only along the edges of the flange-plate contacting each other, the prying force can be calculated. The linear distribution of the prying force is shown in Figure A.7. For each area the prying force can be divided into three linear distributed forces, each opposing the bending moment along one side of the trapezium. The prying force Q_1 acting on Area 1 thus becomes:

$$Q_1 = Q_{11} + Q_{12} + Q_{13}.$$

To find Q_{11} trapezium A (Area 1) is analysed. According to Figure A.8 the linear distributed prying force at a distance x from the bending axis is:

$$q_x = \frac{q_{w1}}{h_1} x.$$

The bending moment acting on a small segment ds , caused by the prying force is

$$dM = q_x x ds$$

$$\text{with } ds = \frac{s_2 + 2x_{\min w}}{h_1} dx.$$

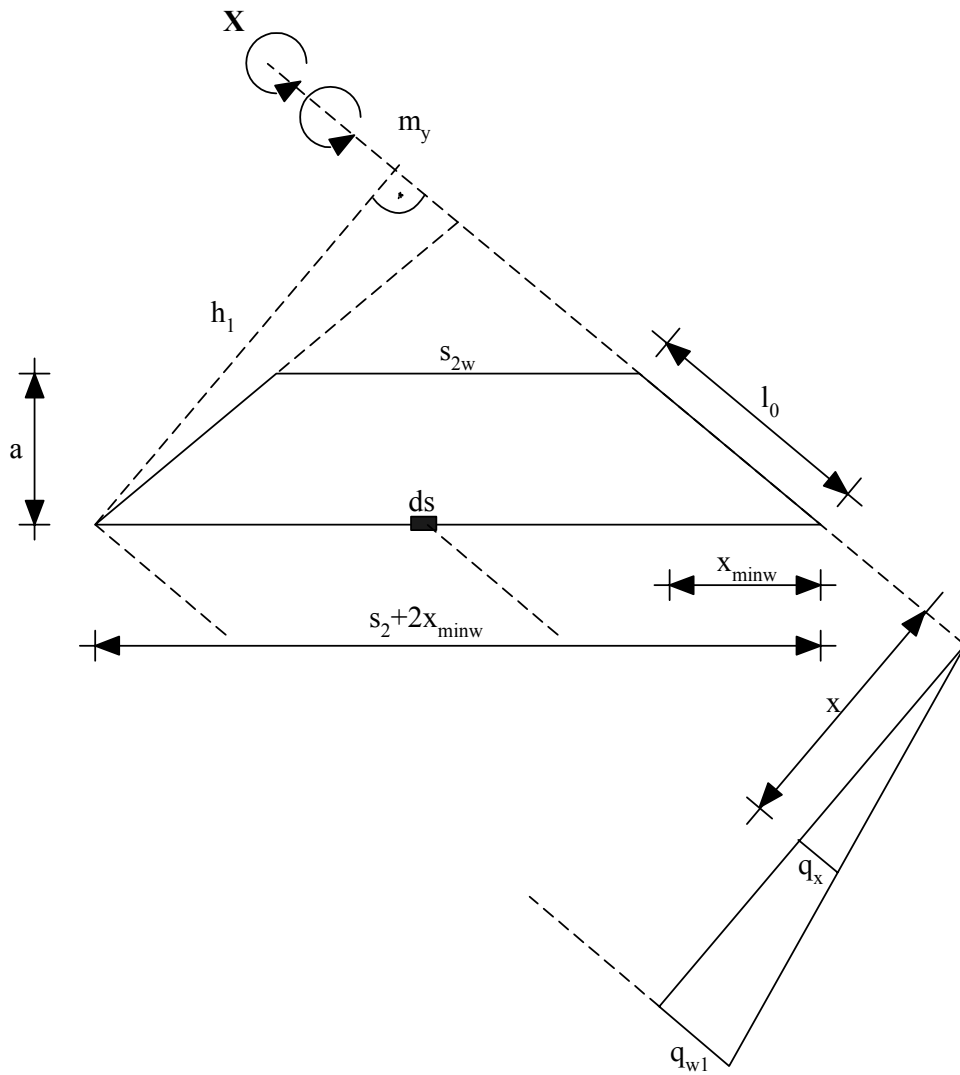


Figure I.8 Distribution of the prying stress

The bending moment about the X-Axis due to the prying force is:

$$M_1 = \int dM = \frac{q_{w1}}{h_1} \frac{s_2 + 2x_{\min w}}{h_1} \int_0^{h_1} x^2 dx = \frac{1}{3} \frac{a(s_2 + 2x_{\min w})^2}{l_0} q_{w1}$$

This moment has to balance the plastic moment m_y of the flange-plate, thus:

$$M_1 = l_0 m_y.$$

Solving this equilibrium for q_{w1} , q_{w1} becomes:

$$q_{w1} = \frac{3l_0^2 m_y}{a(s_2 + 2x_{\min w})^2}$$

The prying force balancing the plastic moment along this side then becomes:

$$Q_{11} = \int_0^{h_1} q_x ds = \int_0^{h_1} \frac{q_{w1}}{h_1} \frac{s_2 + 2x_{\min w}}{h_1} x dx = \frac{1}{2} (s_2 + 2x_{\min w}) q_{w1}$$

Inserting the earlier calculated q_{w1} , and knowing that $l_0^2 = a^2 + x_{\min w}^2$, the prying force Q_{11} is then:

$$Q_{11} = \frac{3}{2} \frac{a^2 + x_{\min w}^2}{a(s_{2w} + 2x_{\min w})} m_y.$$

In the same way the prying forces Q_{12} and Q_{13} are found:

$$Q_{12} = Q_{11} = \frac{3}{2} \frac{a^2 + x_{\min w}^2}{a(s_{2w} + 2x_{\min w})} m_y$$

$$Q_{13} = \frac{s_{2w}}{a} m_y$$

Using the above derivation, the prying forces acting on Area 2 to 4 are found. The total prying force acting on the flange-plate connection is thus:

$$Q = Q_1 + Q_2 + Q_3 + Q_4 = 2 \left[\frac{3(1 + (\frac{x_{\min h}}{a})^2)}{\frac{s_{2h}}{a} + 2\frac{x_{\min h}}{a}} + \frac{3(1 + (\frac{x_{\min w}}{a})^2)}{\frac{s_{2w}}{a} + 2\frac{x_{\min w}}{a}} + \frac{s_{2h} + s_{2w}}{a} \right] m_y$$

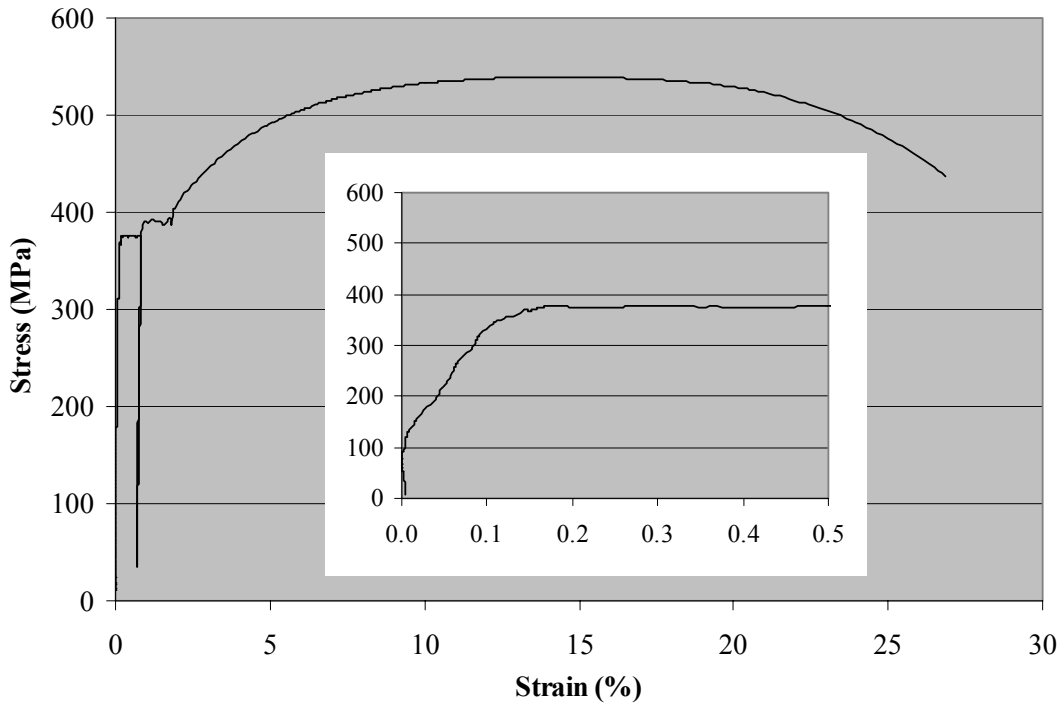
APPENDIX PART II

Experimental Study	II-2
Tensile coupon Tests	II-2
Square Hollow Section (200 x 6.3 mm)	II-2
Square Hollow Section (200 x 12.5 mm)	II-2
Gusset Plate ($t_p = 12$ mm)	II-3
Gusset Plate ($t_p = 20$ mm)	II-3
Gusset Plate ($t_p = 25$ mm)	II-4
Strain Gauge Measurements	II-5
Strain Gauge Measurements of the Hollow Section	II-5
Strain Gauge Measurements of the Gusset Plate	II-9
Numerical Study	II-13
Numerical results	II-13
Results of square connections ($w_i/h_i = 1.00$)	II-13
Results of rectangular connections with $w_i/h_i = 0.67$	II-13
Results of rectangular connections with $w_i/h_i = 0.50$	II-13

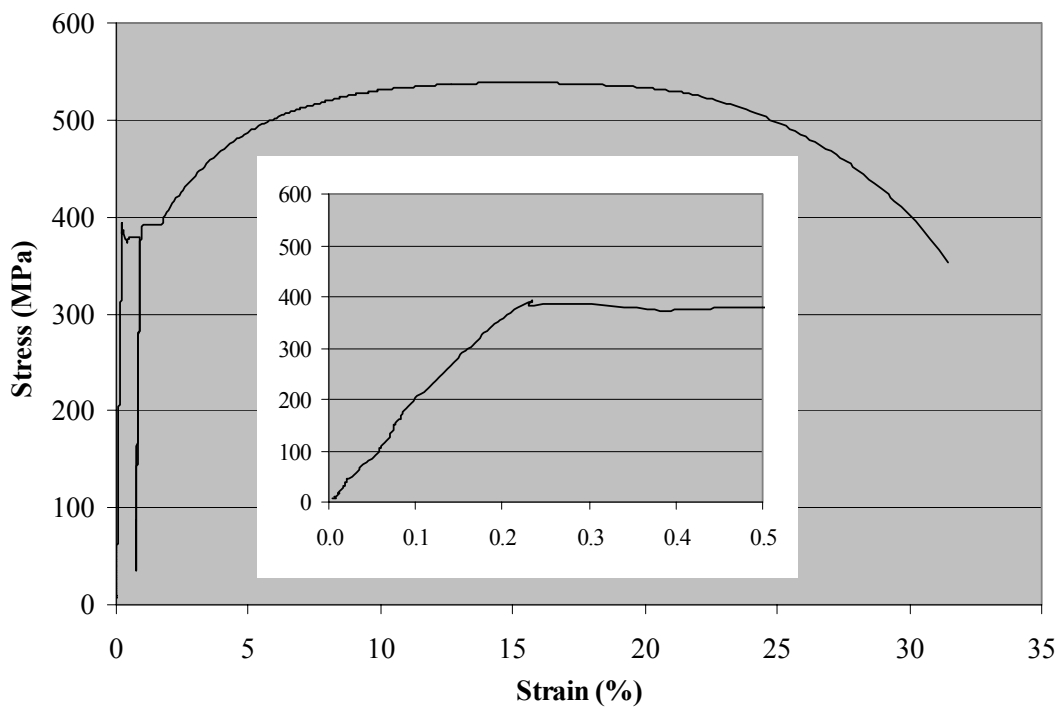
Experimental Study

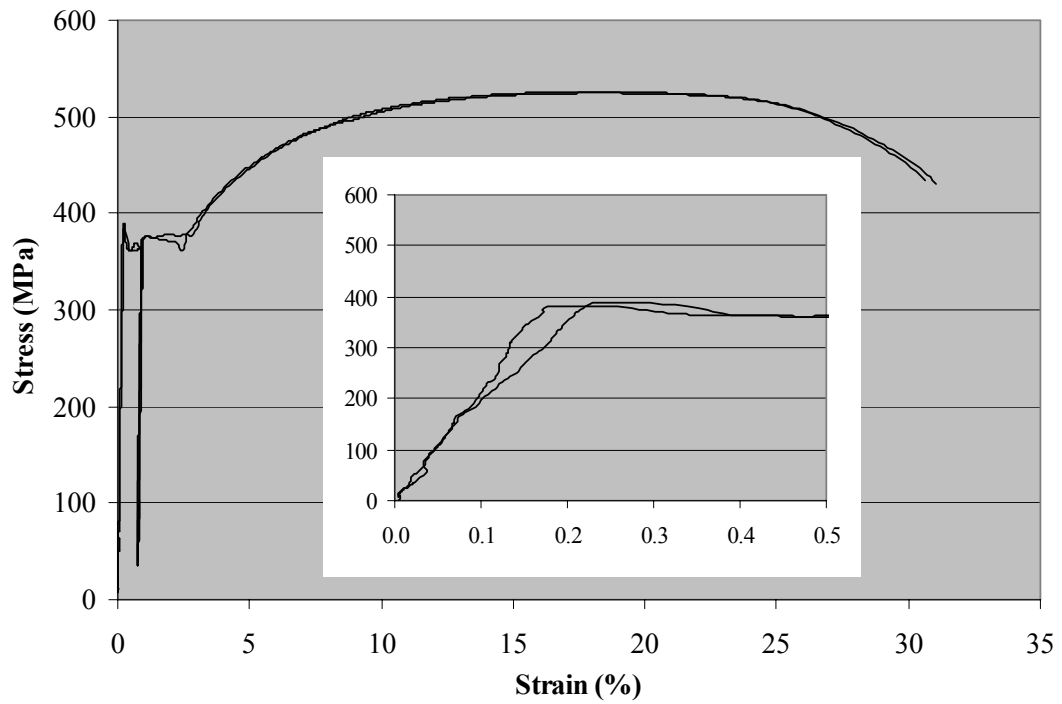
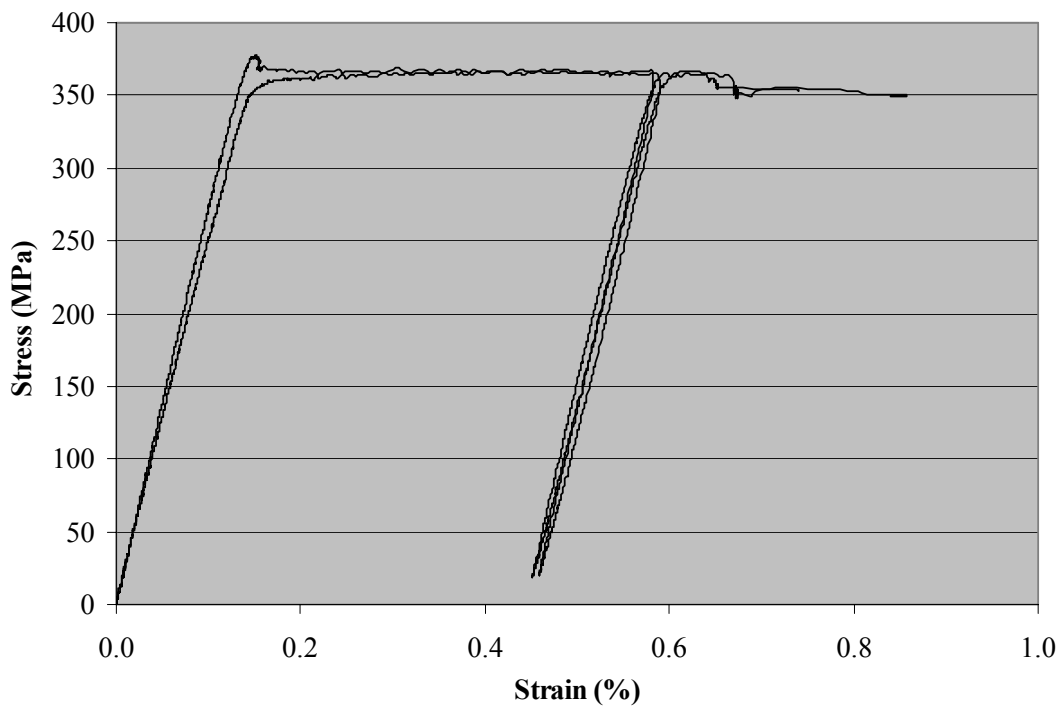
Tensile Coupon Tests

Square Hollow Section (200 x 6.3 mm)

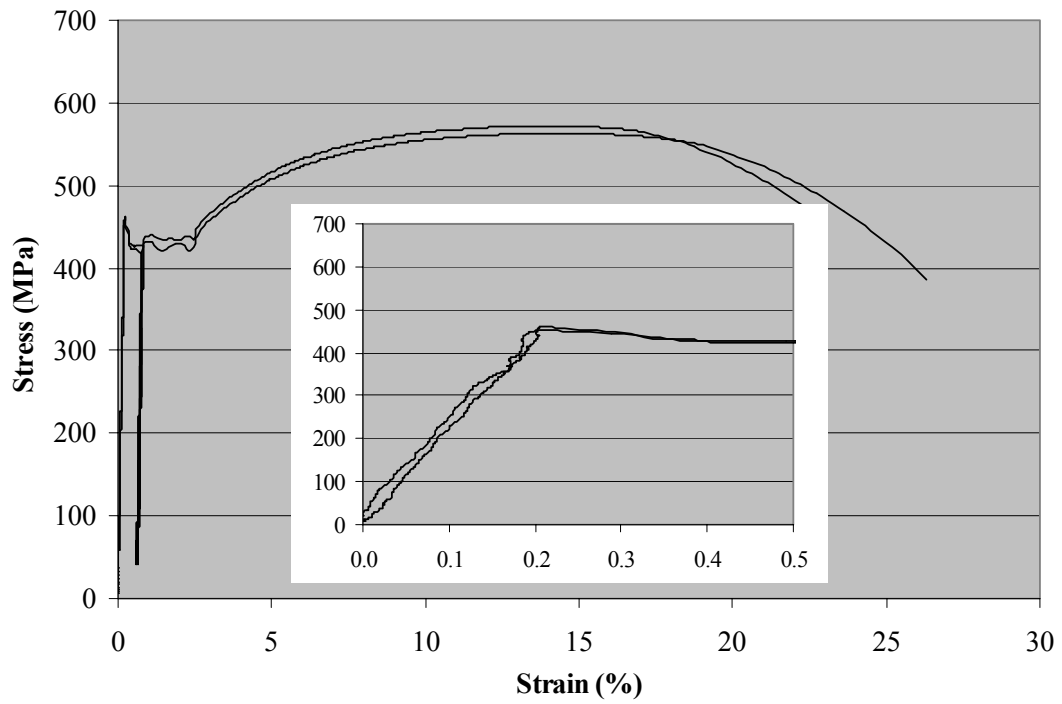


Square Hollow Section (200 x 12.5 mm)



Gusset Plate ($t_p = 12$ mm)**Gusset Plate ($t_p = 20$ mm)¹⁾**

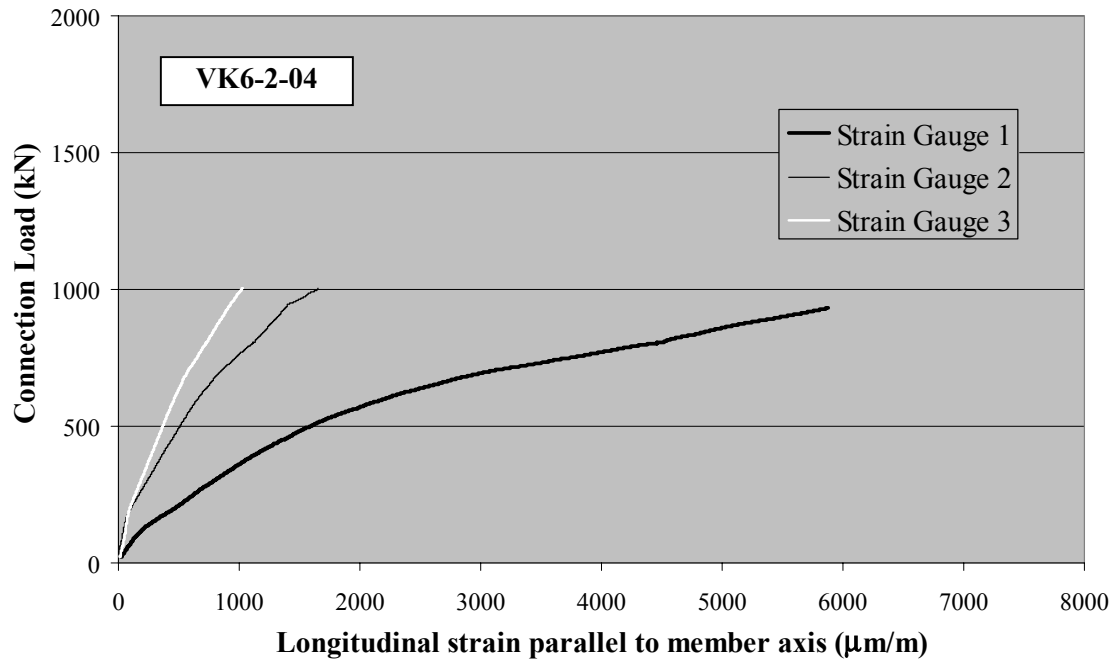
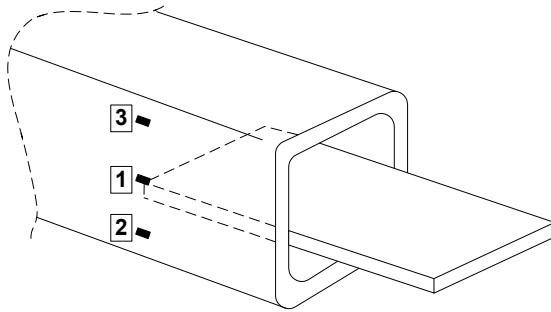
¹⁾ Gauge had to be removed beyond the yield plateau

Gusset Plate ($t_p = 25$ mm)

Strain Gauge Measurements

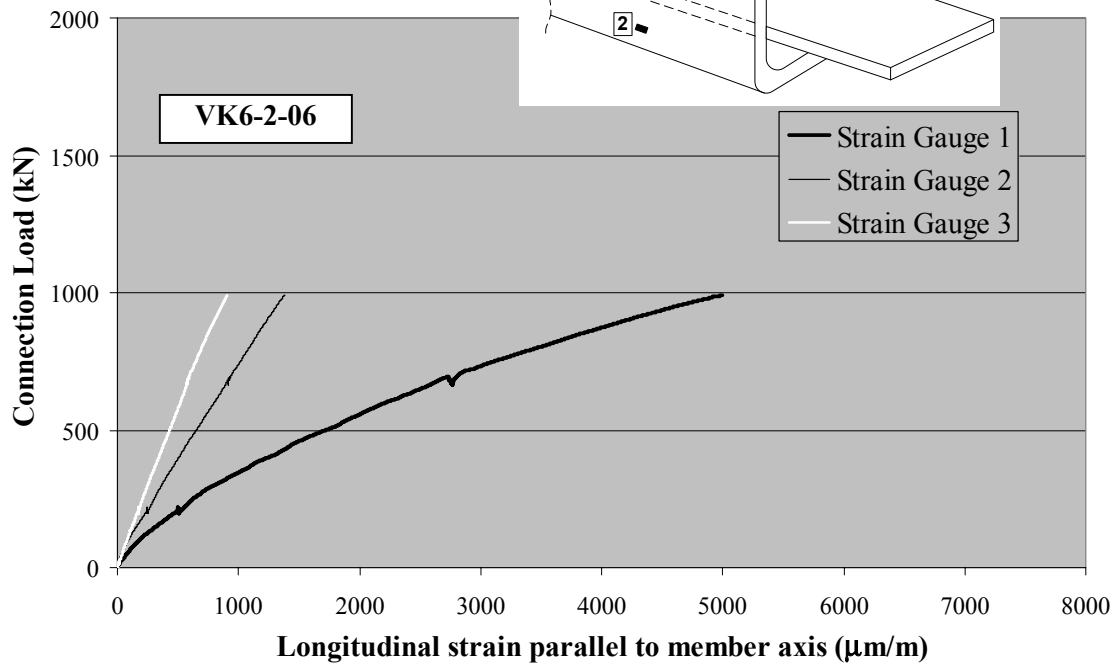
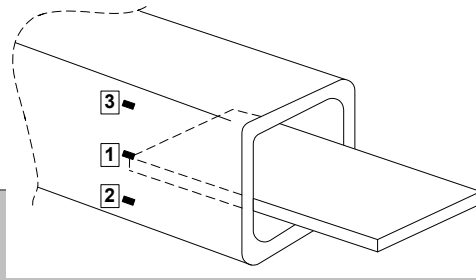
The following graphs show the strains in z-direction (along the axis of the connection) for each specimen. The exact location of each strain gauge can be found in Figure 7.2 in chapter 7.

Strain Gauge Measurements on the Hollow Section

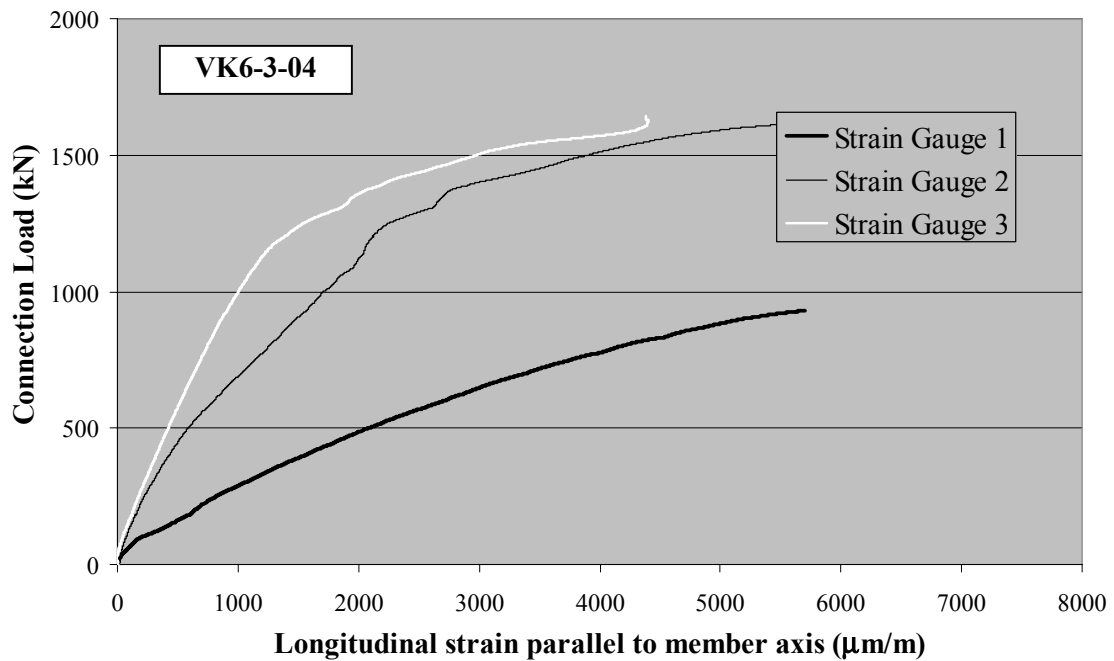


Specimen	h_i (mm)	t_i (mm)	t_p (mm)	w_p (mm)	L_w (mm)	w (mm)	N_{ux} (kN)	Failure Mode
VK6-2-04	200	6.4	12.5	187	160	400	1003	Shear lag failure of the plate and plate tensile failure imminent

Strain Gauge Measurements on the Hollow Section (contd.)

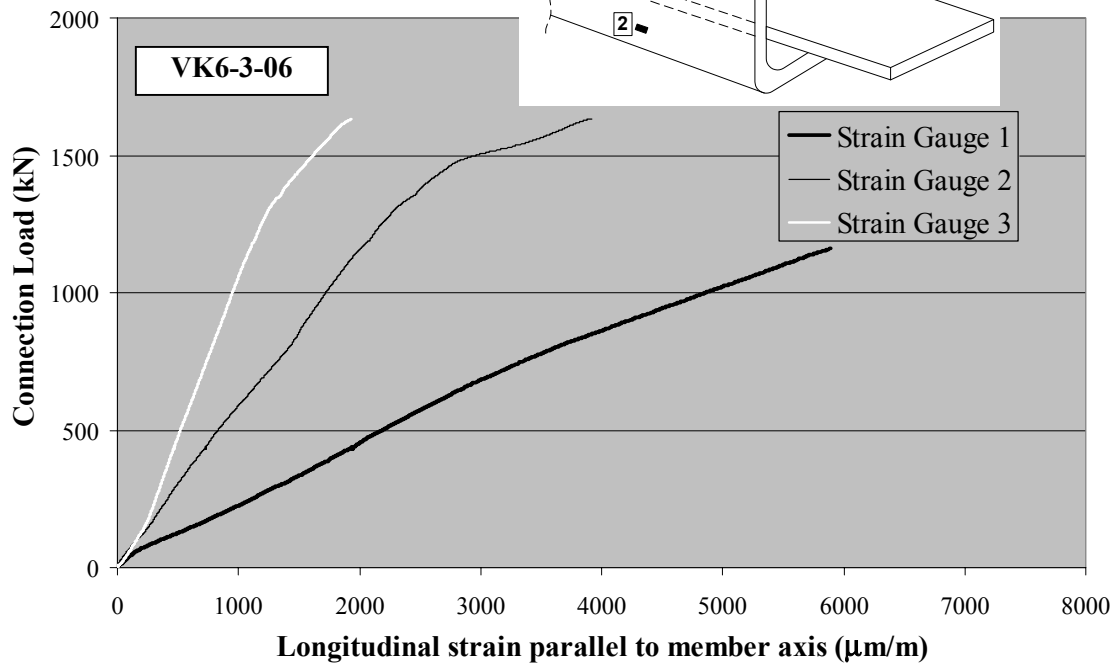
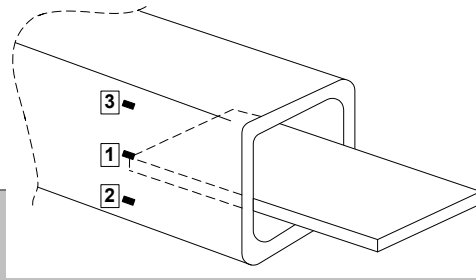


Specimen	h_i (mm)	t_i (mm)	t_p (mm)	w_p (mm)	L_w (mm)	w (mm)	N_{ux} (kN)	Failure Mode
VK6-2-06	200	6.4	12.5	187	240	400	990	Plate tensile failure

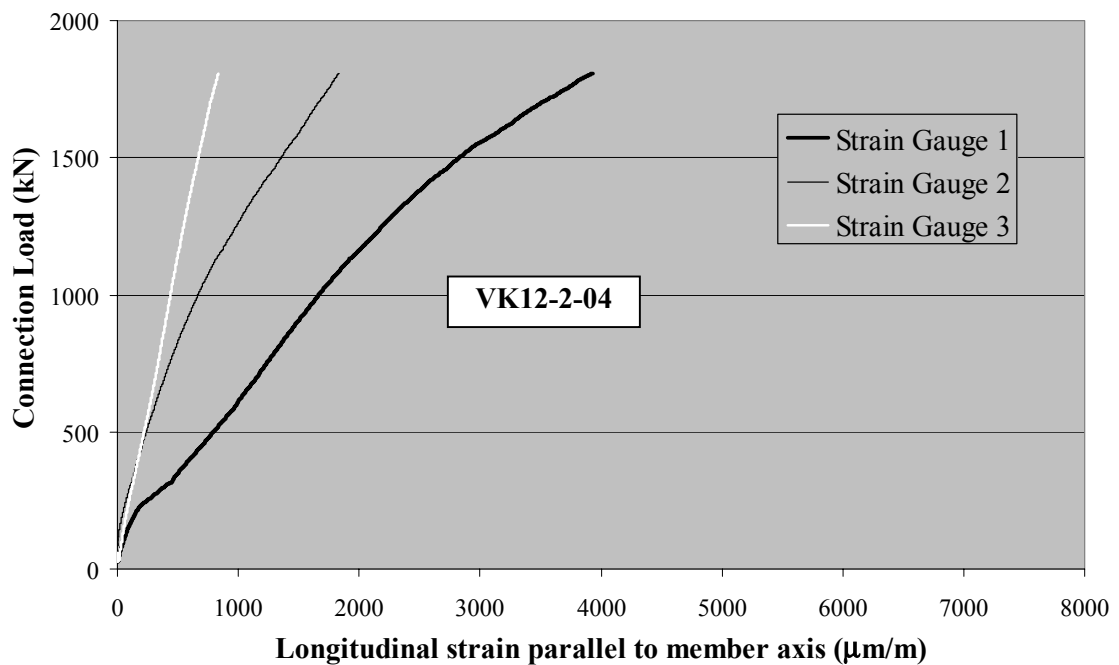


Specimen	h_i (mm)	t_i (mm)	t_p (mm)	w_p (mm)	L_w (mm)	w (mm)	N_{ux} (kN)	Failure Mode
VK6-3-04	200	6.4	20.0	187	160	400	1646	Plate tensile failure

Strain Gauge Measurements on the Hollow Section (contd.)

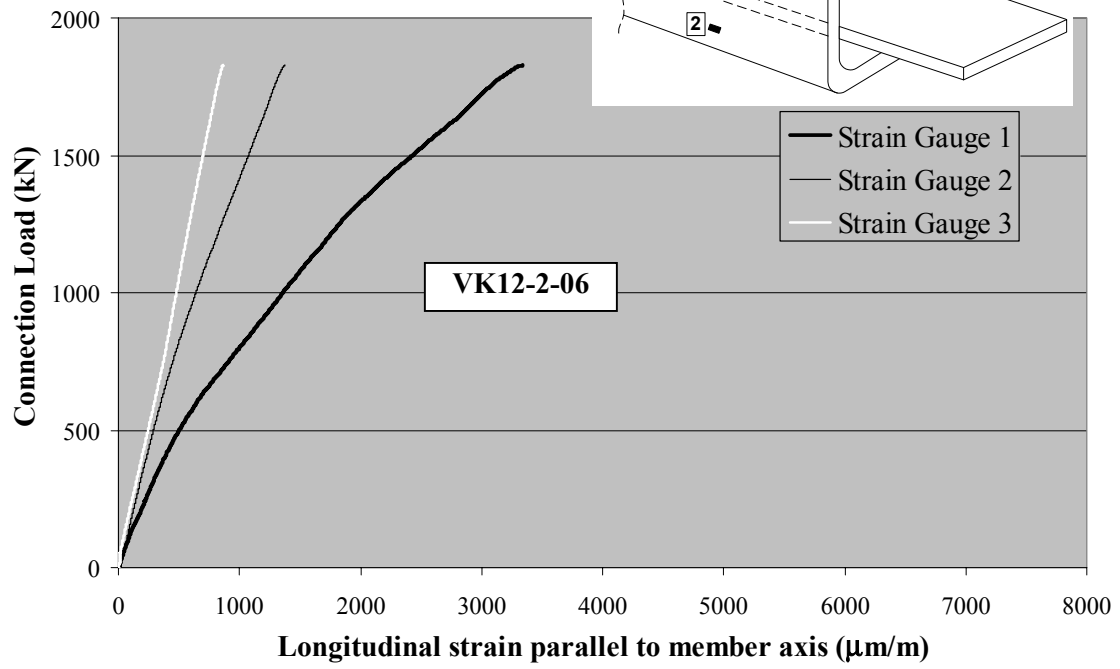


Specimen	h_i (mm)	t_i (mm)	t_p (mm)	w_p (mm)	L_w (mm)	w (mm)	N_{ux} (kN)	Failure Mode
VK6-3-06	200	6.4	20.0	187	240	400	1632	Plate tensile failure



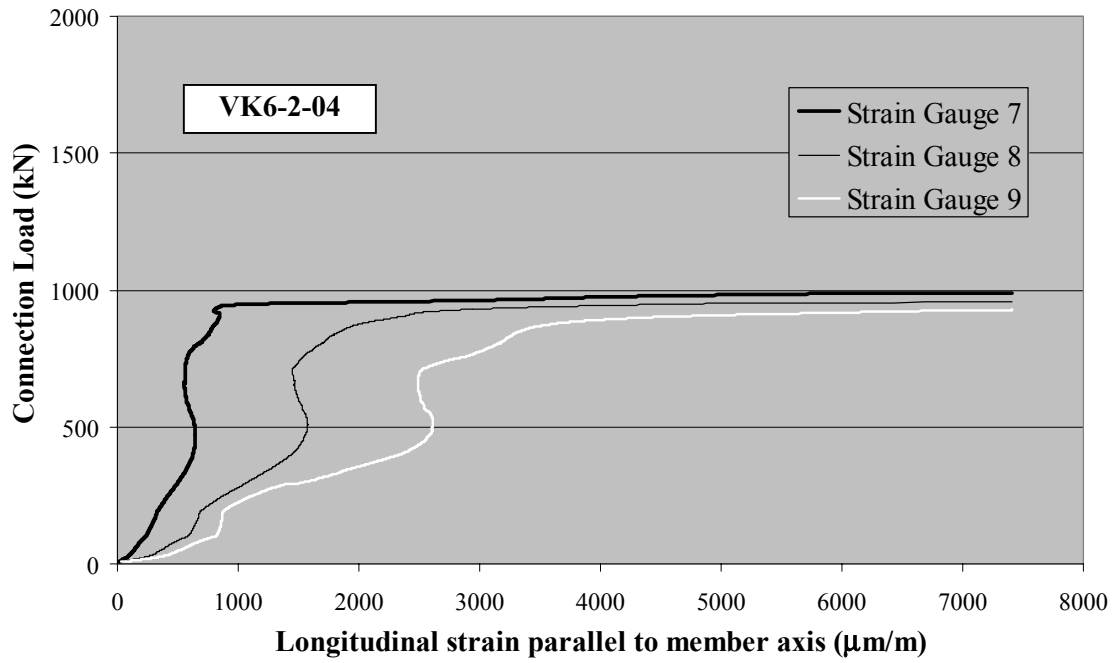
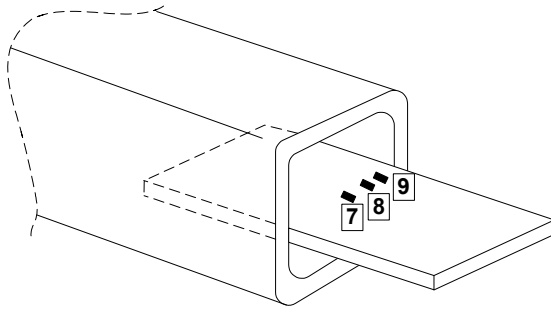
Specimen	h_i (mm)	t_i (mm)	t_p (mm)	w_p (mm)	L_w (mm)	w (mm)	N_{ux} (kN)	Failure Mode
VK12-2-04	199	12.4	24.7	174	160	398	1808	Plate tensile failure

Strain Gauge Measurements on the Hollow Section (contd.)



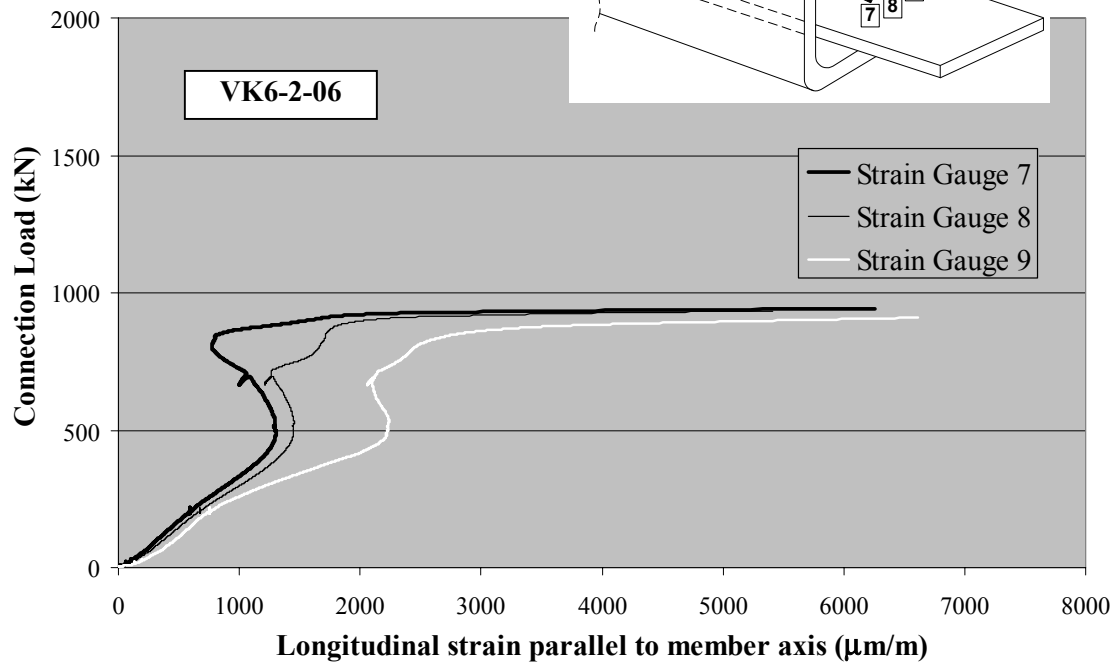
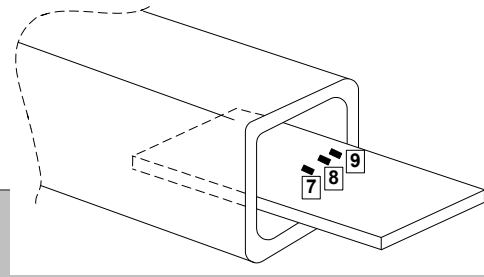
Specimen	h_i (mm)	t_i (mm)	t_p (mm)	w_p (mm)	L_w (mm)	w (mm)	N_{ux} (kN)	Failure Mode
VK12-2-06	199	12.4	24.7	174	240	398	1828	Plate tensile failure

Strain Gauge Measurements on the Gusset Plate

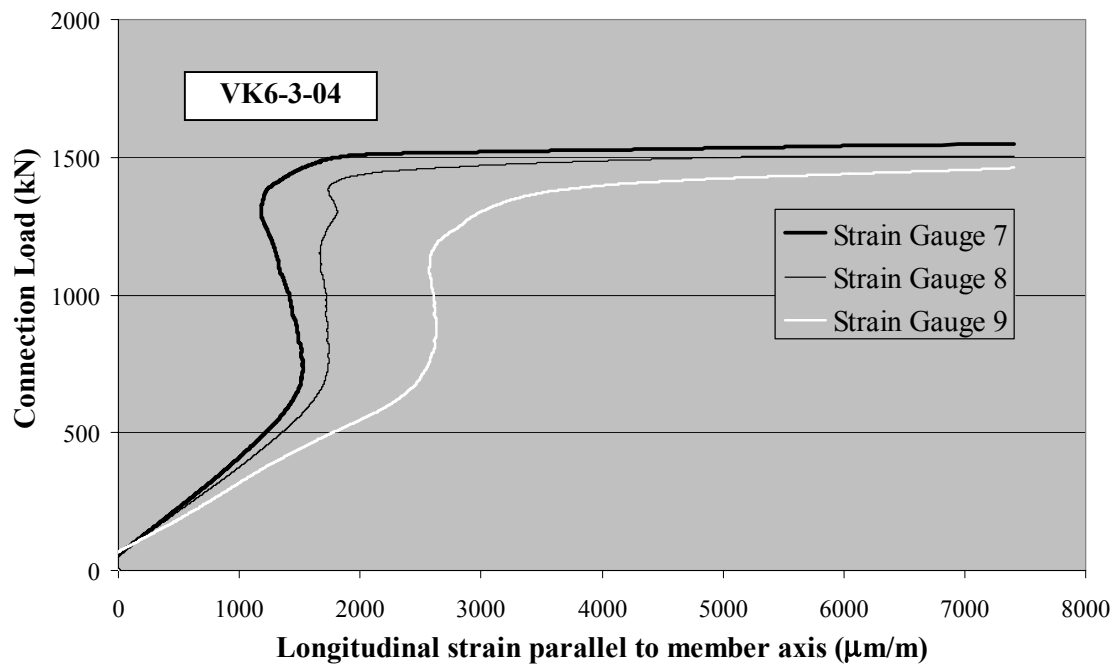


Specimen	h_i (mm)	t_i (mm)	t_p (mm)	w_p (mm)	L_w (mm)	c (mm)	N_{ux} (kN)	Failure Mode
VK6-2-04	200	6.4	12.5	187	160	800	1003	Shear lag failure of the plate and plate tensile failure imminent

Strain Gauge Measurements on the Gusset Plate (contd.)

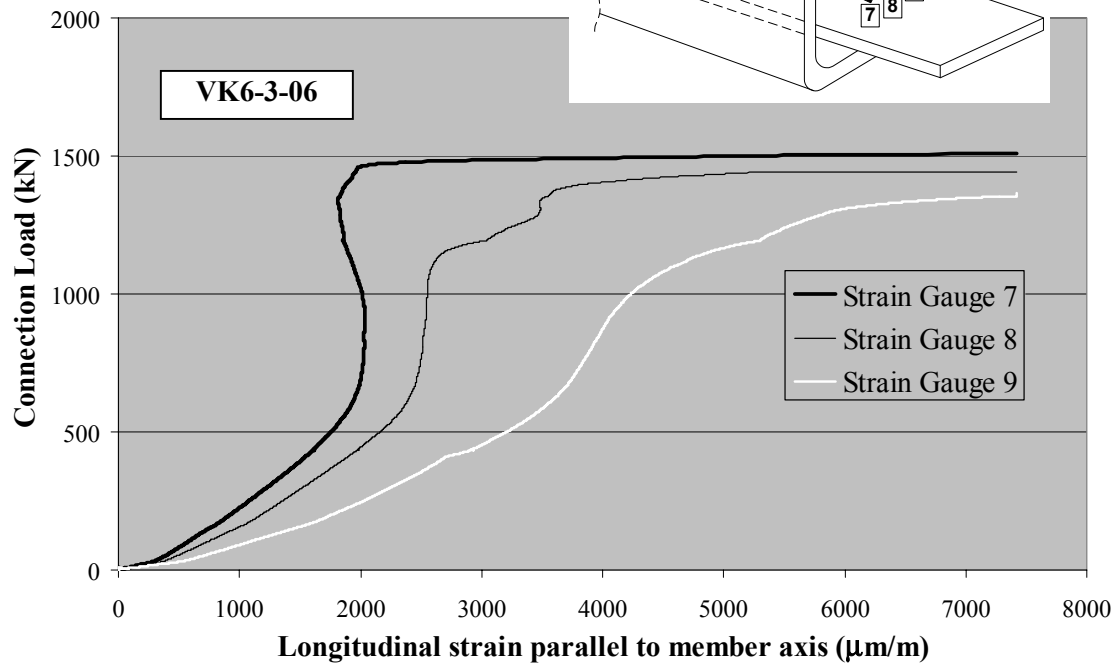
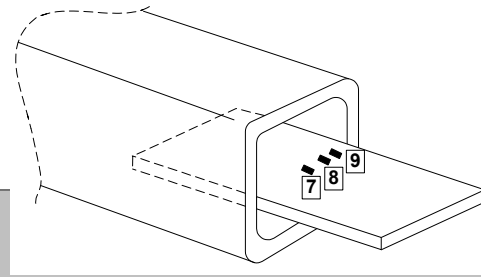


Specimen	h_i (mm)	t_i (mm)	t_p (mm)	w_p (mm)	L_w (mm)	c (mm)	N_{ux} (kN)	Failure Mode
VK6-2-06	200	6.4	12.5	187	240	800	990	Plate tensile failure

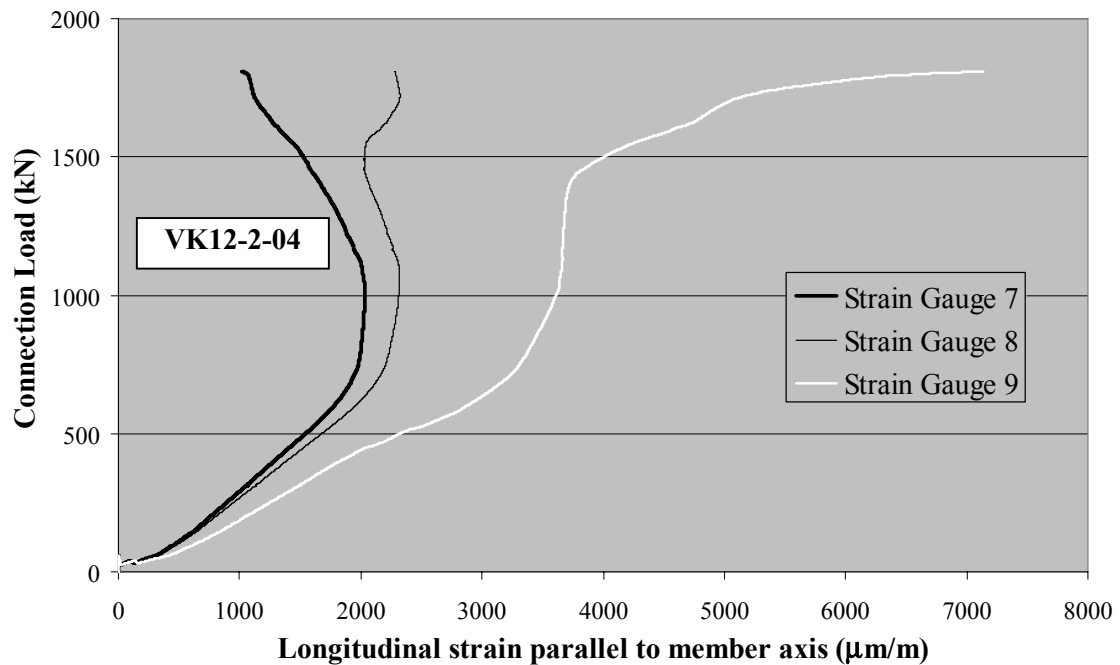


Specimen	h_i (mm)	t_i (mm)	t_p (mm)	w_p (mm)	L_w (mm)	c (mm)	N_{ux} (kN)	Failure Mode
VK6-3-04	200	6.4	20.0	187	160	800	1646	Plate tensile failure

Strain Gauge Measurements on the Gusset Plate (contd.)

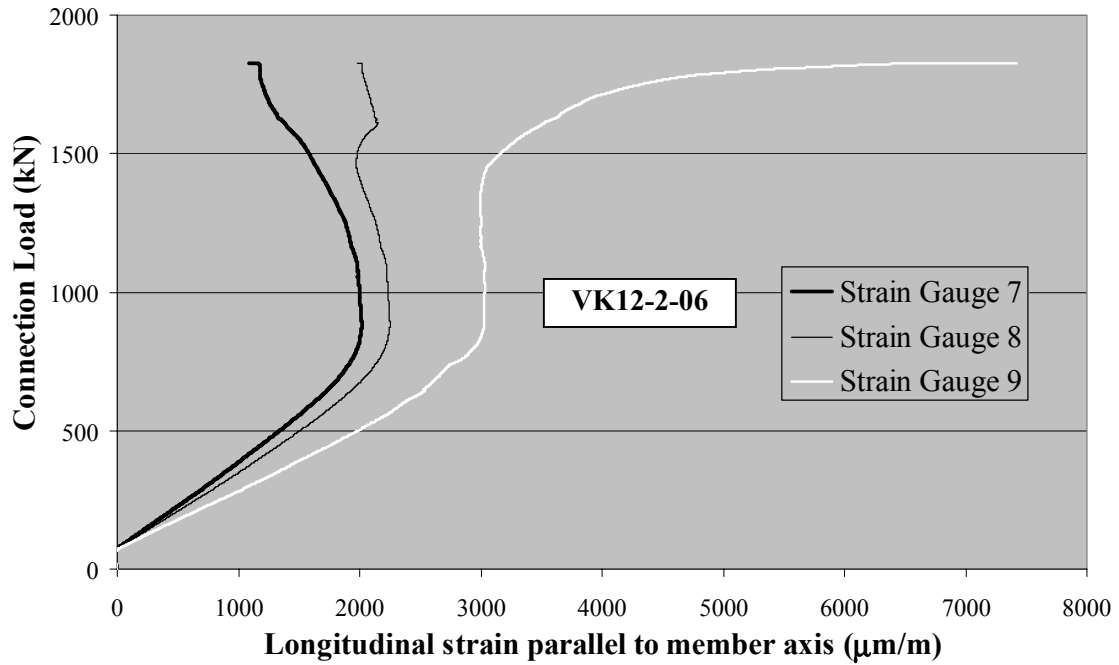
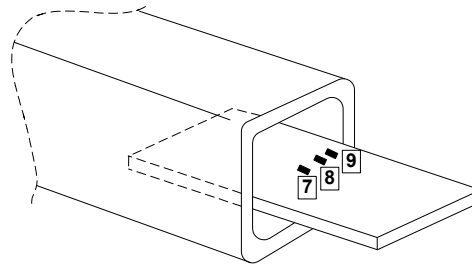


Specimen	h_i (mm)	t_i (mm)	t_p (mm)	w_p (mm)	L_w (mm)	c (mm)	N_{ux} (kN)	Failure Mode
VK6-3-06	200	6.4	20.0	187	240	800	1632	Plate tensile failure



Specimen	h_i (mm)	t_i (mm)	t_p (mm)	w_p (mm)	L_w (mm)	c (mm)	N_{ux} (kN)	Failure Mode
VK12-2-04	199	12.4	24.7	174	160	797	1808	Plate tensile failure

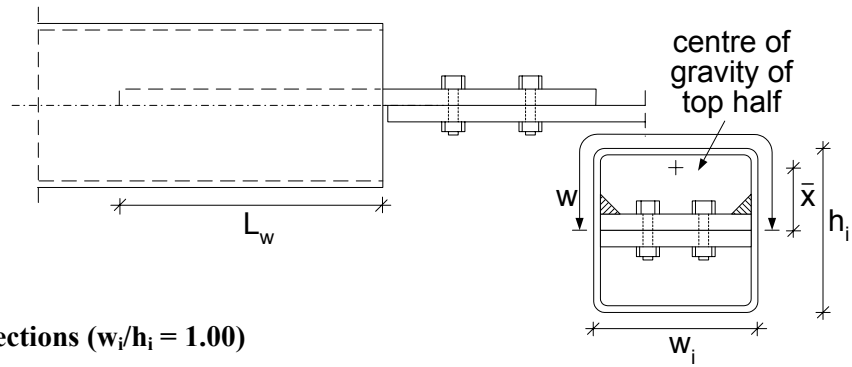
Strain Gauge Measurements on the Gusset Plate (contd.)



Specimen	h_i (mm)	t_i (mm)	t_p (mm)	w_p (mm)	L_w (mm)	c (mm)	N_{ux} (kN)	Failure Mode
VK12-2-06	199	12.4	24.7	174	240	797	1828	Plate tensile failure

Numerical Study

Numerical results

Results for square connections ($w_i/h_i = 1.00$)

Connection	Properties						Parameter			Results	
	w_i (mm)	h_i (mm)	L_w (mm)	w (mm)	\bar{x} (mm)	N_{yi} (kN)	w_i/h_i	L_w/w	\bar{x}/L_w	Connection strength N_{uFE} (kN)	N_{uFE}/N_{yi}
P6 3 04	200	200	160	400	75.0	1144	1.00	0.40	0.47	1049	0.92
P6 3 05			200					0.50	0.38	1243	1.09
P6 3 06			240					0.60	0.31	1397	1.22
P6 3 07			280					0.70	0.27	1513	1.32
P6 3 08			320					0.80	0.23	1559	1.36
P6 3 09			360					0.90	0.21	1575	1.38
P6 3 10			400					1.00	0.19	1587	1.39
P6 3 11			440					1.10	0.17	1590	1.39
P6 3 12			480					1.20	0.16	1590	1.39

Results for rectangular connections with $w_i/h_i = 0.67$

Connection	Properties						Parameter			Results	
	w_i (mm)	h_i (mm)	L_w (mm)	w (mm)	\bar{x} (mm)	N_{yi} (kN)	w_i/h_i	L_w/w	\bar{x}/L_w	Connection strength N_{uFE} (kN)	N_{uFE}/N_{yi}
R15 3 04	200	300	200	500	80.0	1450	0.67	0.40	0.40	1236	0.85
R15 3 06			300					0.60	0.27	1636	1.13
R15 3 08			400					0.80	0.20	1868	1.29
R15 3 10			500					1.00	0.16	1961	1.35
R15 3 12			600					1.20	0.13	1979	1.36

Results for rectangular connections with $w_i/h_i = 0.50$

Connection	Properties						Parameter			Results	
	w_i (mm)	h_i (mm)	L_w (mm)	w (mm)	\bar{x} (mm)	N_{yi} (kN)	w_i/h_i	L_w/w	\bar{x}/L_w	Connection strength N_{uFE} (kN)	N_{uFE}/N_{yi}
R20 3 04	200	400	240	600	83.3	1756	0.50	0.40	0.35	1429	0.81
R20 3 06			360					0.60	0.23	1865	1.06
R20 3 08			480					0.80	0.17	2173	1.24
R20 3 10			600					1.00	0.14	2309	1.31
R20 3 12			720					1.20	0.12	2342	1.33

Lebenslauf

Persönliche Daten

Vor- und Zuname	Silke Willibald
Geburtsdatum	5.10.1973
Geburtsort	Karlsruhe
Eltern	Dipl. Ing. Dieter Willibald, Baudirektor Ulrike Willibald, geb. Stracke
Familienstand	verheiratet

Ausbildung

08/83 - 09/92	Kant-Gymnasium, Karlsruhe Abschluß: Abitur
10/92 - 07/99	Studium des Bauingenieurwesens, Universität Karlsruhe Abschluß: Diplom-Bauingenieur
07/99 – 12/00	Gast-Wissenschaftlicher an dem Department of Civil Engineering an der University of Toronto, Kanada

Berufstätigkeit

10/94 - 04/96	Wissenschaftliche Hilfskraft an dem Institut für Technische Mechanik, Universität Karlsruhe (TH)
01/98 - 06/99	Wissenschaftliche Hilfskraft an der Versuchsanstalt für Stahl, Holz und Steine, Universität Karlsruhe (TH)
seit 01/01	Wissenschaftlicher Mitarbeiter an der Versuchsanstalt für Stahl, Holz und Steine, Universität Karlsruhe (TH)